H AND O ISOTOPE SYSTEMATICS IN VOLCANIC GLASS: HYDRATION EXPERIMENTS AND THEIR APPLICATIONS TO VOLCANIC AND HYDROTHERMAL PROCESSES

by

MICHAEL R. HUDAK

A DISSERTATION

Presented to the Department of Earth Sciences
and the Division of Graduate Studies of the University of Oregon
in partial fulfillment of the requirements
for the degree of
Doctor of Philosophy

September 2021

DISSERTATION APPROVAL PAGE

Student: Michael R. Hudak

Title: H and O Isotope Systematics in Glass Hydration Experiments and their Applications to Volcanic and Hydrothermal Processes

This dissertation has been accepted and approved in partial fulfillment of the requirements for the Doctor of Philosophy degree in the Department of Earth Sciences by:

Prof. Ilya N. Bindeman	Chairperson/Advisor
Prof. James M. Watkins	Core Member
Prof. Paul J. Wallace	Core Member
Prof. Scott A. Blumenthal	Institutional Representative

and

Andrew Karduna	Interim Vice Provost for Graduate Studies

Original approval signatures are on file with the University of Oregon Division of Graduate Studies.

Degree awarded September 2021

DISSERTATION ABSTRACT

Michael R. Hudak

Doctor of Philosophy

Department of Earth Sciences

September 2021

Title: H and O Isotope Systematics in Glass Hydration Experiments and their Applications to Volcanic and Hydrothermal Processes

The goal of my dissertation is to expand the application of H_2O, δD, and $\delta^{18}O$ in silicic volcanic glass to a greater diversity of pyroclast cooling, degassing, and rehydration histories. All pyroclasts must cool from magmatic temperatures and those at Earth's surface, which can affect the distribution of H_2O and its constituent isotopes in glass. Vapor hydration experiments of silicic glass constrain H_2O solubility and diffusivity in glass between 175°C and 375°C. Modeling of the experimental data demonstrates that H_2O diffusivities approximate extrapolations of high temperature relationships, but H_2O solubility in glass is at least 1.5 wt% higher than predicted by extrapolating H_2O solubilities in melts. Next, I evaluate the time evolution of δD in experimental glasses with an isotope reaction-diffusion model. Below 250°C, the δD fractionation between glass and H_2O vapor ($10^3\ln\alpha_{g\text{-}v}$) is between −25‰ and −33‰, overlapping with low temperature D/H $10^3\ln\alpha_{glass\text{-}H2O}$ values. The boundary composition of the model controls the bulk glass composition rather than reactions of H_2O_m to OH^- internal to the glass during hydration. These results enable interpretation of H_2O, δD, and $\delta^{18}O$ in natural samples over a large range of temperature conditions, which I first apply to cooling ignimbrites from the 7700 BP Mt. Mazama eruption and the 1912 Novarupta

eruption. This work also highlights that glass hydration of pumaceous can occur rapidly over days to months and lock in a δD value that records local meteoric waters as a paleoclimate proxy. Finally, I show that glass rehydration can occur even more rapidly on the timescales in eruptive volcanic plumes with meteoric water sources using H_2O–δD compositions in a suite of tephras from the 2009 eruption of Redoubt volcano. Waning influence of a summit glacier has no effect on tephra compositions, suggesting moist air entrainment is the rehydration source. Furthermore, H_2O diffusion modeling illustrates that the temperatures at which erupted material comes into contact with an H_2O is more important than the quench rate of the pyroclast as rehydration can occur at the fastest quench rates if H_2O is available. Tephra H_2O–δD compositions therefore record water-glass interactions in multiple volcanic environments.

CURRICULUM VITAE

NAME OF AUTHOR: Michael R. Hudak

GRADUATE AND UNDERGRADUATE SCHOOLS ATTENDED:

University of Oregon, Eugene, Oregon, USA
The Pennsylvania State University, State College, Pennsylvania, USA
Amherst College, Amherst, Massachusetts, USA

DEGREES AWARDED:

Doctor of Philosophy, Earth Sciences, 2021, University of Oregon
Master of Science, Geosciences, 2016, The Pennsylvania State University
Bachelor of Arts, Geology and Environmental Studies, 2012, Amherst College

AREAS OF SPECIAL INTEREST:

Isotope Geochemistry
Volcanology
Diffusion
Paleoclimate

PROFESSIONAL EXPERIENCE:

Graduate Employee, University of Oregon, 2016-2021

Teaching Assistant, The Pennsylvania State University, 2013-2016

Post-baccalaureate Researcher, Los Alamos National Laboratory, 2012-2013

GRANTS, AWARDS, AND HONORS:

Emeritus Faculty Tribute Fund, University of Oregon, 2020

Bruce L. "Biff" Reed Scholarship, Geological Society of America, 2019

Good Citizen Award, University of Oregon, 2019

James C. and Mary Douglass Stovall Memorial Scholarship, University of Oregon, 2019

John Mason Clarke 1877 Fellowship, Amherst College, 2018, 2017, 2013

Jay M. McMurray Scholarship, University of Oregon, 2018, 2017

Outstanding Teaching Assistant Award, University of Oregon, 2017

Graduate Student Research Grant, Geological Society of America, 2016

Paul D. Krynine Scholarship, The Pennsylvania State University, 2015, 2014

Northeast Section Travel Grant, Geological Society of America, 2015

Hess Corporation Exploration & Technology Scholarship, The Pennsylvania State University, 2014

Charles E. Knopf Sr. Memorial Scholarship, The Pennsylvania State University, 2014

Hiroshi and Koya Ohmoto Graduate Fellowship, The Pennsylvania State University, 2014

Funds for Excellence in Graduate Recruitment, The Pennsylvania State University, 2013

David F. Quinn Memorial Prize, Amherst College, 2012

Richard M. Foose Award, Amherst College, 2011

PUBLICATIONS:

Giachetti, T., **Hudak, M. R.**, Shea, T., Bindeman, I. N., & Hoxsie, E. C. (2020). D/H ratios and H_2O contents record degassing and rehydration history of rhyolitic magma and pyroclasts. *Earth and Planetary Science Letters, 530.* https://doi.org/10.1016/j.epsl.2019.115909

Hudak, M. R., & Bindeman, I. N. (2020). Solubility, diffusivity, and O isotope systematics of H_2O in rhyolitic glass in hydrothermal temperature experiments. *Geochimica et Cosmochimica Acta*, *283*, 222–242. https://doi.org/10.1016/j.gca.2020.06.009

Hudak, M. R., & Bindeman, I. N. (2018). Conditions of pinnacle formation and glass hydration in cooling ignimbrite sheets from H and O isotope systematics at Crater Lake and the Valley of Ten Thousand Smokes. *Earth and Planetary Science Letters*, *500*, 56–66. https://doi.org/10.1016/j.epsl.2018.07.032

Smye, A., Seman, S., **Hudak, M.**, & Crispin, K. (2017). Rates of mantle cooling and exhumation during rifting constrained by REE-in-pyroxene speedometry. *Geochemistry Geophysics Geosystems*. https://doi.org/10.1002/2017GC006957

Wang, P., **Hudak, M. R.**, Lerner, A., Grubbs, R. K., Wang, S., Zhang, Z., et al. (2014). X-ray scattering of calcite thin films deposited by atomic layer deposition: Studies in air and in calcite saturated water solution. *Thin Solid Films, 565*. https://doi.org/10.1016/j.tsf.2014.06.032

ACKNOWLEDGMENTS

I would like to express appreciation to Dr. Ilya Bindeman for taking me on as a student and helping me to have a productive five years here. I also thank my Dr. James Watkins, Dr. Paul Wallace, Dr. Scott Blumenthal, and Dr. Thomas Giachetti for their insights and feedback during this process. In addition, special thanks are due to Dr. James Palandri, whose assistance in the Stable Isotope Laboratory made this work possible. I also thank my coauthors on manuscripts that have come out of my research (including work not presented in this dissertation). I acknowledge that I have benefitted from countless conversations with friends, staff, and faculty at the University of Oregon. Of these, special thanks are due to Madison Myers, Allan Lerner, David Zakharov, and Rachel Hampton. Finally, I would like to thank my sister, Sara, my parents, Mark and Bonnie, and my partner, Nick Holschuh, without whom none of this would have been possible. The investigation was supported in part by a National Science Foundation grant to Dr. Ilya Bindeman, EAR 1822977, two Geological Society of America Graduate Student Scholarships, two Amherst College John Mason Clarke 1877 Fellowships, and 4 scholarships from the Department of Earth Science at the University of Oregon.

For my friends and family, near and far

TABLE OF CONTENTS

Chapter Page

Chapter Page

Chapter Page

Chapter Page

Chapter Page

Chapter Page

LIST OF FIGURES

Figure Page

Chapter II

Chapter III

Figure Page

Chapter V

Chapter VI

Figure Page

LIST OF TABLES

Table Page

Chapter III

Chapter VI

CHAPTER I

INTRODUCTION

Nearly all chemical and physical processes on Earth's surface involve water. Volcanic glass (ash, pumice, and obsidian) and the water that is dissolved within it record a history of Earth surface processes from its eruption as a magma to its subsequent interactions with water in the environment. Isotopes of hydrogen and oxygen are powerful tools that can disentangle various geological processes and water-rock interactions. How these isotopes track water loss and gain from silicic volcanic glasses over a wide range of temperature conditions is at the core of this work.

Through a combination of laboratory experiments and natural samples, this research enables the use of H_2O – and its constituent isotopes (denoted by δD and $\delta^{18}O$) – in glass to be applied to volcanic processes and paleoclimate reconstructions. While behavior of H and O isotopes is relatively well understood at low and high temperatures, this dissertation focuses primarily on hydration of degassed volcanic glass by water vapor at temperatures near 100°C up to the glass transition temperature (T_g), above which the glass begins to act rheologically like a liquid melt (~500°C). This previously poorly explored range characterizes cooling volcanic deposits that interact with environmental waters. Water is critically important in magmatic and volcanic processes at high temperatures but has barely been studied in glasses below T_g and above standard temperature and pressure. This work aims to constrain H_2O solubility and diffusivity as well as hydrogen and oxygen isotope fractionations between glass and H_2O vapor in this temperature gap, through which all volcanic glass must cool.

The first part of the dissertation (Chapters II and III) present glass hydration experiments that constrain properties of H_2O in glass and hydrogen and oxygen isotope fractionations between 175°C and 375°C. The second part of the dissertation applies these results to natural systems where glass hydration occurs at different temperatures over different timescales. Glasses from cooling ignimbrites interrogate lower temperature hydration over weeks to years (Chapter IV) while recently erupted ashes address

hydration in explosive volcanic ash plumes near T_g on timescales of seconds to tens of seconds (Chapter V).

In Chapter II, I use glass hydration experiments to constrain fundamental properties of H_2O in glass, such as solubility and diffusivity. At magmatic temperatures and atmospheric pressure, H_2O solubility in silicic melt is very low (<0.2 wt%) while H_2O diffusivity (D_{H2O}) is very fast. Conversely, at Earth surface temperatures H_2O solubility can be quite high (>4.0 wt%) but with an exceedingly slow D_{H2O}. My experiments assess these properties over an intermediate temperature range of 175°C to 375°C. This chapter also develops a novel oxygen isotope thermometer ($\delta^{18}O$ of water-in-glass or $\delta^{18}O_{wig}$) by determining the equilibrium partitioning of oxygen isotopes as a function of temperature between oxygen within the silicate structure of the glass and the oxygen bound as H_2O dissolved in glass.

In Chapter III, I present a 1D finite difference isotope diffusion-reaction model to understand the equilibrium and kinetic fractionations of hydrogen isotopes in the glass-H_2O vapor system using the experiments from Chapter II. Water in melts and glasses can occur as either H_2O_m or OH^- species and the light isotope of hydrogen (^1H or H) is preferentially incorporated into OH^- groups (rather than H_2O_m) compared to the heavy isotope (^2H or D). The extent to which H_2O_m can convert to OH^- as it diffuses into glass at submagmatic temperatures is unknown and could have a strong effect on bulk glass δD compositions. This work evaluates the extent to which such respeciation is possible at temperatures below T_g and how it may affect the evolution of δD in glass through time.

In Chapter IV, I use δD and $\delta^{18}O$ measured in natural glass of the Crater Lake and Katmai National Parks to investigate the role of H_2O in ignimbrite cooling and the conditions of iconic pinnacle (low temperature fumarole) formation. This chapter compares glasses from hydrothermal features in ignimbrite sheets from these two eruptions. Those from the historical eruption of Novarupta, Alaska in 1912 are shallow in the deposits and offer a complementary view to glasses from the pinnacles exposed in deeply eroded sections of ignimbrite sheets at Crater Lake, Oregon emplaced by the eruption of Mt. Mazama around 7,700 years ago allowing deeper insight into the bottom of the pinnacles. This chapter uses H and O isotope systematics constrained in Chapters II and III.

Chapter V explores another natural application provided by the syn-eruptive rehydration of volcanic ash at Redoubt Volcano, AK using exceptionally well-documented and well-sampled historic explosions from its 2009 eruption. The H_2O–δD compositions of the ash are used to discriminate between secondary hydration by local meteoric water sources and volcanic degassing. This work tests if volcanic glass can be hydrated very rapidly (seconds to minutes) during an eruption in the volcanic plume. The role of eruption through a glacier on this process is evaluated by comparing early and late eruptive products as the ice was cleared from the vent part way through the eruption. Using the experimentally constrained H_2O solubility and D_{H2O} from Chapter II, the timescales of hydration and quenching are compared. These results are used to infer how moisture is entrained in and distributed throughout volcanic plumes.

Finally, Chapter VI constrains the composition of two new H_2O and δD reference materials, or standards, developed at the University of Oregon in the course of this study: an EMORB basaltic pillow glass from the East Pacific Rise (UOB) and the IDDP-1 drill core rhyolite from Krafla, Iceland (UOR).

Chapter II is co-authored with Ilya N. Bindeman and was published in *Geochimica et Cosmochimica Acta* in 2020. Chapter III is co-authored with Ilya N. Bindeman, James M. Watkins, and Jacob B. Lowenstern and is under review at *Geochimica et Cosmochimica Acta*. Chapter IV is co-authored with Ilya N. Bindeman and was published in *Earth and Planetary Science Letters* in 2018. Chapter V is co-authored with Ilya N. Bindeman, Matthew W. Loewen, and Thomas Giachetti and is under review at *Geophysical Research Letters*. Chapter VI is in preparation for submission to *Chemical Geology*. Ilya N. Bindeman and Michael R. Hudak will submit Chapter VI (as joint first authors with coequal contributions) with co-authors James P. Palandri, Haiping Qi, Rastislav Milovský, Richard L. Hervig, and Michael R. Perfit.

CHAPTER II

SOLUBILITY, DIFFUSIVITY, AND O ISOTOPE SYSTEMATICS OF H_2O IN RHYOLITIC GLASS IN HYDROTHERMAL TEMPERATURE EXPERIMENTS

From Hudak, M.R. and Bindeman I.N. (2020). Solubility, diffusivity, and O isotope systematics of H_2O in rhyolitic glass in hydrothermal temperature experiments. *Geochimica et Cosmochimica Acta*, 283, 222-242.

1. Introduction

Water in volcanic glasses and melts has long been recognized as an important tool for understanding magmatic and volcanic processes, igneous phase equilibria, and timescales of volcanic and post-eruptive processes. The physical properties of hydrous melts are well understood in nature and experiments largely because the devolatilization of magma, which is dominated by the exsolution of H_2O in silicic systems, is a primary driver of eruptions and their explosivity (e.g. Eichelberger and Westrich, 1981; Sparks, 1978). The solubility of H_2O in a melt is function of pressure, temperature, and to a lesser degree, the concentrations of other volatile species, namely CO_2 (e.g. Liu et al., 2005; Newman and Lowenstern, 2002). These variables have been constrained by a large number of high- and low-pressure experiments to constrain pre-eruptive storage conditions and degassing behavior in a magmatic conduit (e.g. Ni and Zhang, 2008; Zhang et al., 1991; Zhang and Behrens, 2000). Diffusivity of water in high-temperature systems is especially important for understanding formation and growth of bubbles and subsequent degassing in volcanic conduits because it limits how rapidly H_2O can diffuse out of the melt and into bubbles (Watkins et al., 2012), which can additionally be used as a geospeedometer (Wilding et al., 1995; Zhang et al., 1997; Xu and Zhang, 2002; Zhang et al., 2007).

At Earth surface temperatures, rehydration (also referred to as secondary hydration) of felsic volcanic glasses has significantly different applications, although correcting for rehydration has allowed for more robust interpretations of volcanic

processes. Rehydration of volcanic glass occurs on long timescales that do not make it readily amenable for even years-long experiments to constrain diffusivity, solubility, glass stability, or isotope exchange. There are a few exceptions that rely on the extremely high resolution of ion microprobe depth profiling of experimental and tephrochronologically constrained obsidians, which provides high spatial resolution to resolve micron-length profiles (Riciputi et al., 2002; Anovitz et al., 2004; Anovitz et al., 2008; Anovitz et al., 2009). Otherwise, carefully selected natural samples of known age have been the primary method for evaluating D_{H2O} over a range of glass compositions (e.g. Friedman et al., 1993b, 1993a; Friedman and Smith, 1960; Seligman et al., 2016). These results enable hydration rind thicknesses in obsidian to be used as a proxy for the age of archeological artifact, with the rate of hydration as a function of time or $t^{0.5}$ (e.g. Liritzis and Laskaris, 2011; Michels et al., 1983). In other studies, bulk analytical approaches have also been attempted in long-term (months to years) hydration experiments of thin-walled volcanic ash with isotopically labeled H_2O to assess isotope exchange (Nolan and Bindeman, 2013; Cassel and Breecker, 2017). Ratios of D/H in volcanic glasses have been employed to estimate the D/H ratios of paleo-meteoric waters at the time of pyroclast emplacement as a proxy for paleoaltitude (Cassel et al., 2009; Cassel et al., 2012; Canavan et al., 2014; Cassel et al., 2014; Dettinger and Quade, 2015; Jackson et al., 2019) and paleoclimate (Colwyn and Hren, 2019).

Few studies have targeted an intermediate temperatures range between Earth surface temperatures and ~400°C, appropriate for cooling ignimbrites and lavas or for the formation of perlites (Friedman et al., 1966; Keating, 2005; Bindeman and Lowenstern, 2016; Randolph-Flagg et al., 2017; Hudak and Bindeman, 2018; Seligman et al., 2018). The dynamics of volcanic glass hydration below the glass transition, which we call "hydrothermal" for simplicity, the temperature at which silicate melts begin to exhibit more brittle (~400°C), glass-like behavior (e.g. Dingwell, 1995; Dingwell and Webb, 1990; Hess and Dingwell, 1996) are less well understood for two primary reasons. First, most materials cool and pass through this temperature range relatively quickly. Second, prolonged time at these temperatures induced glass breakdown to secondary alteration products (e.g. clays and zeolites; Cullen et al., 2019). Additionally, in regimes with very slow cooling, vitreous ignimbrites devitrify and grow crystallites and spherulites

(Watkins et al., 2009; Gardner et al., 2012; Von Aulock et al., 2013; Breitkreuz, 2013; Befus et al., 2015). However, hydrothermal glass hydration occurs in a number of settings including in subglacial (Wilding et al., 2000; Stroncik and Schmincke, 2001; Thien et al., 2015) or submarine eruptions (e.g. Mitchell et al., 2018) and cooling ignimbrites (Keating, 2005; Randolph-Flagg et al., 2017; Hudak and Bindeman, 2018; Seligman et al., 2018) and plays a critical role in the formation of perlite (Friedman et al., 1966; Von Aulock et al., 2013; Bindeman and Lowenstern, 2016). Hydrothermal hydration experiments can provide constrains on H_2O diffusivity and solubility that can aid in interpreting the volatile record of glasses from these settings. Experiments can also help inform both the interpretation of a new oxygen isotope tool that measures the $\delta^{18}O$ of that water-in-glass ($\delta^{18}O_{wig}$) that excludes silicate-bound oxygen and the mechanism of oxygen isotope exchange between glass or rhyolite and water.

In this study, we experimentally investigate the dynamics of glass hydration and the behavior of water in glass over a range of hydrothermal temperature conditions that all glasses pass through during the cooling. We evaluate the extent to which well-constrained relationships between temperature, H_2O solubility, and D_{H2O} can be extrapolated below the glass transition. Furthermore, we seek to understand how oxygen isotopes exchange both between glass and an external fluid and within the glass between the silicate and the water dissolved in glass.

2. Experimental methods

2.1 Experimental materials and material preparation

Three natural obsidians were used in the hydration experiments, two of which are anhydrous and one that has been rehydrated and converted to perlite. The first anhydrous glass (0.08 wt.% H_2O), and the main glass used in all experiments, comes from a low silica rhyolite (LSR) obsidian flow at Newberry volcano, Oregon, USA. (Common abbreviations and notations are provided in Table A1.) Feldspar phenocrysts are rare (<5%) and the obsidian is relatively microlite-poor (Manga, 1998). Electron probe microanalysis (EPMA) give a mean glass SiO_2 of 71.45 wt.% (0.72 wt.%, 1σ) while total alkalis ($Na_2O + K_2O$) are relatively high at 11.15 wt.% (0.39 wt.%, 1σ). Major element concentrations of starting materials and ratios of non-bridging oxygen to tetrahedrally

coordinated cations (NBO/T), which provide structural information about the degrees of polymerization, are given in Tables A1.1-A1.3 and Figure A1.1.

Four particle size fractions were used over the course of the experiments. Particle sizes for abraded LSR glasses were determined using a Microtrac PartAn3D particle size analyzer that gives mean particle dimensions and the calculated effective radius (r_{eff}) of each batch of particles (Trafton et al., 2019; Appendix A2). At 225°C and 375°C, a single size fraction of rounded particles with an effective radius (r_{eff}) of 160 μm were used. At 175°C, three particle sizes were used. Two were rounded and have r_{eff} of 95 μm and 155 μm. The third set of particles were not abraded, but sieved to a size fraction of 53-105 μm, which corresponded to the maximum dimension of the intermediate axis diameter. (In figures, this is given as r = 26-53 μm for comparison to the measured and modeled effective radii of larger particle size.) A later set of experiments at 225°C use these three size fractions, once most of the 160 μm radius particles were consumed. At 275°C, the abraded particles with r_{eff} of 95 μm and 155 μm were used. (Particle sizes are given in Table A2.)

The second anhydrous rhyolite is a high silica rhyolite (HSR) from the Summit Lake flow at Yellowstone, USA (0.15 wt.% H_2O). The glass has 75.11 wt.% SiO_2 (0.51 wt.%, 1σ) and 9.52 wt.% alkalis (0.22 wt.%, 1σ; Table A1.4). The Summit Lake flow has 3-6% crystallinity dominated by quartz and feldspar (Loewen et al., 2017), and these were avoided during by hand-picking glass under a microscope. This glass was only used for experiments at 225°C because of the more limited amount of material available and because it more or less duplicates the major element chemistry of the Nez Perce perlitic rhyolite. Particle size distributions were not made prior to the experiments, so an effective radius is not given.

The third rhyolitic glass comes from the Nez Perce flow which, like the Summit Lake glass, is a rhyolite from the Central Plateau in Yellowstone. This glass is a perlite, a rehydrated high-Si rhyolite glass (76.02 ± 0.54 wt.% SiO_2, 1σ) that is used to assess isotopic exchange between glass and water through time. This perlitic material has onion skin-like, curvilinear fractures with higher water "skins" around central less hydrous spherical cores. The skins naturally separate, sloughing off the obsidian cores as a result of rapid hydration and volume change (Figure 1). Perlite cores and skins have identical

major element compositions within 1σ when normalized on an anhydrous basis. Skins and cores are relatively uniform in size and shape and were not sieved. Perlite skins have shorter dimensions (10s of μm) than the perlite cores (100s of μm). Perlite cores having lower H_2O than the hydration rinds or outer skins, both in their H_2O_{bulk} measurements (<0.75 wt.% vs. ≥2 wt.%) and spot analyses of total H_2O (H_2O_t; <0.5 wt.% vs. ≥1.5 wt.%; Bindeman and Lowenstern, 2016). Crystallinity is low (<5%) and a population of pyroxene microlites exists but does not appear to affect hydration of the glass.

Two waters were used in the hydration experiments. The first and primary H_2O used in the experiments is an isotopically-labeled mixture of water used in earlier hydration experiments (Nolan and Bindeman, 2013) and Fiji Water®. The very high $\delta^{18}O$ values (+56‰) of the H_2O in the Nolan and Bindeman (2013) was useful for their slower, lower T experiments, but was too heavy to be used directly in these experiments in case the glasses approached the $\delta^{18}O$ of the experimental H_2O and required large extrapolations beyond our silicate standards. Fiji Water® is an internal laboratory standard with known compositions for H and O isotopes that allowed us to design a mixture with target $\delta^{18}O$ and δD compositions. The experimental water was analyzed at IsoLab at the University of Washington on a Picarro L2120i cavity ringdown spectrometer (Table A1.5). Samples were measured in duplicate, with each duplicate consisting of a set of 10 analyses, the first 5 of which are discarded to avoid memory effects. Means of $\delta^{18}O$ are (5.93 ± 0.09)‰ and (5.83 ± 0.04)‰, and means of δD are (74.97 ± 1.42)‰ and (76.17 ± 2.22)‰ (errors are 2σ). We use the mean of these duplicate analyses: 5.88‰ $\delta^{18}O$ and 75.6‰ δD. The second experimental H_2O is a mixture of H_2O and D_2O in an approximately 1:1 ratio, which is used specifically for the NanoSIMS diffusion profile measurements. Combinations of water, glasses, and glass size fractions used in the experiments are given in Table A3.

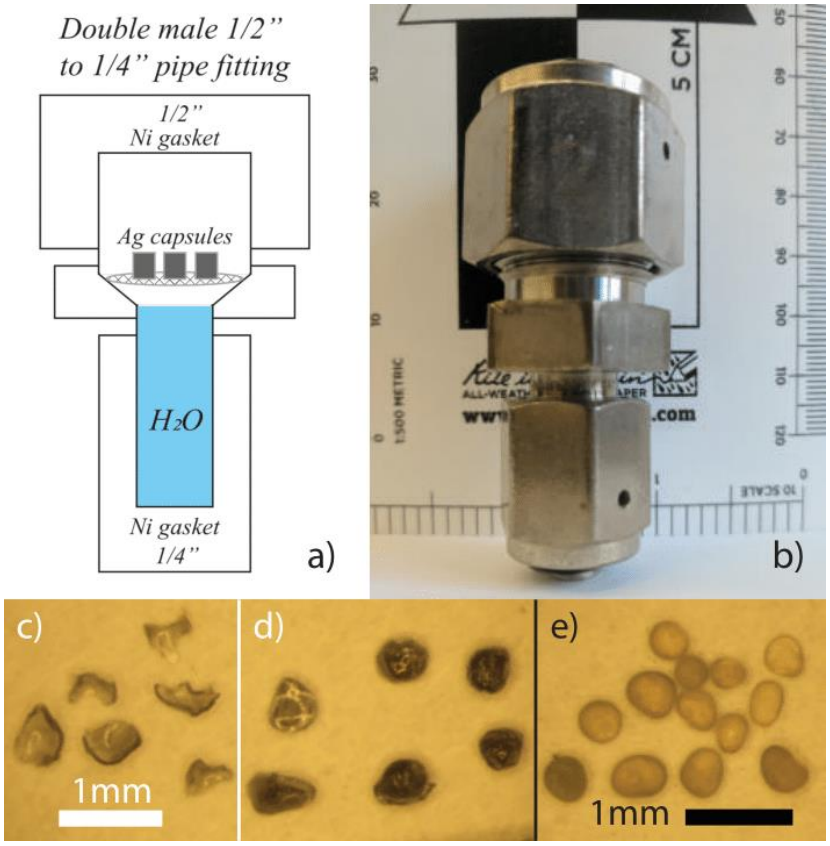

Figure 1. Schematic (a) and photo (b) of the experimental vessels for glass hydration by water vapor and the experimental materials (c-e). High-Si perlites are separated into skins (c) and cores (d). Note the rims on the cores are likely skins that have not broken off. Abraded LSR particles were sieved to several size fractions including 250-350 μm (e) for experiments. The white and black scale bars correspond to (c,d) and (e), respectively.

2.2 Experimental design

The experimental vessel is fashioned out of a double male stainless-steel fitting that is ½" on one end and ¼" (12.7 mm and 6.35 mm, respectively) on the other end and sealed with nickel gaskets (Figure 1). Within the fitting, there is a beveled rim at the transition between the two widths. It has a volume of 2.3 cm^3 when sealed. Experiments were run for hours to months at 175°C, 225°C, 275°C and 375°C. Vessels were loaded with 0.36 mL of experimental H_2O for 175°C, 225°C, and 375°C experiments; and 0.40 mL were loaded for the 275°C experiments. This volume of water greatly exceeds the mass of water that can diffuse into a few tens of mg of glass, so it may be considered an infinite reservoir that would not change in isotopic composition for the duration of the experiment.

The vessel was oriented with the ¼" side down. Stainless-steel mesh was placed on the bevel to suspend the samples above the liquid water. The silver capsules loaded with glass were placed on the mesh and the vessel was sealed with Ni gaskets. A muffle furnace was pre-heated to the desired temperature and the vessels were placed inside. Fractionations between liquid and vapor phases are corrected for the O isotope compositions of the hydrating H_2O vapor are given in Table A1.6 and are calculated using Horita and Wesolowski (1994). When extractions of glass were made from the experiments after cooling to room temperature, the experimental water was removed and replaced with new experimental H_2O in case of H_2O loss and/or fractionation during the extraction.

3. Analytical methods

Total H_2O, bulk $\delta^{18}O$, and water-in-glass $\delta^{18}O$ measurements were conducted on a gas source MAT 253 isotope ratio mass spectrometer (IRMS). Experimental glasses dried between 110-150°C for at least 1 hour in a vacuum oven and no longer than overnight to remove any adsorbed water before they were weighed and loading for analysis. This drying method successfully reproduces H_2O concentrations measured by manometry or Fourier-transform infrared spectroscopy (Martin et al., 2017). For bulk H_2O and $\delta^{18}O_{wig}$ analyses, 1-4 mg of glass were weighted on a high precision balance with 0.002 mg precision for masses <10 mg and loaded into Ag foil capsules and sealed. Samples and standards were dried overnight at between 110-150°C in a vacuum over to ensure any adsorbed water was removed.

Analyses of H_2O_{bulk} and $\delta^{18}O$ of water-in-glass ($\delta^{18}O_{wig}$) were conducted with a high temperature conversion elemental analyzer (TC/EA) interfaced with the MAT 253 IRMS. Samples were introduced into the TC/EA down a glassy carbon tube inside a furnace at 1450°C. Upon melting, volatiles in the sample are liberated where they react with the glassy carbon in a pyrolysis reaction that generates H_2 and CO gas. These gases are transported to an open split by a He carrier gas. A reference gas of known composition is also introduced into the open split to monitor instrument stability. Both the sample gas and the reference gas are introduced to the IRMS from the open split. Separate analytical sessions for H_2 and CO were conducted for bulk H_2O and $\delta^{18}O_{wig}$,

respectively. Mica standards USGS57 (biotite) has 3.60 wt.% H_2O and is used for H_2O_{bulk} calibration. It is analyzed 3-5 times throughout each analytical session for H_2O. In 9 analytical sessions, the 2σ on this standard never exceeded 0.20 wt.% H_2O. This error is within the 6% 2σ reproducibility that Martin et al., (2017) report for samples >3 wt.% H_2O_{bulk}. The $\delta^{18}O_{wig}$ data are calibrated with USGS water standards (W-62001, VSMOW, USGS-47, and USGS-53). Despite the reductive environment, no detectible oxygen is given off for the silicates. Additionally, fractionation of $\delta^{18}O$ is <1‰ between oxygen in water-in-glass and oxygen structurally bound in the glass silicate the during thermal decomposition and simultaneous pyrolysis (Seligman and Bindeman, 2019). See Seligman and Bindeman (2019) for further $\delta^{18}O_{wig}$ methods and discussion. The limited amount of experimental glass removed at each extraction only permitted one H_2O_{bulk} and one $\delta^{18}O_{wig}$ analysis. Therefore, we use the maximum 2σ (0.20 wt.%) for H_2O_{bulk} in the USGS57 biotite standard from the 9 H_2O_t analytical sessions. Water standards used to calibrate $\delta^{18}O_{wig}$ have lower errors than solid samples. Therefore, we take the maximum 1σ (1.5‰) $\delta^{18}O_{wig}$ error reported for rhyolitic and dacitic glasses measured by Seligman and Bindeman (2019) as a conservative instrumental error.

Bulk $\delta^{18}O$ measurements are made on 1-2 mg of material fluorinated by BrF_5 and using a 9.6 μm CO_2 laser, with a chamber connected to a line connected to the MAT 253 IRMS. The laser chamber is pretreated with BrF_5 reagent until acceptable blanks (<0.1 μmol) are achieved. Sample yields are typically within 15-25 μmol. Samples are introduced in single blocks from the 12-sample turret, which is hosted in a custom-built vacuum airlock chamber. This prevents premature mass loss in reactive samples during reaction of the glass with BrF_5 during pretreatment of the laser chamber. Samples are converted to a gas by a laser in the presence of BrF_5. The sample gas is purified by a series of liquid nitrogen traps and a Hg diffusion pump to separate the O_2. The O_2 is converted to CO_2 by a carbon rod before being introduced to the mass spectrometer for analysis. Samples were analyzed and normalized with 2-4 Gore Mountain garnet standards (UOG) in each of the 4 analytical sessions. As with the TC/EA H_2O_{bulk} sessions, limited sample material prevented duplicate analysis and 1σ is taken from the standard measurements, which is ≤0.1‰ for 3 of the sessions. The standards in the session for 175°C experimental glasses yielded a 1σ of 0.27‰. Isotope compositions are

expressed in delta notation relative to Vienna Standard Mean Ocean Water (VSMOW). Oxygen isotope data is presented in delta notation according to Eq. 1 for both bulk $\delta^{18}O$ and $\delta^{18}O_{wig}$.

$$\delta^{18}O = \left({}^{18/16}O_{sample} / {}^{18/16}O_{VSMOW} - 1\right) \times 1000 \qquad (Eq. 1)$$

The diffusion profiles of H and D in a low-Si rhyolite glass were acquired with a Cameca NanoSIMS 50L ion microprobe at Caltech. A 40-spot line scan with a ~2μm step was measured perpendicularly to the glass surface. On each spot, an 8 keV Cs^+ primary beam of ~100 nm in size (~20 pA) was used to sputter the sample in a 1x1 μm rastering mode. Secondary ions (H^- and D^-) of −8 keV were simultaneously collected with electron multipliers (EMs). A pre-sputtering of 60 sec was applied to get rid of the gold coating and surface contamination. To avoid edge effects, secondary signals were only collected from the center 0.8x0.8 μm of the 1x1 μm crater with electronic gating. The total data acquisition time on each spot was about ~400 sec (200 frame X 2.048 sec/frame). The mass resolving power (MRP) at the EM detector for D^- was >2000, more than enough to resolve D^- from any possible H_2^- interference. Electron microprobe data were collected on a Cameca SX100 at the University of Oregon using a 15 kV beam running at 15 nA for Na, K, Si, Al, Fe, Mg, Ca, and Ti. The alkalis were analyzed first, followed by Si and Al. A time-dependent intensity (TDI) correction was applied to these elements. EPMA analyses were calibrated with a set of 13 standard. Five high purity (>99.98%) synthetic oxides (MnO, SiO_2, TiO_2, MgO, and NiO) and 2 synthetic NIST glasses (K-411 and K-412) were used along with mineral specimens including a synthetic forsterite, synthetic chlorapatite, nepheline, diopside, orthoclase, and magnetite.

4. Results

4.1 Bulk H_2O concentrations in glass

The 175°C experiments utilized three particle sieve fractions of LSR glass: 250-350 μm, 105-250 μm, and 53-105 μm. The larger two size fractions were abraded and have effective radii (r_{eff}) of approximately 155 and 95 μm, respectively (Appendix A2). All three sizes show increases in H_2O (Figure 2a) with time, reaching H_2O_{bulk} concentrations of 0.65, 1.03, and 2.75 wt.% H_2O_t (from largest to smallest) by the end of the 6000 hour-long experiment. This contrasts the Nez Perce perlite skins, which

dehydrate from initial H_2O_{bulk} contents of 2.89 wt.%. The perlite skins lose ~0.15-0.2 wt.% and do not fully recover to their initial bulk H_2O content. The perlite cores increase to 2.64 wt.% H_2O_{bulk}, approaching the H_2O_{bulk} of the perlite skins after 6000 hours. This experiment allows us to constrain the solubility of H_2O in this high silica glass at 175°C to ~2.75 wt%. By the end of the experiment at 6000 hours, the smallest LSR particles catches up to the perlite bulk H_2O concentrations at 2.75 wt.%.

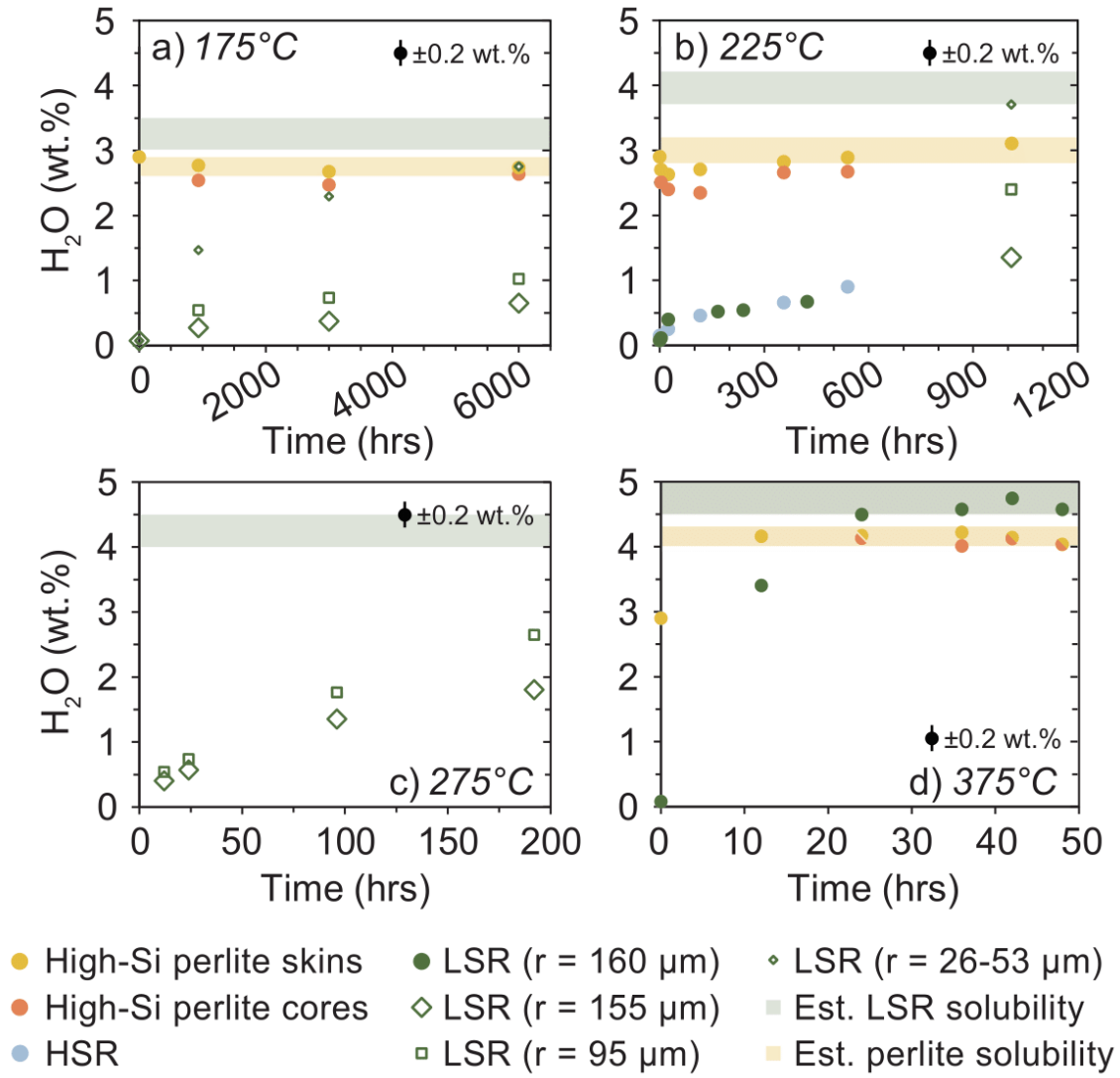

Figure 2. Bulk H_2O TC/EA measurements from experiments at 175°C (a), 225°C (b), 275°C (c), and 375°C (d). In all experiments, all anhydrous glasses (HSR and LSR) increase in H_2O with time while perlites dehydrate slightly at 175°C, dehydrate and then recover at 225°C, and increase in H_2O at 175°C. Error bars indicate 2σ reproducibility of standards.

At 225°C, both LSR and HSR show similar bulk H_2O trends that increase relatively linearly through time at 225°C (Figure 2b). The largest LSR particle size in the 1010 hour-long experiment (r_{eff} = 155 μm) is roughly comparable to the particle sizes of the initial set of experiments and continues the linear bulk H_2O trend (r_{eff} = 160 μm). The smallest size fraction has the highest H_2O_{bulk} concentration (3.70 wt.%) and the largest size fraction has the lowest concentration (1.35 wt.%) in the 1010 hour-long experiment. Hand-picked perlite skins and cores remain around 3.0-3.1 wt.% H_2O through time, although they both show evidence for dehydrating initially before recovering. Zones within the perlite with H_2O_t greater than H_2O solubility will dehydrate faster than zones of lower H_2O_t will hydrate because of the H_2O concentration dependence of D_{H2O}., which may cause H_2O_{bulk} to decrease before recovering. This indicates that H_2O solubility in low silica rhyolitic glass at 225°C and 2.55 MPa is no less than, and perhaps a few tenths of wt.% higher than the maximum measured H_2O_{bulk} of 3.7 wt.%. The H_2O solubility is slightly lower for high silica rhyolite, around 3.1 wt.% H_2O_{bulk} based on the plateau in the times series (Figure 2b).

Hydration occurs much more quickly above 250°C. In the 275°C experiments, only the intermediate (r_{eff} = 95 μm) and large (r_{eff} = 155 μm) LSR glasses were used. The intermediate particle size shows more rapid hydration than the large particles, reaching 2.65 wt.% H_2O_{bulk} after 192 hours while the larger particles have 1.80 wt.% bulk H_2O after the same amount of time (Figure 2c). After 192 hours, the particles began sintering and developed an opaque coating, so the experiment was terminated.

Water content in the LSR glass increased rapidly in the 375°C experiments and plateaued around 4.6 wt.% H_2O_{bulk} by 24 hours at 375°C (Figure 2d). The LSR glass (r_{eff} = 160 μm) peaks at 42 hours at 4.75 wt.%, but at all other durations after 12 hours, remains between 4.50-4.57 wt.% H_2O_{bulk}. The perlites skins and cores also reached higher water contents within 24 hours but are somewhat lower than the initially anhydrous glass at ~4.1 wt.% in each time interval, with a maximum concentration in the skins at 36 hours with 4.22 wt.% H_2O.

In summary, our experiments showed that low-Si rhyolite has higher H_2O solubility than high-Si rhyolite, likely by ~0.5 wt.% H_2O. The smallest LSR particles and the hydrous high-Si perlites, which should most rapidly approach the limit of H_2O

solubility in rhyolitic glass, appear to record increasing solubility with increasing pressure and temperature.

4.2 Oxygen isotope compositions

4.2.1 Bulk $\delta^{18}O$ of glass

The bulk $\delta^{18}O$ results at 175°C and 225°C show little change in the low-Si anhydrous glasses and gradual change in the high-Si hydrous perlites (Figure 3a,b; Table 4). The LSR obsidian, does not deviate more than ~0.3‰ in $\delta^{18}O_{bulk}$ from the initial starting composition of 5.95‰, even after 3000 hours. In contrast, the initially hydrous perlites (2.89 wt.%) increased by 1.2‰ $\delta^{18}O_{bulk}$ over the same interval (Figure 3a). The difference in behavior between smallest LSR glasses and the thin high-Si perlite skins suggests that for significant oxygen isotope exchange to occur between glass and water, the glass must first be hydrated. Incomplete hydration at 175°C therefore limits the extent to which the $\delta^{18}O$ of the bulk glass can be modified after 3000 hours.

The data from the 225°C experiments record the same $\delta^{18}O$ behavior as observed in the 175°C experiments, in which the high-Si perlites steadily increase with time while the LSR obsidian is slow to change. The perlites increased by 5‰ from 2.89‰ to 7.93‰ $\delta^{18}O_{bulk}$ in 1010 hours at a nearly linear rate, whereas the intermediate sized LSR particles have increased by <1‰ from 5.95‰ to 6.69‰ $\delta^{18}O_{bulk}$ (Figure 3b). The smallest particle size of LSR glass reached a $\delta^{18}O_{bulk}$ value of 9.60‰ after 1010 hours, which is greater than the perlite $\delta^{18}O_{bulk}$. While higher in $\delta^{18}O$ than the perlites, the relative change from the initial $\delta^{18}O$ of the two glasses is less in the LSR glass relative to the perlites, so this higher $\delta^{18}O$ does not necessarily represent more significant exchange. However, given the bulk H_2O content of 3.7 wt.% and the short diffusion length scales required, the smallest LSR particles may be fully hydrated allowing for more rapid $\delta^{18}O$ exchange between glass and water.

If the oxygen isotope compositions of the experimental glasses are dominantly controlled by the extent of hydration, then only completely hydrated glasses will record a $\delta^{18}O$ composition in equilibrium with the fluid. In this case, equilibrium is only attained in the 375°C experiments where there is evidence for complete hydration halfway through the duration of the experiment from the plateau in bulk H_2O. At this temperature

with a $\delta^{18}O$ of +5.88‰ fluid, elevated glass $\delta^{18}O_{bulk}$ values of +9 to +10‰ are achieved within 24 hours in both the LSR glasses and high-Si perlites and subsequently plateau (Figure 3c). This gives an equilibrium oxygen isotope fractionation between glass and H_2O ($10^3ln\alpha_{glass\text{-}H2O}$) of 3-4‰ between glass and water at 375°C, and is consistent with predicted rhyolite-H_2O fractionation ($10^3ln\alpha_{rhyolite\text{-}H2O}$) of 4.04‰ using equilibrium $\delta^{18}O$ fractionation factors for albite-H_2O (O'Neil and Taylor, 1967) and quartz-H_2O (Sharp et al., 2016) in their eutectic proportions (2:1; Bindeman and Lowenstern, 2016; Hudak and Bindeman, 2018). Our data validates that that this simple quartz and albite approximation for rhyolite $\delta^{18}O$ fractionation is appropriate to use in the hydrothermal temperature window in which we conduct these experiments.

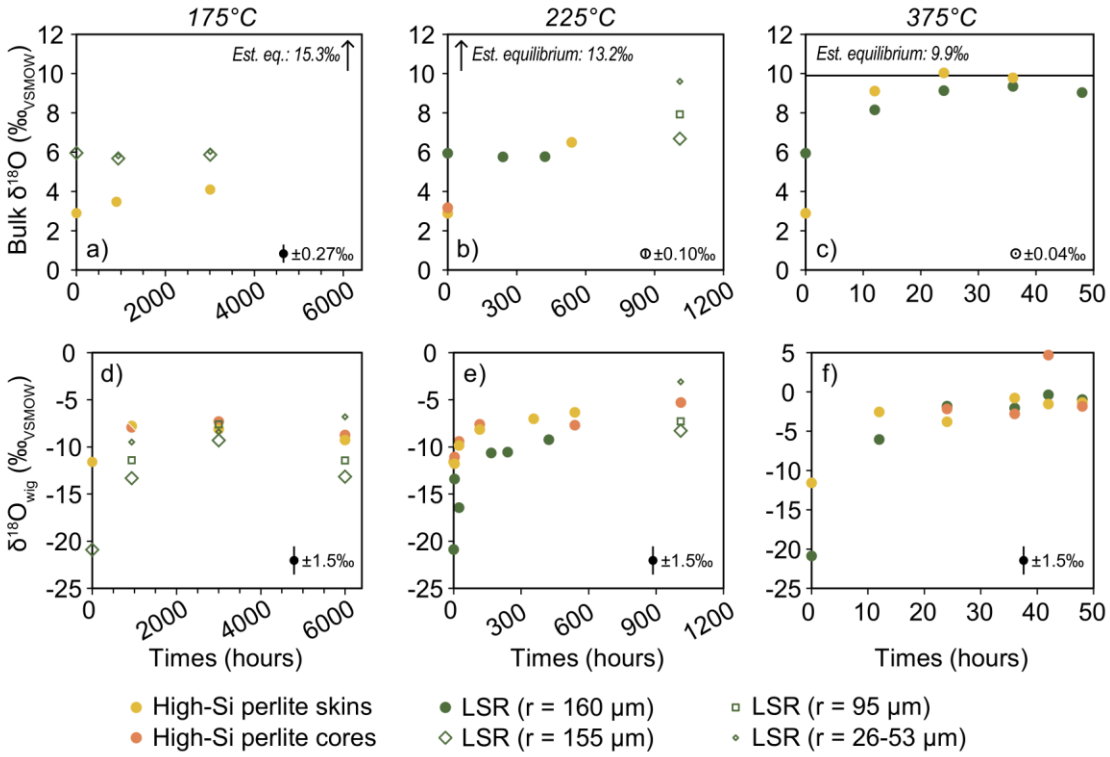

Figure 3. Bulk $\delta^{18}O$ (a-c) and $\delta^{18}O_{wig}$ (d-f) measurements from experiments at 175°C (a,d), 225°C (b,e), and 375°C (c,f). Bulk $\delta^{18}O$ does not change as much at 175°C or 225°C as it does in 375°C where hydration is complete, and the glass achieves equilibrium with the H_2O. The $\delta^{18}O_{wig}$ (d-f) approaches a plateau at all temperatures, suggesting that local equilibrium within the glass has been achieved. Equilibrium $\delta^{18}O$ of the glass is predicted by combining the $10^3ln\alpha_{albite\text{-}H2O}$ (O'Neil and Taylor, 1967) and $10^3ln\alpha_{quartz\text{-}H2O}$ (Sharp et al., 2018) in the eutectic proportions of albite and quartz in rhyolite.

4.2.2 $\delta^{18}O$ of water-in-glass

We employ a rarely reported parameter that can shed light on oxygen isotope systematics called the $\delta^{18}O$ of water-in-glass, or $\delta^{18}O_{wig}$, which represents the H_2O-bound oxygen atoms within the hydrous glasses (Bindeman and Lowenstern, 2016; Hudak and Bindeman, 2018; Seligman and Bindeman, 2019). Oxygen that is structurally bonded in the silicate does not contribute to this parameter, even in redox-sensitive Fe-silicates (Seligman and Bindeman, 2019). At all temperatures, $\delta^{18}O_{wig}$ increases with time for both low-Si anhydrous obsidian and high-Si perlites. The noisiest data comes from the 175°C time series (Figure 3d). All the glasses increased in $\delta^{18}O_{wig}$ until 3000 hours (except for the perlite skins which showed effectively no change between 935 and 3000 hours with a 0.3‰ decrease) and nearly all samples decreased between 3000 and 6000 hours. The only glass to increase over this final time interval, and to show constant increases through the entire experimental duration are the small LSR particles, which ended at −6.8‰ $\delta^{18}O_{wig}$. The large and intermediate sized LSR particles showed the largest decreases of nearly 4‰ to −13.2‰ and −11.4‰ $\delta^{18}O_{wig}$, respectively, −16.7‰ and −14.9‰ below the H_2O vapor composition of 3.5‰ $\delta^{18}O$. These compositions are identical to the 935 hour-long $\delta^{18}O_{wig}$ compositions. The perlite skins and cores also decreased by ~1‰ between 3000 and 6000 hours to −9.3‰ and −8.7‰ $\delta^{18}O_{wig}$, respectively.

The data from the 225°C experimental glasses show a more consistent increase though time (Figure 3e). At the shortest durations (≤24 hours) and lowest H_2O_{bulk} contents, the LSR $\delta^{18}O_{wig}$ are variable, but demonstrate an increase through time reaching −9.2‰ by 423 hours. Both large (r_{eff} = 155 μm) and intermediate (r_{eff} = 95 μm) LSR particle sizes at 1010 hours can be interpreted as an extension of the shorter duration LSR particles (r_{eff} = 160 μm). These achieve $\delta^{18}O_{wig}$ values of −8.3‰ and −7.3‰, respectively, after 1010 hours of hydration. The smallest LSR particles reach a maximum $\delta^{18}O_{wig}$ of −3.1‰, which is greater than any of the perlite data. The perlites have an exponential trend through time that increases quickly initially and then begins to plateau towards the end of the experimental duration. Perlite skins and cores increase together and the cores reach −5.3‰ after 1010 hours.

The glasses reach consistent $\delta^{18}O_{wig}$ values between −2.0‰ and −0.4‰ $\delta^{18}O_{wig}$ at longer durations and temperatures >250°C. Two outliers of 4.5‰ after 192 hours at

275°C and 4.7‰ after 42 hours at 375°C are more than 5‰ higher than any other $\delta^{18}O_{wig}$ values at those temperatures and are therefore not considered to be representative. The 375°C experimental glasses increase in $\delta^{18}O_{wig}$ especially quickly, with the LSR particles and the perlites attaining the same values by 24 hours and slowly increasing together within error until the end of the experiment at 48 hours (Figure 3f). Given that the bulk H_2O content of these particles plateaued at similar timescales, suggesting complete hydration, the $\delta^{18}O_{wig}$ of the LSR particles can be interpreted to be effectively equilibrated with the $\delta^{18}O$ of the fluid of 5.9‰. Values averaging −1.2‰ for LSR and high-Si perlite skins after 36 hours suggest that the equilibrium fractionation between $\delta^{18}O_{wig}$ and the $\delta^{18}O$ of the hydration water ($10^3\ln\alpha_{wig\text{-}H2O}$) is approximately −7‰; and the $10^3\ln\alpha_{glass\text{-}wig}$ is ~11-12‰.

The $\delta^{18}O_{wig}$ data increases through time in all samples at 225°C and 375°C and in the smallest, highest bulk H_2O LSR particles from the 175°C experiments. Only minor shifts in the bulk $\delta^{18}O$ occur in the 175°C and 225°C experiments and the $\delta^{18}O_{wig}$ tracks the bulk $\delta^{18}O$ in the 375°C experiments. Therefore, the plateaus through time observed in the $\delta^{18}O_{wig}$ data at lower temperatures (Figure 3d,e) alone do not provide enough information to tell if the fluid $\delta^{18}O$ composition or the glass $\delta^{18}O$ composition control the $\delta^{18}O_{wig}$.

4.3 NanoSIMS D and H profiles

One hydration experiment used a mixture of deuterated water (~99.9% D_2O) and Fairbanks tap water ($\delta D = -152‰$) in 1:1 proportions so that D and H profiles in experimental glass could be measured independently at high resolution by NanoSIMS. This experiment lasted 334 hours at 225°C. Spots with a 1 μm diameter were collected every 1-2 μm (Figure 4a, Table A3.1). Hydrogen and deuterium are measured as $^1H^+$ and $^2H^+$, respectively. Backgrounds for H are much higher than for D and H is more readily detected by SIMS than D (Anovitz et al., 2008). Once this is corrected and the D profile (in counts) were scaled to match the H profile, no difference in profile shape or diffusion profile length could be detected at this resolution. The half-fall distances – the distance at which the concentration in the diffusion profile is half the difference of the boundary and background concentrations – are at approximately 8 μm in the corrected data for both D

and H and are as wide at the precision of measurement. This suggests that there is not a kinetic isotope effect resulting from faster D or H diffusion into glass. The lack of kinetic isotope effects in D/H fractionation during glass hydration is consistent with previous work (Shelby, 1977; Anovitz et al., 2008; Roskosz et al., 2018).

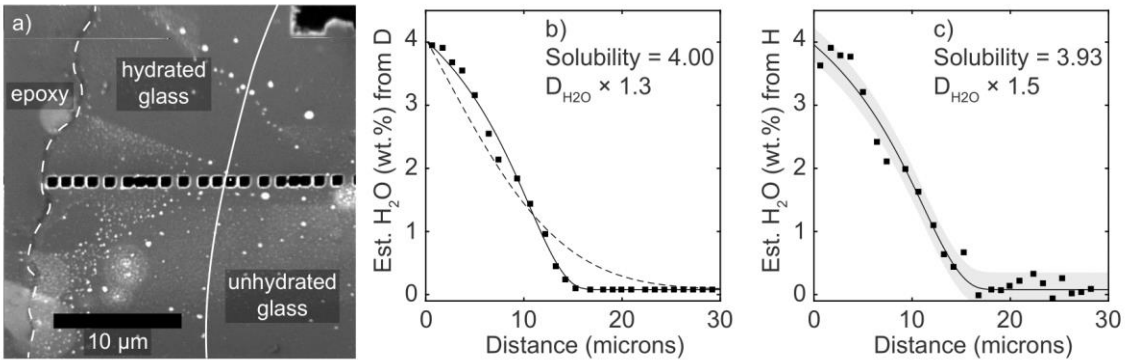

Figure 4. NanoSIMS 0.8x0.8 μm measurements on LSR glass from a 334 hour-long experiment at 225°C with half D_2O and half Fairbanks tap water (normal H_2O) spaced every 1-1.5 μm (a). The dashed line shows the edge of the glass and the solid line shows the approximate distance over which H_2O has been added to the glass. Example NanoSIMS diffusion profiles (solid curves) for D (b) and H concentrations (c) scaled to 0.08 wt.% H_2O in the interior and 3.95 wt.% at the boundary to match the diffusivity modeling. These profiles yield D_{H2O} values of 1.3 (D) and 1.5 (H) times greater than extrapolated from the Zhang and Behrens (2000) model. Best fit solubility concentrations are 4.00 and 3.93 wt.% H_2O, respectively. A constant D_{H2O} is modeled in (b; dashed line) to underscore the importance of the H_2O concentration dependence of D_{H2O}. The shaded region of (c) is 2σ of the 27 points of H background measurements beyond the diffusion front.

Hydrogen profiles yield D_{H2O} estimates that are marginally faster than those modeled for the D profiles but have slightly lower best fit solubilities for the boundary condition (see Section 5.1. for details of diffusion modeling). Some of this difference may arise from imperfect scaling of the data because the background of the H profile includes both 0.08 wt.% water in the glass and residual H_2O vapor in the vacuum chamber. We emphasize that the NanoSIMS data are semi-quantitative in terms of absolute abundances of D and H (but not in width), so the results are informative in that they constrain how D_{H2O} and H_2O solubility co-vary and in the overall length scale of H_2O diffusion. Profiles are scaled to 3.95 wt.% H_2O_t at the boundary for D (Figure 4b), and because the boundary at the rim for the H is lower than the next two points in the profile, the second point in the H profile is arbitrarily scaled to match the second point in

the D profile (Figure 4c). The resulting H_2O solubilities for D and H are 4.00 wt.% and 3.93 wt.%, respectively. The D_{H2O} estimates for are 1.3 times greater for D and 1.5 times greater for H than predicted for the relevant P-T-X_{H2O} conditions in high temperature extrapolations of Zhang and Behrens (2000). These correspond to D_{H2O} values at glass rim (assuming the rim has H_2O_t concentrations equaling the H_2O solubility) of 8.31×10^{-13} cm^2s^{-1} for D and 9.21×10^{-13} cm^2s^{-1} for H. The dashed line in Figure 4b represents the average of the maximum and minimum D_{H2O} values (4.303×10^{-13} cm^2s^{-1}) in a non-H_2O concentration dependent diffusion model. It returns the same mass of H_2O diffused into the glass as the H_2O concentration-dependent model but does not fit the data. Using a constant diffusivity yields a functional form of an error function as opposed the observed "snowplow" form. (We use the snowplow analogy to describe the region of high concentrations that arise near the boundary of the model as a result of the concentration dependence of D_{H2O}. This occurs when the boundary has higher concentrations of the diffusive species than the background in the rest of the model). This demonstrates that H_2O concentration dependent model is appropriate for modeling D_{H2O} in rhyolitic glasses at hydrothermal temperatures, but that constant D_{H2O} values can be used for comparison.

5. Discussion

We investigate three interrelated processes – H_2O diffusivity, H_2O solubility, and $\delta^{18}O$ exchange in glass in our hydrothermal temperature experiments from 175 to 375°C. Diffusion of molecular water in rhyolitic melts is the primary mechanism for the movement of oxygen within the silicate and this facilitates isotope exchange between external fluids and the melt (Behrens et al., 2007). Below magmatic temperatures, as we demonstrate here, H_2O_m diffusion in glass is likewise the fastest mechanism for $\delta^{18}O$ exchange between glass and a fluid. Therefore, D_{H2O} in glass should place the greatest constraint on the rate $\delta^{18}O$ exchange between glass and a fluid because self-diffusion (diffusion achieved by individual atoms changing their position with one another within a solid phase) is orders of magnitude slower. Above 400°C, D_{H2O} in rhyolitic glasses and melts is well-constrained experimentally (Delaney and Karsten, 1982; Lapham et al., 1984; Zhang et al., 1991; Zhang and Behrens, 2000; Liu et al., 2005; Ni and Zhang, 2008). At Earth surface temperatures, many authors have constrained D_{H2O} in glass and

their data points to diffusivities largely between 10^{-17} to 10^{-19} m^2s^{-1} Friedman and Smith, 1960; Friedman and Long, 1976; Friedman and Obradovich, 1981; Anovitz et al., 2004; Yokoyama et al., 2008; Anovitz et al., 2009; Rogers and Duke, 2011; Stevenson et al., 2013; Giachetti et al., 2015; Giachetti et al., 2020).

This compilation demonstrates that D_{H2O} for surface conditions is higher than extrapolations from the high temperature data by roughly 2 orders of magnitude, although both high and low temperature trends follow an Arrhenius relationship (Figure 5; Table A3.2). It is imperative to understand the transitional behavior of D_{H2O} between high and low temperature regimes over the hydrothermal temperature range, which could shed light on this discrepancy. Molecular water is the diffusive species in both melts (e.g. Behrens et al., 2007; Zhang et al., 1997, 1991) and in glasses at low temperature (e.g. Anovitz et al., 2008; Nolan and Bindeman, 2013). For example, in both high and low temperature experiments, the functional form of the H_2O diffusion profiles have the same "snowplow" that results from the H_2O concentration dependence of D_{H2O} at high temperature.

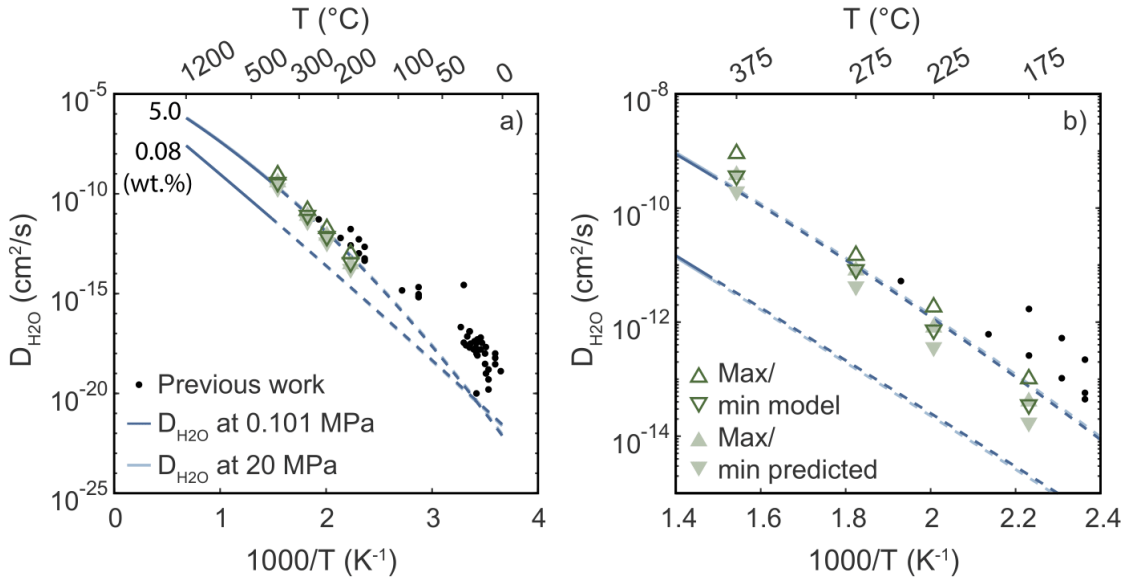

Figure 5. Results from this study are compared to high T extrapolations for diffusivity of water in melts and glass (Zhang and Behrens, 2000) and a compilation of low T diffusivities of water in glass (a; Table A3.2). High T models cannot be extrapolated to Earth surface temperatures, which are off by ~2 orders of magnitude. The high T models do better over the range of hydrothermal T (175-375°C) in this study, remaining within a factor of 5.5 at maximum over the relevant P-T-X_{H2O} (b).

5.1 H_2O solubility in rhyolitic glass

Hydration experiments conducted here between 175-375°C and at pressures of 0.89 to 21 MPa refine H_2O solubility in glass below the glass transition (Figure 6). Precise H_2O solubility data for silicic glasses in this hydrothermal temperature range is virtually non-existent. Well-accepted solubility models at magmatic temperatures, constrained by experiments no lower than 400°C, act as a primary point of comparison for the maximum bulk H_2O contents observed in this study. The results from these experiments demonstrate that both the LSR glass and the high-Si perlites are >1 wt.% more hydrated than predicted by extrapolating H_2O solubilities from VolatileCalc (Newman and Lowenstern, 2002) or Liu et al. (2005; Figure 6). An isobaric 1 MPa curve is also shown to help consider the pressure dependence of H_2O solubility (Liu et al., 2005). This curve shows a decrease in solubility with increasing temperature, which suggests that the higher H_2O_{bulk} concentrations are likely more a function of pressure than temperature. In one experiment by Liu et al. (2005), reproducible and higher than expected H_2O concentrations are achieved and omitted from their model, which they justify by proposing that the P-T-X conditions of the experiment put it into a regime of secondary hydration (Ryan et al., 2015). While pressure surely plays a role in controlling the solubility of H_2O in rhyolitic glass, there is to date no predictive model that we are aware of that can disentangle the role of pressure and temperature below 400°C.

Our most confident H_2O solubility estimates come from 375°C, where all investigated glasses have achieved complete hydration, and 225°C where the perlites have plateaued in H_2O_{bulk} and the smallest LSR particle size is likely to be completely hydrated. At 375°C and 21 MPa, the LSR glass reaches at 4.65 ± 0.15 wt.% H_2O_{bulk} and the high-Si perlites plot round 4.12 ± 0.1 wt.% H_2O_{bulk} compared to a predicted 3.11 wt% H_2O_{bulk} at these P-T conditions from VolatileCalc (Newman and Lowenstern, 2002) and 2.79 wt.% H_2O_{bulk} from the model of Liu et al., (2005). At 225°C and 2.55 MPa, the measured bulk H_2O concentrations exceed the high temperature model predictions (1.18 wt.% H_2O and 1.46 wt.% from Liu et al., (2005) and Newman and Lowenstern (2002), respectively) by even more than the 375°C experimental glasses. The smallest size fraction of LSR obsidian achieves 3.70 wt.% H_2O_{bulk} after 1010 hours, which we consider to be the solubility. The relative offset of ~0.6 wt.% bulk H_2O between the LSR and the

perlites is maintained at this lower temperature as the high-Si perlites do not exceed 3.10 wt.% H_2O_{bulk}.

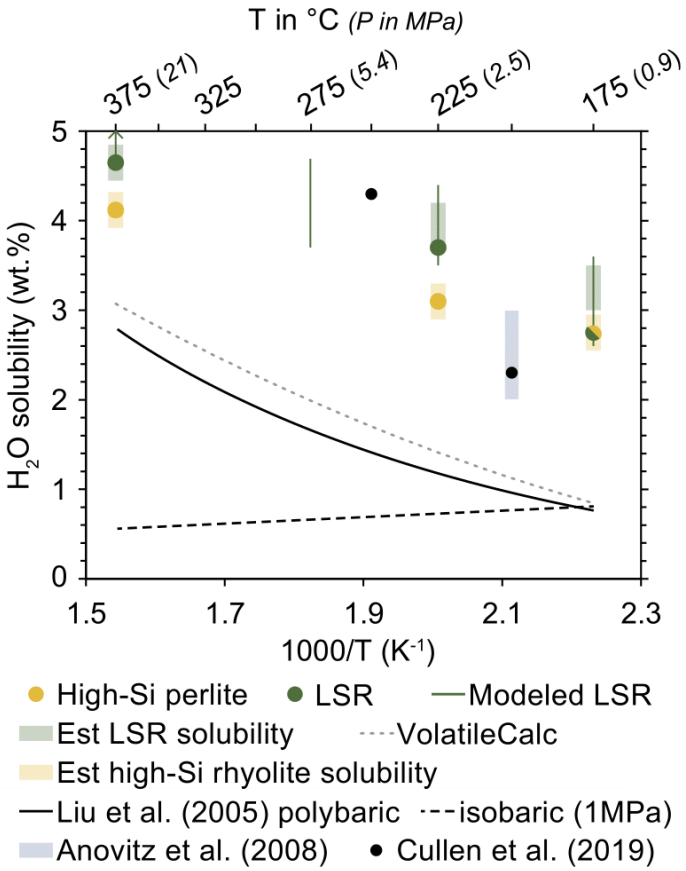

Figure 6. Estimated H_2O solubilities (shaded) as a function of 1/T for LSR and high-Si perlites are compared to predictions from VolatileCalc (Newman and Lowenstern, 2002) and Liu et al., (2005) for the P-T conditions of the experiments and an isobaric model at 1 MPa. An estimate from Anovitz et al. (2008) and the H_2O content of 2 hydrothermal experiments from Cullen et al. (2019) are also shown. For diffusivity modeling, the range of H_2O solubilities used (green bars) is expanded by 2σ (or 0.2 wt.%) of TC/EA bulk H_2O measurements.

At 175°C or 275°C, the LSR glasses do not achieve complete hydration at the conclusion of the experiments. Instead, the results at 225°C and 375°C, and an experiment from Cullen et al. (2019) at 250°C can assist in estimating H_2O solubility at these temperatures by extrapolation. If we assume the relationship between 1/T (in Kelvin) and H_2O solubility is linear, the fit to the available H_2O data gives a possible upper limit of ~3.2-3.4 wt.% H_2O_t. The 175°C perlites remain unchanged after 6000 hours and match the H_2O_{bulk} of the smallest LSR particles at an H_2O_{bulk} of 2.75 wt.%,

suggesting that is the solubility of high-Si rhyolitic glass. Then if we apply observation of the ~0.6 wt.% offset between high-Si perlites and LSR solubility at 225°C and 375°C, this also gives an estimate solubility consistent with the linear 1/T-H_2O solubility fit of approximate 3.3 wt.% H_2O_{bulk}. The linear extrapolation yields an H_2O solubility estimate of ~4.1-4.3 wt.% H_2O_t at 275°C.

This difference in H_2O solubility between the perlitic high-Si rhyolite and LSR glass is likely related to glass chemistry and/or structure. Higher silica generally correlates with higher NBO/T ratios, since Si is the dominate cation occupying tetrahedrally coordinated sites. Both silica (Friedman and Long, 1976) and the degree of polymerization recorded by lower NBO/T ratios (Behrens and Nowak, 1997; Nolan and Bindeman, 2013) have been identified as primary controls on H_2O solubility and/or diffusivity in rhyolitic melts and glasses. Other differences in major elements likely also play a role, especially alkalis which are mobile and may exchange with hydrogen or H_2O_m or during more advanced stages of alteration after hydration (e.g. Cerling et al., 1985; Friedman and Long, 1976), although we do not observe evidence for systematic alkali mobility (Figure A1.1) or glass decomposition in experimental glasses (Figure A1.2-A1.3). In our experiments, the LSR has a higher NBO/T of 0.07 than either the HSR (0.035) or the perlites (0.01), primarily because of the difference in SiO_2, but also because of the much higher alkali content of the LSR (which increases NBO).

In summary, we observe H_2O solubility in high-Si perlite that is ±0.2 wt.% of the following values: 2.75 wt.% at 175°C, 3.1 wt.% at 225°C, and 4.1 wt.% at 375°C. The H_2O solubility for low silica rhyolitic glass is ±0.3 wt.% for the lower temperature results and ±0.2 wt.% for the 375°C results centered around 3.3 wt.% at 175°C, 3.9 wt.% at 225°C, 4.2 wt.% at 275°C, and 4.8 wt.% at 375°C. [These error ranges are determined in part by the reproducibility of bulk H_2O on the TC/EA, which is within 6% of the bulk H_2O concentration when H_2O_{bulk} > 3.0 wt.% (Martin et al., 2017).] We attribute this difference in solubility to the differences in major element chemistry and any effect this may have on glass structure.

5.2 Diffusion modeling of H_2O in rhyolitic glass

To model the TC/EA bulk H_2O data and the NanoSIMS D and H profiles, we employ a 1D finite difference diffusion in spherical coordinates use the output to compute simultaneous mass balance calculations. Only LSR obsidian particles (initially 0.08 wt.% H_2O_{bulk}) are modeled because they are used in experiments at all temperatures. To adequately capture the H_2O concentration dependence of D_{H2O}, we employ the D_{H2O} model of Zhang and Behrens (2000) as a starting point (Eq. 2). Their D_{H2O} is calibrated to experiments above 400°C, so our model follows the approach of Seligman et al. (2016) in assuming that functionally Zhang and Behrens (2000) is correct and where the diffusivity is adapted by a constant prefactor to fit the data.

$$D_{H_2O_t} = prefactor \times Xexp(m)\left\{1+\exp\left[\begin{array}{c}56+\mathrm{m}+\mathrm{X}\left(-34.1+\frac{44{,}620}{\mathrm{T}}+\frac{57.3P}{T}\right)\\ -\sqrt{X}\left(0.091+\frac{4.77\times10^6}{T^2}\right)\end{array}\right]\right\} \quad (Eq.\,2)$$

Here, X is the mole fraction of H_2O_t on a single oxygen basis, $m = -20.79 - (5030/\mathrm{T}) - (1.4\mathrm{P}/\mathrm{T})$, T is temperature in Kelvin, and P is pressure in MPa. The H_2O concentration dependence of D_{H2O} gives rise to the following form of Fick's first law of diffusion in spherical coordinates (Eq. 3).

$$\frac{\partial C}{\partial t} = \frac{2}{r}D\frac{\partial C}{\partial r} + D\frac{\partial^2 C}{\partial r^2} + \frac{\partial C}{\partial r}\frac{\partial D}{\partial r} \quad (Eq.\,3)$$

Here, C is the concentration of H_2O_t in mole fraction, t is time in seconds, r is the radius of the sphere in μm, and D is the modified H_2O_t concentration dependent diffusivity of Zhang and Behrens (2000) in $\mu m^2/s$. Spheres with radii of 160 μm, 155 μm, or 95 μm are used based on the size data for the various batches of abraded particles (Table 2). Each model discretizes the radius into nodes of 1 μm and the concentrations of H_2O_t at each node are weighted by their volume in a sphere to sum the mass of bulk H_2O in in the model particle at each time step.

5.2.1 Diffusion modeling of bulk H_2O concentrations through time

Mass balance calculations are coupled with the diffusion model and applied to the TC/EA bulk H_2O data to fit D_{H2O} over a reasonable range of H_2O solubilities at each

temperature. In the following discussion of the model results, H_2O solubility is only achieved at the surface of the glass where it is assigned as the boundary condition. For clarity and to distinguish from the measured data, we refer to this boundary condition H_2O solubility in the model as the saturation concentration, or C_{sat}. Diffusivity and C_{sat} have an inverse relationship. The greater the diffusivity, the more rapidly the bulk H_2O content of the glass increases. Therefore, when diffusivity is increased, the C_{sat} boundary condition must be lowered to compensate in order to fit the measured H_2O_{bulk} time series. Examples of some of the chi-squared best fits D_{H2O} for are shown for each temperature (Figure 7) but are non-unique solutions and the relationship that defines the best fit D_{H2O} as it varies with C_{sat} are shown in Figure 8. The boundary condition corresponding to the glass-water interface uses a prescribed C_{sat} for the H_2O_t while the rest of the glass and is initially 0.08 wt.% H_2O_t with the interior boundary condition set to equal the adjacent node (in case the hydration front should reach the glass interior by the end of the model run, as it does at 375°C). Some rhyolite hydration research suggests that H_2O surface concentrations and solubility in rhyolitic glass increases exponentially through time with progressive hydration, and on very short length scales (Anovitz et al., 2004). However, pending better verification of how H_2O solubility changes through time in our samples, our models do not take this into account. We thus only present diffusion and mass balance models that have a constant H_2O_t concentration for the boundary condition.

Unlike high temperature extrapolations of H_2O solubility, absolute D_{H2O} values solubility (Figure 8a) and D_{H2O} prefactors of the Zhang and Behrens (2000) diffusivity equation (Figure 8b), show only a subtle increase in H_2O diffusivity compared to extrapolations. Our diffusivity prefactors vary within half an order of magnitude of the high temperature relationships. The chi-square best fit models in Figure 7 can explain the trends of H_2O_{bulk} in LSR obsidian through time with progressive hydration. The dashed lines represent 10% variation in the effective radius of the glass particles, which illustrate that small variation in the 1-3 mg aliquots of particles extracted from the experiments could explain much of the spread in the bulk H_2O data. The models do best at fitting the 95 μm radius particles at 175°C (Figure 7a) and the 160 μm radius particles 225°C (Figure 7b) and 375°C data (Figure 7d). Water concentrations greater than model predictions could result from microfractures and cracks in the glass that decrease the

effective radius of the modeled particle, while observed H_2O_{bulk} less than model predictions early in the experiments could reflect increased H_2O solubility with time as suggested by Anovitz et al., (2004). From this diffusivity and mass balance modeling, the results of which are consistent with NanoSIMS (Section 5.5.2) and two-particle mass balance methods (Section 5.2.3), we conclude that D_{H2O} prefactors for our experimental temperatures are consistently 1.5-4 times greater than extrapolated from the H_2O_t, T, and P dependent diffusivity equation of Zhang and Behrens (2000).

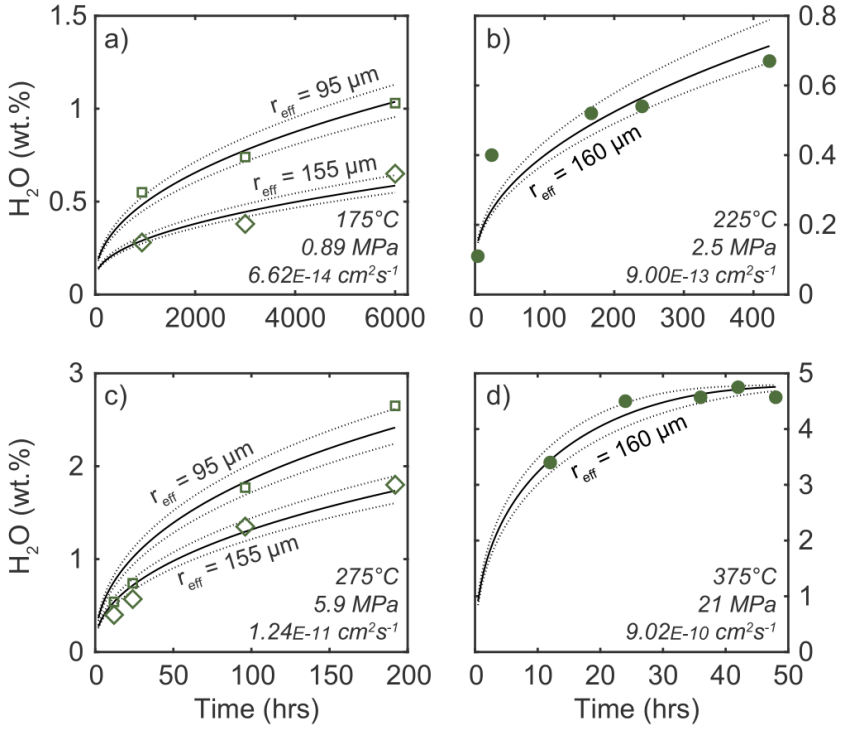

Figure 7. Best fit curves from diffusion and mass balance models for observed H_2O concentrations at 175°C (a), 225°C (b), 275°C (c), and (d). Models employ initial conditions of 0.08 wt.% H_2O and boundary conditions of 3.3 wt.% H_2O at 175°C (a), 3.8 wt.% at 225°C (b), 4.2 wt.% at 275°C (c), and 4.8 wt.% at 375°C. The H_2O concentration dependent diffusivity of Zhang and Behrens (2000) is multiplied by constant factor between 1.6-4.6 for each model. Dashed lines are 10% deviations from the effective particle radii.

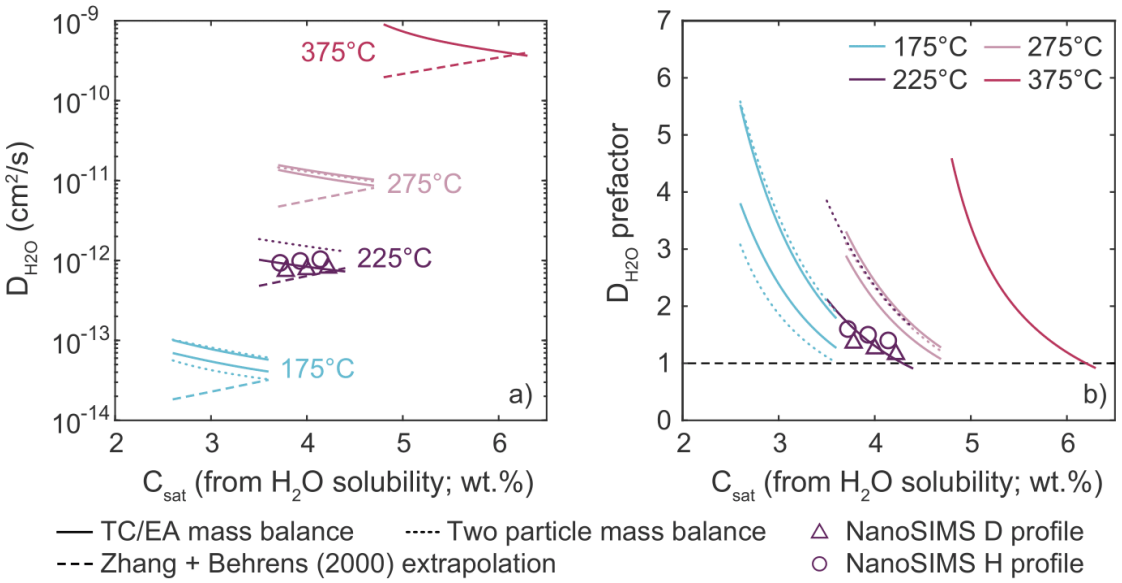

Figure 8. C_{sat} vs. D_{H2O} on an absolute scale (a) and vs. a D_{H2O} prefactor (a scaling coefficient) that scales the high temperature extrapolations of Zhang and Behrens (2000) at the relevant P-T-X_{H2O} conditions. Diffusion and mass balance models using TC/EA data are shown with solid and dotted lines and the NanoSIMS models are shown with solid symbols. The slopes of the TC/EA based models and the NanoSIMS models differ, but routinely yield D_{H2O} values 1.5-4.5 times great than the high temperature extrapolations.

5.2.2 Diffusion modeling NanoSIMS D and H profiles

Raw counts of H and D from the NanoSIMS data are scaled to three different surface concentrations (3.7, 3.95, and 4.2 wt.% H_2O_t) based on the TC/EA data and solubility estimates given in Section 5.1. The results serve three primary purposes. First, it serves as a direct way to understand how H_2O solubility and diffusivity co-vary with time to produce the correct profile shape without having to be constrained by mass balance calculations and uncertainties in particle size distribution. As with the mass balance approach, changing the scaling of the profile to different values of C_{sat} for the boundary conditions requires the D_{H2O} to decrease if the H_2O solubility is increased in order to fit a diffusion profile of a given length. We observe this inverse correlation in the best fits of D_{H2O} and C_{sat} in both D and H profiles (Figure 4b,c). The slope is different from the TC/EA diffusion and mass balance results, however, and is especially notable on the plot of absolute D_{H2O} values (Figure 8a). The NanoSIMS modeling yields a trend that has a linear low-angle positive slope. This is because the diffusion profile length never changes in the NanoSIMS data, so only the concentration dependence of D_{H2O}

causes the best fit C_{sat} value at the boundary of the model to change. This contrasts the mass balance modeling where the length scale of diffusion is allowed to vary so long as the bulk H_2O concentrations are fit. With higher modeled C_{sat}, H_2O diffusion must also be slowed (independent of the concentration dependence of D_{H2O}) in the mass balance model to reproduce the observed TC/EA measurement of H_2O_{bulk}. This results in a shallower slope to the C_{sat}-D_{H2O} relationship for the NanoSIMS data. Nevertheless, the NanoSIMS model suggests that over the most reasonable range of H_2O solubility at 225°C (3.7-4.2 wt.% H_2O_t), D_{H2O} is less than a factor of two greater than high temperature extrapolations to hydrothermal temperatures.

The second purpose that the NanoSIMS measurements and modeling serve are that they verify the assumption that H_2O diffusion has the same functional form below the glass transition as it does at higher temperature (see dashed curve for constant D_{H2O} comparison in Figure 4b). Other authors had previous demonstrated this using depth profiling by SIMS measured similarly shaped profiles on a scale of less than 4 μm (Riciputi et al., 2002; Anovitz et al., 2008; Anovitz et al., 2009). However, on such short length scales with complex interfacial dynamics, it had had not yet been evaluated to what extent H_2O concentration dependence propagated into glass. For example, recent H_2O_t profiles measured by microRaman spectroscopy with a resolution of 1 μm from samples that are thought to have experience rapid hydrothermal temperature hydration (T ~ 400°C) showed a combination of diffusion profiles that have the functional form of an error function and those that have the functional form that arises from a concentration dependent D_{H2O} (Mitchell et al., 2018b). Successful imaging of the diffusion profiles by NanoSIMS for both H and D show that even at longer durations, this behavior propagates tens of μm into glass under hydrothermal conditions.

Finally, we compare this H_2O concentration dependent model to diffusion models with constant D_{H2O} so that these results may be compared to D_{H2O} values derived for Earth surface temperatures, as these values as typically given as singular values. Using a constant D_{H2O} that is equal to half of our maximum D_{H2O} returns a profile with the form of an error function that does not fit the NanoSIMS data. However, when this profile is integrated it yields a total mass of H_2O in the glass that is within 2% of the total mass of H_2O yielded by the H_2O concentration dependent model (Figure 4b,c). This confirms that

H_2O diffusivity values constrained at low temperature can be directly compared to our modeled ranges of D_{H2O} values in the models (Figure 8). The NanoSIMS data verifies that for a reasonable range of solubilities of H_2O in glass at 225°C, the D_{H2O} in rhyolitic glasses requires the functional form of D_{H2O} at magmatic temperatures, and within an order of magnitude greater than high temperature extrapolations.

5.2.3 Two particle D_{H2O} and H_2O solubility calculations from bulk H_2O of different particle sizes

Different particle sizes at the same experimental duration allow for mass balance calculations to predict the diffusive length of H_2O_t and its solubility in glass. For both 95 μm and 155 μm the solubility required to yield the observed H_2O_{bulk} concentrations can be calculated for every diffusion length according to Eq. 4. The modeled range of distances correspond to the diffusive lengths at which the total mass of H_2O added to the glass is equal to the product of the modeled C_{sat} and modeled distance (Figure 9). This distance corresponds to the inflection point in the diffusion profile (which is negligibly greater than the half-fall distance, and therefore used to approximate it).

$$C_{sat} = \left(\frac{1}{m_{hyd}/m_{tot}}\right) \times \left[H_2O_{bulk} - 0.08\left(1 - \frac{m_{hyd}}{m_{tot}}\right)\right] \quad (Eq.\ 4)$$

In this equation, C_{sat} is the H_2O solubility, m_{hyd} and m_{tot} refer to the mass of H_2O in the glass from secondary hydration and the bulk H_2O concentration. The measured H_2O concentration by TC/EA is given as H_2O_{bulk}. The m_{hyd} is calculated for distances from 0.1-50.0 μm in increments of 0.1 μm by assuming a density of constant density for rhyolite of 2600 kg/m^3 and that the particles are spheres. The radii are permitted to vary by 10% in these calculations in order to ensure that an analytical solution is possible. This produces a range of possible diffusive lengths constrained to ±2 μm, with the range increasing at longer durations and faster D_{H2O}. The distances at which m_{hyd} for the two particle radii and their respective H_2O_{bulk} concentrations yield the same C_{sat} reflect a non-unique, but analytically solvable combinations of H_2O solubility and D_{H2O}. The diffusion model is then run for each C_{sat} to find the D_{H2O} value that correlates with the modeled distance from the equation above. It is important to note that this mass balance model makes no assumptions about P, T, or H_2O effects on solubility. It simply reconciles D_{H2O} and H_2O solubility values that can produced the observed bulk H_2O concentrations in the

TC/EA data for 2 particle sizes that have been hydrated for the same length of time under the same P-T-X_{H2O} conditions.

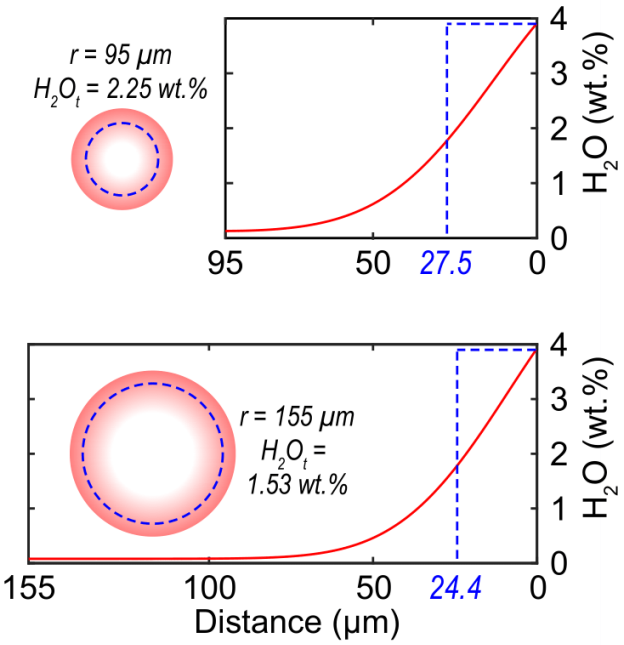

Figure 9. Example illustrations of models from the two-particle method. For a given H_2O solubility (3.9 wt.%), there is a diffusive length that can produce the observed H_2O_{bulk} concentrations in different sized particles, which can be correlated to a specific D_{H2O}. The spherical geometry of the diffusion model yields slightly different diffusive lengths. Fitting a D_{H2O} to diffusive length in the larger particle gives a minimum estimate of D_{H2O}, in this case a prefactor of 2.57.

However, Figure 9 shows that smaller particles will achieve longer diffusive lengths faster intrinsically because of the spherical geometry of the diffusion model. After 1010 hours of hydration, this produces a 3.1 μm difference in diffusive lengths (Figure 9) for the necessary m_{hyd} for each particle size. Since this approximates the range of acceptable diffusive lengths by allowing a ~10% variation in the particle radii, we simply use the median value and fit D_{H2O} to this distance using the larger particle size, which makes the modeled D_{H2O} values in Figure 8 best estimates, perhaps on the minimum side for this method.

5.2.4 H_2O diffusivity summary

The D_{H2O} results from multiple types of diffusion modeling (Figure 8) are all broadly consistent, whether they come from TC/EA diffusion mass balance approaches (bulk method, high sensitivity) or from NanoSIMS diffusion models (in situ method, low

sensitivity). The 3 types of models return diffusivity prefactors between 0.9 and 5.5 over this 200°C temperature range for which there is scant data in the literature (Friedman and Long, 1976; Mazer et al., 1991). This indicates that extrapolations of high temperature H_2O diffusivity models perform well below the glass transition and can be extended to this sub-magmatic temperature range, but this partially depends on having accurate H_2O solubility estimates because of the H_2O concentration dependence of D_{H2O}. As we demonstrated, the high temperature extrapolations for the H_2O solubility fail to predict our observed H_2O_{bulk} concentrations.

Other factors, such as chemical composition and relative humidity, have also been shown to influence D_{H2O}. Two studies above 100°C, but below the 400°C give D_{H2O} higher than our modeling results (Friedman and Long, 1976; Mazer et al., 1991). Both studies, which just used optical microscopic thickness measurements, note that the D_{H2O} in rhyolitic glass appears to be somewhat composition-dependent, but only Mazer et al. (1991) calculated D_{H2O} at hydrothermal temperature for more than one composition. Using a different glass than Newberry volcano, Oregon LSR obsidian (or Icelandic Kerlingerfjöll obsidian in Friedman and Long, 1976) may have provided more overlap with the results of Mazer et al. (1991). Their results were also relative humidity-dependent (ours are at 100% humidity), so their lowest, most comparable D_{H2O} was determined from a 60% relative humidity experiment. This may indicate that dehydration experiments at temperatures near the glass transition (e.g. Zhang and Behrens, 2000) may yield lower D_{H2O} values around 400-500°C thereby pulling the high temperature calibration to lower values.

The D_{H2O} results presented here are bracketed by high temperature extrapolations to our experimental temperatures and two previous studies (Friedman and Long, 1976; Mazer et al., 1991; Zhang and Behrens, 2000) that ventured into the hydrothermal temperature range. The best fit D_{H2O} prefactors by any method do not exceed 5 times the extrapolation of Zhang and Behrens (2000). We note that this increase in D_{H2O} between 175°C to 375°C is a much smaller correction than is required to explain D_{H2O} values at Earth surface temperatures, so we propose that our model results best apply to systems with high water-rock ratios that are near or above the boiling point of H_2O.

5.3 Oxygen isotope systematic of glass hydration

Rarely reported $\delta^{18}O$ of water-in-glass analyses demonstrate that H_2O_m in glass dominates the oxygen isotope systematic of glass during hydration as it is the primary vehicle for exchange (Figure 10). To underscore the importance of H_2O in glass on the bulk $\delta^{18}O$ composition, just 4 wt.% H_2O_t will comprise ~7% of the molar proportion of oxygen in the glass. Thus, the addition of this H_2O alone can exert a strong effect on the bulk $\delta^{18}O$ of the glass even without exchanging with the silicate matrix. For example, in both perlites and LSR obsidian at 375°C (4.0-4.8 wt.% H_2O_{bulk}), $\delta^{18}O$ of the oxygen structurally bound in silicate ($\delta^{18}O_{sil}$) calculated from mass balance is lower than the $\delta^{18}O_{bulk}$ by approximately +1‰ because of the high H_2O_{bulk} content (Figure 10). Notably, meteoric waters are commonly much more depleted in $\delta^{18}O$ than our experimental water (+5.88‰ $\delta^{18}O$), so this effect is likely even more pronounced in natural systems (Seligman and Bindeman, 2019).

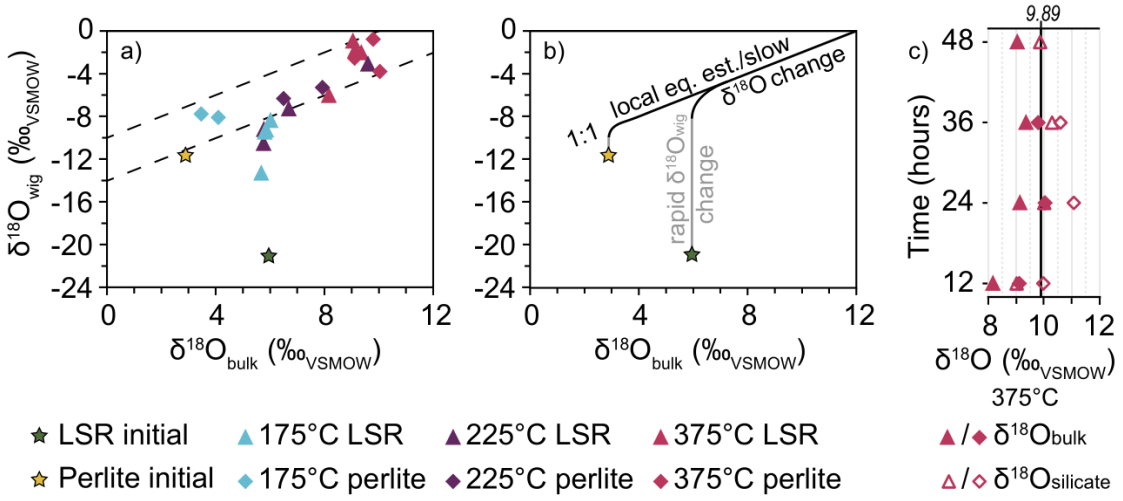

Figure 10. The relationship between $\delta^{18}O_{bulk}$ and $\delta^{18}O_{wig}$ follows a similar trend across all temperatures (a). The high-Si perlites follow a linear trend to higher $\delta^{18}O_{bulk}$ and $\delta^{18}O_{wig}$ whereas the initially anhydrous LSR seems to increase at constant $\delta^{18}O_{bulk}$ before increasing in $\delta^{18}O_{wig}$ along the same trend as and at similar values to the perlites. This is shown schematically in (b) where $\delta^{18}O_{wig}$ rapidly equilibrates locally with the $\delta^{18}O_{bulk}$ and then both $\delta^{18}O$ parameters increase slowly together towards the equilibrium glass value. $\delta^{18}O_{bulk}$ and $\delta^{18}O_{silicate}$ straddle the predicted equilibrium value for rhyolite (9.89 ‰) with the experimental water $\delta^{18}O$ composition (c).

At our hydrothermal temperatures, H_2O_m molecules exchange their oxygen with the oxygen bound in silicate glass, so $\delta^{18}O_{wig}$ can be used to trace the progress of $\delta^{18}O$ of

the bulk glass towards equilibrium. In the LSR glasses, only the 375°C experiments and the smallest LSR at 225°C were sufficiently long in duration to become fully hydrated and attain bulk $\delta^{18}O$ compositions in equilibrium with the hydration water, which we interpret from plateaus in bulk H_2O, $\delta^{18}O_{wig}$, and $\delta^{18}O_{bulk}$ after just 24 hours. This observation that glass exchanges silicate-bound oxygen more readily once hydrated via the diffusion of molecular H_2O through the glass explains why the perlites begin to acquire a higher bulk $\delta^{18}O$ while the anhydrous LSR obsidian is slower to change in the lower temperature experiments.

While bulk glass-water oxygen isotope equilibrium requires complete hydration, before the silicate can exchange completely with external fluid, local equilibration of $\delta^{18}O_{wig}$ with the $\delta^{18}O$ of the bulk silicate glass does not. Within this conceptual model, two equilibrium relationships – a $10^3\ln\alpha_{wig\text{-}H2O}$ and a $10^3\ln\alpha_{glass\text{-}wig}$ – together govern the $10^3\ln\alpha_{glass\text{-}H2O}$ relationship. Bulk $\delta^{18}O$ and $\delta^{18}O_{wig}$ from all experimental temperatures track the nature of oxygen isotope exchange in these two intermediate steps (Figure 10a,b). The perlites form a nearly linear trend across all temperatures with a slope of ~1. The LSR glass, on the other hand, increase in $\delta^{18}O_{wig}$ without increasing in bulk $\delta^{18}O$ until they reach the trend of the perlites, at which point they increase along the same nearly 1:1 trajectory.

The relatively constant offset between $\delta^{18}O_{wig}$ and $\delta^{18}O_{bulk}$ (Figure 10) can also be coarsely applied as a thermometer in glasses that have been rehydrated in excess of 2 wt.% H_2O in hydrothermal systems. We speculate that local equilibrium is quickly attained between the oxygen in molecular H_2O and oxygen in neighboring silicate bonds even when hydration is incomplete. Once the H_2O_m and the silicate glass reaches a local equilibrium with the surrounding glass, the offset between $\delta^{18}O_{wig}$ and $\delta^{18}O_{bulk}$ will be maintained during subsequent hydration as H_2O_m continues to drive oxygen isotope exchange within the glass. During this process, local equilibrium should cause bulk $\delta^{18}O$ and $\delta^{18}O_{wig}$ to migrate to higher values along a trend with a slope of 1 and we observe a slope of ~1.1 (Figure 10b). Although the $10^3\ln\alpha_{glass\text{-}wig}$ is not highly sensitive to temperature over the 175°C to 375°C range of these experiments relative to our conservative estimate for analytical precision (Figure 10a), the 375°C experimental glasses seem to have slightly smaller magnitude glass-wig fractionation (+10 to +11‰)

than the 175°C glasses (+13 to +14‰). Collectively, data from all temperatures converges at a $10^3\ln\alpha_{glass\text{-}wig}$ of approximately +12.0.

This interpretation differs somewhat from the previous studies that argue that the $\delta^{18}O_{wig}$ approximates the $\delta^{18}O$ of the hydration waters (Bindeman and Lowenstern, 2016; Hudak and Bindeman, 2018; Seligman and Bindeman, 2019). In the case of Seligman and Bindeman (2019) which use glasses hydrated at Earth surface temperatures, hydration and exchange between the silicate and the water in glass may not have proceeded rapidly, so the $\delta^{18}O_{wig}$ may simply record the $\delta^{18}O$ of the hydration waters. With hydration temperatures of ~100°C, the lowest reported Nez Perce perlite $\delta^{18}O_{wig}$ measurement is −14.9‰ (Bindeman and Lowenstern, 2016), which approaches the modern meteoric $\delta^{18}O$ of −17‰ in thermal waters in Yellowstone (Sturchio et al., 1990). This seemed to support the idea that very little O isotope fractionation occurred between meteoric waters and the water in glass. If, as we argue in this work across all temperatures, the difference reflects rapid attainment of local O isotope equilibrium, $10^3\ln\alpha_{glass\text{-}wig}$ may instead be considered as a thermometer. Bindeman and Lowenstern (2016) and Hudak and Bindeman (2018) argue for hydration around the boiling point of H_2O at ~100°C. Thus, the similar mean $10^3\ln\alpha_{glass\text{-}wig}$ values of 13 Yellowstone perlites of +14.0‰ ± 1.6‰ (1σ) and 18 Crater Lake pinnacle glasses +13.9‰ ± 2.2‰ (1σ) are an extension of our experimental results. Our experiments and these results from previous studies on natural systems represent a ~4‰ spread in $10^3\ln\alpha_{glass\text{-}wig}$ over a nearly 300°C temperature range – from +14‰ at 100°C to +10‰ at 375°C.

6. Conclusions

We evaluated the solubility and diffusivity of H_2O in glass, and O isotope systematics of glass hydration over a hydrothermal temperature and pressure range (175-375°C, 0.89-21 MPa). Our results on H_2O systematics in glass bridge a gap between those better studied high temperatures and Earth surface temperatures and exhibit some key similarities and differences that allow the following conclusions to be made.

1) Our rhyolitic glasses (including both high and low silica rhyolites) yield H_2O solubility ranges of: 2.75-3.4 wt.% (175°C, 0.89 MPa), 3.1-4.2 wt.% (225°C, 2.55 MPa), and 4.1-5.0 wt.% (375°C, 21 MPa), which are 1-2 wt.% higher than predicted by

extrapolation from high temperature solubility models (Newman and Lowenstern, 2002; Liu et al., 2005). Pressure is likely partly responsible for the higher solubility at 375°C and 21 MPa (no less than 4.5 wt.%) compared to 175°C and 0.89 MPa (no greater than 3.4 wt.%). However, it cannot explain the 1-2 wt.% higher concentrations than predicted by extrapolations from high temperatures. This marks a significant difference in the H_2O solubility mechanism(s) below the glass transition. A high humidity likely also plays a role as many D_{H2O} and H_2O solubility estimates come from dehydration experiments.

2) Low-Si rhyolite has higher H_2O solubility than high-Si rhyolite by ~0.5 wt% at 175°C, 225°C, and 375°C, which may be related to the higher NBO/T ratios of high silica rhyolite.

3) NanoSIMS measurements of D and H profiles show a "snowplow" functional form resulting from D_{H2O} dependence on H_2O content, as is also observed in silicate melts at magmatic temperatures.

4) Modeled D_{H2O} values plotted against 1/T exhibit an approximate, linear Arrhenius relationship with D_{H2O} values up to 5.5 times greater than extrapolation of higher T experiments (Zhang and Behrens, 2000), depending on the chosen solubility for the relevant P-T-X_{H2O} conditions. The continuation of high temperature D_{H2O} relationships, however, does depend on having high H_2O solubility.

5) Oxygen isotopes are exchanged in two steps: first via H_2O_m diffusion into glass, then by local exchange with silicate. We observe that initially anhydrous glasses show limited exchange with bulk glass $\delta^{18}O$ (except for at 375°C), but initially hydrous perlites begin to exchange with added H_2O and change bulk $\delta^{18}O$ immediately. The $\delta^{18}O_{wig}$ approaches local equilibrium with the $\delta^{18}O_{glass}$ rapidly (within weeks at 225°C and within days at 375°C) and subsequent back-diffusion of lighter $\delta^{18}O$ H_2O_m out of the glass drives $\delta^{18}O_{wig}$ and $\delta^{18}O_{glass}$ towards higher $\delta^{18}O$ values in equilibrium with the external water.

6) This isotope diffusion-reaction process appears to be achieved quickly in the 375°C experiments where complete hydration occurs after 2 days. The $\delta^{18}O_{bulk}$ of 9-10‰ and a $\delta^{18}O_{wig}$ of ~−1‰ indicate $10^3\ln\alpha_{glass\text{-}wig}$ is 10-11‰. The equilibrium $10^3\ln\alpha_{glass\text{-}wig}$ seems to be locally achieved rapidly at all temperatures and $10^3\ln\alpha_{glass\text{-}wig}$ is ~14‰ and ~10‰ between 100°C to 375°C.

7) Using our methods, we cannot detect kinetic isotope fractionation of D relative to H. This, along with the evidence from O isotopes indicate that D/H isotope exchange via H_2O_m, appears to be the main isotope exchange mechanism between silicate glass and water.

7. Bridge

Chapter II quantifies H_2O solubility and diffusivity in silicic volcanic glasses using glass hydration experiments under hydrothermal conditions. Critically, H_2O solubility is at least 1.5 wt% higher than predicted from extrapolation of magmatic solubility relationships for any given temperature-pressure condition. Additionally, D_{H2O} is within an order of magnitude of high temperature (>400°C) extrapolations in melts and glasses. Together these results demonstrate not only that glass hydration is possible, but that it should proceed with ease in environments where H_2O is readily available. The novel application of $\delta^{18}O_{wig}$ also strongly suggests that H_2O_m is the carrier of H into the glass, which helps to streamline modeling of H isotope fractionation during hydration in Chapter III. In the next chapter, I show δD results in these experiments through time and evidence for partial repartitioning of H_2O_m to OH^- in the glasses. To understand the equilibrium and kinetic isotope fractionations during diffusion and this speciation reaction, I employ a 1D finite difference reaction-diffusion model. However, this model reveals that the δD composition of the boundary controls the bulk δD composition of the glass rather than kinetic effects from reaction or diffusion.

CHAPTER III

HYDROGEN ISOTOPE FRACTIONATION BETWEEN VOLCANIC GLASS AND WATER VAPOR BETWEEN 175°C AND 375°C

From Hudak, M.R., Bindeman, I.N., Watkins, J.M., and Lowenstern, J.B. Hydrogen isotope fractionation between volcanic glass and water vapor between 175°C and 375°C. In review at *Geochimica et Cosmochimica Acta*.

1. Introduction

Water is ubiquitous both on the surface and within the Earth. As the most abundant volcanic volatile and the primary driver of volcanic eruptions, the solubility, diffusivity, and speciation of H_2O in silicate melts have been thoroughly investigated at magmatic temperatures over a large range of compositions in natural samples and in experiments (e.g. Stolper, 1982; Silver et al., 1990; Zhang et al., 1991; Zhang et al., 1997; Withers et al., 1999; Zhang, 1999; Zhang and Behrens, 2000; Newman and Lowenstern, 2002; Liu et al., 2005; Ni and Zhang, 2008; Coumans et al., 2020). Volcanic glasses that have rehydrated in the presence of water after eruption have provided complementary constraints on these properties of H_2O in glass at low temperatures (e.g. Friedman and Long, 1976; Anovitz et al., 2008; Giachetti et al., 2015). Hydrogen isotopic studies of water in glass serve to disentangle magmatic degassing and secondary hydration (Seligman et al., 2016; Martin et al., 2017; Hudak and Bindeman, 2018; Seligman et al., 2018; Giachetti et al., 2020) and can be used to investigate both high and low temperature processes. At higher temperature, obsidian pyroclasts and flows become isotopically lighter as volcanic degassing progresses, and these trends can be modeled to determine degassing style (e.g. Taylor et al., 1983; Newman et al., 1988; Dobson et al., 1989; Castro et al., 2014; Seligman et al., 2016; Walter and Castro, 2020). As degassed glass rehydrates in the environment, it records the composition of the local meteoric water, making δD in glasses a viable paleoclimate proxy (e.g. Cassel et al., 2014, 2012, 2009; Colwyn and Hren, 2019; Dettinger and Quade, 2015; Friedman et al., 1993b; Hudak and Bindeman, 2018; Jackson et al., 2019; Seligman et al., 2016).

Constraints on H_2O behavior and isotope systematics in volcanic glasses at intermediate temperatures between magmatic conditions and those at Earth's surface are less well constrained (Friedman and Long, 1976; Mazer et al., 1991; Anovitz et al., 2004; Hudak and Bindeman, 2020). Broad similarities and difference between the behavior of H_2O in melts and glasses are understood, particularly for silicic compositions (i.e. dacites and rhyolites) and can inform our expectations of H_2O behavior in glass in this intermediate temperature window. Of the two species of H_2O present in silicate glasses and melts – molecular water (H_2O_m) and hydroxyl (OH^-) – H_2O_m is the diffusive species at all temperatures (e.g. Zhang et al., 1991; Behrens et al., 2007; Hudak and Bindeman, 2020). However, a critical difference between glasses and melts is the ability of H_2O to repartition into OH^-. The equilibrium speciation in melts is constrained as a function of temperature, total water (H_2O_t) concentration, and bulk composition (Stolper, 1982; Silver et al., 1990; Zhang et al., 1997; Ihinger et al., 1999; Withers et al., 1999; Newman and Lowenstern, 2002; Coumans et al., 2020). Generally, this reaction is not thought to proceed below the glass transition temperature (T_g), which is the temperature at which melt begins to exhibit the mechanical and thermodynamic properties of a glass. T_g is a function of bulk composition, cooling rate, and volatile concentration, and is generally no lower than 400°C (e.g. Dingwell, 1995; Dingwell et al., 1996; Dingwell, 1998; Giordano et al., 2005; Del Gaudio et al., 2007). The extent to which H_2O_m can repartition into OH^- in glasses is critical for understanding hydrogen isotope compositions in volcanic glass. Hydrogen isotope fractionation between melt and H_2O vapor at magmatic conditions is strongly dependent on the proportion of OH^- to H_2O_m as OH^- strongly favors ^1H (H) over ^2H (D; Dobson et al., 1989), while at low temperatures OH^- is effectively inert so the glass-H_2O fractionation depends solely on H_2O_m during rehydration.

All melts must cool below T_g and through the temperature window between magmatic and ambient conditions. Even at fast quench rates, interactions and reactions between H_2O vapor and a melt or glass are possible on short timescales and diffusive length scales. Therefore, the reaction rates between H_2O_m and OH^- and the hydrogen isotope fractionations between these species must be better understood to interpret the record of H_2O in volcanic glass. This study combines glass hydration experiments, bulk hydrogen isotope measurements, and a new isotope diffusion-reaction model to

investigate to what extent partitioning between H_2O_m and OH^- occurs in a glass at high, but submagmatic temperatures below T_g and how this reaction would affect the hydrogen isotope composition of the glass.

2. Methods

2.1 Experimental materials and design

Glass hydration experiments were conducted to constrain hydrogen isotope fractionation between glass and H_2O vapor over a hydrothermal temperature range relevant to many cooling eruptive products (Randolph-Flagg et al., 2017; Hudak and Bindeman, 2018; Mitchell et al., 2018b; Seligman et al., 2018; Rempel and Bindeman, 2019). Water and three natural rhyolitic volcanic glasses with known δD were loaded together into stainless-steel vessels and held isothermally in a muffle furnace for hours to months. (Particles used for the diffusion modeling were air abraded into spheres and oblate ellipsoids with mean radii of 95-160 μm; described in Hudak and Bindeman, 2020.) Glasses were suspended above the liquid H_2O in Ag capsules to facilitate vapor hydration. Two initially anhydrous glasses are from a low silica rhyolite (LSR) from Newberry volcano, Oregon, USA (0.08 wt% H_2O, −100.8‰ δD) and a high silica rhyolite (HSR) from the Summit Lake flow at Yellowstone, Wyoming, USA (0.15 wt% H_2O, −115‰ δD). These are used primarily for constraining the D/H $10^3\ln\alpha_{glass\text{-}H2O}$ because the secondary H_2O will quickly swamp residual magmatic H_2O in the glass. Naturally rehydrated high-Si perlites from the Nez Perce flow in Yellowstone (~2.90 wt% H_2O, −180.5‰ δD) serve as a counterpoint to assess D/H exchange between glass and water through time. The hydration water had a δD of +75.6‰ and a $\delta^{18}O$ of +5.9‰. Further details of the experimental design and chemical characterization of the starting glasses are reported in Hudak and Bindeman (2020).

2.2 Analytical methods

Simultaneous analyses for H_2O_t and δD relied on milligram quantities of glass and were conducted on a Finnegan MAT253 isotope ratio mass spectrometer equipped with a high-temperature-conversion, elemental analyzer (TC/EA) at the University of Oregon. Mica standards USGS57 (biotite) and USGS58 (muscovite) are used for calibration and are analyzed 3-5 times throughout each analytical session (Qi et al., 2017), commonly

also with an internal laboratory biotite standard, BUD. Isotope compositions are expressed in delta notation relative to Vienna Standard Mean Ocean Water (VSMOW). See Martin et al. (2017) for more details about the thermal decomposition of glass and pyrolysis method. Water concentration maps were made using transmission Fourier transform infrared spectroscopy (FTIR) on a ThermoNicolet iN10-MX at the USGS in Menlo Park, CA, utilizing an MCT-A detector. Maps were made with aperture-IR spot sizes of 8x8 μm and 20x20 μm for the 225°C and 375°C experiments, respectively. We used a default spectral resolution of 8 cm^{-1} and other defaults discussed in Lowenstern and Pitcher (2013). Water concentrations were quantified by means of the near IR peaks at 4500 and 5210 cm^{-1} using the method of Zhang et al. (1997). Secondary electron images of the surfaces of the 275°C and 375°C glasses were taken using a FEI Quanta 200 ESEM/VPSEM microscope at 2.0 keV and 10 Pa.

2.3 Isotope Notation

Analytical results are presented in delta notation:

$$\delta D_{\text{glass}}(‰) = 1000\left(R^{\text{D/H}}_{\text{glass}}/R^{\text{D/H}}_{\text{VSMOW}} - 1\right), \qquad (1)$$

where $R^{D/H}_{\text{VSMOW}}$ = 1/6420 is the isotopic ratio of the standard. Equilibrium isotope partitioning between glass and fluid phases is given as:

$$\alpha^{\text{D/H}}_{\text{g-v}} = R^{\text{D/H}}_{\text{glass}}/R^{\text{D/H}}_{\text{vapor}} = \frac{1000 + \delta D_{\text{glass}}}{1000 + \delta D_{\text{vapor}}}. \qquad (2)$$

Values for $\alpha_{\text{g-v}}$ are generally close to 1.000 and can be more directly compared to the compositions of the two phases in units of ‰ using the expression, $10^3 \ln\alpha_{\text{g-v}}$. Direct comparison of the glass δD results to the δD of the fluid uses ΔD notation where

$$\Delta D_{\text{g-v}} = \delta D_{\text{glass}} - \delta D_{\text{vapor}}. \qquad (3)$$

This can be calculated for any individual δD result. However, we instead use $10^3 \ln\alpha_{\text{g-v}}$ notation throughout the text, but limited to the longest duration experiments where glass-vapor isotopic equilibrium is approximated by a plateau in the δD time series, in which case

$$10^3 \ln\alpha^{\text{eq}}_{\text{g-v}} \approx \Delta D_{\text{g-v}}. \qquad (4)$$

When there are large differences in the isotopic composition of glass versus vapor, $10^3 \ln\alpha_{\text{g-v}}$ diverges from $\Delta D_{\text{g-v}}$. However, even for the largest magnitude

fractionations observed in this study, $10^3 \ln\alpha_{g\text{-}v}$ diverges from $\Delta D_{g\text{-}v}$ never differ by more than 3‰, which is within the analytical precision of our measurements.

3. Analytical results

3.1 TC/EA δD results

Results of experiments are presented in Figures 1-3 and include time series measurements of reaction products progressively taken away in the course of experiments lasting from 4 hours to 250 days. Experiment duration scales with the diffusivity of H_2O in rhyolite glass, which is described by an exponential function (e.g. Zhang and Behrens, 2000). All experimentally hydrated glasses experienced an increase in δD from their initial hydrogen isotope compositions (<−100‰) towards the H_2O vapor (minimum of +69.5‰), and with the exception of the 275°C experiments, the δD values continued to increase monotonically with duration (Figure 1). Initially anhydrous obsidians form sublinear δD trends when plotted against the natural logarithm of time (Figure 1a), while the naturally rehydrated perlites form linear trends consistent with a constant isotope exchange rate (Figure 1b).

3.1.1 Below 250°C results

We separate the results into two regimes: above and below 250°C. Results below 250°C are shown in Figure 2. In these experiments, the δD of glass steadily increased to high positive δD values. In LSR, the initial increase in δD was relatively rapid resulting in an asymptotic approach of glass δD towards a composition in equilibrium with the H_2O vapor. At 175°C, this trend is apparent in all LSR particle sizes (Figure 2a). The largest size fraction (r_{eff} = 155μm, rounded) increased most slowly in δD towards the vapor composition of +69.5‰. The intermediate particle size (r_{eff} = 95μm, rounded) increased in H_2O and δD at a rate between the larger and smaller particle sizes and achieved a maximum δD of 27.6‰. The smallest particle size (r_{eff} = 26-53μm, angular) yielded the highest δD values of +45.3‰ and +48.3‰ after 3000 and 6000 hours, respectively (Table 1). The δD between these two experiments effectively remained unchanged even though the experimental duration was doubled and an additional ~0.5 wt% H_2O diffused into the glass, reaching 2.75 wt% (Figure 2b). The mean difference between glass and H_2O vapor δD for these two results gave an equilibrium D/H $\alpha_{g\text{-}v}$ of

0.979, which corresponds to a $10^3\ln\alpha_{g\text{-}v}$ of −21.5‰. Both anhydrous glasses, LSR and HSR, similarly asymptotically approached an equilibrium glass δD plateau at 225°C (Figure 2c; Table 1). The LSR glasses hydrated for at least 240 hours (>0.5 wt% H_2O), with just one exception, and converged on a mean δD value of 32.6‰ regardless of particle size (n=4, 4.3‰ 2σ). This mean glass δD corresponds to an $\alpha_{g\text{-}v}$ of 0.960 and a $10^3\ln\alpha_{g\text{-}v}$ of −40.5‰. The HSR achieved a notably higher maximum δD value of +46.0‰, corresponding to an $\alpha_{g\text{-}v}$ of 0.973 and a higher minimum value for $10^3\ln\alpha_{g\text{-}v}$ of −27.6‰. The H_2O-δD evolution of glasses at 225°C (Figure 2d) followed a similar trajectory as the glasses in the 175°C experiments (Figure 2b). The δD of the anhydrous glasses increased rapidly at low H_2O and then plateaued above 1 wt%.

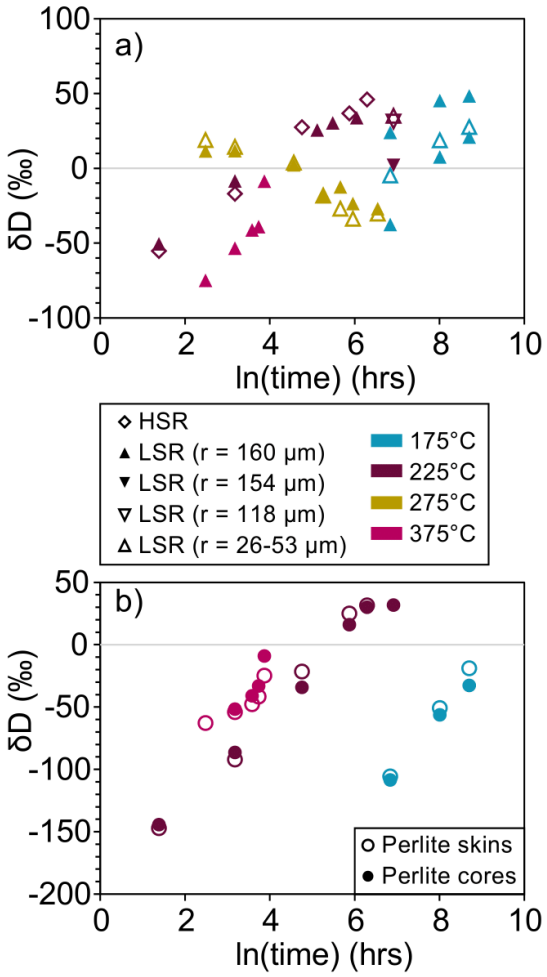

Figure 1. The natural log of time in hours vs. bulk δD measurements for initially anhydrous rhyolite glass (a) and hydrous perlites (b).

Material	*Effective radius (μm)*	*Duration (hours)*	*H_2O (wt.%)*	*δD (‰)*	$\alpha_{g\text{-}v}$	$10^3 ln\alpha_{g\text{-}v}$ *(‰)*
Initial Experimental Glass Compositions						
LSR	n/a	0	*0.08*	-100.8		
HSR	n/a	0	*0.15*	-115.0		
Perlite skins	n/a	0	*2.90*	-180.5		
175°C Experimental Results						
LSR	155	935	*0.28*	-37.6		
LSR	155	3000	*0.38*	7.5		
LSR	155	6000	*0.65*	20.9		
LSR	95	935	*0.55*	-4.8		
LSR	95	3000	*0.74*	18.7		
LSR	95	6000	*1.03*	27.6	0.961	-39.9
LSR	26-53[a]	935	*1.47*	23.9		
LSR	26-53[a]	3000	*2.29*	45.3	0.977	-22.9
LSR	26-53[a]	6000	*2.75*	48.3	0.980	-20.0
Perlite skins	n/a	935	*2.77*	-108.5		
Perlite skins	n/a	3000	*2.68*	-56.3		
Perlite skins	n/a	6000	*2.74*	-32.7		
Perlite cores	n/a	935	*2.54*	-105.6		
Perlite cores	n/a	3000	*2.47*	-50.9		
Perlite cores	n/a	6000	*2.64*	-18.8		
225°C Experimental Results						
LSR	160	4	*0.20*	-50.6		
LSR	160	24	*0.40*	-8.5		
LSR	160	167	*0.52*	25.6		
LSR	160	240	*0.54*	30.4	0.958	-42.7
LSR	160	423	*0.67*	33.8	0.961	-39.4
LSR	155	1010	*1.35*	2.0		
LSR	95	1010	*2.40*	35.0	0.963	-38.2
LSR	26-53[a]	1010	*3.70*	31.2	0.959	-41.9
HSR	n/a	4	*0.15*	-55.2		
HSR	n/a	24	*0.25*	-17.0		
HSR	n/a	116	*0.46*	27.4		
HSR	n/a	356	*0.66*	36.8		
HSR	n/a	539	*0.90*	46.0	0.973	-27.6

Table 1. Total H_2O and δD data for experimental glasses. Errors for δD are <3‰ (1 s.d., n = 3-5) for standards USGS57 and USGS58. Italicized H_2O_t concentrations are from Hudak and Bindeman (2020). [a]The smallest particle sizes could not be measured, so the range of radii given is half of the sieve fraction for these particles (53-105 μm).

Chapter III, Section 3.1.1.

Table 1, continued.

Perlite skins	n/a	4	*2.70*	-147.1		
Perlite skins	n/a	24	*2.63*	-92.1		
Perlite skins	n/a	116	*2.71*	-21.5		
Perlite skins	n/a	356	*2.82*	25.0		
Perlite skins	n/a	539	*2.89*	31.6	0.959	-41.5
Perlite cores	n/a	4	*2.51*	-144.3		
Perlite cores	n/a	24	*2.40*	-86.4		
Perlite cores	n/a	116	*2.34*	-34.2		
Perlite cores	n/a	356	*2.66*	16.1		
Perlite cores	n/a	539	*2.67*	30.0		
Perlite cores	n/a	1010	*3.10*	31.8	0.960	-41.3
275°C Experimental Results						
LSR	155	12	*0.40*	11.5		
LSR	155	24	*0.57*	11.8		
LSR	155	96	*1.35*	2.3		
LSR	155	192	*1.80*	-18.3		
LSR	155	288	2.29	-12.4		
LSR	155	386	2.76	-23.6	0.906	-98.9
LSR	95	12	*0.54*	18.9		
LSR	95	24	*0.74*	14.3		
LSR	95	96	*1.77*	3.7		
LSR	95	192	*2.65*	-18.3		
LSR	95	288	2.95	-27.0	0.903	-102.4
LSR	95	386	3.37	-33.7	0.896	-109.3
375°C Experimental Results						
LSR	160	12	*3.40*	-74.9		
LSR	160	24	*4.50*	-53.5		
LSR	160	36	*4.57*	-41.3		
LSR	160	42	*4.75*	-39.1		
LSR	160	48	*4.57*	-8.7	0.922	-81.6
Perlite skins	n/a	12	*4.16*	-62.8		
Perlite skins	n/a	24	*4.17*	-54.0		
Perlite skins	n/a	36	*4.22*	-47.8		
Perlite skins	n/a	42	*4.14*	-41.7		
Perlite skins	n/a	48	*4.03*	-24.8	0.907	-98.0
Perlite cores	n/a	24	*4.13*	-51.7		
Perlite cores	n/a	36	*4.02*	-41.0		
Perlite cores	n/a	42	*4.12*	-33.0		
Perlite cores	n/a	48	*4.04*	-9.1	0.921	-82.0

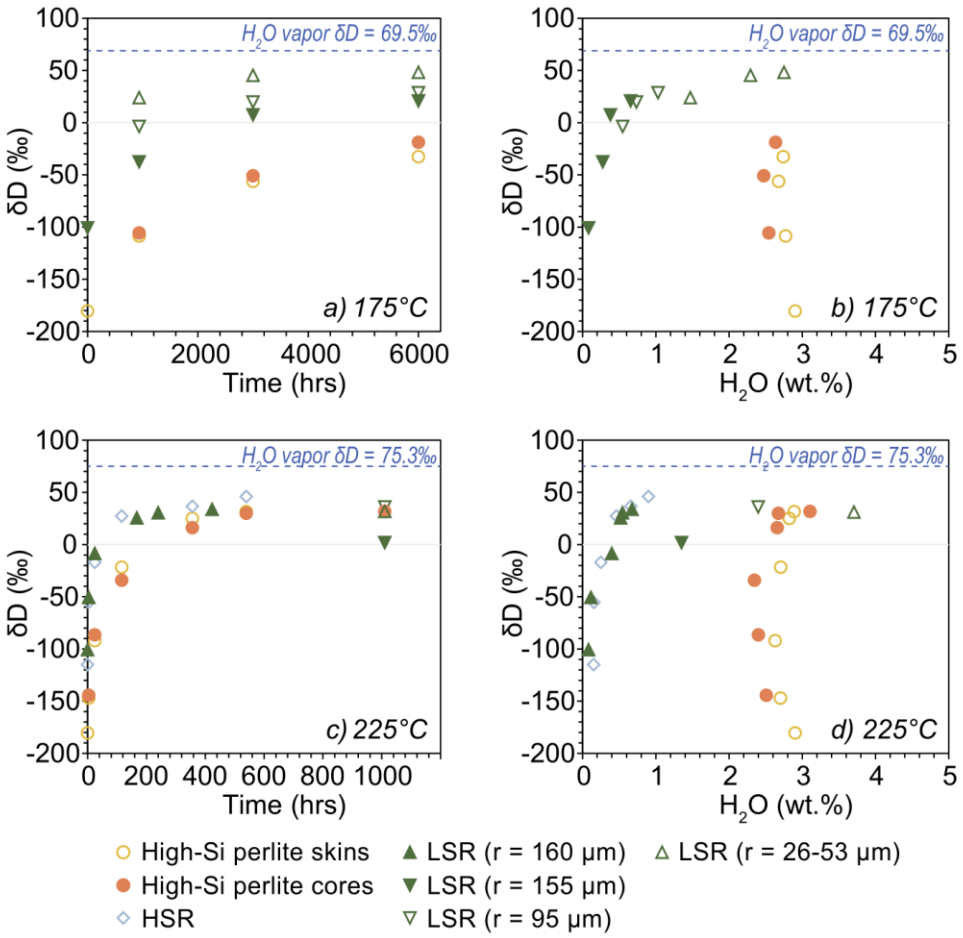

Figure 2: Bulk glass δD measurements from experiments at 175°C (a,b) and 225°C (c,d). Experimental glasses asymptotically approach the δD of the H_2O vapor through time (a,c; dashed line). Initially anhydrous glasses increase in H_2O with time while perlites dehydrate by no more than 0.2 wt.% before recovering to higher H_2O (b,d).

The perlites also increased asymptotically in δD through time below 250°C. Because they contained nearly 3 wt%, the experimental water added could not simply overprint the δD of preexisting meteoric and magmatic H_2O in the glass, which resulted in a slower increase toward the equilibrium glass δD value (Figure 2a). At 175°C, neither the perlite skins nor cores ever achieved positive δD values. Even in the 6000-hour-long experiments the maximum observed δD value was −18.8‰ (Table 1). But at 225°C, perlite skins and cores attained identical δD values comparable to the LSR δD values, yielding an $\alpha_{g\text{-}v}$ of 0.959 and a $10^3 \ln\alpha_{g\text{-}v}$ of −41.4‰. The perlites dehydrated with the earliest increases in δD (Figure 2b,d) in both of these sets of experiments. While the 175°C perlites never fully recovered their initial H_2O concentration of 2.9 wt% (in the

skins), the perlites at 225°C eventually increased to 3.1 wt% H_2O as their δD approached the plateau of +31.7‰. This dehydration was minimal, never registering more than 0.3 wt% decrease from the initial H_2O. The perlites at 225°C eventually recovered their initial H_2O content and reached a maximum of 3.1 wt% H_2O after 1010 hours of hydration.

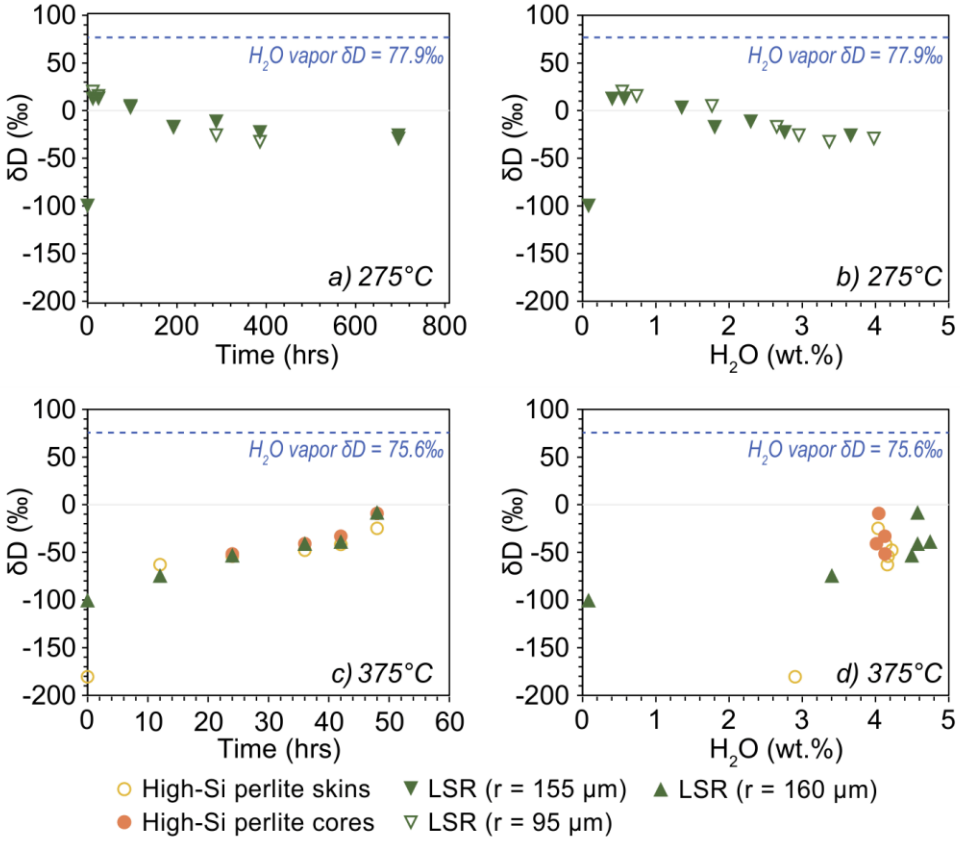

Figure 3: Bulk glass δD measurements from experiments at 275°C (a,b) and 375°C (c,d). Experimental glasses never exceed +20‰ and remain isotopically light relative to the δD of the H_2O vapor (dashed line). At 275°C, the glass increases dramatically in the shortest duration experiment before decreasing (a), which differs from the 375°C trend that increases through time (c). Linear increases in H_2O through time at 275°C cause the H_2O trend to mirror the time series (b), which again differs from the 375°C glasses that rapidly reach their H_2O solubility and slowly increase in δD.

3.1.2 Below 250°C results

The higher temperature glasses acquired much lower δD values than those in experiments below 250°C despite gaining more H_2O (Figure 3). The δD time series at 275°C is the most enigmatic of all the experiments. After just 12 hours, both LSR glass particle sizes (r_{eff} of 95 μm and 155 μm) increased by more than 110‰, plateaued at 24

hours, and decreased thereafter until the end of the experiment at 696 hours (Figure 3a). This trend was mirrored in the δD-H_2O evolution of LSR glass, where H_2O steadily increased to 3.7 and 4.0 wt% while δD decreased to −27.1‰ and −30.4‰ for particles with 155 μm and 95 μm radii, respectively (Figure 3b). The minimum δD value of −33.7‰ in these experiments was achieved after 386 hours in the intermediate particle size (r_{eff} = 95μm). Unlike the other experiments the decrease in δD for majority of the time series does not yield a simple minimum or maximum $\alpha_{g\text{-}v}$. However, the δD values may have plateaued between −23‰ and −34‰ with a mean of −28.1‰ (n = 3) in samples with ≥3 wt% H_2O (Figure 3a,b). Assuming this represents a plateau for the equilibrium δD composition for glass, these results suggest $\alpha_{g\text{-}v}$ of 0.900 and a $10^3\ln\alpha_{g\text{-}v}$ of −106‰ at 275°C. If a similar initial increase in δD occurred in glass in the 375°C experiments, the temporal sampling resolution was not fine enough to capture it. The δD of LSR particles (r_{eff} = 95μm) increased for each duration (Figure 3c), but H_2O plateaued after 24 hours (Figure 3d). Even after just 12 hours at 375°C, the LSR glass had 3.40 wt% H_2O. Through 42 hours, it appears as though the δD composition of the glass had plateaued with time. However, it increased suddenly in slope to a δD value of −8.7‰ after 48 hours. Conservatively, this yields a minimum $\alpha_{g\text{-}v}$ of 0.922 and a $10^3\ln\alpha_{g\text{-}v}$ of −82.0‰ at 375°C

Perlites followed a very similar time-δD evolution to the LSR despite their large initial differences in both H_2O and δD (Figure 3c). Even the abrupt increase in δD between 42 and 48 hours was not limited to the LSR glass. The perlite cores jumped to −9.1‰ δD while the skins increased less dramatically to −24.8‰ at 48 hours. The result for the cores was effectively identical to that of the LSR with a $\alpha_{g\text{-}v}$ of 0.921 and a $10^3\ln\alpha_{g\text{-}v}$ of −81.6‰. The perlite skins and cores plateaued in H_2O immediately even as δD continued to slowly increase (Figure 3d). All measured H_2O results were 4.12 ± 0.11 wt% H_2O, which is within analytical precision of the TC/EA for high H_2O samples (Martin et al., 2017).

3.2 FTIR results

The distribution of water and its species in a glass can be determined using FTIR spectroscopy. Mid-IR spectra of an LSR particle from a 240-hour-long and a 423-hour-long experiment at 225°C showed no apparent increase in OH^- with the addition of H_2O_m

to glass during rehydration (Figure A.1). Measurements taken from the interior of the glass particles, which have not been affected by secondary hydration, show approximately 0.1 wt% H_2O_t at the 3500 cm^{-1} peak and effectively no H_2O_m at the 1600 cm^{-1} peak. The ~0.1 wt% H_2O can be attributed entirely to OH^-, consistent with the 1 atm solubility of water in obsidian. The rim of the glass shows no apparent change to the OH^- concentration, but an addition of 0.4-0.5 wt% H_2O_m at the 1600 cm^{-1} peak for both the 240 and 423 hour-long durations for H_2O_t of 0.5-0.6 wt% at the 3500 cm^{-1} peak (Figure A.2). After 48 hours at 375°C and 21 MPa, LSR obsidian is fully hydrated and has clearly begun to repartition H_2O_m into OH^-. Both the 1600 cm^{-1} and the 3500 cm^{-1} peaks in thin glass wafers are oversaturated in IR spectra, so the near-IR peaks were used to determine H_2O_m and OH^-. The near-IR 5200 cm^{-1} peak and the 4500 cm^{-1} peak indicate that there is approximately 5.9 wt% H_2O_m and 1.0 wt% OH^-, respectively (Figure A.3). Attenuated total reflectance (ATR) FTIR (Lowenstern and Pitcher, 2013) spectra confirmed that the glass everywhere contained a homogeneous 6.9 wt% H_2O_t.

3.3 SEM results

Secondary electron images show the surface textures of the glasses from the 275°C and 375°C (Figure A4-A7). At 275°C, perlitic fractures appeared in the glass by 192 hours and surface alteration is observed only on the surface of the glass with an optical microscope (Figure A4a-d). At focal lengths inside the glass, plagioclase microlites are clear and no novel secondary phases have appeared in the glass (Figure A4b) as they do at glass surface (Figure A4c). Larger cubic secondary phases with widths up to 10 μm are interspersed fairly homogeneously within a thinner, wispy layer less than 5 μm in thickness. After 386 hours, the larger cubic phases are not present but the wispy mat ~5 μm in thickness remains (Figure A5). In both experiments, the underlying glass is scalloped, consistent with glass dissolution. The longer duration experiment appears to have undergone more heterogeneous but more extensive dissolution, particularly at the glass-microlite interface. Even within the same particle, there are places where the glass is flat, planar, and smooth (Figure A5b,c), whereas in other locations scalloping is observed and plagioclase microlites extend out from wells in the glass (Figure A5d-f). Glasses from the 375°C experiments have a more uniform layer of rhombic to dodecahedral phases that are uniform in size, not exceeding 5 μm in diameter (Figure A6-

A7). The distribution of these phases is heterogeneous, densely clustered in places and virtually absent in others on the same glass particle.

4. Interpretations of glass hydration experiments

4.1 Repartitioning of H_2O_m to OH

The low concentrations of H_2O_t in the 225°C LSR glasses (<0.6 wt%) result from short diffusion profiles measured in these samples (Hudak and Bindeman, 2020) as well as challenges in obtaining concentration measurements at the edge of a doubly polished section through a sphere. The measured OH^- concentrations do not provide evidence for H_2O_m to OH^- repartitioning at 225°C even in the longest duration runs, but because the H_2O_t concentrations are low, minor repartitioning is not likely to be measurably different. By contrast, the proportion of H_2O_t that is OH^- in the LSR glass hydrated for 48 hours at 375°C is ~1.0 wt% and very close to the equilibrium speciation predicted by Ihinger et al. (1999), whose models extend down to 400°C. This near match may suggest that the repartitioning of the diffusive species (H_2O_m) into OH^- is near equilibrium (Figure 4a).

Other recent experimental data plotted on Figure 4a show relationships between OH^- and H_2O_t that are more linear between 150-300 °C. The solid black symbols are FTIR data from wet fault gouge experiments run at 300°C and regardless of the extent of hydration, the OH^-/H_2O_m ratios remain consistent (Table A.4; Proctor et al., 2017). These data, along with those from hydration experiments by Cullen et al. (2019), have a positive linear correlation with temperature (Figure 4b). The 200°C data are consistent with expected OH^- and H_2O_t concentrations extrapolated from high temperature relationships (Ihinger et al., 1999). However, their 250°C experiment yields higher OH^- concentrations than predicted, causing a temperature estimate ~70°C in excess of the 250°C curve. The linear relationship of temperature and OH^-/H_2O_m ratios in these two studies suggest that the H_2O speciation below the glass transition, T_g, may be controlled by a fundamentally different mechanism than above T_g in a melt-like regime. The data from our 375°C experiment is not inconsistent with this as it approaches the T_g (Giordano et al., 2005) and may surpass it given that T_g decreases at slower cooling rates (Wilding et al., 1995; Dingwell et al., 1996; Wilding et al., 1996; Dingwell, 1998; Giordano et al., 2008) and these experiments are isothermal and relatively long duration.

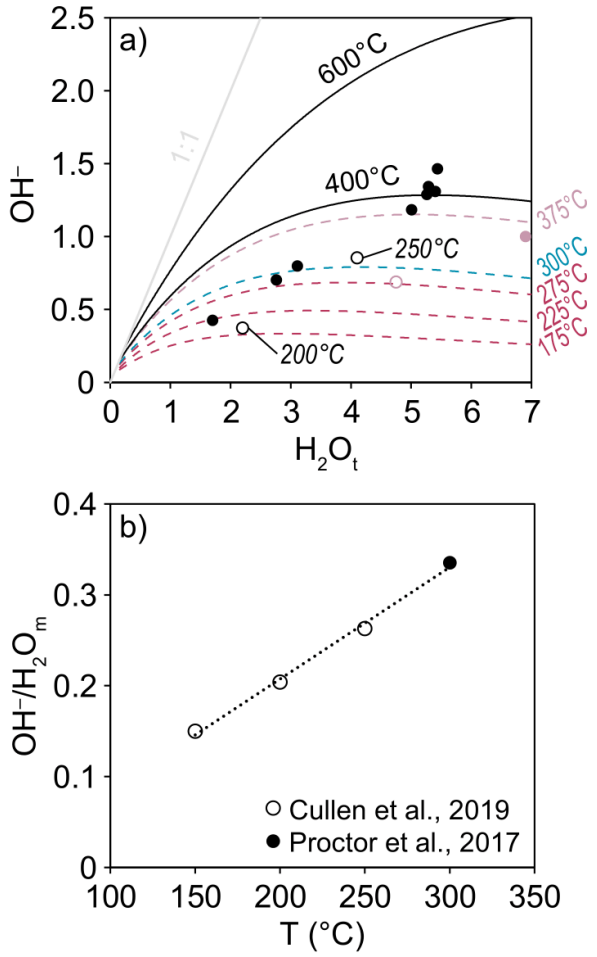

Figure 4. H_2O speciation results from experimental rhyolitic glass. (a) OH^-/H_2O_m ratios appear to have a linear relationship with T at all concentrations (Cullen et al., 2019; Proctor et al., 2017). This ratio does not change with bulk H_2O contents between 1.5-5.0 wt.% in the fault gouge experiments of Proctor et al. (2017) at 300°C (b). Solid curves show equilibrium OH^- concentrations as a function of T and H_2O_t from Ihinger et al. (1999). Dashed curves are extrapolations of the Ihinger relationship to sub-magmatic T. Solid pink circle is from the 48 hour-long 375°C experiment. Open pink circle maintains OH^-/H_2O_m ratio from FTIR, but adjusts H_2O_t to the concentration measured by TC/EA.

4.2 Hydrous mineral framework for equilibrium D/H fractionation

Hydrogen isotope $10^3\ln\alpha_{g\text{-}v}$ values were hypothesized to increase linearly with temperature as a function of $1/T^2$ (Hudak and Bindeman, 2018) from −33‰ at room temperature (Friedman et al., 1993a; Seligman et al., 2016) to ~0‰ at magmatic temperatures for molecular H_2O (Dobson et al., 1989). Results from these experiments paint a more complicated picture of the $1/T^2$—$10^3\ln\alpha_{g\text{-}v}$ relationship. The maximum magnitude $10^3\ln\alpha_{g\text{-}v}$ are taken from the longest duration experiments (plotted as purple

diamonds) and vary between particle sizes and glass compositions (Figure 5; Table 1). Below 250°C, the smallest and most extensively hydrated glass particles at 175°C suggest a $10^3\ln\alpha_{g\text{-}v}$ of approximately −22‰, which is higher than the $10^3\ln\alpha_{g\text{-}v}$ of −33‰ at room temperature while multiple types and particle sizes of glass converge on a $10^3\ln\alpha_{g\text{-}v}$ of approximately −41‰ at 225°C, which is lower than the room temperature value. Glass-vapor D/H fractionations become extreme above 250°C with $10^3\ln\alpha_{g\text{-}v}$ of less than −80‰. These results may be contextualized and partially understood by considering the hydrogen isotope fractionations of other hydrous phases that can form during the decomposition of volcanic glass.

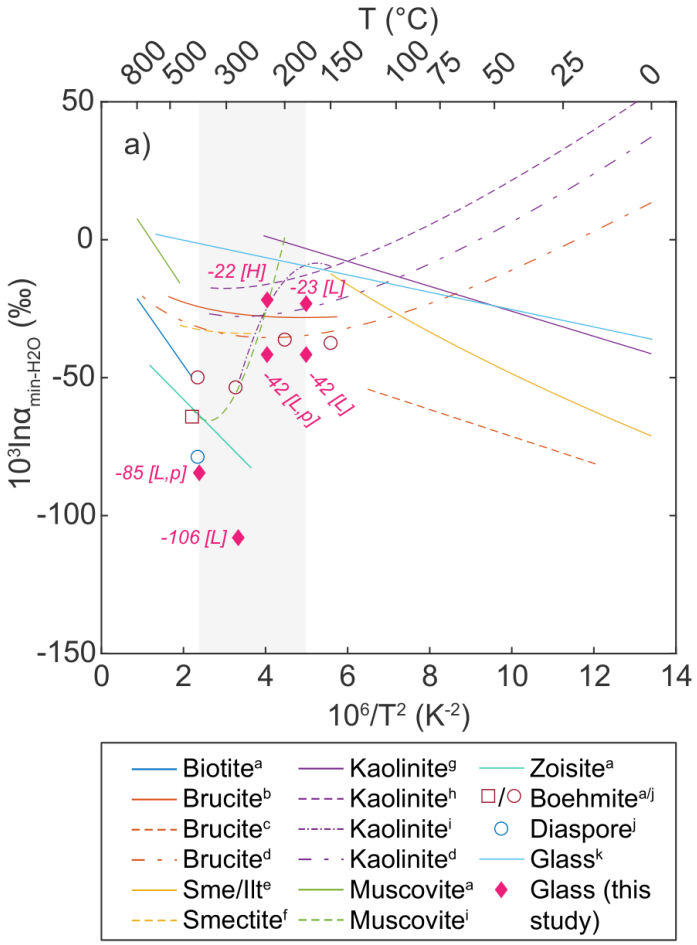

Figure 5. Hydrogen isotope fractionation factors for hydrous minerals and H_2O ($10^3\ln\alpha_{min\text{-}H2O}$) as a function of $1/T^2$. Pink diamonds are the $10^3\ln\alpha_{min\text{-}H2O}$ values from the δD results of the longest duration hydration experiments. L = LSR, H = HSR, p = perlite. [a]Suzuoki and Epstein (1976); [b]Satake and Matsuo (1984); [c]Xu and Zheng (1999); [d]Meheut et al., (2010); [e]Capuano (1992); [f]Yeh (1980); [g]Lambert and Epstein (1980); [h]Sheppard and Gilg (1996); [i]Vennemann and O'Neil (1996); [j]Graham et al. (1980); [k]Hudak and Bindeman (2018).

Hydrogen isotope fractionations between hydrous minerals and H_2O ($10^3 ln\alpha_{min\text{-}H2O}$) are compiled in Figure 5 to create a framework for interpreting the glass δD compositions and to account for possible contributions from secondary phases observed as surface coatings on the higher temperature experimental glasses (Figure A.5-A.8). The grey shaded region represents our 175°C to 375°C experimental temperature range. Above these temperatures, the equilibrium $10^3 ln\alpha_{min\text{-}H2O}$ (in ‰) uniformly decreases with decreasing temperature in muscovite and biotite (Suzuoki and Epstein, 1976), brucite (Satake and Matsuo, 1984; Méheut et al., 2010), and smectite (Yeh, 1980). Below this temperature window, both increases in $10^3 ln\alpha_{min\text{-}H2O}$ (Sheppard and Gilg, 1996; Méheut et al., 2010) and decreases in $10^3 ln\alpha_{min\text{-}H2O}$ (Lambert and Epstein, 1980; Capuano, 1992; Xu and Zheng, 1999) have been reported with decreasing temperature. Within our experimental temperature window, the $1/T–10^3 ln\alpha_{min\text{-}H2O}$ relationships for hydrous minerals are diverse. For example, D/H fractionation between kaolinite and H_2O may increase dramatically (Vennemann and O'Neil, 1996), subtly increase (Sheppard and Gilg, 1996; Méheut et al., 2010), or decrease with decreasing temperature (Lambert and Epstein, 1980). Kaolinite is perhaps the best analog mineral for silicic volcanic glasses, but these results do not provide a consistent expectation for the behavior of hydrogen isotopes in volcanic glass at hydrothermal temperatures.

Hydrogen isotope systematics in hydrous minerals are complex and involve multiple mechanisms. In high temperature minerals that lack hydrogen bonds, such as micas and amphiboles, the composition of the octahedrally-coordinated cations seems to be the primary control on D/H fractionation (e.g. Suzuoki and Epstein, 1976). The strength of hydrogen bonding, and therefore bond length and OH^- stretching frequencies, largely controls the magnitude of the D/H fractionation in minerals that have hydrogen bonds (e.g. Dobson et al., 1989; Graham et al., 1980; Méheut et al., 2010) and this bonding is likely more analogous to the accommodation of hydrogen in the glass structure than the bonding of H to octahedrally-coordinated cations at high temperature. Hydrous phases with weaker bonds and lower OH^- stretching frequencies include aluminum oxide hydroxides such as diaspore, boehmite, and zoisite (Suzuoki and Epstein, 1976; Graham et al., 1980). Pectolite (not shown), which is a metasomatic sodium calcium hydroxide silicate mineral has been reported to have D/H fractionations

of up to 400‰ lighter than coexisting H_2O, has a very low OH stretching frequency of 1600 cm^{-1} (Kuroda, 1979; Wenner, 1979).

Secondary mineral growth and glass decomposition alone cannot explain the experimental results as no mineral-H_2O systems induce the large magnitude D/H fractionations reported above 250°C. This is especially true given that secondary phases occur only as a surface coating on the glass and not in the interior of the hydrous glass particles. Despite this, secondary phases may have a significant role to play in the glass-vapor system. As a surface coating they comprise a boundary layer that may regulate both how water diffuses into the glass and the D/H composition of the water diffusing in (see Section 6.3 for modeling implications). Even if secondary phases do not play a role, the relationship between stretching frequency and $10^3 ln\alpha_{min\text{-}H2O}$ in hydrous minerals informs how hydrogen may be accommodated into the glass structure. This suggests that the formation OH^- groups in glass should drive D/H fractionation based on the large $10^3 ln\alpha_{OH\text{-}vapor}$ values at magmatic temperatures (Dobson et al., 1989) and that a kinetic model is necessary for understanding this reaction within glass during glass hydration via H_2O_m diffusion.

4.3 Tasks for numerical modeling

Plateaus in the δD time series should reflect the equilibrium glass δD and the $10^3 ln\alpha_{g\text{-}v}$. At lower temperatures, the particle sizes are large relative to the D_{H2O} resulting in incomplete hydration at the maximum experimental duration. Isotope diffusion modeling of the experimental data can yield more quantitative constraints on $10^3 ln\alpha_{g\text{-}v}$ at each temperature than the incomplete plateaus in the data. Through modeling that incorporates reaction kinetics internal to the glass, we seek to explain: 1) the rate of change of δD as a function of H_2O solubility and diffusivity; 2) the relative effects of kinetic and equilibrium D/H fractionation; 3) rates of repartitioning of H_2O_m to OH^-; 4) the anomalous δD time series of the >250°C experiments.

5. Kinetic model for H isotope uptake into silicic volcanic glass

These isothermal glass hydration experiments provide a unique δD time series that we use to develop a kinetic model for the hydration process. We specifically explore the effects of isotope diffusion and isotope reaction kinetics between H_2O_m and OH^- and

assess what parameters and boundary conditions are required to reproduce the observed trends in both low- and high-temperature experiments. (Table 2 defines the parameters.)

Symbol	Meaning	Default value	Reference/Note/Range
Part I: Reaction and diffusion parameters			
K_{eq}	Equilibrium constant	exp(1.89-3120/T_K)	Ihinger et al. (1999)
k_{+1}	Forward rate constant (s^{-1})	10^{-5} to 10^{-10}	Assumed constant
k_{-1}	Backward rate constant (s^{-1})	$k_{-1}=k_{+1}/K_{eq}$	Assumed constant
$D_{H_2O_m}$	Diffusivity of molecular water	See Eq. 13	Hudak and Bindeman (2020)
D_{OH}	Diffusivity of hydroxyl	$\ll D_{H_2O_m}$	Zhang et al. (1991)
Part II: Isotopic parameters			
$\alpha^{eq}_{glass-vapor}$	Equilibrium fractionation factor between water vapor and dissolved water	~1.000	0.960 to 1.000
$\alpha^{eq}_{OH\text{-}H_2O_m}$	Equilibrium fractionation factor between hydroxyl and dissolved water	~0.955	0.900 to 1.000
α_f	Kinetic fractionation factor for forward rxn	Free parameter	0.900 to 1.000
α_b	Kinetic fractionation factor for backward rxn	$\alpha_f \cdot \alpha^{eq}_{OH\text{-}H_2O_m}$	-
a_{+1}	Forward rate constant for isotope rxn (s^{-1})	$\alpha_f \cdot k_{+1}$	-
a_{-1}	Backward rate constant for isotope rxn (s^{-1})	$a_{+1}/(K_{eq}\alpha^{eq}_{OH\text{-}H_2O_m})$	-
$D_{D_2O_m}$	Diffusivity of heavy molecular water	$\leq D_{H_2O_m}$	0.5 to 1 (Lapham et al., 1984)
D_{OD}	Diffusivity of heavy hydroxyl	$\leq D_{OH}$	0.5 to 1 (Lapham et al., 1984)

Table 2. Reaction, diffusion, and isotope parameters for the 1D diffusion-reaction model.

5.1 Repartitioning of H_2O_m to OH

Hydrogen in silicate melts and glasses is partitioned between at least two species, H_2O_m and OH^-, according to the following reaction:

$$H_2O_m \text{ (glass)} + O \text{ (glass)} \underset{k_{-1}}{\overset{k_{+1}}{\rightleftharpoons}} 2OH^- \text{ (glass)}, \qquad (5)$$

where the *k*'s are reaction rate constants. The hydroxyl may be bonded to Si, Al, Na, or other cations but is nevertheless typically treated as a single species. The relative abundance of H_2O_m and OH^- at equilibrium is given by the equilibrium constant:

$$K_{eq} = \frac{k_{+1}}{k_{-1}} = \frac{[OH^-]^2}{[H_2O_m][O]}, \qquad (6)$$

where brackets are activities approximated by mole fractions on a single oxygen basis (Zhang, 2008). The equilibrium constant depends on temperature as K_{eq} = exp(1.89-3120/T_K), which comes from experiments that were conducted at 400-600°C (Ihinger et al., 1999). The conversions between mole fractions and weight fractions are given by Zhang (2008):

$$[H_2O_t] = \frac{\frac{C}{18.015}}{\left[\frac{C}{18.015}+\frac{(1-C)}{W}\right]} \qquad (7)$$

$$[H_2O_m] = [H_2O_t](H_2O_m)/C \qquad (8)$$

$$[OH] = 2([H_2O_t] - [H_2O_m]) \qquad (9)$$

$$[O] = 1 - [H_2O_m] - [OH^-] \qquad (10)$$

where parentheses indicate mass fraction, C is the mass fraction of H_2O_t (i.e., wt%/100) and W = 32.49 g per mole of oxygen is the molar mass of dry rhyolite.

5.2 Governing equations

In our experiments, hydrogen enters the glass particles in the form of H_2O_m and either stays in that form or it reacts with anhydrous oxygen to form OH^- as it diffuses inwards. For simplicity we approximate the glass particles as spherically symmetric so that we can treat the problem as one-dimensional. Diffusion of a multispecies component in spherical coordinates is then described by a set of coupled diffusion-reaction equations:

$$\frac{\partial[H_2O_m]}{\partial t} = \frac{1}{r^2}\left(\frac{\partial}{\partial r}\left(D_{H_2O_m}\frac{\partial[H_2O_m]}{\partial r}\right)\right) + \frac{k_{+1}}{K_{eq}}[OH^-]^2 - k_{+1}[H_2O_m][O], \qquad (11)$$

and

$$\frac{\partial[OH^-]}{\partial t} = \frac{1}{r^2}\left(\frac{\partial}{\partial r}\left(D_{OH^-}\frac{\partial[OH^-]}{\partial r}\right)\right) - \frac{k_{+1}}{K_{eq}}[OH^-]^2 + k_{+1}[H_2O_m][O], \qquad (12)$$

where r is the radial distance from the center of the spherical particle, and $D_{H_2O_m}$ and D_{OH^-} are the diffusivities of H_2O_m and OH^-, respectively. (The use of mole fraction for concentration is equivalent to units of moles/m^3 if the molar mass and density of the glass are constant.) The diffusion part of these expressions has been well studied (Zhang et al., 1991; Zhang et al., 1997; Zhang and Behrens, 2000; Behrens et al., 2007; Giachetti et al., 2015; Coumans et al., 2020; Hudak and Bindeman, 2020) and the diffusivity of H_2O_m in rhyolite can be described by:

$$D_{H_2O_m} = A \times \exp\left[\left(14.08 - \frac{13{,}128}{T_K} - 2.796\frac{P}{T_K}\right) + [H_2O_t]\left(-27.21 + \frac{36892}{T_K} + 57.23\frac{P}{T_K}\right)\right], \quad (13)$$

where P is pressure in MPa and A is a prefactor constrained by Hudak and Bindeman (2020) across the 175-375°C range. Diffusion of OH^- is probably negligible (Zhang et al., 1991), but we retain the diffusion term for completeness and consider values for D_{OH^-} ranging from zero to as high as $D_{H_2O_m}$.

In contrast to the diffusion part of these equations, little is known surrounding the kinetics of the speciation reaction, especially at the low temperatures relevant to our experiments. For simplicity, we adopt a rate law for an elementary reaction and treat k_{+1} as a constant that is independent of $[H_2O_t]$. If k_{+1} is large, the reaction is fast and any excess H_2O_m gets immediately converted to OH^- (according to the equilibrium constant K) as it diffuses into the glass. If k_{+1} is small, the reaction is slow and essentially none of the H_2O_m gets re-speciated to OH^-. We treat k_{+1} as an unknown and explore the full range of behaviors.

5.3 Isotopologue ratios versus isotope ratios

In the model we treat all oxygen as being in the form of ^{16}O and only consider the five isotopologues involving H-D substitution: H_2O, HDO, D_2O, OH^-, and OD^-. We can calculate the relative abundances of water isotopologues by assuming H and D are randomly distributed among them:

$$[H_2O] = P(1,1) = (0.999885)^2 \approx 0.999770 \quad (14)$$

$$[HDO] = P(1,2) = 2(0.999885)(0.000115) \approx 0.000230 \quad (15)$$

$$[D_2O] = P(2,2) = (0.000115)^2 \approx 1.3225 \times 10^{-8} \quad (16)$$

where the P's refer to probabilities and the numerical values are based on an arbitrary natural distribution of H and D. The probability of HDO is multiplied by 2 because D may occupy either site to make HDO or DHO. Without rounding, these probabilities sum exactly to 1. The D/H ratio of water is related to the isotopologue abundances through

$$R_{H_2O} = \left(\frac{D}{H}\right)_{H_2O} = \frac{2[D_2O]+[HDO]}{[HDO]+2[H_2O]}. \quad (17)$$

Importantly, R_{H_2O} can equivalently be expressed in either of the following ways without losing any information:

$$R_{H_2O} = \left(\frac{[D_2O]}{[H_2O]}\right)^{1/2} = \left(\frac{(0.000115)(0.000115)}{(0.999885)(0.999885)}\right)^{1/2} \qquad (18)$$

or

$$R_{H_2O} = \frac{\frac{1}{2}[HDO]}{[H_2O]} = \frac{\frac{1}{2}(2)(0.999885)(0.000115)}{(0.999885)(0.999885)}. \qquad (19)$$

Given these relationships, if we know the HDO or the D_2O concentration, we can calculate δD. We therefore do not need to keep track of both HDO and D_2O in the model, but rather, can simplify things by choosing one or the other.

5.4 Isotope partitioning between dissolved species

With H_2O_m, HDO_m, OH^-, and OD^- as components, we have the following speciation reactions:

$$H_2O_m\ (glass) + O\ (glass) \underset{k_{-1}}{\overset{k_{+1}}{\rightleftarrows}} 2OH^-\ (glass), \qquad (5)$$

$$HDO_m\ (glass) + O\ (glass) \underset{a_{-1}}{\overset{0.5a_{+1}}{\rightleftarrows}} OD^-\ (glass) + OH^-\ (glass), \qquad (20)$$

$$HDO_m\ (glass) + O\ (glass) \underset{a_{-1}}{\overset{0.5a_{+1}}{\rightleftarrows}} OH^-\ (glass) + OD^-\ (glass), \qquad (21)$$

and

$$D_2O_m\ (glass) + O\ (glass) \underset{b_{-1}}{\overset{b_{+1}}{\rightleftarrows}} 2OD^-\ (glass). \qquad (22)$$

Although the second and third reactions (Eq. 20 and 21) appear to be identical, the two H-bearing products of the reaction need to be treated as separate species for isotope mass balance purposes. This is a nuanced point, but when written as above, the reactions become analogous to the oxygen isotope mass balance expressions in the CO_2 hydration and hydroxylation reactions, in which there are two O-bearing reactants and one O-bearing product (Christensen et al., 2021). The factor of ½ on a_{+1} can be interpreted as follows: the change in concentration of each of the two OD^- species is proportional to ½ the concentration of HDO_m. The factor of ½ is thus necessary to satisfy the equilibrium

condition, and it arises from the relationship between isotope ratios and isotopologue ratios, as can be seen through the following equalities (see also Table 3):

$$\alpha^{eq}_{OH\text{-}H_2O_m} = \frac{\left(\frac{D}{H}\right)_{OH^-}}{\left(\frac{D}{H}\right)_{H_2O_m}} = \frac{\left(\frac{[OD^-]}{[OH^-]}\right)}{\left(\frac{0.5\,[HDO_m]}{[H_2O_m]}\right)} = \frac{\left(\frac{[OD^-][OH^-]}{0.5[HDO_m][O]}\right)}{\left(\frac{[OH^-]^2}{[H_2O_m][O]}\right)} = \frac{A_{eq}}{K_{eq}} = \frac{\left(\frac{a_{+1}}{a_{-1}}\right)}{\left(\frac{k_{+1}}{k_{-1}}\right)} = \frac{\left(\frac{a_{+1}}{k_{+1}}\right)}{\left(\frac{a_{-1}}{k_{-1}}\right)} = \frac{\alpha_f}{\alpha_b}, \qquad (23)$$

Where $\alpha_f = a_{+1}/k_{+1}$ and $\alpha_b = a_{-1}/k_{-1}$ are the kinetic fractionation factors for the forward and backward reactions, respectively. The value of the equilibrium fractionation factor is about 0.955±0.005 between 530 and 750°C (i.e., OH^- is lighter than H_2O_m by some 45±5‰; Dobson et al., 1989; Walter and Castro, 2020), and we expect OH^- to be even lighter than H_2O_m at lower temperatures. The kinetic fractionation factors are unknown at any temperature, but in general, α_f is expected to be less than unity and α_b can be determined from α_f and $\alpha^{eq}_{OH\text{-}H_2O_m}$.

5.5 Governing equations with isotopes

The four reactive-transport equations that we solve numerically are:

$$\frac{\partial[H_2O_m]}{\partial t} = \frac{1}{r^2}\left(\frac{\partial}{\partial r}\left(D_{H_2O_m}\frac{\partial[H_2O_m]}{\partial r}\right)\right) + k_{-1}[OH^-]^2 - k_{+1}[H_2O_m][O], \qquad (24)$$

$$\frac{\partial[0.5HDO_m]}{\partial t} = \frac{1}{r^2}\left(\frac{\partial}{\partial r}\left(D_{HDO_m}\frac{\partial[HDO_m]}{\partial r}\right)\right) + a_{-1}[OD^-][OH^-] - 0.5a_{+1}[HDO_m][O], \qquad (25)$$

$$\frac{\partial[OH^-]}{\partial t} = \frac{1}{r^2}\left(\frac{\partial}{\partial r}\left(D_{OH^-}\frac{\partial[OH^-]}{\partial r}\right)\right) - k_{-1}[OH^-]^2 + k_{+1}[H_2O_m][O], \qquad (26)$$

$$\frac{\partial[OD^-]}{\partial t} = \frac{1}{r^2}\left(\frac{\partial}{\partial r}\left(D_{OD^-}\frac{\partial[OD^-]}{\partial r}\right)\right) - a_{-1}[OD^-][OH^-] + 0.5a_{+1}[HDO_m][O], \qquad (27)$$

Given the H_2O_t (in wt%) along with the D/H ratio of the glass (R_{tot}), it is straightforward to calculate the mole fractions of the D-bearing isotopologues. The three equations to solve for the three unknowns (D_2O_m, HDO_m, and OD^-) are:

$$R_{tot} = \frac{2D_2O_m + HDO_m + OD^-}{2H_2O_m + HDO_m + OH^-}, \qquad (28)$$

$$\alpha^{eq}_{OH\text{-}H_2O_m} = \frac{\left(\frac{D}{H}\right)_{OH^-}}{\left(\frac{D}{H}\right)_{H_2O_m}} = \frac{\left(\frac{[OD^-]}{[OH^-]}\right)}{\left(\frac{0.5\,[HDO_m]}{[H_2O_m]}\right)}, \qquad (29)$$

and

$$a_{-1}[OD^-][OH^-] = 0.5a_{+1}[HDO_m][O]. \qquad (30)$$

Combining these three equations leads to a quadratic expression for HDO_m:

T (°C)	*P (MPa)*	δD_{vapor}	$\alpha_{OH\text{-}H2Om}$	*A*	*Initial* H_2O_t *(wt%)*	*Initial* δD_{glass}	*Eq. Boundary* H_2O_t *(wt%)*	*Initial Boundary* δD_{glass}	*Initial Boundary* $\Delta D_{glass\text{-}vapor}$	a_{+1}/k_{+1}	*Eq.* $\Delta D_{H2Om\text{-}vapor}$	$\alpha_{H2Om\text{-}vapor}$
175	0.89	69.5	0.96	4	0.08	-100.8	3.5	36.5	-33	0.95	-27.1	0.975
225	2.54	75.3	0.96	1.5	0.08	-100.8	3.9	50.3	-25	0.95	-17.1	0.984
275	5.94	77.9	0.96	2.5	0.08	-100.8	4.2	-22.1	-100	0.95	-90.9	0.916
375	21	75.6	0.96	4	0.08	-100.8	5.5	-24.4	-100	0.95	-88.3	0.918
275*	5.94	77.9	0.96	2.5	0.08	-100.8	4.2	21.7	[a]	0.95	–	–
375*	21	75.6	0.96	4	0.08	-100.8	5.5	-101.9	[b]	0.95	–	–

Table 3. Initial and boundary conditions for the model fits in Figure 7 and in Figure 8. A is a prefactor assigned to H_2O_m diffusivity and the equilibrium H_2O_t at the boundary are taken from H_2O_t diffusivity and solubility constraints in Hudak and Bindeman (2020). The δD of glass is prescribed at the boundary to calculate the equilibrium $\alpha_{H2Om\text{-}vapor}$, which is then held constant for Figure 7, but allows the bulk δD at the boundary to evolve. For *Figure 8, a time-δD relationship is prescribed at the boundary equal to the best fit polynomial to the raw data. The relationships for 275°Ca and 375°Cb are as follows: a) $\delta D_{BC} = (2.679E^{-4})t2 - 0.2474t + 21.7$; and b) $\delta D_{BC} = (1.727E^{-3})t^3 - 0.1232t^2 + 3.804t - 101.9$, where time (t) is in hours and δD is in ‰.

$$\left(\frac{1}{\alpha^{eq}_{OH\text{-}H_2O_m}}\frac{0.5a_{+1}}{a_{-1}}\frac{[O]}{[OH^-]^2}\right)[HDO_m]^2 + \left(1 + \frac{0.5a_{+1}}{a_{-1}}\frac{[O]}{[OH^-]} - R_{tot}\right)[HDO_m] -$$

$$R_{tot}(2[H_2O_m] + [OH^-]). \quad (31)$$

The four reactive transport equations are solved numerically by finite differences using model parameters listed in Table 3. The concentrations and δD values of each species are stored at each time step. Average H_2O concentrations and isotopic compositions are calculated by integration over the grain radius.

5.6 Model behavior + validation

For model validation runs, the glass starts with a uniform water concentration (0.1 wt%) and isotopic composition (δD = 0‰) equal to that of the vapor composition (δD = 0‰). The default boundary condition is one of local equilibrium at the δD interface between the glass and vapor, which means that the concentrations of H_2O_m and HDO_m at the boundary are constant. For these runs, T = 275°C, P = 5.94 MPa, and there is no D/H fractionation between H_2O_m and vapor ($\alpha_{H2Om\text{-}vapor}$ = 1.000). The five model outputs shown in Figure 6 have the same initial and boundary conditions but different mass-dependent diffusion and reaction parameters.

In the first two models there is effectively no reaction of H_2O_m to OH^- ($k_{+1} = 10^{-10}$), so at the boundary, H_2O_t is equal to 4.0 wt% and only 0.07 wt% remains as OH^-. In first case, we set the diffusivities of H_2O and HDO as being equal. The resulting diffusion profile shows the typical concentration dependence of H_2O diffusion in silicate melts and glasses and there is no change to δD spatially (Figure 6a) or through time (Figure 6b). The time evolution of this model shows the H_2O_t of the bulk glass increasing asymptotically towards the H_2O solubility of the glass. In the second case, the H_2O diffusivity (D_{H2O}) differs from the HDO diffusivity (D_{HDO}). We set $D_{DHO} = 0.973D_{H2O}$ as the maximum difference, which is based on Graham's law for molecular gases:

$$\frac{D_{HD^{16}O}}{D_{H_2{}^{16}O}} = \sqrt{\frac{m_{H_2{}^{16}O}}{m_{HD^{16}O}}} = \sqrt{\frac{18.011\ amu}{19.017\ amu}} = 0.973 \qquad (X).$$

The behavior of H_2O_t is negligibly different from the previous model where D_{H2O} is equal to D_{HDO}, but a strong depletion in δD occurs at the diffusion front in the hydration profile (Figure 6c). At the initiation of hydration, the bulk δD of the glass drops as H_2O diffuses in more quickly than HDO. As this low δD diffusion front advances into

the glass through time, the mass of HDO dissolved in the glass catches up to the mass of H_2O and this drives a gradual recovery of the bulk glass towards the initial δD of 0‰ (Figure 6d). A maximum depletion of −8.0‰ in δD arises in this scenario. More realistic D_{DHO} values induce smaller isotopic variations, consistent with studies of D/H diffusion in silicic glasses and melts that observe no diffusively driven kinetic hydrogen isotope fractionation (Shelby, 1977; Anovitz et al., 2008; Roskosz et al., 2018).

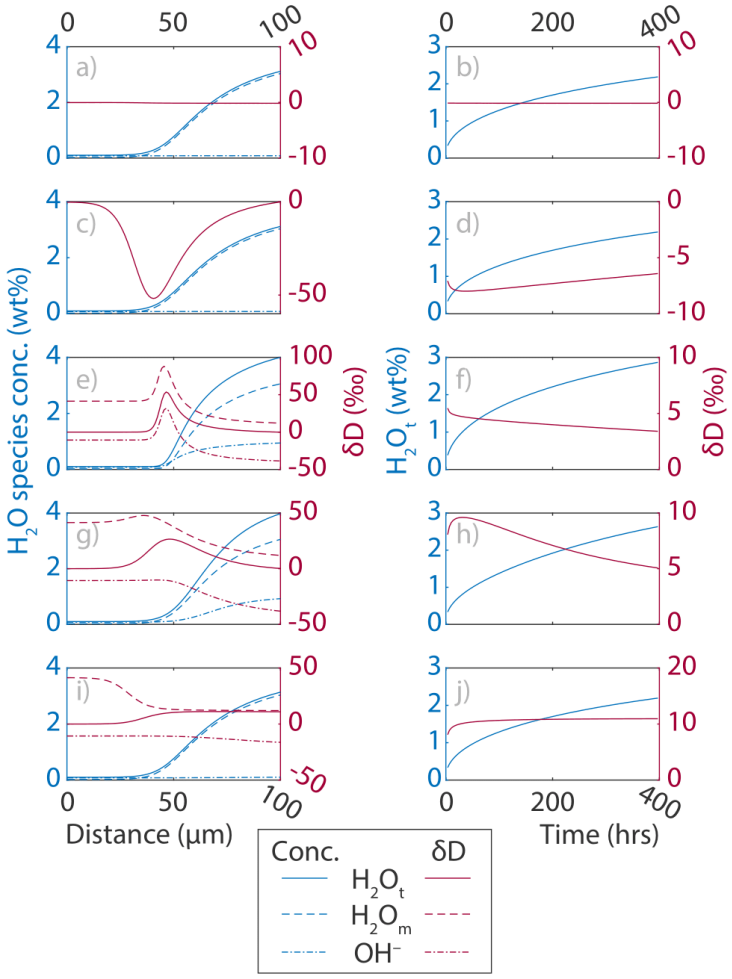

Figure 6. These models validate the isotope diffusion-reaction model and highlight the effects of different parameters on model behavior. Left panels show concentration profiles of H_2O_t, H_2O_m, and OH^-, and their isotopes as a function of distance from the glass edge. Right panels show bulk H_2O_t and δD evolution through time. Simple diffusion with no isotope fractionation or reaction (a,b) are compared to the effects of differential diffusivity of $H2O_m$ and HDO (c,d), as well as fast (e,f), intermediate (g,h), and sluggish (i,j) forward reaction rates (k_{+1}) for $H_2O_m + O \rightarrow 2OH^-$.

The final three models evaluate the effects of respeciation on glass δD compositions through space and time. All three models apply a $\alpha_{OH\text{-}H2Om}$ = 0.950 and a $\alpha_{H2Om\text{-}vapor}$ = 1.000, but each explores different reaction kinetics. The forward reaction rates are effectively instantaneous in the first model ($k_{+1} = 10^{-4}$), intermediate in the second model ($k_{+1} = 10^{-6}$), and sluggish in the last model ($k_{+1} = 10^{-8}$). With near instantaneous reactions rates, a high δD pulse is concentrated at the diffusion front (Figure 6e). The offset between the δD of H_2O_m and the δD of OH^- is approximately constant because fast exchange kinetics maintains the equilibrium OH^--H_2O_m fractionation during diffusion. The δD of H_2O_t is closer to which ever species is in greater abundance and is thus closer to the δD of H_2O_m in the hydrated portions of the glass. Fast kinetics result in an early spike in the bulk δD of the glass that decays relatively quickly (Figure 6f). Intermediate reaction rates cause a lower amplitude, longer wavelength δD peak behind the diffusion front as H_2O_m is more slowly converted to OH^- (Figure 6g). This results in a delay of the peak bulk glass δD composition in time and a higher maximum glass δD value (9.6‰ at ~32 hours; Figure 6h). In the final case where reaction rates are very slow, but a large $\alpha_{OH\text{-}H2Om}$ exists, the glass is dominated by H_2O_m, so the δD of H_2O_t approaches the δD of H_2O_m (Figure 6i). This results in an enrichment in the bulk glass δD that is still increasing by the end of the model (Figure 6j).

Major observations from this model validation are twofold. First, faster diffusion of the lighter isotopologue of water (H_2O_m) relative to the heavier isotopologue (HDO_m) imparts a δD depletion on the bulk glass, which is in contrast to the enrichment in bulk glass δD that occurs from H_2O_m to OH^- reactions. The magnitudes of the isotopic shifts are similar though, between 5‰ and 10‰ in either direction, so neither diffusion nor reaction alone is sufficient to generate the δD values observed in the experimental glasses. The other important observation is that non-instantaneous reactions cause "overshoots" of the equilibrium δD value for the bulk glass for a given δD composition of a coexisting vapor. The magnitude and duration of the overshoot is dependent upon the reaction rate. Faster reaction rates (larger k_{+1} values) cause smaller magnitude, shorter duration overshoots of bulk glass δD.

6. Model fits to data

6.1 Local equilibrium boundary conditions

The initial experimental glass is 0.08 wt% H_2O_t and −100.8‰ δD. Using the equations in Section 5, H and D are partitioned into the four H_2O species – OH^-, OD^-, H_2O_m and HDO_m – in their equilibrium proportions. Similarly, a bulk δD and H_2O_t solubility are assigned at the boundary. The equilibrium concentrations of H_2O_m and HDO_m are implemented at the boundary and are held constant thereafter to assume H_2O_m—vapor equilibrium. At the boundary node, intermediate and slow reaction kinetics allow for OH and OD to continue to increase at the boundary through time until they have reached their equilibrium concentrations. The initial and boundary conditions are given in Table 3 and apply to each k_{+1} value shown in Figure 7.

6.2 Model (mis)fits to the data

Model fits to the bulk glass δD data at temperatures lower that 250°C are unable to discriminate between near instantaneous, intermediate, and sluggish reaction rates as they all produce similar fractionations (Figure 7a,b). Modeled bulk H_2O_t concentrations through time are somewhat sensitive to the forward k_{+1} reaction rate (Figure A.9), but this can be compensated for by small increases in H_2O solubility or diffusivity and does not strongly affect bulk glass δD evolution. One possible reason the model is relatively insensitive to internal kinetic effects is that relatively low equilibrium OH^-/H_2O_m ratios may not leverage a large enough influence on the δD of H_2O_m at these temperatures (Figure 4a; Ihinger et al., 1999; Zhang, 2008).

The model produces good fits to the δD time series using $10^3\alpha_{g\text{-}v}$ of −33‰ and −25‰ at 175°C and 225°C, respectively. In both cases an $\alpha_{OH\text{-}H2Om}$ of 0.960 is assumed, and the main effect of changing this parameter is that $\alpha_{H2Om\text{-}vapor}$ adjusts accordingly at the boundary. The modeled $10^3\ln\alpha_{g\text{-}v}$ for these two lower temperature experiments are more consistent with the hypothesis that D/H fractionations between glass and H_2O vapor should increase with increased temperature (Hudak and Bindeman, 2018). On the other hand, the model is unable to fit the data at temperatures above 250°C by modulating reaction rate (k_{+1}) or mass-dependent kinetic fractionation (a_{+1}/k_{+1}) alone (Figure 7c,d). For example, the effect of reaction rates is greatest at the highest temperature (375°C) where the glass has been fully hydrated. It results in a 9‰ spread in the bulk glass δD

over the modeled timescales at 375°C, 4.5‰ at 275°C, and less than 2‰ below 250°C. Instead these non-monotonic increases in bulk glass δD data reveal that the bulk δD mimics the δD at the glass-vapor boundary, suggesting that the local equilibrium boundary condition may not be valid in the high temperature experiments.

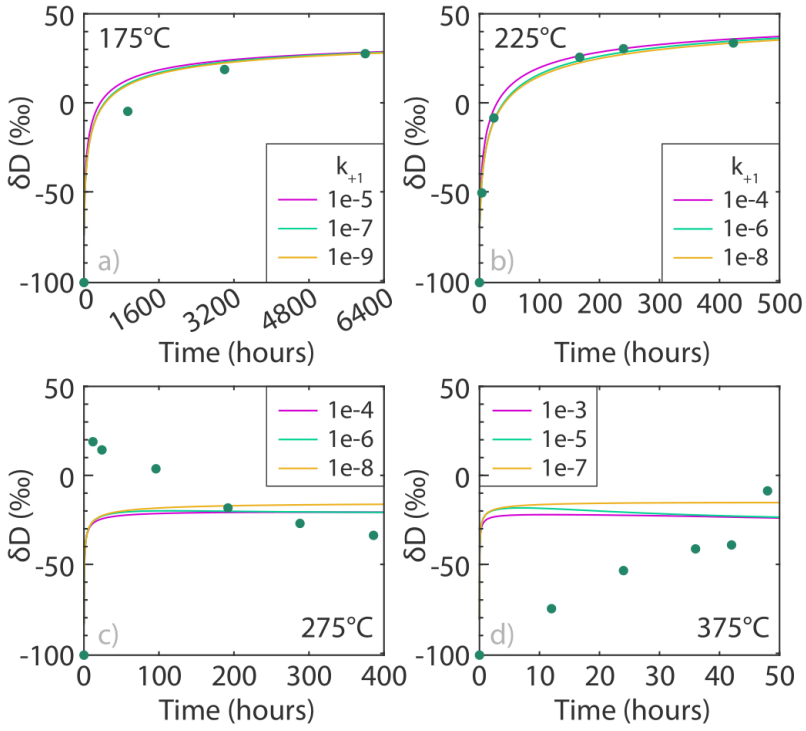

Figure 7. Preferred model results for glass H_2O and δD for each temperature: a) 175°C, b) 225°C, c) 275°C, and d) 375°C. Boundary conditions for the models are given in Table 3.

6.3 Relaxing the local equilibrium boundary condition

The local equilibrium boundary condition implies fast exchange between H_2O_m and water vapor at the boundary. It also implies that the glass-vapor boundary is not physically changing through time, an assumption that is belied by the SEM images showing partial dissolution of the glass and formation of secondary phases in the high temperature experiments. Without clear guidance for how to incorporate complex reactions on the surfaces of the particles, we instead use the bulk δD data to constrain the time evolution of the δD at the boundary. Figure 8 shows polynomial fits (dashed lines) to the bulk δD data that are then applied as time-dependent boundary condition. The

resulting model outputs (solid curves) use the same $\alpha_{OH\text{-}H2Om}$ and a_{+1}/k_{+1} values as the models in Figure 7 at intermediate values of k_{+1}. We note however, that slower or faster kinetics can produce similar fits to the data. Overall, these results show how the bulk δD closely mimics the time-evolving δD at the boundary. Hence, the secondary phases that form at the boundary are important insofar as they act as a filter through which the water vapor gets into the glass. The fact that the high temperature experiments never reached a plateau in δD can be attributed to ongoing reactions at the vapor-glass interface.

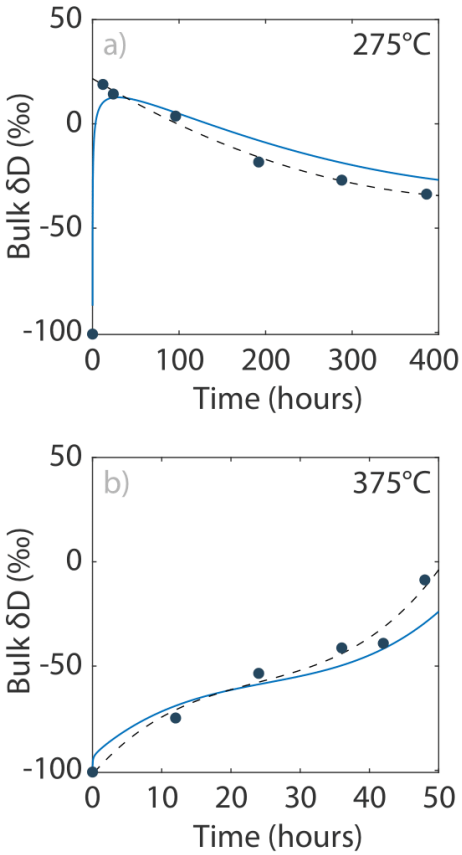

Figure 8. Models to the data (solid curves) – using a bulk glass δD boundary condition that changes through time according to the polynomial fits to the time-δD results (dash lines) – show that the δD composition of the boundary largely dictates the bulk glass δD through time.

The insensitivity of the model to mass-dependent diffusion and reaction parameters in the lower temperature experiments also applies to the higher temperature experiments. One caveat of the local equilibrium condition in the model is that diffusion of H_2O_m and HDO_m into the glass is unidirectional in the model because all 4 water

species – H_2O, HDO, OH, and OD – are treated separately and are always at their maximum concentration at the boundary. However, the perlites in the low temperature experiments show that that water can diffuse back out of the boundary because their bulk δD changed dramatically as their H_2O_t remained relatively constant, so unidirectional H_2O_m diffusion may affect the ability of the model to fit the data. The low temperature δD plateaus through time may be reasonably well fit by the model because hydration remains unidirectional at low degrees of hydration and slow diffusivities. Comparatively, the breakdown and the dissolution of glass at the boundary observed at >250°C is more likely to violate the local equilibrium boundary condition assumption at high temperatures (Figure A.5-A.8).

6.4 Summary of D/H fractionation in the glass-H_2O systems

Extreme fractionations in the high temperature experimental glasses present a significant challenge in fitting a $1/T^2$—$10^3\ln\alpha_{g\text{-}v}$ relationship to the observed and modeled results. Instead, we present a conceptual framework for considering H isotope fractionation in silicic volcanic glass. Figure 9 shows the existing hydrogen isotope literature $10^3\ln\alpha$ data for low temperature glass-H_2O and magmatic temperature OH-vapor and H_2O_m-vapor. Studies of natural glasses corrected for their magmatic H_2O content find a $10^3\ln\alpha_{glass\text{-}H2O}$ of −33‰ reported for Earth surface temperatures (blue box; Friedman et al., 1993a; Seligman et al., 2016) and ~−30‰ around 100°C (purple box; Hudak and Bindeman, 2018). At low temperatures, H_2O in glass is almost entirely H_2O_m, so Hudak and Bindeman (2018) use the H_2O_m-vapor fractionation factors of Dobson et al. (1989; blue circles) to extrapolate $10^3\ln\alpha_{glass\text{-}H2O}$ across an intermediate temperature range, assuming no H_2O_m repartitioned below T_g. Here we interpret this to reflect a $10^3\ln\alpha$ relationship for H_2O_m-vapor rather than for bulk glass-H_2O (Figure 9, blue curve). A linear extrapolation of $10^3\ln\alpha_{OH\text{-}vapor}$ from magmatic temperatures (green circles; Dobson et al., 1989) yields a range of ~−70‰ to −80‰ between 175°C and 225°C. A polynomial fit extends to much lower $10^3\ln\alpha_{OH\text{-}vapor}$ values.

Evidence for repartitioning in these experiments and in other studies indicate that a $10^3\ln\alpha_{g\text{-}v}$ should depend on the OH^-/H_2O_m ratio of the glass. Grey and black dashed curves represent expected $1/T^2$—$10^3\ln\alpha_{g\text{-}v}$ relationships at various OH^-/H_2O_m ratios. The lower temperature $10^3\ln\alpha_{g\text{-}v}$ data (pink diamonds) and model results (black diamonds)

mostly fall below OH^-/H_2O_m ratios of 0.5 or 0.2 depending on which OH-vapor extrapolation is used. This is broadly consistent with the expected OH^-/H_2O_m ratios from Figure 4. By contrast, the high temperature $10^3\ln\alpha_{g\text{-}v}$ are only consistent with the more extreme $10^3\ln\alpha_{OH\text{-}vapor}$ extrapolation of Dobson et al. (1989). This may indicate that the boundary layer on the glass regulating diffusion of H_2O into the glass and exchange between the glass and the H_2O vapor is dominated by OH^-. This is consistent with a major conclusion of the modeling – that the δD of the glass boundary is the primary control on the bulk glass δD. The FTIR results for the fully hydrated glasses at 375°C yield an OH^-/H_2O_m ratio of ~0.2, so an OH^- rich boundary could reconcile this relatively low measured OH^-/H_2O_m ratio with the extreme $10^3\ln\alpha_{g\text{-}v}$ values that are achieved above 250°C.

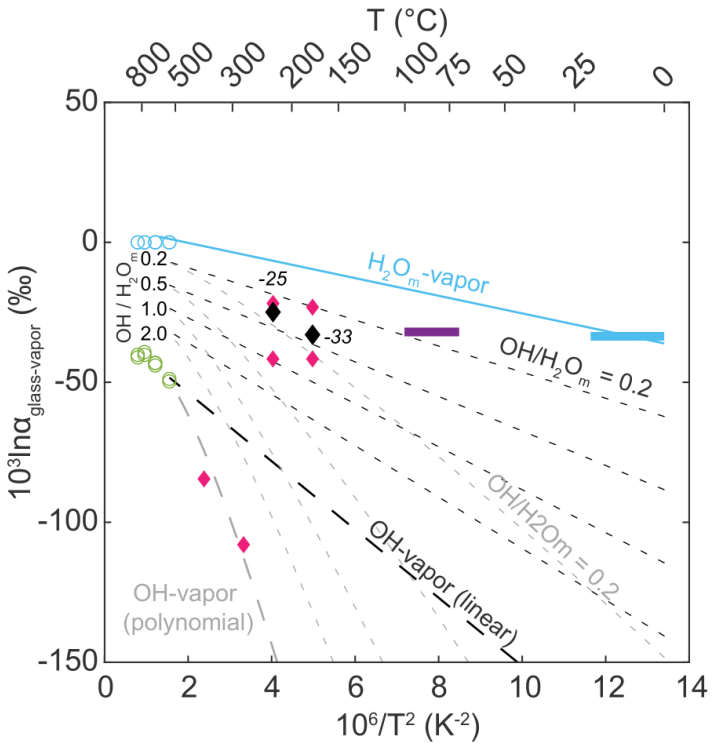

Figure 9. $1/T^2$ - $10^3\ln\alpha$ relationships in the glass/melt-H_2O system. Blue curve is a reinterpretation of the bulk glass-H_2O relationship of Hudak and Bindeman (2018) as a H_2O_m-vapor relationship extrapolated between low T (Friedman et al., 1993b; Seligman et al., 2016) and high T (Dobson et al., 1989). Purple box for glass-H_2O at 100°C recorded in natural samples (Hudak and Bindeman, 2018). Dashed curves represent theoretical bulk glass-H_2O fractionations at various OH^-/H_2O_m ratios in glass or melt. Pink diamonds are raw data from experiments (see Figure 5) and black diamonds are model results. Results from below <250°C are generally consistent with measured and expected OH^-/H_2O_m ratios while >250°C results are consistent only with OH-

dominated systems and an extreme extrapolation of Dobson et al. (1989) OH-vapor fractionations (green circles) to sub-magmatic T.

7. Applications

Untangling the proportion of secondary water added to ash or pumice after an eruption and the proportion of primary undegassed magmatic H_2O remains a challenge (Giachetti et al., 2015; Giachetti and Gonnermann, 2013; Seligman et al., 2016, Giachetti et al., 2020). Analyzing tephras to understand degassing and eruptive processes requires being able to correct for water from rehydration. Conversely, those interested in using secondary water to reconstruct paleo-meteoric water composition – and therefore paleoclimate or paleoaltitude (e.g. Cassel et al., 2014, 2012, 2009; Colwyn and Hren, 2019; Dettinger and Quade, 2015; Friedman et al., 1993b; Hudak and Bindeman, 2018; Jackson et al., 2019; Seligman et al., 2016) – need to have constraints on the initial magmatic H_2O concentration and composition.

7.1 Paleoclimate and paleoaltitude reconstruction

Modeled $10^3\ln\alpha_{g\text{-}v}$ values of −33‰ and −25‰ between 175°C and 225°C suggest that hydrogen isotope fractionation in silicic volcanic glass at hydrothermal conditions increases with temperature only modestly from room temperature to at least 250°C (−33‰; Friedman et al., 1993a; Seligman et al., 2016). This suggests that rapidly hydrated glasses at hydrothermal conditions do not record the H isotope compositions of meteoric water very differently from slowly hydrated glass at low temperatures. Although the experimental results above 250°C are not an extension of this $1/T—10^3\ln\alpha_{g\text{-}v}$ relationship, there are two reasons why these conditions are not applicable to natural samples on long time scales. First, sustained hydration temperatures above 250°C in hydrothermal systems cause rhyolitic glass to break down (Cullen et al., 2019). This is also observed in fumarolic cracks that gave the Valley of Ten Thousand Smokes in Alaska its name (Papike, 1992; Kodosky and Keith, 1993; Kodosky and Keith, 1995) and had temperatures sustained well over 250°C for at least a decade (Griggs, 1922). Second, there are multiple lines of evidence from modeling and natural samples that converge on hydration temperature of ~100°C in slowly cooled volcanic deposits. Hudak and Bindeman (2018) show that the closure temperatures in thin-walled glass shards or pumices in cooling ignimbrites is around 100°C. Finite element modeling shows that the

phase transition between vapor and liquid water fixes the temperature at the boiling point within ignimbrites for prolonged periods of time (Keating, 2005). Both oxygen isotope evidence from hydrothermal pinnacles in the Valley of Ten Thousand Smokes and Crater Lake (Hudak and Bindeman, 2018; Hudak and Bindeman, 2020) and mineralogic evidence from the columns in the Bishop Tuff (Randolph-Flagg et al., 2017) corroborate glass hydration temperatures ~100°C near the boiling point. So even if hydration occurs above 250°C, the δD of glass should be reset at lower temperatures, as the perlites δD time series demonstrate is possible in hydrous glasses.

While this study does not directly apply to the low ambient temperatures prevalent at the Earth's surface, it shows that at temperatures at least as low as 175°C, H isotopes in glass will freely exchange with H_2O vapor in both hydrous and anhydrous glasses. This is an important observation because one of the outstanding issues surrounding the application of δD in volcanic glass to paleoclimate applications is the long-term fidelity of H isotopes in glass. Over 10s to 100s of ka, δD in glass seems to be resilient to environmental reequilibration following initial hydration as demonstrated in the late Pleistocene and Holocene tephra in the Andes (Jackson et al., 2019). But δD fidelity in glass is less certain on timescales of tens of Ma and both experimental and natural sample validations at Earth surface temperatures present challenges. The slow diffusion of H_2O in silicic glass at Earth surface temperatures prevents more than a few microns of penetrative depth on experimental timescales, even at elevated temperatures. Nolan and Bindeman (2013) placed ash in heavy water (+600‰) at 20°C, 40°C, and 70°C for months to years and observed changes in the δD composition at all temperatures. Cassel and Breecker (2017) reproduce this result, but by additionally rinsing the samples in hydrofluoric acid to remove the gel layer that forms on the glass-water interface, they restore the original composition of their older tephras (>10^4 yrs). They argue that this helps to bolster the earlier arguments of Friedman (1993b; 1993a) that once hydrated, silicic glasses will retain the δD imparted by the original hydration waters. However, depth profiling of experimentally hydrated obsidian by $H_2{}^{16}O$, $H_2{}^{18}O$, and $D_2{}^{16}O$ show that H and O exchange with the glass and facilitate the loss of ions that were originally in the silicate to the environment (Anovitz et al., 2009). They conclude

that using δD for paleoclimate should at most be limited to fully hydrated materials and even then, it should be treated with skepticism.

Our results reaffirm the conclusions of Anovitz (2009) that chemical and isotopic exchange can occur across a boundary layer at the glass surface. So if this behavior, where H_2O in glass – and its isotopes – is exchangeable, can be extended to lower temperatures, then the long-term fidelity of δD in volcanic glass is primarily a function of very low D_{H2O}. This implies that tephra clast size or bubble wall thickness should be considered along with the age of the tephra in interpreting δD in glass. Issues with long geologic timescales notwithstanding, δD in glass is a robust recorder of paleo-meteoric water compositions (e.g. Dettinger and Quade, 2015; Jackson et al., 2019; Seligman et al., 2016), and this work expands and simplifies the application of this proxy to glasses with diverse thermal histories. We propose that the fast D_{H2O} in glass at hydrothermal temperatures – several orders of magnitude faster at these temperatures than at 0-25°C – enables hydrothermally hydrated glass to be used as a more precise snapshot of climate (over days to weeks) at the time of eruption and emplacement, rather than a climate or altitude signal integrated over thousands of years of slow hydration.

7.2 Magma-water and magma-ice applications in volcanology

The clear break in H isotope systematics above and below ~250°C, although still not completely understood, suggest that short timescales high temperature interactions between glass and water could be imparted to the glass. Pumices from the 2012 submarine eruption of Havre volcano in the Kermadec Arc have high H_2O concentrations at the rims of vesicle bubble walls and low H_2O in the interior. Diffusion profiles are of sufficient length that high temperatures are required, so Mitchell et al. (2018b) advocate for ~400°C hydration temperatures on the scale of a few minutes. A follow up study shows that a subset of samples from this eruption record δD values consistent with depletions on the order of our observed $10^3 \ln\alpha_{glass\text{-}H2O}$ in >250°C hydration experiments (Mitchell et al., 2018a). Oxygen isotope thermometer techniques developed by Seligman and Bindeman (2019) and Hudak and Bindeman (2020) also support the high hydration temperature. Hydrogen and oxygen isotopes could therefore record magma-water in submarine or magma-ice interactions in subglacial settings.

Finally, the isotope reaction-diffusion model could be further constrained by and applied to higher temperature glasses and melts. Discrete domains of textures and H_2O and CO_2 concentrations within obsidian pyroclasts indicate they are incrementally assembled by sintering of ash on the walls of volcanic conduits syn-eruptively (Castro et al., 2014; Watkins et al., 2016; Gardner et al., 2017). Volatile diffusion studies give timescales of pyroclast assembly (Watkins et al., 2016) and decompression histories (Watkins et al., 2012) and these could be good targets for constraining hydrogen isotope fractionation between OH-H_2O_m using our model as a model domain within a pyroclasts could be chosen far from any changing melt-vapor boundary condition. Melt embayments are increasingly used to constrain magma decompression and ascent rates (Humphreys et al., 2008; Lloyd et al., 2014; Ferguson et al., 2016; Myers et al., 2016; Myers et al., 2018; Moussallam et al., 2019). These could be a good complement for constraining this fractionation as well as the H_2O_m-vapor fractionation since one boundary in that system is open to devolatilization and the change in H_2O_t and OH/H_2O_m equilibrium are well understood at those conditions. Isotope diffusion in embayments may additionally help discriminate among different decompression histories that produce similar H_2O_t profiles from the vapor bubble inward.

8. Conclusions

1) Below 250°C, the time evolution of bulk glass δD is asymptotic and approaches a plateau representing the equilibrium glass δD composition. This contrasts with the time series of δD in experiments conducted above 250°C that record strong δD depletions in the glass that do not evolve asymptotically and therefore do not record a simple constant $10^3 \ln\alpha_{g\text{-}v}$.

2) At 375°C, the glasses have up to 1.0 wt% of OH^- distributed homogenously throughout the fully hydrated glass. This reaffirms observations in both experimental studies (Proctor et al., 2017; Cullen et al., 2019) and in natural samples (Bindeman and Lowenstern, 2016) that document OH^- formation below the glass transition temperature.

3) Based on the strong vapor-OH^- fractionations observed in melts (Dobson et al., 1989), and the correlation between OH^- stretching frequencies and $10^3 \ln\alpha$ values between hydrous phases and fluids (Suzuoki and Epstein, 1976; Graham et al., 1980; Dobson et

al., 1989), we develop an isotope-reaction model for hydrogen during volcanic glass hydration that incorporates the reaction $H_2O_m + O \rightleftharpoons 2OH^-$ internal to the glass during hydration.

4) Modeled $10^3 ln\alpha_{g\text{-}v}$ for D/H are approximately −33‰ and −25‰ at 175°C and 225°C, respectively. These results suggest that H isotope fractionation changes more modestly with increasing temperature than previously estimated (Hudak and Bindeman, 2018). At these conditions, the isotope reaction-diffusion model fits the data well but cannot distinguish between fast or slow reaction kinetics for $H_2O_m + O \rightleftharpoons 2OH^-$.

5) Therefore, rapid hydration of silicic volcanic glass at these temperatures will faithfully record the δD of meteoric water similarly to the −33‰ at room temperature (Friedman et al., 1993a; Seligman et al., 2016), making δD in silicic volcanic glass a viable snapshot paleoclimate or paleoaltitude proxy.

6) The time evolution of bulk glass δD in experiments above 250°C record strong depletions that cannot be explained by reasonable parameters in our isotope reaction-diffusion model. However, we are able to exclude multiple hypotheses in isolation for the observed δD depletions including: i) simple equilibrium $10^3 ln\alpha_{glass\text{-}H2O}$ fractionations between glass and vapor, ii) kinetic isotope effects associated with isotopologues of H_2O (or H_2 or H^+) of different masses, iii) the breakdown of glass into secondary minerals (as they are volumetrically minor), and iv) a diffusion-reaction model that assumes local equilibrium to govern incomplete chemical reactions between H_2O_m and OH^- within glass.

7) Model behavior is most sensitive to changes in the boundary condition and reveals that some combination of factors, likely glass dissolution and/or secondary mineral formation on the glass surface, regulates the bulk δD of the glasses at 275°C and 375°C. While intermediate values for the forward reaction rate, k_{+1}, do produce the apparent overshoot of the equilibrium glass δD, this is likely of secondary importance after the boundary condition.

8) We suggest that this H isotope reaction-diffusion model has broad application to volatile diffusion in obsidian pyroclasts and melt embayments at higher temperatures which may shed light on conduit processes. In both cases, boundary conditions can be

ignored (obsidian pyroclasts) or the boundary can be designed to evolve according to well constrained OH^-/H_2O_m and H_2O_t as a function of P-T-X_{H2O} (embayments).

9. Bridge

Chapter III investigates that kinetic isotope effects associated with diffusion and the internal reaction between H_2O species during glass hydration are shows neither has a strong influence on bulk glass δD compositions. Rather, changes of the δD composition at the boundary of the glass dictate the bulk composition. Equilibrium fractionation, $10^3\ln\alpha_{g\text{-}v}$, at 175°C and 225°C approximates both the range of δD fractionation in rhyolitic melts and at low temperatures (approximately −30‰ ± 10‰). The initial data in the 275°C also suggests a $10^3\ln\alpha_{g\text{-}v}$ of a similar magnitude. Results from 275°C and 375°C are complicated by glass dissolution and secondary phase formation on the glass surface, which are interpreted to affect the δD composition of the boundary even as the interior of the glass remains pristine. While the isotope diffusion-reaction model will be useful for other applications (δD variability in obsidian pyroclasts or melt embayment profiles), the key result of this study is that an approximate $10^3\ln\alpha_{g\text{-}v}$ of −30‰ can be applied to glass-vapor or melt-vapor interactions at all temperature during hydration or dehydration. In Chapter IV, the H and O isotope systematics constrained by the experiments in Chapters II and III are used to understand the role of H_2O in ignimbrite cooling at Crater Lake, OR and the Valley of Ten Thousand Smokes, AK. Glass hydration is found to occur at ~100°C in fumarolic mounds and pinnacles in these ignimbrite sheets as H_2O percolates into the deposit during cooling. This work expands these isotopes in silicic glass as paleoclimate proxies to volcanic products emplaced at high temperatures.

CHAPTER IV

CONDITIONS OF PINNACLE FORMATION AND GLASS HYDRATION IN COOLING IGNIMBRITE SHEETS FROM H AND O ISOTOPE SYSTEMATICS AT CRATER LAKE AND THE VALLEY OF TEN THOUSAND SMOKES

From Hudak, M.R. and Bindeman I.N. (2018). Conditions of pinnacle formation and glass hydration in cooling ignimbrite sheets from H and O isotope systematics at Crater Lake and the Valley of Ten Thousand Smokes. *Earth and Planetary Science Letters*, 500, 56-66.

1. Introduction

Ignimbrites are globally ubiquitous, and their emplacement can reshape the local landscape and radically affect the biosphere and hydrosphere. Common cooling structures in almost all eroded ignimbrites include mounds, fan-like columnar jointing, and fumarolic pinnacles (e.g. Sheridan, 1970), spectacular structures that can be tens of meters in height (Figure 1). These spires and fins are more resistant to erosion than the surrounding tuff because of cementation by hydrothermal mineral precipitation during cooling. Despite being visually striking and common to almost all silicic volcanic systems, their origin and the temperature of formation have not received much attention. This is additionally surprising given that pinnacles record the role water plays in ignimbrite cooling (Keating, 2005). Gazis et al. (1996) and Holt and Taylor (1998; 2001) used gas escape pipes in ignimbrites of Chegem Caldera (Caucasus, Russia) and Long Valley caldera in California to estimate the temperature of $\delta^{18}O$ depletions in these deposits. Based on low-$\delta^{18}O$ values observed in groundmass, they inferred that these systems are high temperature (>500°C) and short lived, given the preservation of magmatic $\delta^{18}O$ major phenocrysts (Holt and Taylor, 1998). Such an interpretation was deemed consistent with high temperatures measured in fumaroles in the Valley of Ten Thousand Smokes, Alaska (VTTS; Griggs, 1922) and following the 1980 eruption of Mount St. Helens (Banks and Hoblitt, 1981). However, Randolph-Flagg et al., (2017)

used the stability of mordenite, a cementing hydrothermal zeolite, to estimate that the peak temperature of similar Bishop tuff columnar pinnacle structures did not exceed 130°C.

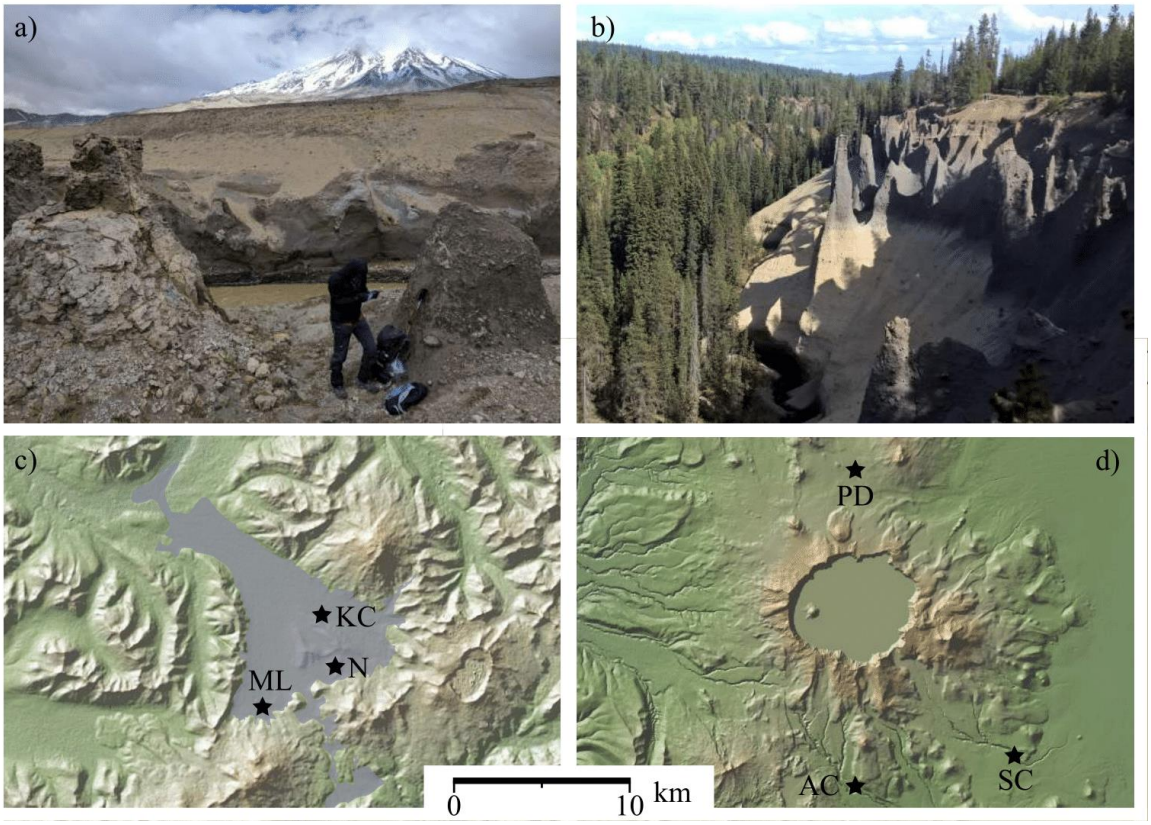

Figure 1. Ignimbrite-water interaction features and maps investigated in this study. Photos of fumaroles from ignimbrites (a) and (b) and the maps of the field locations (c) and (d). Pumices in ignimbrite-hosted fumarolic pinnacles were sampled at the Valley of Ten Thousand Smokes (VTTS) at Katmai National Park, Alaska (a,c) and in Crater Lake National Park and Winema National Forest, Oregon (b,d). Extinct fumaroles from Knife Creek in the VTTS (a) were sampled. Sand Creek, Oregon samples were collected from downstream of the iconic pinnacles at Crater Lake (b). Sample locations are show with stars in the VTTS (c) and in the Crater Lake area (d). The mapped extent of the 1912 Novarupta pyroclastic deposits are shown in a purple overlay from Hildreth and Fierstein (2003). KC = Knife Creek; ML = Mageik Lakes; N = Novarupta; PD = Pumice Desert; AC = Annie Creek, SC = Sand Creek. Maps from GeoMapApp (http://www.geomapapp.org).

Both H and O isotopes in pumice glasses from pinnacles at Crater Lake and the VTTS are used to assess the temperature and timing of pinnacle formation in a cooling ignimbrite and into glass during low T rehydration (also referred to as secondary hydration). For example, with progressive water loss during volcanic degassing, δD_{glass}

decreases with decreasing H_2O (e.g. Taylor et al., 1983). Similarly, diffusion of meteoric water into anhydrous glasses at ambient temperature has allowed δD_{glass} to be used as a proxy for paleoclimate (Friedman et al., 1993b; Seligman et al., 2016) or paleoaltitude (Cassel et al., 2009). Yet few people have applied high-T glass hydration features as a paleoclimate tool (e.g. Bindeman and Lowenstern, 2016). There are several advantages and challenges to using this approach. Glass hydration is well studied at ambient atmospheric (e.g. Friedman and Long, 1976) and high T (>400°C; e.g. Zhang and Behrens, 2000), but not over the relevant 100-400°C range expected in a cooling ignimbrite. Likewise, the fractionation of δD between glass and water is well-constrained at ambient T (Friedman et al., 1993a; Seligman et al., 2016), but unconstrained at hydrothermal temperatures. Combining δD and $\delta^{18}O$ from glasses in these systems may elucidate how and under what conditions water may play a role in ignimbrite cooling. Where water-rock ratios are higher, discrete alteration haloes (e.g. Holt and Taylor, 1998) or layers within a stratigraphic section (Gazis et al., 1996; Holt and Taylor, 2001) can form.

Three main challenges have prevented wider use of δD for paleoclimate studies. First, hydration of volcanic glass at ambient temperatures is extremely slow, (several μm/1000 yrs; e.g. Friedman and Long, 1976) and thus D/H in glass provide centuries to millennia long climate averages (Friedman et al., 1993b). Second, the subsequent fidelity of H isotopes in hydrated glass over long timescales remains an open question given the several μm-thick glass wall thickness of hydrated ashes (Nolan and Bindeman, 2013; Cassel and Breecker, 2017). Finally, while the fractionation factor ($1000\ln\alpha_{glass\text{-}water}$, expressed in ‰) at ambient conditions has been constrained to have a mean value of ~−33‰ (Friedman et al., 1993a; Seligman et al., 2016), higher T fractionation factors are not established, but are expected to be smaller.

To mitigate these challenges, we target initially hot ignimbrite glasses hydrated thoroughly and quickly over tens of microns and at high temperatures (thus small to zero $1000\ln\alpha_{glass\text{-}water}$), happening in the months to decades following ignimbrite emplacement. We select iconic examples of these processes: Crater Lake fumarolic pinnacles and recently exposed fumarolic mounds in the VTTS. Combined use of H and O isotope systematics serves as a hydration thermometer to understand how these features form.

The high water-rock ratio ensures that the hydration waters imprinted their D/H ratios on the glass. Furthermore, this study tests if the coupled use of δD_{glass}—$\delta^{18}O_{glass}$ systematics and parameters that we employ here for the first time ($\delta^{18}O_{water\text{-}in\text{-}glass}$, $\delta^{17}O_{glass}$) a snapshot of meteoric waters as a paleoclimate proxy.

2. Background and Sampling

Upon rapid emplacement, ignimbrites lose heat through conduction into the ground and the atmosphere, through radiative heat loss into the air, and through advective fluid flow via fumaroles and gas escape pipes. The latter process has not been explored in great detail, although finite element modeling suggests it plays a minor role relative to conduction as volatiles are lost in days to weeks and surface waters are unable to penetrate into the ignimbrite interior (Riehle et al., 1995; Keating, 2005). This work considers the iconic Crater Lake pinnacles formed in the Mt. Mazama ignimbrite deposits around Crater Lake National Park, Oregon, USA. The climactic 7.7 ka eruption of Mt. Mazama created 9 km wide caldera, produced 50 km^3 of eruptive products and blanketed much of the northwestern U.S. in ash (Bacon and Lanphere, 2006). In valleys proximal to the incipient crater, loosely welded pumiceous ignimbrite deposits are many 10s of meters thick (Figure 1). Fumarole escape pipes experience vapor phase crystallization and secondary mineralization cements the ignimbrite where fluid flow is concentrated, creating localized zones that are more resistant to erosion than the surrounding material (e.g. Kodosky and Keith, 1995; Papike, 1992). As a result, they are presently exposed as pinnacles and fins that in some locations rise tens of meters above incised stream beds. These features create optimal conditions for high temperature hydration studies as they result from high water-rock ratios.

The 1912 AD Novarupta-Katmai eruption on the Alaska Peninsula offers an excellent historical example for the post-depositional, hydrothermal processes that occur after emplacement of ash-flow tuffs into a river valley filled with snow or onto wet ground. This eruption produced 13-14 km^3 of material that buried a U-shaped valley in several hundreds of meters of ignimbrites and tephra (Hildreth, 1983; Hildreth and Fierstein, 2012). The name, Valley of Ten Thousand Smokes, was aptly given based on observations from expeditions led by R.F. Griggs between 1916-19 who observed

pervasive fumarolic activity throughout the valley (Griggs, 1922). The “smokes” were mostly gone by the 1950s (Hildreth and Fierstein, 2012). These gas escape pipes and fissures, now only barely exposed by erosion (Figure 1, Table C1), aided conduction to efficiently cool the upper portions of the ignimbrite in just a few years.

Both eruptions have similar interstitial rhyolitic glass compositions and display inverted stratigraphy (rhyodacite below crystal rich andesites) reflecting compositional segregation in pre-climactic magma reservoirs. Mt. Mazama is gradationally bimodal, exhibiting andesitic and rhyodacitic pumice clasts throughout the deposit but with an increased proportion of andesitic clasts towards the top (Druitt and Bacon, 1986). Similarly, Novarupta produced abundant initial rhyolite, followed by a mixture of dacite and andesite (Hildreth, 1983). Our study is based on the investigation of this rhyolitic glass in individual pumice clasts collected from pinnacles in both locations that are tied to this inverted stratigraphy. The young age and insufficient river erosion of Novarupta products has prevented the sampling of the earliest and deepest rhyolites in the VTTS, which are not yet exposed. Most samples presented herein are from rhyolitic glasses in the Mt. Mazama rhyodacite and the VTTS dacite. Mt. Mazama climactic glasses are rhyolitic 71.5-74 wt.% SiO_2 (Bacon and Druitt, 1988) and the glass in Novarupta dacites is high-silica rhyolitic >76 wt.% SiO_2 (Avery, 1992; Fierstein and Hildreth, 1992).

In the Mt. Mazama deposits, samples came from 8 different pinnacles and fins that were at least 2 meters in height and commonly higher. These samples were uniformly found in deeply eroded drainages, primarily in Sand Creek, but also from Annie Creek (Figure 1, Table C2). For one particularly well-exposed fin in Sand Creek, the relative position of sample locations to stream bed was recorded over ~25 vertical meters that likely approached the base of the deposit. As erosion is still in progress, pinnacles are taller where the erosion is the deepest. Additionally, altered airfall pumices were collected from very slight topographic highs in the pumice desert in the northern part of Crater Lake National Park, that we hypothesize represent the uppermost portions of discolored fumarolic mounds like those in the Bishop Tuff (Sheridan, 1970), suggesting oxidation was aided by hydrothermal alteration.

In the VTTS, the lesser extent of erosion since 1912 AD permitted sampling of only the uppermost expression of pinnacles. Dacitic pumice clasts were collected from

two locations – along Knife Creek and in the Mageik Lakes area (Figure 1, Table C1). Fewer andesitic clasts were collected from the Mageik Lakes area only. In Knife Creek, hollow gas escape pipes were commonly embedded in mounds that had experienced weaker hydrothermal activity than the pipes. Pumices were collected from these mounds. At Mageik Lakes no gas escape pipes were observed, but sparse, discolored mounds in the ignimbrite were present. Pumices were collected from these areas and from thin >1m tall features that may have represented early pinnacle formation sticking out of the surrounding ignimbrite.

Water samples were collected from 13 lakes within Katmai National Park and Preserve (Table C3) in August 2017 between 12 and 504 m in elevation. Samples were provided by the Southwest Alaska Network (SWAN), part of the Inventory and Monitoring Program of the National Park Service.

3. Methods

Individual pumice clasts (5-20 cm) were lightly crushed by ceramic mortar and pestle, sieved to 105-250 and 250-500 micron size fractions, washed with deionized water, and dried. Individual glass shards were then hand-picked under a microscope to exclude phenocrysts and glass shards with visible alteration or oxidation. Secondary electron microscope (SEM) images (Figure C1) confirm that the glass is unaltered in the interior. These fresh glass separates were used for all bulk isotope and water measurements and were placed in a vacuum oven at ~110°C overnight prior to loading in sample chambers to remove adsorbed water. The brief (or even prolonged) drying procedure does not cause glass to dehydrate or affect the glass δD composition (Nolan and Bindeman, 2013). All analyses were conducted in the Stable Isotope Laboratory at the University of Oregon using a high temperature conversion elemental analyzer (TC/EA) for δD_{glass}, $\delta^{18}O$ of water-in-glass ($\delta^{18}O_{wig}$), and total H_2O in glass (in Ag foils, at 1450°C) and for H and O isotope analyses of waters (by injection and 1400°C). A CO_2 laser fluorination line was used for bulk $\delta^{18}O_{glass}$ and bulk $\delta^{17}O_{glass}$. Both instruments are interfaced with a Thermo MAT253 gas source isotope ratio mass spectrometer (IRMS). These analyses were interspersed with injections of VSMOW and other in-house water standards. Released water is instantaneously converted to H_2 and CO gas by a pyrolysis

reaction with the glassy carbon and passed through a gas chromatographic column using He as a carrier gas, followed by CONFLOW open split analysis against the reference gas of known composition. Hydrogen isotopes and total H_2O are determined from the yield of H_2 with standards USGS57 (biotite) and USGS58 (muscovite; Qi et al., 2017). Further analytical details can be found in Martin et al. (2017) and Text C1. The $\delta^{18}O$ of water-in glass ($\delta^{18}O_{wig}$) was also measured by TC/EA in a separate analytical session from H isotope analyses, using 0.15 μl USGS liquid water standards welded in Ag cups to calibrate the $\delta^{18}O_{wig}$ on a VSMOW scale (Qi et al., 2010). Bulk $\delta^{18}O$ and bulk $\delta^{17}O$ of the glass was analyzed using a home-built airlock sample chamber where glass samples were introduced into the fluorination chamber one by one to prevent premature reaction between the glass and the BrF_5 gas reagent. The produced O_2 gas was purified with a series of liquid nitrogen traps and a Hg diffusion pump and converted into CO_2 by a carbon rod before being introduced into the MAT253-GS-MS (Loewen and Bindeman, 2015).

4. Results

4.1 Katmai surface water isotopes

Measurements of δD and $\delta^{18}O$ from 13 lakes in the Katmai area establish the values for hydration water that diffused into Katmai glasses (a process referred to as secondary hydration) (Figure 2). These data provide a reasonable range of δD and $\delta^{18}O$ composition that could have fed the fumaroles in the VTTS in the weeks to decades following the June 1912 eruption. We observe that δD and $\delta^{18}O$ data from lake waters do not plot on the Alaskan meteoric water line (MWL), which comes from river and stream data (Lachniet et al., 2016), but instead plot at an shallower angle to the MWL between −115.0 and −94.1‰ δD and −16.81 and −12.31‰ $\delta^{18}O$ (Figure 2). Such a relationship is consistent with evaporation from lakes (e.g. Gat, 1996). The slope of the Katmai lakes is 4.63, which is functionally similar to slopes for lakes in other cold and wet climates in the continental US such as Minnesota (5.98) and Wisconsin (3.73; Brooks et al., 2014; Jasechko et al., 2014). However, this shallower trend resulting from evaporation shifts lake waters to the right of the MWL. Several Katmai lakes yield compositions that fall outside of and to the left of the envelope of existing Alaskan data (lower $\delta^{18}O$ and higher

δD). Lachniet et al. (2016) also note that they have a dearth of data from SW Alaska on the Alaska Peninsula where Katmai is located. Therefore, we suggest that this may result from a slightly different local MWL on the Alaska Peninsula than for the rest of mainland Alaska. Future sampling of streams, springs, or precipitation in the Katmai region may reconcile meteoric water compositions better with the Alaskan MWL.

4.2 Bulk H_2O concentration, δD, and $\delta^{18}O$ compositions

4.2.1 Valley of Ten Thousand Smokes glasses

Both δD and $\delta^{18}O$ of Katmai dacitic glasses decrease with increasing H_2O (Figure 3). The H_2O content of fumarolic Katmai glasses spans a large range from 0.76 to 4.18 wt.% and δD_{glass} ranges from −152.1 to −94.2‰. Although the data from Mageik Lakes and Knife Creek form two clusters, together they show continuous trends in isotopic depletions with increasing H_2O: Mageik Lakes glasses are <1.17 wt.% H_2O and >−117.8‰ δD_{glass} while Knife Creek glasses are >2.31 wt.% and <−132.3‰ δD_{glass} (Table C4).

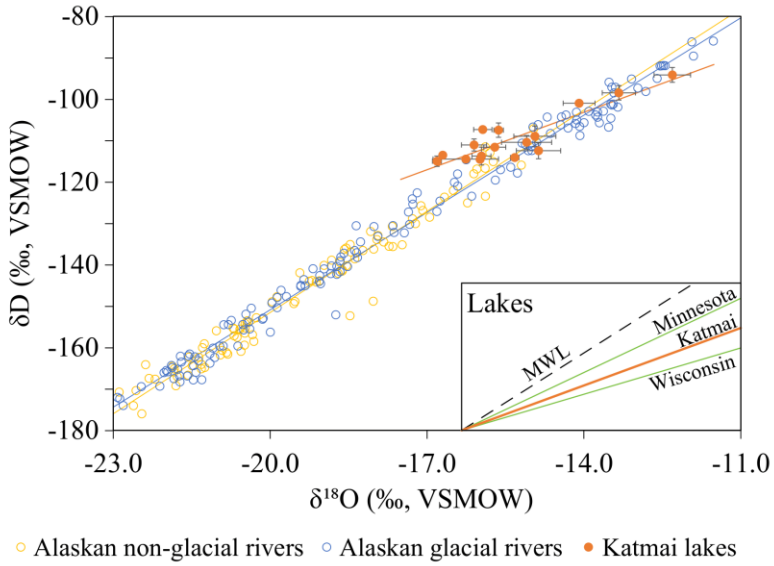

Figure 2. The $\delta^{18}O$ and δD compositions of lake water from Katmai National Park (this work) compared to data from glacially-fed and non-glacial waters across Alaska (from Lachniet et al., 2016). Katmai waters are shown with 1 S.E. for both $\delta^{18}O$ and δD. Note that our Katmai data form a trend at a sharp angle to the Alaskan MWL, consistent with evaporation from lakes or condensates from water vapor. Slopes for lakes in Minnesota and Wisconsin (green) are shown for comparison in the inset (Brooks et al., 2014; Jasechko et al., 2014).

The combined use of δD, $\delta^{18}O$ and H_2O of Katmai glasses (Figure 3) reveals a relationship most consistent with simple addition of meteoric water to glass (rehydration by H_2O diffusion into glass without isotopic exchange between glass and water). The δD_{glass} follows the expected trend of initial rapid depletion with the first 1-2 wt.% of water added to an initially degassed pumice composition, as meteoric hydrogen overwhelms minor remaining magmatic water in glass. At higher water content, δD_{glass} tapers off and plateaus around −150‰ (Figure 3a) following simple water addition model curves. (See Text C2 for full model descriptions.) The δD of the VTTS glasses reaches low values before bulk $\delta^{18}O_{glass}$ begins to show depletion. Unlike the δD_{glass} depletions, bulk $\delta^{18}O$ of VTTS glasses follow a linear trend from 5.38 to 7.12‰ (Figure 3b) of addition of –16.08‰ $\delta^{18}O$ water to glass without a large separation between sample locations. Three andesitic pumices from Mageik Lakes define a narrow range in H_2O from 0.50 to 0.70 wt.%, and in $\delta^{18}O$ from 5.97 to 6.12‰. Their δD_{glass} is variable, spanning from −119.9 to −91.6‰. The continuous isotope trends from the rhyolitic glass in dacitic pumices suggest that the meteoric waters are similar at the two locations, which are in different watersheds on either side of Novarupta (Figure 1), and that they experienced similar conditions during hydration. Overall, these water addition curves indicate that these glasses define a secondary hydration trend best explained by modern local meteoric waters at or near ambient T. Isotopic exchange and equilibration between water and glass are not required to explain the VTTS glass data.

Figure 3. Isotopic correlation of Katmai glasses is modeled with mixing curves of pure addition of water to glass (star denotes the anhydrous magmatic glass). (a) H_2O v. δD mixing curves extend to 4.2 wt.% H_2O, the maximum H_2O concentration of the sample suite. (b) H_2O vs. $\delta^{18}O_{bulk}$. (c) δD v. $\delta^{18}O_{bulk}$, where tick marks on the mixing curve correspond to wt.% H_2O added, which closely correlate to TCEA H_2O concentrations measured in these glasses. Notice that pure addition of meteoric water to glass at Katmai is sufficient to explain simple linear decrease in $\delta^{18}O_{bulk}$ values, and more rapid hyperbolic decrease in δD. The light green field for Mazama pinnacle glasses, shown for comparison and that are explored in Fig 4, show a more dramatic $\delta^{18}O_{bulk}$ changes requiring glass-water interaction rather than simple water addition. Data for andesitic pumices from fumaroles (yellow) and Novarupta dome samples (open circles) are shown for comparison.

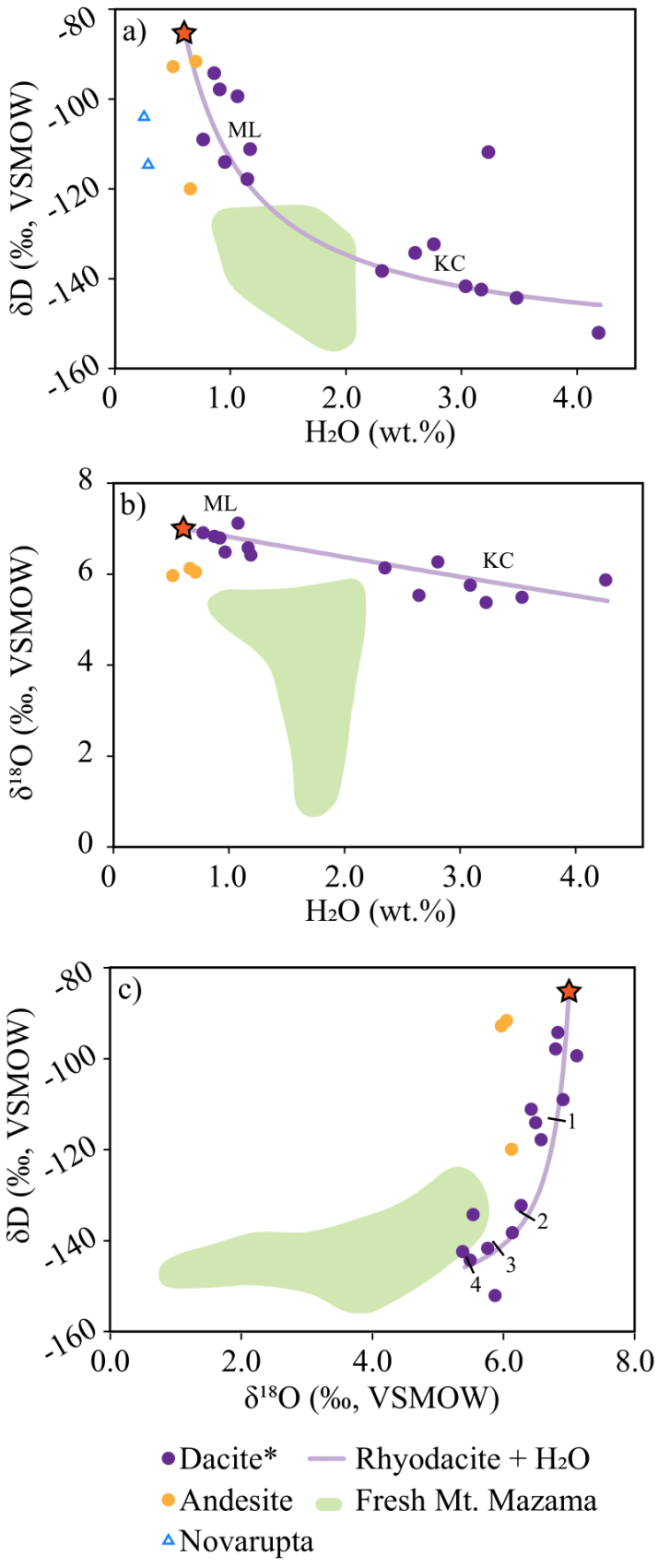
a)
ML
KC
δD (‰, VSMOW)
H₂O (wt.%)
b)
ML
KC
δ¹⁸O (‰, VSMOW)
H₂O (wt.%)
c)
1
2
3
4
δD (‰, VSMOW)
δ¹⁸O (‰, VSMOW)
Dacite*
Andesite
Novarupta
Rhyodacite + H₂O
Fresh Mt. Mazama

4.2.2 Crater Lake glasses

Glass from rhyodacitic pumices from Crater Lake pinnacles have narrow range of H_2O contents (1.55-1.96 wt.%), and δD_{glass} (−147.7 to −132.8‰) relative to the silicic glasses from the VTTS (Figure 4a, Table C5). However, they display a large range in bulk $\delta^{18}O$ glass values from 5.55‰ to depleted values of 0.95‰ (Figure 4b), all of which are lighter than initial magmatic values of ~7‰. Glasses from andesitic pumices have a larger range in H_2O (0.94 to 1.99 wt.%) and δD_{glass} (−152.9 to −112.0‰), but a more limited range in $\delta^{18}O_{glass}$ (3.71 to 5.34‰). Simple addition of water to degassed Cleetwood rhyolite with 0.1 wt.% H_2O (Mandeville et al., 2009; Seligman et al., 2016) or a theoretical less degassed andesite pumice cannot explain trends for either dacitic or andesitic Mazama glasses (Figure 4b; Text C2). Although there is a linear relationship between H_2O and bulk $\delta^{18}O$ for the andesitic glasses, they form a steeper trend towards more depleted values than the water addition curves predict. In fact, the water addition curves do not fit the rhyodacite or andesite data on any of the H_2O-δD-$\delta^{18}O$ plots, which contrasts the VTTS data. (See Text C2 for mixing model assumptions and end member compositions.) In Figure 4c, more than 18 wt.% H_2O would be required to achieve the $\delta^{18}O$ of the lightest rhyodacitic glasses – a full order of magnitude more H_2O than water contained in any of the glasses. Constant H_2O values of ~1.7 wt.% are notably lower than low-T hydration of silicic glass of 3-4 wt.% water (Friedman et al 1993; Seligman et al 2016), as is also exemplified by the Katmai glasses. The strong depletions in $\delta^{18}O_{glass}$ indicate that isotopic exchange proceeded without further hydration at near constant H_2O concentration. This suggests that the glasses were already completely hydrated and water-saturated at the temperatures of continuing isotopic exchange with water fluxing through the ignimbrite. Nearly constant δD_{glass} values suggest that the glass in pinnacles was completely overwhelmed by this water and approached a value in equilibrium with the meteoric water. This behavior in the Mt. Mazama pinnacle glasses, as recorded by both total water and isotopic compositions, differs from the VTTS glasses because of the shallow depth of the VTTS samples in the ignimbrite deposits. Streams around Crater Lake have had much longer to cut down into the ignimbrite deposits where higher temperatures were sustained for longer periods of time and allowed for isotope exchange between water and glass.

Altered airfall pumices have high H_2O (3.54 to 5.23 wt.%) and higher δD_{glass} (−133.2 to −112.0‰) than almost all the pumice glasses collected from pinnacles. Bulk $\delta^{18}O$ are also distinctively heavier (6.08 to 7.08%) than the fresh, pinnacle glasses. Macroscopic alteration and SEM images show that the glass in these pumices contain secondary minerals, which likely fractionated δD_{glass} and $\delta^{18}O_{glass}$ to higher values (Figure 5).

Results from the Crater Lake pinnacles differ from those in previous studies of Mt. Mazama ashes, pyroclasts, and vitrophyres. Mandeville et al. (2009) reported δD_{glass} and H_2O data for samples proximal to Crater Lake that establish broad groups of samples (Figure 5). The first group consists primarily of lavas and vitrophyres, which define an open system degassing trend. The other group is formed largely of pumices that provide evidence for secondary hydration by meteoric waters given their more depleted δD_{glass} at high H_2O. Their rehydrated glasses converge towards an apex with ~3.5 wt.% H_2O and ~−145‰ δD_{glass}. Lower H_2O glasses can be viewed as mixing lines between data points on degassing trend and this single secondary hydration apex. Data from Seligman et al. (2016) of degassed and rehydrated Mt. Mazama pumices and ash across Oregon record an extension of this trend to even lower δD_{glass} values than reported in this study and higher H_2O than was reported by Mandeville et al. (2009). Some data at high water contents trend toward higher δD_{glass} (Seligman et al., 2016) and overlap the altered airfall pumice samples from our study (Table C5).

Figure 4. Isotopic correlation of Mazama glasses that are modeled with water-glass mixing curves from two starting glass compositions (see text for values of end member compositions). (a) H_2O v. δD, (b) H_2O v. bulk $\delta^{18}O$. Mixing curve extends from the initial andesitic and rhyodacitic glasses (blue and orange stars, respectively). Neither glass composition follows the simple addition of water curves for (a) or (b). The rhyodacites have nearly constant H_2O concentrations, indicating that they probably represent the H_2O saturation of water in glass at their hydration T. The rhyodacites and andesites demonstrate greater $\delta^{18}O_{bulk}$ depletion than is required by a simple H_2O addition curves. This suggests significant H and O exchange must have occurred to produce the observed values, which is better illustrated by (c), where $\delta^{18}O_{bulk}$ v. δD is shown. Up to 15 wt.% H_2O addition would be required to explain the isotope compositions of glasses that are uniformly <2 wt.% H_2O. Katmai glasses from fumaroles (see Figure 3) that can be explained by pure water addition are shown as purple fields, with KC denoting Knife Creek and ML denoting Mageik Lakes locations.

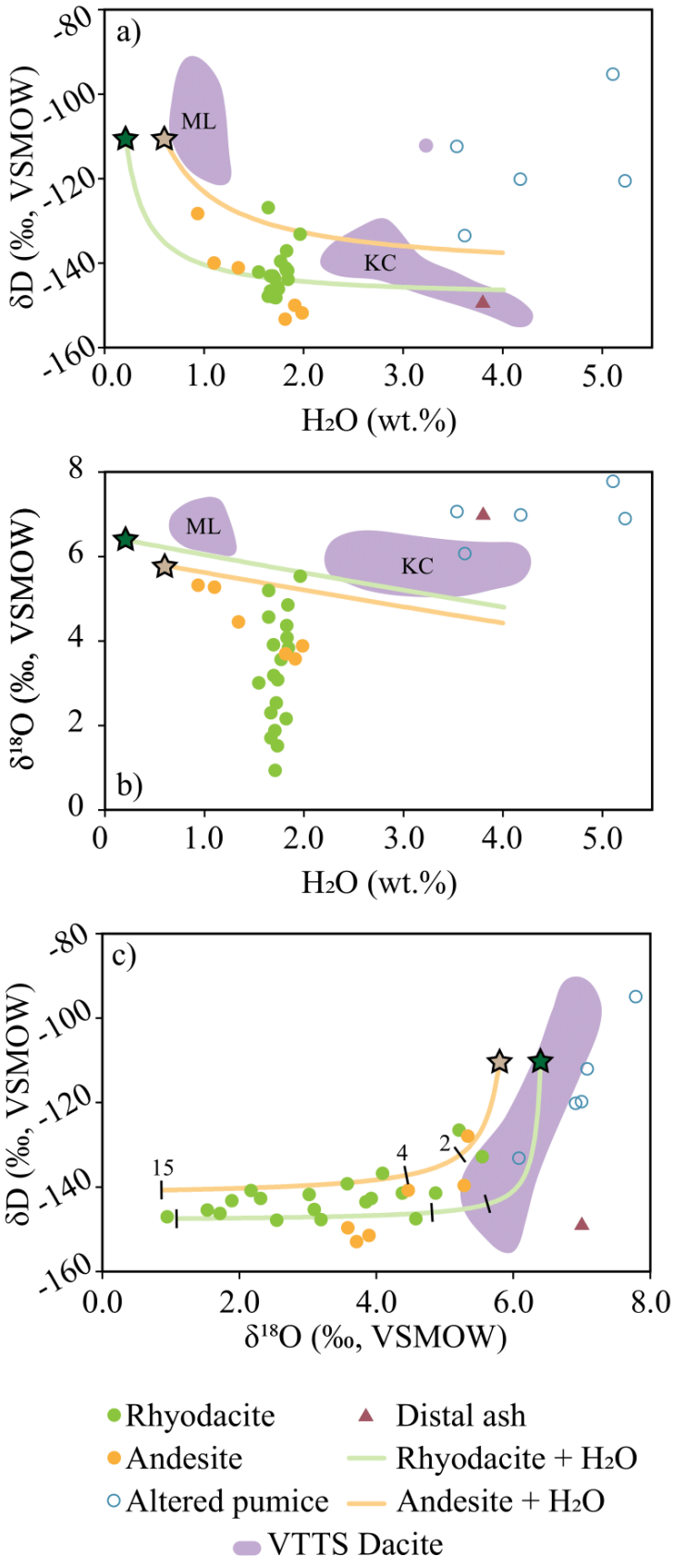
a)
ML
KC
δD (‰, VSMOW)
-80
-100
-120
-140
-160
0.0
1.0
2.0
3.0
4.0
5.0
H₂O (wt.%)
b)
δ¹⁸O (‰, VSMOW)
8
6
4
2
0
c)
15
4
2
0.0
2.0
4.0
6.0
8.0
δ¹⁸O (‰, VSMOW)
Rhyodacite
Andesite
Altered pumice
Distal ash
Rhyodacite + H₂O
Andesite + H₂O
VTTS Dacite

Overall, when compared to the pumices hydrated at ambient temperatures, the pumices from the fumarolic pinnacles presented herein have very comparable lower δD_{glass} end, which likely reflects value of the local meteoric waters. Lower water concentration in the pinnacles reflect higher T hydration because the saturation of H_2O in glass is believed to be lower at higher T and atmospheric P (Anovitz et al., 2008). The water contents and estimated hydration T of Mt. Mazama pinnacle glasses are similar to the ~1.8 wt.% H_2O in many Yellowstone perlites studied by Bindeman and Lowenstern (2016) that were hydrated around 90°C. Although the solubility of water in glass is poorly constrained below magmatic temperatures, these data seem to indicate that water solubility is <2 wt.% at ~100°C, which is lower than the 2-3 wt.% at 200°C estimated by Anovitz et al. (2008).

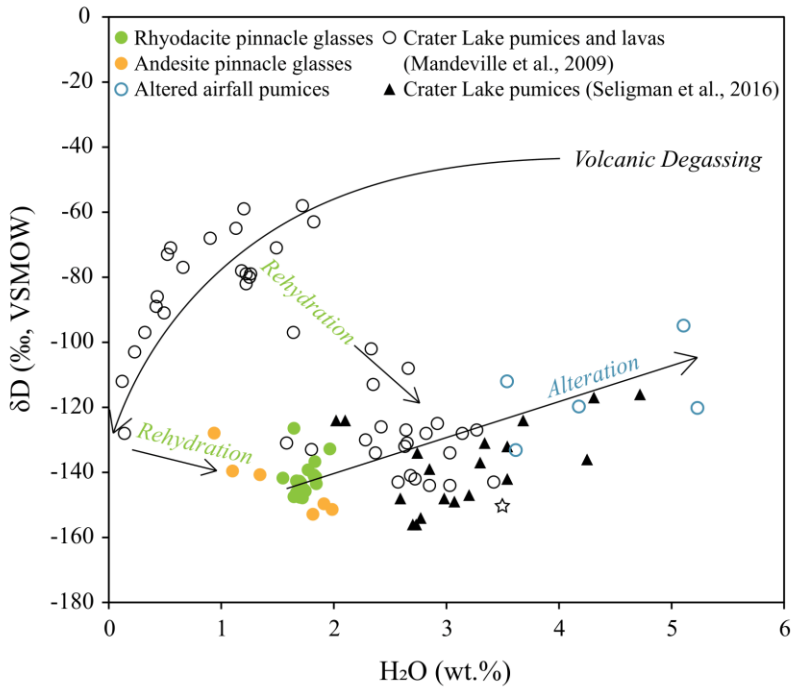

Figure 5. Mt. Mazama glass H_2O and δD compositions from this study and published sources. The Mandeville et al. (2009) dataset documents pumices and lavas that they model as an open system degassing trend. Seligman et al. (2016) data includes rehydrated Mazama glasses from central Oregon. Notice that both Mandeville et al. (2009) and Seligman et al. (2016) datasets include secondary hydrated glasses that have been hydrated by local waters at mean annual temperatures. Pinnacle glasses from this work were hydrated at hydrothermal temperatures (~100°C, see text) and plot more tightly at with lower H_2O concentrations than low-T hydration data. These data suggest that our δD have more fully and uniformly equilibrated with local meteoric water at higher T and lower water solubility of glass.

4.3 Oxygen isotope systematics in glass

4.3.1 $\delta^{18}O$ of water-in-glass ($\delta^{18}O_{wig}$)

In order to gain further insight into the water-glass interaction, we measured the $\delta^{18}O$ of water-in-glass (called $\delta^{18}O_{wig}$) released by TC/EA pyrolysis. Mass balance calculations using $\delta^{18}O_{wig}$, the bulk $\delta^{18}O_{glass}$, and the H_2O content allow estimation of $\delta^{18}O_{anhydrous\ silicate}$ to be used for isotope thermometry. Despite the variability of $\delta^{18}O_{wig}$, they show a scattered positive correlation with $\delta^{18}O_{silicate}$ (Figure 6) along the 125 ± 25°C isotherm of glass-water equilibrium. Although the uncertainty for these measurements is assumed to be ±1.5‰ (corresponding to ±20°C temperature estimates), all hydration temperature estimates from this method are below 200°C. We consider this result to be a robust indication that pinnacles record formation or last isotopic equilibration (i.e. closure) at or near the boiling temperature of water.

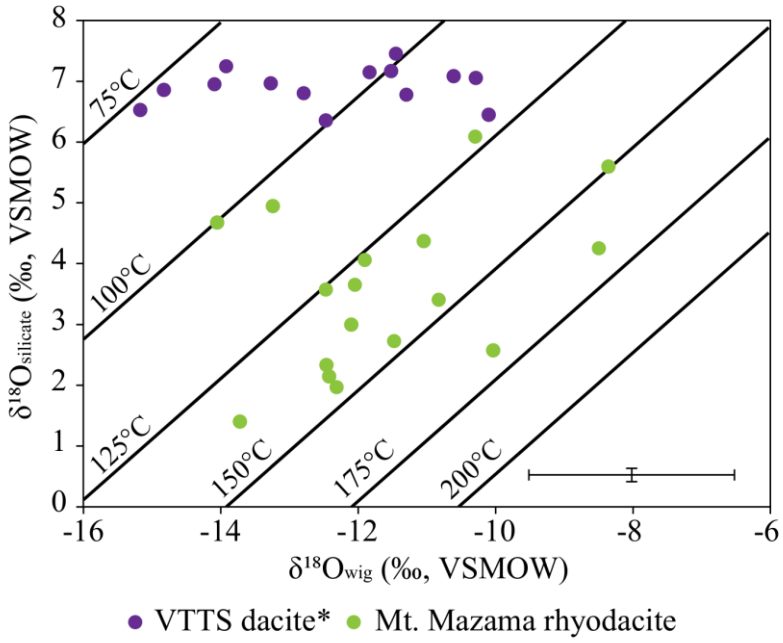

Figure 6. O isotope systematics of the two components of hydrous glass: $\delta^{18}O$ of silicate ($\delta^{18}O_{silicate}$) and $\delta^{18}O$ of water in glass ($\delta^{18}O_{wig}$). $\delta^{18}O_{sil}$ is calculated using $\delta^{18}O_{bulk}$ and $\delta^{18}O_{wig}$. Solid black isotherms are calculated from equilibrium fractionation between rhyolite and water (see text). Most glass hydration temperatures for Mazama rhyodacitic glasses (green) are estimated to be between 125-150°C for different and sometimes very depleted $\delta^{18}O_{bulk}$ values. VTTS dacitic glasses (purple) hydrated by pure water addition (Figure 3) have constant $\delta^{18}O_{silicate}$. This graph suggests $\delta^{18}O_{wig}$ can be used as a tool to record hydration and equilibration temperatures. Error bars in the bottom right are approximately analytical error of $\delta^{18}O_{wig}$ and propagated error of $\delta^{18}O_{sil}$.

Katmai dacites range from −15.2 to −10.1‰ in $\delta^{18}O_{wig}$ without a large change in $\delta^{18}O_{silicate}$. They nominally span even lower temperature range <125°C than the Mt. Mazama data. However, as is argued above, Katmai data can be explained by simple water addition without much isotopic exchange (Figure 3). As thermometry interpretations in Figure 6 require substantial oxygen isotope exchange, if not total equilibration, the Katmai data only hint at the temperatures at the onset of O isotope exchange between meteoric water, water in glass, and silicate glass.

4.3.2 Triple oxygen isotopes of Crater Lake pinnacle glasses

Two samples recording the highest water-rock ratio of Mt. Mazama pinnacle glasses were also analyzed alongside with a mantle standard in the same analytical session for $\delta^{17}O$ so that the $\Delta'^{17}O$ may be calculated with ±0.01‰ precision. The relationship between rocks or minerals and the meteoric waters with which they have equilibrated is more apparent when expressed by $\Delta'^{17}O$, where $\Delta'^{17}O$ represents the linearized deviation from a reference line equal to $\delta'^{17}O - 0.5305 * \delta'^{18}O$ with a slope of 0.5305 (Matsuhisa et al., 1978). For the estimated $\delta^{18}O$ composition of Mt. Mazama hydration waters (-16.9 ± 0.6‰) the corresponding $\Delta'^{17}O_{water}$ from the MWL is 0.076‰ (Figure 7; Luz and Barkan, 2010). In linearized $\delta'^{18}O$-$\delta'^{17}O$ coordinates, triple oxygen fractionation follows the relationship in Equation 1.

Eq. 1: $$ln(\alpha^{17/16}_{glass-water}) = \theta_{glass-water}\, ln(\alpha^{18/16}_{glass-water})$$

Figure 7 of $\delta'^{18}O$ vs. $\Delta'^{17}O$ yields a $\Theta_{glass\text{-}water}$ of ~0.525. The empirical, temperature-dependent equation provided for $\Theta_{silica\text{-}water}$ by Sharp et al. (2016) and Pack and Herwartz (2014) both predict a value of 0.525 at 100°C. Greater values for Θ are characteristic for lower temperatures and Θ is theoretically 0.5305 at infinite T. For example, shales have a $\Theta_{shale\text{-}water}$ of ~0.523 at low T (Bindeman et al., 2018). The curved fractionation line emanating from the Mt. Mazama waters on the MWL shows equilibrium fractionations for silica-water in grey (Sharp et al., 2016) and rhyolite-water in black. Rhyolite is modeled as an albite-quartz mixture (see Section 5.1.1) that should have a functionally similar $\delta'^{18}O$-$\Delta'^{17}O$ fractionation as silica-water (Bindeman et al., 2018). Thus, triple oxygen isotopes from the two lowest $\delta^{18}O$ samples in Mt. Mazama pinnacle glasses provide an intermediate temperature range of ~90-110°C.

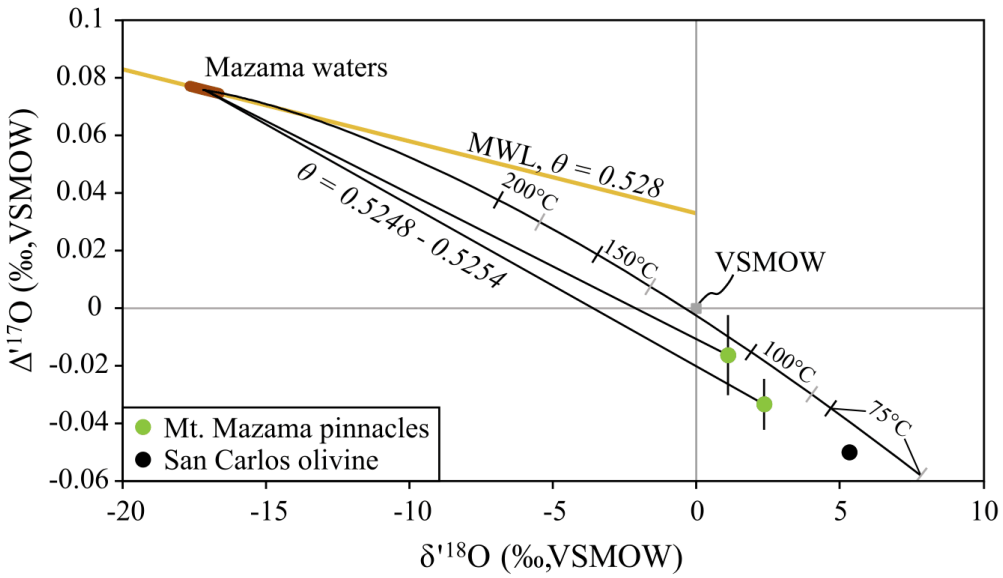

Figure 7. Triple oxygen isotopic values for low- $\delta^{18}O$ Mt. Mazama glasses plotted as $\delta'^{18}O$-$\Delta'^{17}O$ diagram. A projection from the two pinnacle glasses (green) back to the inferred Mt. Mazama hydration waters yields a slope in $\delta'^{18}O$- $\delta'^{17}O$ ($\Theta_{glass\text{-}water}$) of 0.525, which is also predicted for silicate-water at 100°C, suggesting the glasses have equilibrated with water. Error bars show 1 S.E. The MWL (yellow) has a slope of 0.528. Other Θ values are shown for comparison as grey vector for kinetic fractionation (0.518; Pack and Herwartz, 2014) and for shales (0.523; Bindeman et al., 2018). San Carlos olivine (black), which approximates the composition of the mantle and the starting composition for the pinnacles, and VSMOW are also plotted.

4.4 Vertical isotope variations within pinnacles

Vertical variations through a ~25 meter high continuous rhyodacite fin in Sand Creek are observed. Distances between sample collection sites in Figure 8 are 2-4 m in elevation and extend from the valley floor to the highest point of the fin. Contrary to previous work where clear zones of depleted $\delta^{18}O$ were observed within sections of otherwise normal magmatic $\delta^{18}O$ (Gazis and Taylor, 1996; Holt and Taylor, 1998), these glasses are all depleted relative to the initial glass composition. A less depleted zone in the center of the section is recorded by all the isotope parameters for which we have data: δD_{glass}, $\delta^{18}O_{glass}$, and $\delta^{18}O_{wig}$. Relatively constant 1.6-1.8 wt.% H_2O may correspond to H_2O saturation of glass our hydration temperature estimates (~100°C).

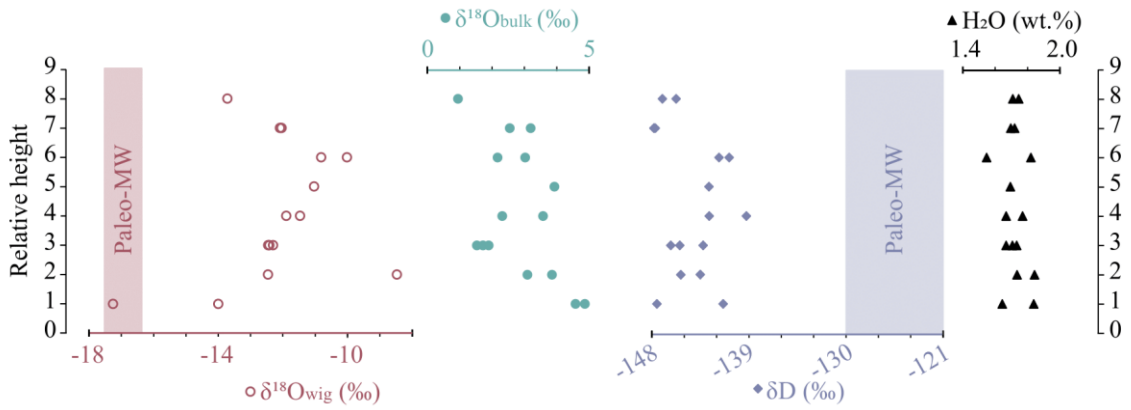

Figure 8. Isotope stratigraphy in a Mt. Mazama fin (sheet-like pinnacle) in Sand Creek locality (Fig 1). Each relative position in the sequence represents 2-4 meters in elevation with a total vertical section of ~25 meters. Water concentrations are near uniform throughout the section. Both oxygen isotopes ($\delta^{18}O_{wig}$ and $\delta^{18}O_{bulk}$) and δD are less depleted in the central part of the sampled section, which may reflect higher closure T associated with more continuous cooling rates in the ignimbrite interior. (See Appendix B for values.)

5. Discussion

5.1 Isotope thermometry of glass hydration

5.1.1 Hydrogen and oxygen isotopes record hydration temperatures around the boiling point of water

Applying equilibrium fractionation ($1000\ln\alpha_{glass\text{-}water}$) equations for δD_{glass} and $\delta^{18}O_{glass}$ permits hydration temperature estimates (Figure 9). A $1000\ln\alpha(^{18}O/^{16}O_{glass\text{-}water})$ can be approximated by the simple linear combination of fractionation factors of quartz and albite. As rhyolites normatively contain approximately two-thirds albite and one-third quartz components in their eutectic proportions, we use the approach of Bindeman and Lowenstern (2016), and use one-third $1000\ln\alpha_{qtz\text{-}water}$ (Sharp et al., 2016) and two-thirds $1000\ln\alpha_{ab\text{-}water}$ albite (O'Neil and Taylor, 1967) to compute rhyolitic glass-water $^{18}O/^{16}O$ fractionation:

Eq. 2: $$1000ln\alpha\left(\frac{^{18}O}{^{16}O}\right)_{glass-water}$$

$$= 3.205 \cdot \left(\frac{1000}{T}\right)^2 - 0.633 \cdot \left(\frac{1000}{T}\right) - 2.74$$

For δD_{glass}, the rhyolite-water D/H fractionation is much less constrained as a function of temperature. Empirical evidence suggests $1000\ln\alpha_{glass\text{-}water} = -33‰$ at ambient

T, which we take to be 10°C ± 10°C (Friedman et al., 1993a; Seligman et al., 2016). Unpublished data from ongoing glass hydration experiments at the University of Oregon point to fractionations of approximately −5.7‰ at 225°C and −10.5‰ at 175°C (Table C6; Figure C2). These results allow a three-point approximation of $1000\ln\alpha(D/H)_{glass\text{-}water}$ over an intermediate temperature range which yields the following relationship (Eq. 3) for $1000\ln\alpha(D/H)_{glass\text{-}water}$:

$$\text{Eq. 3:} \quad 1000ln\alpha(D/H)_{glass-water} = -3.15 \cdot \left(\frac{1000}{T}\right)^2 + 6.12$$

where T is in Kelvin. This equation is intermediate in slope to two experimental studies on kaolinite δD fractionation over hydrothermal temperature ranges (Lambert and Epstein, 1980; Sheppard and Gilg, 1996), which is a common weathering product of volcanic glass and is thought to fractionate H and O isotopes similarly to bulk rhyolite. At any given temperature, these fractionation factors yield $\delta^{18}O$ and δD values for a rhyolitic glass that has completed exchange and equilibrated with a given meteoric water composition. This creates isotherms that are subparallel to the MWL, functionally similar to kaolinite-water and smectite-water fractionation for δD-$\delta^{18}O$ (Sheppard and Gilg, 1996; Mix and Chamberlain, 2014). For a given meteoric water composition, the same approach also yields an isopleth over a range of T (Figure 9).

The isotope exchange recorded by the depleted bulk $\delta^{18}O$ values of Crater Lake pinnacle glasses allows these data to be interpreted with these isotherms, which yield hydration temperatures of 75-100°C (Figure 9). The starting glass composition is approximated by the composition of Cleetwood rhyolite. This value is projected to the fully equilibrated glass compositions for several temperatures along a series of glass-water mixing curves. We use a minimum value of −17.5‰ $\delta^{18}O$ and −130‰ δD (marked by blue star; Figure 9), which falls on the global MWL, for the hydration water and equilibrium glass end members. A solid black line is an isopleth that represents the fully equilibrated glass compositions for this meteoric water composition. The data uniformly fall between the 75 and 100°C isotherms. Each $\delta^{18}O$-δD glass composition therefore represents a precise meteoric water composition and hydration temperature. This approach gives meteoric water compositions between −17.5‰ and −16.3‰ $\delta^{18}O$ and −130‰ and −120‰ δD (opaque blue box; Figure 9).

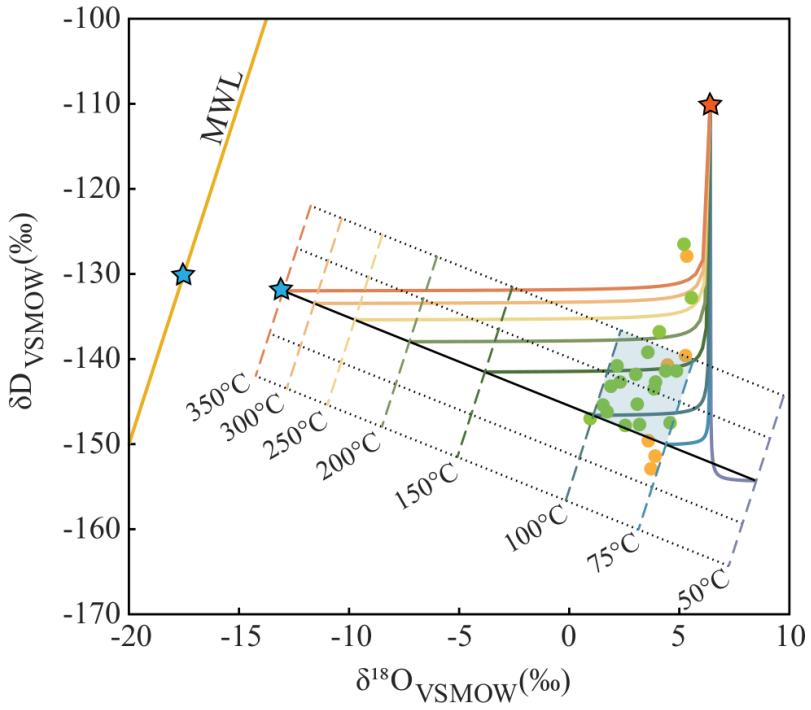

Figure 9. Hydration temperature and meteoric water composition estimates from glass-water H and O fractionation relationships for Mt. Mazama rhyodacitic (green) fumarolic pinnacles. Andesitic glasses are in yellow. See text for isotope fractionation equations used. A star shows an estimated meteoric water composition (-17.5‰ $\delta^{18}O$, -130‰ δD) and dotted lines with negative slope indicate equilibrium hydrothermal products emanating from different meteoric waters on the MWL. Modeled mixing curves between starting unaltered rhyodacite and fully equilibrated hydrothermally altered glass are shown by different color curve, with warmer colors representing higher T and cooler colors representing lower T. Dashed isotherms run subparallel to the MWL and correspond in color to the hydration T mixing curve. The blue shaded region illustrates the range of paleo-meteoric water compositions and hydration/equilibration temperatures that are most probable.

The low temperatures given by the $\delta^{18}O_{glass}$ and δD_{glass} compositions are bolstered by similar estimates from triple oxygen isotopes and the novel $\delta^{18}O_{wig}$ (water-in-glass) parameter that we employ. An underlying assumption for both paleo-meteoric water and temperature estimates is that fluxes of water through the cooling ignimbrite are high enough that the glass is continually reacting with waters emanating from MWL and reacting along computed mixing lines (Figure 9). Triple oxygen isotopes indicate that the glass has equilibrated with the water at 100°C based on the $\Theta_{glass\text{-}water}$ of 0.525 from pinnacle glasses. Temperature estimates of 125-150°C from the $\delta^{18}O_{wig}$ parameter are slightly higher than the $\delta^{18}O_{glass}$—δD_{glass} estimates. The positive correlation between

$\delta^{18}O_{silicate}$ and $\delta^{18}O_{wig}$ (Figure 6) is parallel to computed isotherms, which indicates that the water is equilibrating with the glass at roughly constant T. If oxygen isotope exchange between glass and water is incomplete, a trend like the one observed in the VTTS data would be expected, in which addition of light meteoric water to the glass does not change the $\delta^{18}O_{silicate}$. Given the ±1.5‰ and ±20°C uncertainties in accepted fractionation factors and the errors in the $\delta^{18}O_{wig}$ measurements, these T estimates are overlap with the estimates from better calibrated H and O isotope systematics. This result supports using the $\delta^{18}O_{wig}$ as a thermometer with further development of the proxy. All 4 of our isotope proxies yield similar results, which strengthens our interpretation of ignimbrite hydration around ~100°C by approximately −17‰ $\delta^{18}O$ and −125‰ δD hydration waters.

5.1.2 Water in cooling ignimbrites

Multi-isotopic insight into cooling ignimbrites strongly suggests that despite long cooling histories from estimated emplacement temperatures of >600°C (Griggs, 1922; Banks and Hoblitt, 1981) at both VTTS and Mazama, glass hydration only begins near the boiling point of water and/or likely records the isotopic closure temperature. This is very different than earlier conclusions by Gazis and Taylor (1996) and Holt and Taylor (1998) who used $\delta^{18}O$ only to infer higher temperatures (>500°C) in bulk analysis of large quantities (15-30 mg) of variably devitrified and recrystallized groundmass. Modeling of Bishop Tuff column formation by Randolph-Flagg et al. (2017) using mordenite stability showed that water did not percolate down to a depth of 200 m in the ignimbrite until temperatures were below 130°C. Hydration temperature of Yellowstone perlites have been similarly interpreted to be ~100°C (Bindeman and Lowenstern, 2016). Below, we provide a simple physical explanation to the observed phenomena.

In Sand Creek where the ignimbrite is estimated to be ~60 m thick (Druitt and Bacon, 1986), relatively low vapor pressures can keep the ignimbrite dry. At 125°C, the vapor pressure is 2.32 bars if both liquid and vapor water are present and this can resist a hydrostatic pressure equivalent to ~15 m of water. Therefore, water should not infiltrate the ignimbrite until near boiling T. Therefore, glass hydration is unlikely to proceed until temperatures are cool enough to sustain water in the liquid phase. Modeling by Keating (2005) matches Crater Lake ignimbrite thicknesses, so given his modeled temperature

curves we can infer that most hydration (and thus pinnacles formation) will occur between 5-40 years after emplacement.

Our temperature estimates are inferred to reflect closure temperatures (T_c) for water, and therefore, hydrogen. Using the equation of Dodson (1973), we are able to match our 75-125°C temperature range to cooling rates of 0.02-0.35°C/yr (Figure C3). Using a conservative diffusive length-scale for bubble wall half-thickness of 7.5 μm and a shape constant of 15, which reflects a geometry between a sheet and a cylinder, a T_c of 100°C yields a cooling rate of 0.04°C/yr. At faster cooling rates, T_c is much higher. For example, T_c is 200°C at a rate of 3.8°C/yr, and 300°C at 73.7°C/yr. Ignimbrite cooling rates are typically 2-3 orders of magnitude faster on average than ~0.04°C/yr, more consistent with these higher closure temperatures. However, the temperature can be held constant at ~100°C for long periods of time as water vapor can more readily redistribute heat (Keating, 2005). The near surface and basal parts of the ignimbrite may sustain boiling temperatures for years, so slow cooling rates are applicable to the glasses and T_c calculations.

5.2 Paleoaltitude – Meteoric waters at Mt. Mazama, 7.7 ka

The array of Mt. Mazama data in Figure 9 suggests a meteoric water composition of approximately −16.9‰ $\delta^{18}O$ and −125‰ δD. Through a ~25m section of the ignimbrite water-rock interaction may be heterogenous with slightly variable mean δD and $\delta^{18}O$ water compositions, temperatures, or cooling rates during their formation (Figure 10). Crater Lake water has been reported to be between −77.3 to −80‰ δD and −9.4 to −10‰ for $\delta^{18}O$, while springs have a mean δD of −101.9 and a mean $\delta^{18}O$ of −14.25‰ and are as light as −110.5‰ and −15.45‰ for δD and $\delta^{18}O$, respectively (Thompson et al., 1987). However, our paleo-meteoric water estimate is −16.9‰ ± 0.6 ‰ using Figure 9. The lower $\delta^{18}O$ hydration waters either reflect that climate at the time of the climactic Mt. Mazama eruption was 3.0-4.7°C cooler (Dansgaard, 1964) or that there was water source coming from an elevation 1.05-1.77 km higher than currently given the 1.8‰/1000m $\delta^{18}O$ gradient for precipitation in the central Oregon Cascades just north of Crater Lake (James et al., 2000). Globally stable Holocene temperatures (Masson et al., 2000; Mayewski et al., 2004) and the clear evidence that Mt. Mazama once rose much higher, indicate that these depleted isotope data reflect high elevation sources of water on

the former edifice. This would require groundwater to have traveled along deep pathways before emerging in springs >1000m lower in elevation. This has been observed in the central Oregon Cascades at springs on the Metolius River, for example (James et al., 2000; Manga, 2001). These authors also find that the residence times of deeply flowing groundwater from higher altitude sources is longer than the time it takes for the interior of a 60 m ignimbrite to cool (Keating, 2005). Therefore, we favor high elevation snow and ice on the former Mt. Mazama edifice and deep groundwater flow paths to Sand Creek or springs upstream to explain our inferred paleo-meteoric water values.

5.3 Model for pinnacle formation at low T (100°C)

Low T hydration in the Mt. Mazama pinnacles suggests that these formations do not represent vigorous fumaroles. Jointing from cooling and contraction of the ignimbrite enabled measurement of near magmatic temperatures within ignimbrites days to years after their deposition (Griggs, 1922; Banks and Hoblitt, 1981). However, in the VTTS, the cooling joints that acted as fumaroles are encrusted with white, red, and purple phases. Fresh, glassy pumices alone may indicate low T water-rock interaction. Columns formed by surface water percolation deep into the Bishop Tuff contain mordenite, a zeolite stable below 130°C (Randolph-Flagg et al., 2017). Pinnacles and columns represent late-stage cooling in the ignimbrite, at which time they begin to hydrate and undergo isotopic exchange. Ignimbrite remains dry, expelling external water vapor until the internal temperature approaches the boiling point of water. (This may also be necessary to prevent glass dissolution or devitrification; see Text C3-C4, Figure C4, Tables C7-C8.) Our conceptual model for pinnacle formation begins with ignimbrite emplacement (Figure 10a). With progressive cooling, joints form that may host fumaroles (Figure 10b). Years to decades later, water can flux through the ignimbrite and precipitate phases that cement the pinnacles together within the matrix (Figure 10c). Hydration and isotope exchange between glass and water occur at this stage, before erosion finally exposes them (Figure 10d). This model is somewhat different from that of Randolph-Flagg et al. (2017) because it calls upon groundwater rather than surface water to hydrate the pinnacles, although these models are not incompatible. Groundwater from a high elevation source is necessary to reconcile the depleted δD_{glass} and $\delta^{18}O_{glass}$ isotope data that the pinnacle glasses record since they are strongly shifted away from the modern

meteoric water values and the likely meteoric water isotope values 7.7 ka. Emergent springs feeding streams could then percolate down through the upper portion of the ignimbrite in the incipient channels of the streams where the pinnacles are now found. Water sources from above and below help to explain the greater depletions in H and O isotopes near the top and the bottom of the deposit than in the interior (Figure 8). Groundwater is likely to concentrate in paleo-valleys at the contact between bedrock and the ignimbrite and stream channels are likely to reoccupy these paleo-valleys. Pinnacle formation may be especially robust in this setting.

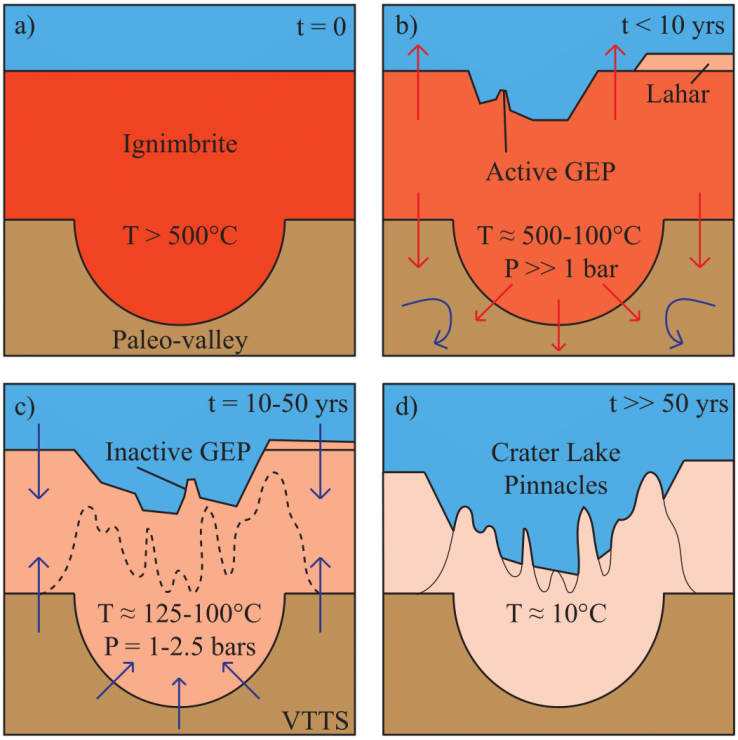

Figure 10. Conceptual model of pinnacle formation at Crater Lake and the VTTS. Ignimbrite is emplaced (a) and gas escape pipes (GEP) and fractures degas (red arrows) most residual magmatic volatiles from the ignimbrite interior at near magmatic temperatures (b). These fumaroles do not directly represent the pinnacles which form late as is evident from isotopic systematics results of this work. Instead, they effectively keep water from percolating into the ignimbrite. Pinnacle formation begins during very late-stage cooling (c) once the interior of the deposit has cooled to near the boiling point of water once water can percolate inward (blue arrows). Panel (c) likely reflects recent pinnacle development and modern surface features (and possibly ongoing pinnacle formation in the thickest parts) of the VTTS. At this point, glass hydration and isotope exchange between glass and water begins, as does precipitation of secondary minerals in the ignimbrite matrix. Decades to millennia later, 10s of meters of erosion expose pinnacles, as we observe at Crater Lake today (d).

6. Conclusions

Hydrogen and oxygen isotopes in glasses from ignimbrite-hosted pinnacles record the thermal conditions of pinnacle formation and the composition of the meteoric waters that fluxed through the ignimbrite during the final stages of cooling. Here, we further demonstrate that water-rock interactions at elevated temperatures in pinnacles and other rapidly hydrated glasses can be exploited to reconstruct paleo-meteoric water composition. Barely exposed tops of the Katmai fumarolic mounds, which cooled quickly because of their proximity to the surface of the deposit and the erosion that has exposed them in less than 100 years, record simple addition of water and only subtle $\delta^{18}O_{glass}$ depletion. Strong depletions in $\delta^{18}O$ require more time and should be found in ignimbrite interiors like at Crater Lake. Our δD_{glass} data and multiple oxygen isotope proxies indicate that the temperatures of Mt. Mazama pinnacle hydration and isotope exchange occurred near 100°C. The preservation of glass itself may be indicative of lower and geologically short-lived hydrothermal temperatures. The low T of hydration and O isotope exchange indicates that cooling ignimbrite acts as an open system, expelling any volatile phases until temperatures are low enough to allow external waters to invade the cooling deposit, which is independently consistent with previous numerical modeling of a cooling deposit. Therefore, we conclude that pinnacles represent late-stage cooling features in ignimbrites. The $\delta^{18}O_{wig}$ data yield comparable T estimates of 125-150°C that are within error of the other T estimates. This is the first use of a new $\delta^{18}O_{glass}$—$\delta^{18}O_{wig}$ proxy that can work as an inter-glass (or inter-mineral) isotope thermometer and merits further development in glass and other hydrous minerals. The combined δD—$\delta^{18}O$ analysis of glass from pinnacles adds a new dimension to the δD_{glass} method for reconstructing paleoclimate or paleoaltitude. At 75-100°C, hydration can proceed much faster (years) than at ambient atmospheric temperatures (1000s of years), providing a valuable snapshot of the meteoric water and climate at the time of ignimbrite emplacement. In the Crater Lake pinnacles, glasses record δD and $\delta^{18}O$ values that are lower than are observed for modern springs. Altitudinal isotope hydrology suggests the source of water was snowmelt or glacial meltwater from at least 3 km elevation on the higher pre-collapse edifice. This provides a constraint for the minimum elevation of Mt. Mazama, which is more than 1 km higher than the present-day lake level. This work

demonstrates that low hydrothermal temperatures of pinnacle formation are still elevated enough to reliably record the H and O isotopic compositions shortly after ignimbrite emplacement. This novel paleoaltitude or paleoclimate tool using isotopes in rapidly hydrated glass could be further improved with additional constraints on isotope fractionation between silicic glass and water or hydrologic modeling efforts to understand if water in pinnacles primarily is sourced from surface waters or groundwater.

7. Bridge

Chapter IV highlights that glass hydration in transient hydrothermal systems, such as in cooling ignimbrites, can occur on relatively short timescales. Further, the δD of glass in these systems reliably captures the δD composition of meteoric waters at the time of emplacement. Because glass hydration proceeds very slowly at standard temperature and pressure (~1 μm/1000 yrs), I demonstrate that this faster, higher temperature hydration of glass can be used as a snapshot paleoclimate proxy that can be associated with ages taken from geochronology in the same samples. Chapter V evaluates whether volcanic glass in atmospheric eruptive columns can facilitate glass hydration through glass-vapor (or magma-ice) interactions even faster before the ash is deposited.

CHAPTER V

SYN-ERUPTIVE HYDRATION OF VOLCANIC ASH RECORDS SPATIAL VARIATION OF AIR ENTRAINMENT IN ERUPTIVE PLUMES

From Hudak, M.R., Bindeman, I.N., Loewen, M.W., and Giachetti, T. Syn-eruptive hydration of volcanic ash records spatial variation of air entrainment in eruptive plumes. In review at *Geophysical Research Letters*.

1. Introduction

Interaction of external water with magma can increase eruption explosivity (Mastin et al., 2009b; Zimanowski et al., 2015). In the ash plume of an explosive eruption, efficient entrainment of atmospheric moisture facilitates plume rise as vapor condensation produces latent heat and increases buoyancy (Woods, 1993; Herzog et al., 1998). Condensed vapor also affects ash dispersal (Schwaiger et al., 2012) as H_2O condensation on pyroclasts causes aggregation of accretionary lapilli during collisions between particles (e.g., Brown et al., 2010, 2012; Gilbert & Lane, 1994).

Environmental water begins to hydrate volcanic glass slowly after an eruption and becomes measurable as quickly as in 10^1-10^4 years (Giachetti and Gonnermann, 2013). While no systematic work has tested whether hydration can occur during eruption in subaerial settings, syn-eruptive glass hydration has been document in a submarine setting (Mitchell et al., 2018b). Should hydration occur in volcanic plumes, tephra may provide novel insight to spatial or temporal variation in moisture entrainment of eruptive columns as few methods can detect the real time extent of magma-water interactions (Büttner et al., 1999; Mastin et al., 2009).

Hydrogen isotopes (δD) in volcanic glass are powerful tracers of H_2O diffusion to and from a fluid phase (degassing and resorption/hydration, respectively) that are sensitive to variable degassing or hydration in eruptive columns. Water occurs in silicate melts and glasses as molecular water (H_2O_m) and hydroxyl (OH^-), the former being the only effective diffusing species (e.g., Zhang et al., 1991; Zhang & Ni, 2010). Hydroxyl groups have an affinity for ^1H (or H) over ^2H (or D), so melts become increasingly

depleted in D relative to H during magmatic degassing to lower total H_2O (H_2O_t) contents (Dobson et al., 1989). This trend has been well-documented by obsidian pyroclasts in rhyolites (Figure 1a; Castro et al., 2014; Giachetti et al., 2020; Mandeville et al., 2009; Newman et al., 1988; Taylor et al., 1983). Degassed glasses hydrate slowly at low temperatures and record δD ($\delta D(‰) = 1000 \times [D/H_{sample}/D/H_{standard} - 1]$) values that are lower than those of the H_2O in the surface environment by approximately 33‰ (Friedman et al., 1993a; Seligman et al., 2016). Therefore, in most settings, hydration leads to decreases in δD with increasing H_2O_t, the opposite of degassing (Figure 1a). In this way, H_2O–δD systematics in glass can discriminate between degassing and hydration (e.g., Seligman et al., 2016).

Melts commonly degas to <0.5 wt% H_2O and <80‰ δD during eruption as ascending magma decompresses and the H_2O solubility of the melt approaches ~0.1-0.3 wt% at atmospheric pressures and magmatic temperatures (e.g., Liu et al., 2005). Though hydration has been increasingly recognized as a process that can overprint magmatic water concentrations in porous pyroclasts (Giachetti & Gonnermann, 2013; Giachetti et al., 2015; Seligman et al., 2016), this process has been thought to occur over 10^1–10^4 year timescales, with the short end of this range occurring in warmer climates (Anovitz et al., 2006).

Within a volcanic plume, high temperatures could result in rapid hydration of volcanic glass. Results from recent glass hydration experiments with H_2O vapor or supercritical fluid below the glass transition temperature show that the H_2O solubility in rhyolitic glass is at least 1.5 wt% higher than predicted by extrapolations of magmatic solubility models between 150°C and 375°C at the relevant P-T conditions (Anovitz et al., 2008; McIntosh et al., 2014; Proctor et al., 2017; Cullen et al., 2019; Hudak and Bindeman, 2020). It is therefore plausible that syn-eruptive hydration of tephra occurs in subaerial environments with abundant H_2O. Furthermore, the H_2O–δD systematics could track changes in magma-H_2O interactions over the course of an eruption or spatial variability of atmospheric moisture within the plume.

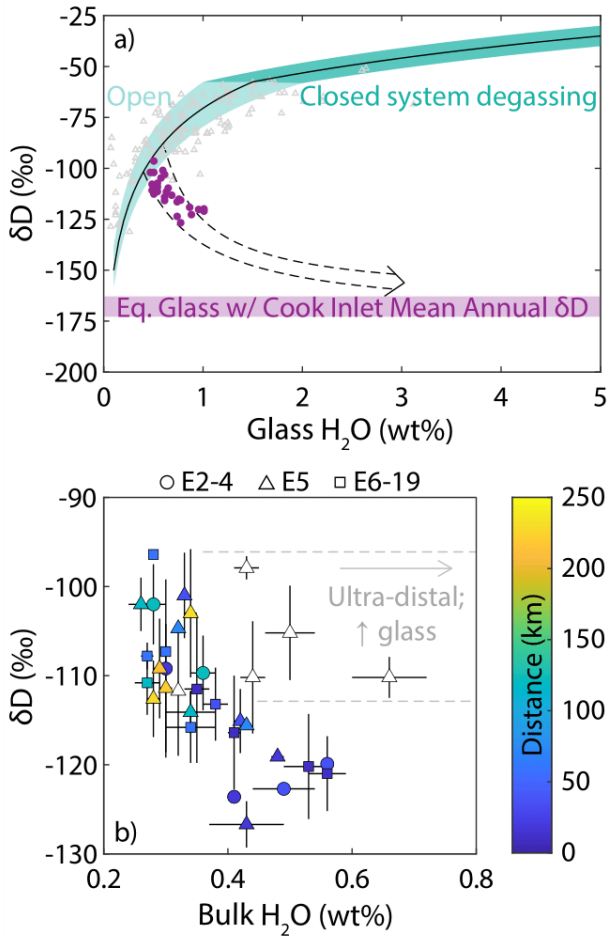

Figure 1. (a) Typical volcanic degassing (green) and hydration (dashed lines) H_2O–δD trends, plotted together with measurements of δD vs. H_2O in 63-125 μm fractions of 2009 Redoubt tephra (purple dots, corrected for crystal content) and obsidian pyroclasts from the western US (grey triangles; Giachetti et al., 2020; Mandeville et al., 2009; Newman et al., 1988; Taylor et al., 1983). While the obsidians broadly conform to the degassing trends, corrected glass H_2O values from Redoubt ash samples are clearly enveloped by hydration curves with meteoric H_2O. (b) δD vs. H_2O as measured in 63-125 μm fractions of 2009 Redoubt bulk tephra (i.e., glass and crystals). Early stages of the eruption interacted with an overlying glacier (circles, events 2-4) which was removed before or during event 5 (triangles) and then erupted without direct magma-ice interactions (squares, events 6-19). Colors represent the depositional distance from the vent. Open circles are fine ultra-distal tephras (>270 km) that are likely higher in water because of a higher glass fraction. Error bars are 1σ (b).

In this contribution, we examine H_2O–δD values in fresh ash erupted from Redoubt Volcano, Alaska, in 2009 in order to evaluate the role of degassing and/or hydration, both within the distribution of volcanic plumes and over the course of an eruption. Nineteen discrete explosive events occurred over about three weeks (Bull and

Buurman, 2013) and were sampled within 4 months following the eruptive sequence (Wallace et al., 2013). Therefore, this sample suite is ideal for testing both the extent to which direct magma-ice interactions are necessary for hydration, and where moisture is present and available in the plume.

2. Materials and methods

A set of 24 ash samples were selected from the Alaska Volcano Observatory collection representing explosive eruptive events throughout the eruption, and samples from single events that were deposited from 8 to 300 km away from the vent. Samples were disaggregated in an unheated ultrasonic bath for 5 minutes and wet-sieved. Some samples with larger volumes were split on a Frantz magnetic separator at a current of 0.8A in an attempt to enrich the glass fraction. Both nonmagnetic and weakly magnetic separates were analyzed.

Aliquots of 4-6 mg of ash from the 63-125 μm sieve fractions were loaded in Ag capsules for analysis by High Temperature Conversion Elemental Analyzer (TC/EA) configured to a MAT-253 isotope ratio mass spectrometer (IRMS) at the University of Oregon following the methods described in Martin et al. (2017). Muscovite and biotite standards, USGS57 and USGS58 (Qi et al., 2017), and an internal laboratory muscovite standard (BUD) were each analyzed 3-5 times in each of the 4 analytical sessions. Mica reference material reproducibility (2 s.d.) never exceeded 0.1 wt% H_2O or 5.5‰ for δD for any standard in any analytical session. Glass H_2O content, which is corrected for crystal content from the bulk ash H_2O results using data from Coombs et al. (2013), is discussed throughout the text and plotted in figures, except for Figure 1b where the raw bulk ash H_2O data are plotted. (See Text S1 and Figure S1-2 for discussion.)

3. Ash H_2O-δD results and discussion

3.1 Magmatic degassing vs. glass hydration

Bulk ash H_2O and δD negatively correlate (Figure 1b; Tables S1, S2), with a δD of ~−100‰ at a bulk H_2O of ~0.3 wt% decreasing to δD of ~−125‰ at a bulk H_2O of ~0.5 wt%. The comparative effects of degassing and hydration are illustrated in Figure 1a using the VolcDeGas model of Walter and Castro (2020) for degassing and calculations

for hydration as outlined by Hudak and Bindeman (2018). We model degassing using a combination of closed and open system degassing with a transition between regimes at 1.5 ± 0.5 wt% H_2O. This approximates the H_2O solubility of silicic melt at reasonable depth (at ~20 MPa or 800 m) where this degassing transition would occur (Giachetti et al., 2020). Alternative degassing histories produce the same general trend using other styles of degassing, such as batched degassing (e.g., Taylor et al., 1983; Castro et al., 2014). The model begins with an initial H_2O of 5.0 wt%, constrained by estimates of 4-5 wt.% water made by plagioclase hygrometry (Coombs et al., 2013), and a δD of −35‰ estimated from amphibole δD values (Suzuoki and Epstein, 1976; Supporting Information Table S3, Figure S3). Obsidian pyroclasts from the western United States are broadly consistent with the degassing models, which decrease in δD with H_2O (Taylor et al., 1983; Newman et al., 1988; Rust et al., 2004; Mandeville et al., 2009; Giachetti et al., 2020). The glass H_2O and δD values from Redoubt ash follow a starkly opposing trend to what these models and previous studies show for magmatic degassing.

To model hydration, mixing calculations between a degassed glass and the local meteoric H_2O are shown in Figure 1a. The glass end member is represented H_2O–δD values on the degassing curve at 0.5 ± 0.1 wt% H_2O, which is consistent both with the lowest glass H_2O concentrations (0.46 wt%) and the magmatic H_2O modeled in porous pyroclasts from other continental arcs (Giachetti et al., 2020). The meteoric H_2O is the mean annual δD composition of −130‰ δD for precipitation at sea level in Anchorage (Bailey et al., 2019) projected to −140‰ δD for the elevation of the Redoubt summit (~−0.3‰/100m elevation; Poage & Chamberlain, 2001) and a hydrogen isotope fractionation factor of −33‰ between glass and H_2O for the full temperature interval (Hudak et al., 2018). The resulting envelope of hydration curves encompasses nearly the full data set. This trend is a hallmark of hydration by meteoric water (Figure 1a; Mandeville et al., 2009; Seligman et al., 2016, 2018; Hudak and Bindeman, 2018).

3.2 Temperatures and timescales of glass hydration

To gain insight into the timescales of hydration, we apply the H_2O concentration dependent H_2O_t diffusivity relationship of Zhang and Behrens (2000) to isobaric quenching at 0.1 MPa using a linear 1D finite difference model. Resulting profiles are integrated to calculate the bulk H_2O_t of the glass. We assume that degassing occurs at

magmatic temperatures and that hydration only proceeds below T_g, which occurs at a minimum temperature of around 500°C in silicic melts (Giordano et al., 2005; Giordano et al., 2008). Diffusion occurs in the model from the glass-vapor interface into the glass with a H_2O solubility boundary condition of 4 wt% in a glass with initial H_2O content of 0.45 wt%, an initial condition below all glass H_2O. (Most glass occurs as surface coatings on phenocrysts, so we assume H_2O diffusion occurs from only one direction.)

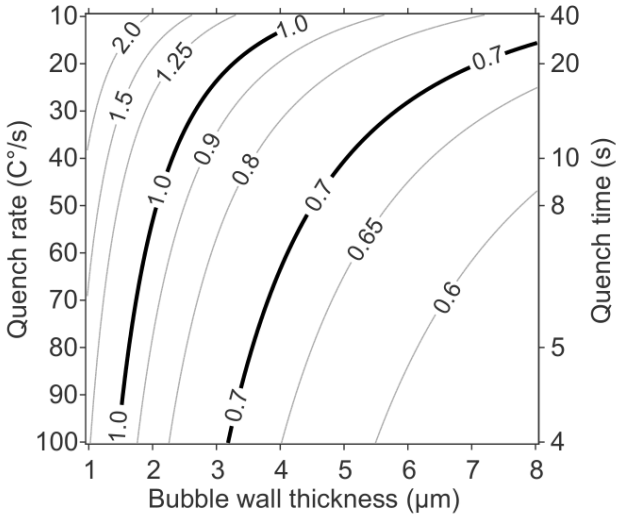

Figure 2. Modeled glass H_2O_t concentrations in tephra hydrated during quenching from 500°C to 100°C with a constant H_2O solubility of 4 wt%, based on estimates for this T range from Hudak and Bindeman (2020). Hydrated tephra has a glass H_2O content between 0.7 and 1.0 wt%, which are outlined by thick white contours.

The glass H_2O compositions of 0.7-1.0 wt% in more extensively hydrated Redoubt ash are reproduced at all quench rates at the observed bubble wall thicknesses (Figure 2), even for a maximum of ~100 C°/s for fine ash in air (Moitra et al., 2018). The lowest H_2O_t in the model domain is 0.56 wt% at the fastest quench rate in the thickest bubble wall, higher than the minimum glass H_2O of 0.46 wt%. Hudak and Bindeman (2020) constrained the diffusivity of H_2O_t (D_{H2O}) in glass to be up to 4 times the H_2O concentration dependent D_{H2O} of Zhang and Behrens (2000) between 175°C and 375°C. Using 4 × D_{H2O} here produces the same Figure 2 with the x-axis doubled (from 1-8 μm to 2-16 μm) as $x = \sqrt{Dt}$. Therefore, the modeled glass H_2O is a minimum estimate for the given timescales and length scales. We note that over the 10 years between eruption and analysis, the D_{H2O} at Earth surface temperatures cannot produce glass H_2O >0.65 wt% in this model using a mean bubble wall thickness of 1 μm. Not only can glass partially

hydrate while quenching, but it can also do so even on timescales as short as 4 seconds. This modeling supports the inference from our dataset that glass hydration can occur in volcanic eruptive columns.

3.3 Evaluating H_2O sources with glass hydration timing and ash dispersal proxies

The Redoubt summit vent was cleared of overlying Drift Glacier Data before or during the fifth of the nineteen explosive events (Waythomas et al., 2013), and ash is subdivided by event number to evaluate the role of magma-ice interactions in this trend (Figures 1b and 3). If the glacier is the hydration source for Redoubt ash, then high H_2O and low δD should be constrained to events 2-5 that erupted through and cleared Drift Glacier. However, ash compositions span the full range of H_2O–δD regardless of the presence (events 2-4) or absence (events 6-19) of ice at the vent, indicating that direct magma-ice interactions are not responsible for the hydration of Redoubt tephra.

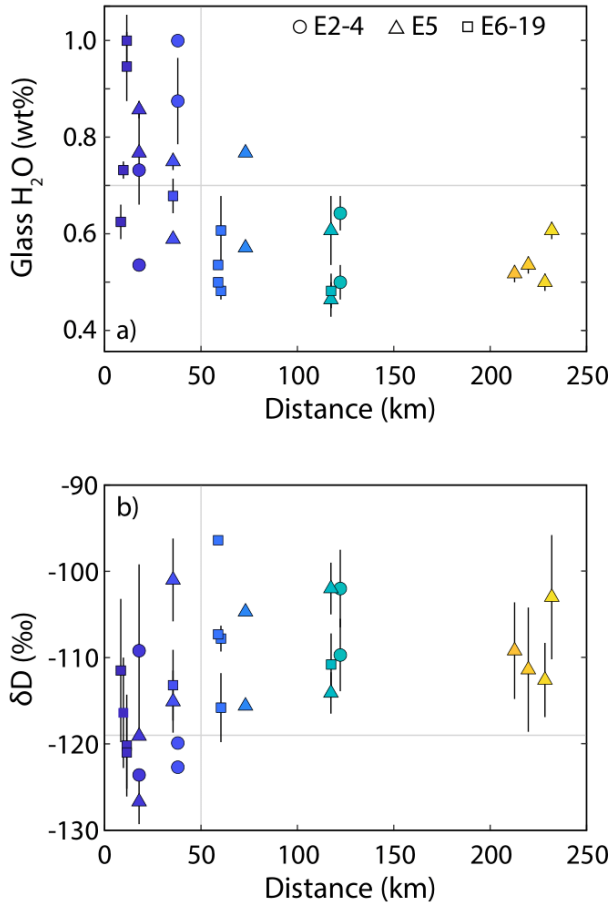

Figure 3. Glass H_2O (a) and δD (b) as a function of distance from the vent in 63-125 μm fractions of 2009 Redoubt tephra. Beyond 50 km, hydration >0.7 wt% H_2O in the glass

occurs only in one sample and δD <−119‰ is absent. Errors from measured bulk tephra H_2O are scaled with corrected glass H_2O. Colors correlate with distance as in Figure 1b.

Instead, we hypothesize that glass must hydrate through interactions with atmospheric H_2O vapor entrained in the hot plume during eruption. The role of dynamics within the plume is also implicated by the correlation between the extent of hydration and the depositional distance from the vent. Bulk H_2O concentrations in tephra decrease away from the vent (Figure 3a) while δD increases (Figure 3b). If the final magmatic H_2O before hydration commenced is allowed to vary between 0.4 and 0.6 wt% (as in Figure 1a), then any glass with H_2O >0.7 wt% has been hydrated by at least 0.1 wt% H_2O. This is used as an arbitrary boundary between more and less extensively hydrated glass, also corresponding to ~−119‰ δD in the hydration model.

High glass H_2O and low δD values indicate more extensive hydration by meteoric water and this population is limited to within 50 km of the vent. Excluding ultra-distal samples (Figure 1b), 93% of the ash samples collected from >50 km from the vent has glass H_2O contents <0.7 wt% compared to 31% collected <50 km away (Figure 3a). Similarly, 54% of the proximal samples have δD values of <119‰ while none at distances >50 km has depletions beyond −119‰ (Figure 3b). This observation requires a mechanism within the plume to account for preferential removal of more extensively hydrated material closer to the vent.

4. Implications for atmospheric volcanic plume dynamics

We have established that tephra from the 2009 Redoubt record evidence for syn-eruptive hydration, and diffusion models corroborate the idea that this process can occur rapidly during quenching over the required diffusive length scales. Yet, where this hydration occurs, why some ash samples show no evidence for hydration, how variably hydrated material remains segregated in the plume, and why hydrated tephra fall out proximally remain important questions.

Here we present a conceptual model that conforms to plume dynamics, the observed H_2O–δD trends, and constraints from previous studies on the 2009 eruption of Redoubt (Figure 4). The highest temperatures in the plume are immediately adjacent to the vent and as the plume rises, it cools through two primary mechanisms. Both efficient heat transfer from pyroclasts to entrained air and continued decompression causes gas

expansion and cooling (e.g., Sparks, 1986). Provided there is a sufficient mass flux, the plume convectively rises and cools until it reaches neutral buoyancy in the atmosphere where it spreads out laterally (e.g., Mastin, Guffanti, et al., 2009; Woods & Bursik, 1991).

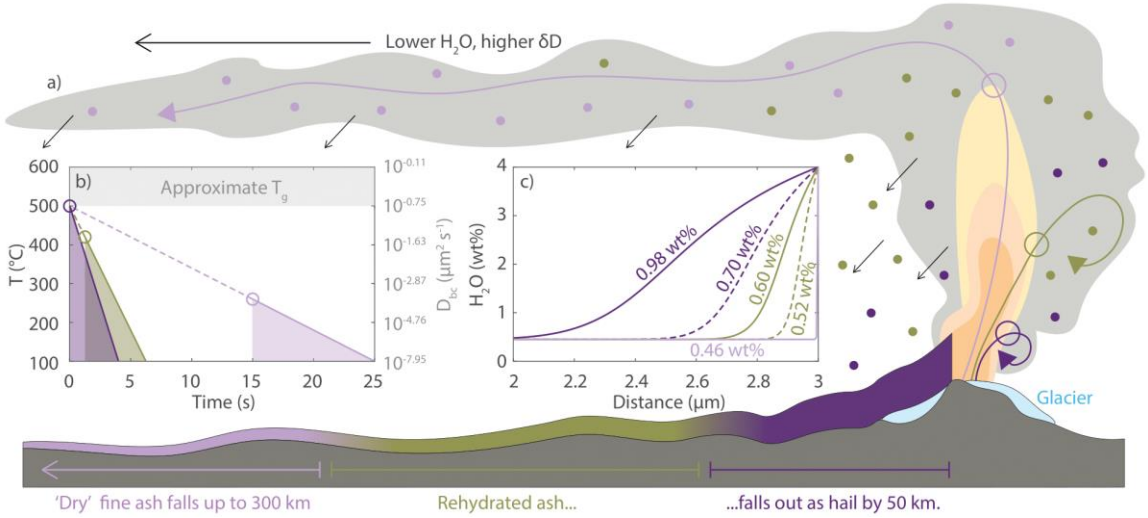

Figure 4. (a) Conceptual model tracking the temperature-time path and timing of interaction with atmospheric moisture of three hypothetical ash particles (open circles), resulting in (b) three different quench rates of 80°C/s, 64°C/s, and 16°C/s, and (c) diffusion profiles. The fastest quenching pyroclasts gain the highest amount of H_2O because they encounter H_2O at the highest temperatures. D_{bc} in (b) is the minimum D_{H2O} at the glass boundary for the corresponding T. Values on the curves (c) indicate volume integrated total water content after hydration: 0.46, 0.52, 0.70 wt% for the D_{H2O} of Zhang and Behrens (2000) and 0.46, 0.60, and 0.98 wt% adding the D_{H2O} coefficient of Hudak and Bindeman (2020).

Rapid glass hydration can occur in this framework where rapid air entrainment brings hot pyroclasts into contact with local atmospheric H_2O. Both the temperature-time path and the timing of interaction with atmospheric water vary depending on the lateral location of an ash particle within the plume (Figure 4a). A particle located close to the margins of the plume will interact with the atmosphere earlier and hydration will start at a temperature close to T_g. However, this ash will remain hot for a relatively short amount of time (Figure 4b; dark purple and green curves). Conversely, ash particles located towards the center of the plume quench more slowly but will encounter atmospheric moisture much higher in the atmosphere and at lower temperatures, where D_{H2O} is orders of magnitude lower than at T_g (Figure 4b, light purple curve). The location and temperature at which ash first interacts with H_2O in each model is indicated by an open

circle (Figures 4a and 4b). Pyroclasts subjected to the three quench rates in Figure 4b corresponding to different trajectories in the plume (Figure 4a) result in significantly different diffusion profiles in a 3 μm thick bubble wall (Figure 4c) and final glass H_2O contents. While diffusion profiles are all less than a micron, they produce bulk H_2O concentrations of up to 0.98 wt%. Dashed profiles use the D_{H2O} expression of Zhang and Behrens (2000) as a minimum and solid profiles use a maximum D_{H2O} coefficient of 4 (Hudak and Bindeman, 2020). Pyroclasts that quickly encounter atmospheric moisture are more likely to be hydrated than more slowly quenched materials that are colder when they first encounter atmospheric moisture.

Syn-eruptive hydration is thus most likely to occur near the vent in marginal regions of the plume (Figure 4a), where hot ash quickly interacts with the atmosphere. Moisture to drive hydration may have come from one or more sources near the vent. While the presence of ice during eruption is not essential to cause glass hydration, the role of the glacier cannot be entirely discounted. Precursory activity in the months leading up to the eruptive sequence melted more than 3×10^6 m^3 of ice (Waythomas et al., 2013), which could have largely saturated the summit of the edifice. Fumarolic activity in the summit crater could have contributed to a local, high humidity environment near the vent ideal for rapid moisture entrainment. Alternatively, convective eddies in the plume could facilitate glass hydration provided ash encounters entrained atmospheric moisture at sufficiently high temperatures, close to the glass transition.

Tephra that has avoided hydration (light purple dots in Figure 4a) must have remained at least partially spatially and/or temporally segregated from more extensively hydrated material (dark purple and green dots) and the wetter portions of the plume. Three-dimensional numerical models of developing plumes show a hot jet region of the plume that interacts minimally with marginal vortices that entrain air (e.g., Suzuki and Koyaguchi, 2013, 2015). Such a jet region protected from interactions with atmospheric moisture may allow tephra to cool down sufficiently, so hydration is limited once it encounters moisture, relatively high in the atmosphere.

Finally, the notable formation and deposition of accretionary lapilli during the 2009 Redoubt eruption (Wallace et al., 2013; Van Eaton et al., 2015), can help explain the spatial pattern of hydrated tephra deposits. Radar measurements of the plume

associated with event 5 tracked the development of accretionary lapilli rather than plume height. Although the plume continued to rise and expand, radar measurements of the plume top began to decrease (Mastin et al., 2013), matching 3D models of accretionary lapilli formation and removal. Liquid H_2O films condensed on individual particles and facilitated accretion during particle-particle collision, sometimes in multiple episodes (e.g., Brown et al., 2010, 2012; Gilbert & Lane, 1994), as inferred from internal structures of frozen Redoubt lapilli (Van Eaton et al., 2015). Moister, marginal regions of the plume where glass hydration is favored would also favor the formation of accretionary lapilli and may explain the preferential removal of hydrated tephra closer to the vent. The fine tephra, invisible to the radar, that remained suspended in the plume at high altitudes (Van Eaton et al., 2015; Mastin et al., 2013) comprise the non-hydrated samples deposited at distances >50 km in our data set (Figure 3, 4a).

5. Conclusions

Proximal ash from the explosive sequence of the 2009 Redoubt eruption records syn-eruptive hydration by local meteoric water, a novel observation in a subaerial eruption. More hydrated glass (high H_2O and low δD) is deposited in proximal locations <50 km from the vent, whereas more distal ash is poorly rehydrated. For volcanic glass to hydrate on the timescales of an eruption and quenching, ash must encounter H_2O at high temperatures near T_g. We propose a model in which ash hydrates from entrained air along the plume margins but close to the vent where the plume remains at relatively high temperatures. These ash particles are preferentially deposited near the vent while the drier central jet core of the plume remain effectively isolated from entrained atmospheric moisture until the jet region has expanded and cooled to well below the temperature required for rapid hydration.

The H_2O–δD composition of recently erupted volcanic ash has applications to both paleoclimate and to understanding moisture entrainment in plumes. Meteoric water δD compositions can vary dramatically over short distances, such as over and across a mountain range (e.g., Kendall & Coplen, 2001; Poage & Chamberlain, 2001). Therefore, partial syn-eruptive glass hydration may not accurately record the δD of local waters where ash is deposited. Instead, we propose that H_2O–δD data obtained on fresh airfall

tephra may be the first geochemical data that can compare possible time-temperature histories to particle trajectories in numerical models of eruptive plumes and to tephra dispersion models.

6. Bridge

Chapter V shows that H_2O can diffuse into glass on very short timescales at near magmatic temperatures. Therefore, the utility of H_2O in volcanic glass is not limited to magmatic applications in melt inclusions or low temperature paleoclimate reconstruction. Chapters IV and V demonstrate that H_2O, δD, and $\delta^{18}O$ in silicic volcanic glasses can inform a host of processes from eruption and transport to emplacement and cooling. Chapter VI works to develop rhyolitic and basaltic glass standards for bulk analysis by TC/EA to address a pressing and growing need for community H_2O and δD standards in hydrous volcanic glasses.

CHAPTER VI

RHYOLITIC AND BASALTIC GLASS REFERENCE MATERIALS FOR TC/EA ANALYSIS: INVESTIGATION OF WATER EXTRACTION AND D/H RATIOS

This chapter is in preparation for *Chemical Geology*. Ilya N. Bindeman and Michael R. Hudak will submit Chapter VI as joint first authors with coequal contributions. Co-authors include James P. Palandri, Haiping Qi, Rastislav Milovský, Richard L. Hervig, and Michael R. Perfit.

1. Introduction

Hydrogen isotopic investigations of hydrous phases are relevant to many fields of geosciences as water-rock interactions are ubiquitous in sedimentary, igneous, metamorphic, and planetary processes; and therefore, efforts to measure H isotope ratios in rocks accurately and precisely has long been a focus of mass spectrometry development. Conventional analysis of waters or extraction of hydrogen from solid phases for isotope analysis employed native metals like uranium (Bigeleisen et al., 1952; Friedman and Smith, 1958; Godfrey, 1962) and zinc (Friedman, 1953; Coleman et al., 1982; Kendall and Coplen, 1985; Vennemann and O'Neil, 1993) heated to high temperatures. These off-line methods reduced liberated H_2O and converted it into H_2 for measurement before introducing the gas into the mass spectrometer. Additional off-line methods varied slightly and liberated H_2, converted it to H_2O with CuO, and reduced it back to H_2 with hot U (Suzuoki and Epstein, 1976).

Development of online continuous flow isotope ratio mass spectroscopy (CF-IRMS) accelerated experimentation of novel, high temperature conversion (HTC) methods as it greatly reduced the necessary mass of material (e.g., Begley and Scrimgeour, 1996; Burgoyne and Hayes, 1998; Hilkert et al., 1999; Midwood and McGaw, 1999; Sharp et al., 2001). Techniques using chromium (Gehre et al., 1996; Greenwood, 2018), nickel (Begley and Scrimgeour, 1996), manganese (Tanweer and

Han, 1996), and Pt-Mg (Halas and Jasińska, 1996) have been published, but the implementation of glassy carbon as a catalyst for the pyrolysis reaction of $C + H_2O \rightarrow H_2 + CO$, first used for oxygen and nitrogen in organic materials (Brand et al., 1994), also proved to be useful for hydrogen isotope analyses. The Thermo TC/EA has since become the primary analytical method for hydrous minerals (Sharp et al., 2001). This has led to the routine analysis of micas and amphiboles (Deering et al., 2012; Underwood et al., 2012; Underwood et al., 2013), clays (e.g. Bauer & Vennemann, 2014), volcanic glass (e.g. Martin et al., 2017; Seligman et al., 2016), epidote (Pope et al., 2009; Pope et al., 2014; Zakharov et al., 2019; Zakharov and Bindeman, 2019), apatite (Greenwood, 2018), and even nominally anhydrous minerals like garnet and pyroxene (Gong et al., 2007; Gong et al., 2010).

With multiple techniques applied to such a diversity of materials, we note however that there is significant disagreement between different labs in terms of standardization. A method for sealing water standards in Ag tubing (Qi et al., 2010) has enabled an inexpensive and widely available common standardization. While a community need remains for phase-specific interlaboratory reference materials (RMs) to minimize matrix effects in the measurement of these phases, efforts are being made to address this issue. For instance, the recent development of USGS biotite and muscovite RMs on the VSMOW-SLAP scale involved interlaboratory comparisons of several different HTC techniques and mass spectrometers (Qi et al., 2017).

This paper aims to develop two RMs for H_2O and hydrogen isotopes in well-studied natural silicic and mafic volcanic glasses for a growing variety of volcanological and paleoclimate applications. Hydrogen isotopes in volcanic glasses were first measured in the 1950s by Friedman and Smith (1958), but it would take 25 years before these types of measurements were put into context (Taylor et al., 1983). This pioneering work investigated volcanic degassing styles in rhyolitic eruption and was quickly followed by additional research on natural samples and experimental studies (Newman et al., 1988; Anderson and Fink, 1989; Dobson et al., 1989; Taylor, 1991). Non-unique solutions to degassing pathways limited further development until the advent of CF-IRMS. Applications of hydrogen isotopes to volcanic degassing has been revisited and expanded

to interrogate more specific conduit processes (Rust et al., 2004; Mandeville et al., 2009; Castro et al., 2014; Giachetti et al., 2020; Walter and Castro, 2020).

Not all H_2O in volcanic glass is residual magmatic water, however. It has long been recognized that H_2O in the environment slowly diffuses back into glass through time (Friedman and Smith, 1960). Because hydrogen isotope compositions of precipitation are strongly temperature dependent (Craig, 1961; Dansgaard, 1964), volcanic glasses hydrated by meteoric waters were proposed as a paleoclimate proxy (Friedman et al., 1993a; Friedman et al., 1993b). While this requires some effort to disentangle magmatic and meteoric H_2O contribution from the glass (Seligman et al., 2016), sample preparation (Dettinger and Quade, 2015) and TC/EA methods (Martin et al., 2017) have been developed and widely implemented (Mulch et al., 2008; Cassel et al., 2012; Cassel et al., 2014; Hudak and Bindeman, 2018; Seligman et al., 2018; Jackson et al., 2019).

Here we report results from the investigation of two glasses, a basalt and a rhyolite, that span several years of efforts in the University of Oregon Stable Isotope Lab employing a TC/EA configured to a Thermo MAT-253 and confirmed in two other labs: USGS Reston Stable Isotope Lab and Slovak Academy of Sciences.

1.1 Selection of reference materials

Well studied and abundant natural, crystal poor basalt (UOB) and rhyolite (UOR) glasses that were rapidly quenched at high pressures were chosen to develop H_2O and δD glass standards. The UOB standard is an enriched mid-ocean ridge basalt (EMORB) pillow glass from an off-axis pillow mound on the northern East Pacific Rise (Goss et al., 2010; Waters et al., 2011; Perfit et al., 2012) that was quenched at a depth of 2660 m; sufficient to retain its magmatic H_2O of 0.36 wt% measured in this work. Several other EMORB samples were also collected from this pillow mound with the submersible Alvin during dive 2489 and yield H_2O concentration ~0.4 wt% (le Roux et al., 2006). The UOR standard is the rhyolite from the IDDP-1 drill core at Krafla volcano in northern Iceland. Quenched *in-situ*, UOR has been extensively studied and found to have the expected H_2O content and OH/H_2O ratios for the depth at which it was encountered, ~2100 km (Elders et al., 2011; Zierenberg et al., 2013). Subsets of the most typical bulk material were separated to create a more homogenous material. Homogeneous natural glasses with

elevated H_2O contents are advantageous because they can be processed in large quantities that can be widely and commonly used across laboratories. Chemical analyses of UOR and UOB RMs are provided in Table 1.

Standard	Sample	Location description	Depth (m)	Lat (N)	Long (W)	SiO_2 (wt%)	TiO_2 (wt%)
UOB	ALV 2489-3*	EPR off-axis pillow mound	2664	9.52920	-104.2258	50.97	1.83
UOR	JB2**	IDDP-1 drillhole, Iceland	2100	65.71587	-16.76453	74.93	0.42

Standard	Al_2O_3 (wt%)	FeO (wt%)	MnO (wt%)	MgO (wt%)	CaO (wt%)	Na_2O (wt%)	K_2O (wt%)	P_2O_5 (wt%)	Total (wt%)
UOB	14.48	10.71	0.20	6.69	11.03	3.26	0.41	0.28	99.87
UOR	11.86	2.96	0.07	0.35	1.65	4.00	2.72	0.07	99.20

Table 1. Chemical analysis of reference materials. *Analysis from Waters et al. (2011), depth is below sea level. **Analysis reported in Zierenberg et al. (2013), depth refers to rhyolite intersection by IDDP-1 drillhole.

2. Methods

Large chunks of pristine rhyolite and basaltic glasses were separated under the microscope from felsite inclusions in rhyolites, and orange Mn-oxide coatings on basalts. Samples were sonicated in deionized water several times for 15-30 min to remove dust and particulates. Basaltic glasses were additionally soaked in 60:40 mix 1.4 N HCl and 30% H_2O_2 to remove Mn oxides and hydroxides as well as organics and carbonates (Goss et al. 2010). All samples were sonicated in deionized water and ethanol to remove dust and particulates, and sieved into size fractions for analysis.

The general methods and conditions for HTC analyses are broadly similar between the three laboratories and differences are described in Table 2. Thermo high temperature conversion elemental analyzers (TC/EA) are interfaced with a Thermo MAT-253 isotope ratio mass spectrometer (IRMS) at the University of Oregon (UOSIL), Slovak Academy of Sciences (SAS), and with a Thermo Delta+ XP IRMS at USGS Reston. Approximately 1-31 mg of sample are loaded into Ag capsules depending on the

expected H_2O content of the glass and the IRMS. In most cases, samples are dried for at least 1 hour in a vacuum drying oven. Furnaces in all three HTC systems are operated at ≥1400°C and gas chromatographs are operated at ≤90°C. Samples are dropped from autosamplers into a graphite crucible in the furnace where they are melted to liberate H_2O and reduced by glassy carbon to convert it to H_2 gas for analysis. Helium carrier gas flushes extracted volatiles to the IRMS at rates of 80-120 mL/min. Reference waters and micas in Ag tubing are run concurrently for H_2O and δD calibration.

Laboratory	Instruments	Methods and Conditions
University of Oregon Stable Isotope Laboratory (UOSIL)	Thermo-Finnigan TC/EA with Thermo MAT-253 IRMS and Thermo ConFlo IV gas introduction system	80 mL/min He flow; glassy carbon tube and chips; 1450°C furnace; 70°C gas chromatograph (GC) after 300°C overnight bake out
USGS Reston Stable Isotope Laboratory (RSIL)	Thermo-Finnigan TC/EA with Thermo Scientific Delta Plus XP IRMS and Thermo ConFlo IV gas introduction system	110 mL/min H flow; glassy carbon tube and chips; 1450°C furnace; 90°C GC
Slovak Academy of Sciences Laboratory of Isotope and Organic Geochemistry (SAS)	Thermo Scientific Flash 2000 HT Plus with Thermo MAT-253 IRMS and Thermo ConFlo IV gas introduction system	80 mL/min He flow; glassy carbon tube; 1400°C furnace; 90°C GC

Table 2. Instruments, methods, and experimental conditions for HTC analyses.

For spot analysis of H_2O and δD, glasses were analyzed by secondary ion mass spectrometry (SIMS) with a Cameca IMS 6f at Arizona State University. We used a primary beam of Cs^+ accelerated to +10,000 volts while the sample was held at −5000V. The 1–2 nA beam was rastered over a 30 x 30 μm^2 area on the sample, but the transfer optics and field aperture were selected to allow only secondary ions derived from a 15 μm diameter circular area in the center of the sputtered crater into the mass spectrometer. Prior to collecting ion intensities, the sample was "pre-sputtered" with a 35 x 35 μm^2 raster for 4 minutes. Secondary ions with −5000 ± 20 eV total energy were allowed into the mass spectrometer and were detected by peak switching the magnetic field. A typical analysis involved counting $^1H^-$ for 1s and $^2H^-$ for 10s in each cycle, repeating for ~100

cycles. At the end of the 100 cycles, the secondary ion magnetic field was shifted to detect the matrix species $^{16}O^-$ for 5s. Hydrogen and deuterium ions were detected using an electron multiplier, but the $^{16}O^-$ signal was measured using a Faraday cup. Parameters are summarized in Table 3.

Primary beam:	Cs+
Primary source potential:	10 kV
Primary current:	1-2 nA
Primary raster (pre-sputter):	35 x 35 µm2
Primary raster (analysis):	30 x 30 µm2
Secondary ion beam:	negative
Sample potential:	-5 kV
Secondary ion energy:	-5000±20 eV
Analyzed diameter:	15 µm
Electron Multiplier:	1H-, 2H-
Faraday cup:	16O-

Table 3. Analytical conditions for $^2H^-/^1H^-$ and H^-/O^- in glass on the Cameca 6f SIMS at Arizona State University.

3. Results

3.1 Isotopic and chemical homogeneity

Isotopic homogeneity and chemical homogeneity were evaluated in bulk glasses at the University of Oregon Stable Isotope Laboratory (UOSIL) by TC/EA and on small spatial scales within and between individual glass particles at the Arizona State University Secondary Ion Mass Spectrometry (SIMS) Laboratory on a Cameca IMS 6f SIMS. All samples were analyzed for bulk H_2O and δD at UOSIL. Each individual analysis is plotted in Figure 1a and means with 1 s.d. are plotted in Figure 1b. New TC/EA analyses of UOR and UOB and standards are given in Tables 4 and 5, respectively.

3.1.1 Reference materials and standardization

The choice of reference materials can have significant effects on calibrating samples. Ideally, matrix-matched RMs should be used when possible. Mica standards biotite (USGS57, δD = −91.5‰ VSMOW) and muscovite (USGS58, δD = −28.4‰) RMs are used (Qi et al., 2017) along with a low δD internal laboratory standard used at the

University of Oregon Butte Montana muscovite, (BUD, −151‰ δD) for all UOR and UOB data. In three analytical sessions for UOB and one for UOR, a combination of water RMs from the USGS welded in Ag cups were analyzed as well, including VSMOW, GISP, USGS47, and W62001 (Table 6). Calibration of the glasses with mica RMs produced neither consistently higher nor lower δD values than water RMs (Figure 2). However, in no analytical run did the mica and water RMs yield glass δD results >5‰ different. All results are here on reported normalized to the USGS mica standards.

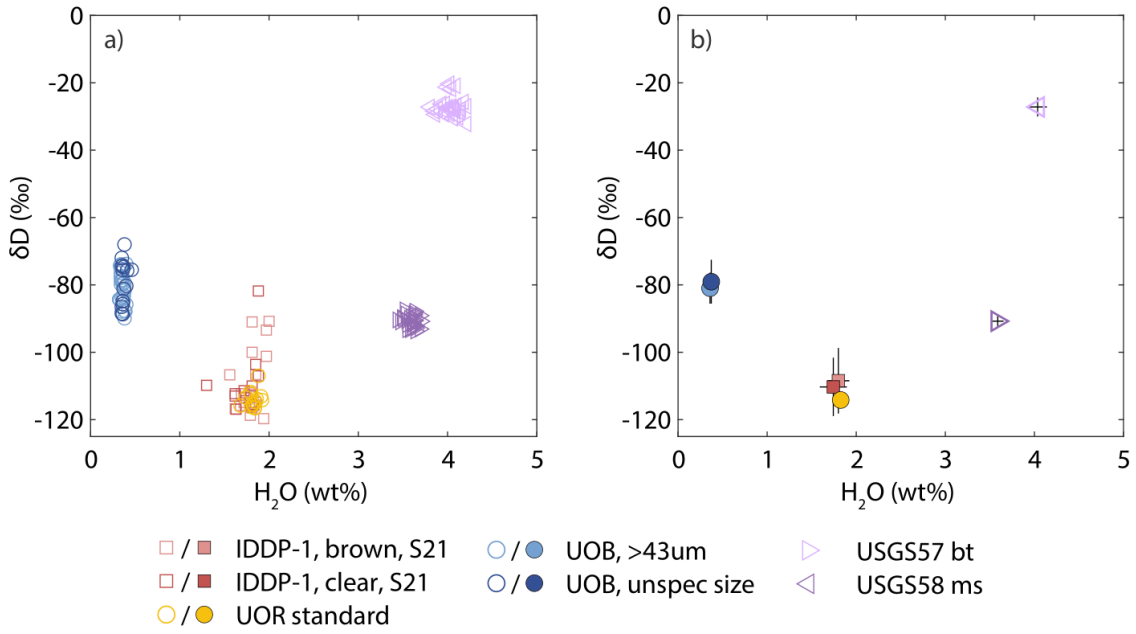

Figure 1. H_2O and δD data analyzed by TC/EA in the UO Stable Isotope Lab. (a) All data for UOR and UOB with data for USGS mica standards. Brown and clear UOR glasses published in Saubin et al. (2021) were selected to capture the full heterogeneity of IDDP-1 drill cuttings and rhyolite petrology. The material for the UOR standard is more homogenous. UOB is subdivided into analyses 1) with record size fractions in excess of 43 um and 2) unspecified size fractions. Less than 43 um size fractions are excluded because they absorb water and may contain alteration products. (b) Means with 1 s.d. We note the UOR δD reproducibility, and UOR and UOB H_2O reproducibility is as good or better than mica standards.

3.1.2 Homogeneity of H_2O_t and δD in bulk materials by TC/EA

Analyses of rhyolitic glass, UOR, by TC/EA at UOSIL are highly reproducible for both H_2O and δD with 1.83 ± 0.06 wt% (1 s.d.) and −114.2 ± 2.4‰ (1 s.d. n = 16), respectively. These results are comparable to the error on the mica standards of Qi et al. (2017), for both H_2O and δD (Table 7; Figure 1b). The UOR results represent study of a

carefully selected split of IDDP-1 rhyolitic. The analyses of this split are compared to the previously published data collected at UOSIL for a time series of the IDDP-1 rhyolite drill core "eruption", which included the full diversity of glass textures and colors (Saubin et al., 2021). The earlier results are within error of the above-stated H_2O content of UOR glass that represent just one time interval for eruption and include the predominant brown glass but show slightly lower mean H_2O and larger errors for both clear (1.74 ± 0.15 wt%, 1 s.d.) and brown, opaque glasses (1.80 ± 0.12 wt%, 1 s.d.). The δD values from Saubin et al. (2021) are higher and also have higher standard deviations: −110.3 ± 8.7‰ (1 s.d.) for clear glasses and −108.4 ± 9.7‰ (1 s.d.) for brown glasses. However, because their study additionally investigated how H_2O varied with glass color and vesicularity, larger variation in measured values is expected relative to the UOR split that has been carefully selected for homogeneity.

Date of analysis	H_2O (wt%)	δD (permille)	Size fraction (um)	Mass (mg)	RM type
2/4/2015	1.84	-116.6			
2/4/2015	1.84	-116.5			
2/4/2015	1.92	-114.2			
2/4/2015	1.91	-113.1			
2/4/2015	1.88	-107.0			
2/4/2015	1.80	-112.4			
2/4/2015	1.80	-116.2			
2/4/2015	1.82	-115.4			
5/21/2010	1.68	-115.8			
5/21/2010	1.85	-114.8			
10/18/2019	1.74	-113.4 -109.4	125-250	2.124	micas VSMOW, USGS47
10/18/2019	1.82	-115.5 -111.5	125-250	1.926	micas VSMOW, USGS47
10/18/2019	1.79	-111.8 -107.9	50-125	1.811	micas VSMOW, USGS47
10/18/2019	1.82	-115.6 -111.6	50-125	2.027	micas VSMOW, USGS47
10/18/2019	1.84	-114.5 -110.5	<50	2.278	micas VSMOW, USGS47
10/18/2019	1.86	-113.8 -109.8	<50	2.141	micas VSMOW, USGS47

Table 4. UOR H_2O and δD results from UOSIL.

Date of analysis	H_2O (wt%)	δD (permille)	Size fraction (um)	Mass (mg)	RM type
8/16/2018	0.40	-85.8	43-63	4.330	micas
8/16/2018	0.38	-89.9	43-63	6.290	micas
8/16/2018	0.35	-83.7	50-250	4.77	micas
8/16/2018	0.39	-87.8	50-250	5.33	micas
8/16/2018	0.37	-84.8	50-250	11.25	micas
8/16/2018	0.40	-73.8	50-250	0.968	micas
6/19/2020	0.65	-90.4	<43	5.181	micas
6/19/2020	0.63	-92.4	<43	5.581	micas
6/19/2020	0.65	-92.2	<43	5.345	micas
6/19/2020	0.38	-80.6	43-63	4.878	micas
6/19/2020	0.38	-87.7	43-63	6.850	micas
6/19/2020	0.38	-79.3	43-63	5.852	micas
6/19/2020	0.37	-83.0	63-105	7.022	micas
6/19/2020	0.36	-78.7	63-105	5.000	micas
6/19/2020	0.38	-81.7	63-105	6.018	micas
6/19/2020	0.34	-76.4	105-250	3.931	micas
6/19/2020	0.34	-79.8	105-250	5.933	micas
6/19/2020	0.34	-77.5	105-250	8.008	micas
6/19/2020	0.34	-77.7	105-250	10.022	micas
6/19/2020	0.34	-78.7	105-250	12.095	micas
6/19/2020	0.35	-78.6	105-250	9.920	micas
6/19/2020	0.34	-73.9	105-250	7.902	micas
6/19/2020	0.33	-74.3	105-250	5.986	micas
6/19/2020	0.34	-75.2	105-250	3.989	micas
10/13/2020	0.33	-84.4 -79.4	105-250	8.03	micas VSMOW, USGS47
10/13/2020	0.32	-84.3 -79.4	105-250	7.67	micas VSMOW, USGS47
10/13/2020	0.35	-87.9 -82.7	250-500	6.25	micas VSMOW, USGS47
10/13/2020	0.36	-79.7 -75.1	250-300	5.65	micas VSMOW, USGS47
10/13/2020	0.91	-100.2 -95.2	<43	5.82	micas VSMOW, USGS47
10/13/2020	1.12	-95.7 -90.9	<43	5.65	micas VSMOW, USGS47
10/13/2020	0.36	-77.6 -74.1	43-63	6.40	micas VSMOW, USGS47
10/13/2020	0.37	-83.4 -79.5	43-63	7.53	micas VSMOW, USGS47

Table 5. UOB H_2O and δD results from UOSIL.

Chapter VI, Section 3.1.2.

Table 5, continued.

6/11/2018	0.35	-88.5	6.048	micas
6/11/2018	0.38	-68.0	6.061	micas
6/11/2018	0.41	-75.7	6.073	micas
7/5/2018	0.37	-81.2	7.40	micas
		-83.1		W62001, USGS47, GISP
7/5/2018	0.37	-74.7	4.11	micas
		-76.6		W62001, USGS47, GISP
7/5/2018	0.35	-86.5	5.85	micas
		-88.5		W62001, USGS47, GISP
7/5/2018	0.36	-84.8	6.018	micas
		-86.8		W62001, USGS47, GISP
7/5/2018	0.36	-85.7	6.016	micas
		-87.7		W62001, USGS47, GISP
7/5/2018	0.36	-88.7	6.069	micas
		-90.7		W62001, USGS47, GISP
9/13/2018	0.40	-80.3	6.10	micas*
9/13/2018	0.46	-75.5	4.10	micas*
10/18/2019	0.36	-75.6	6.052	micas
		-74.3		VSMOW, USGS47
10/18/2019	0.35	-72.0	5.905	micas
		-70.9		VSMOW, USGS47
10/18/2019	0.35	-74.4	6.143	micas
		-73.2		VSMOW, USGS47
10/24/2019	0.36	-74.2	5.943	micas

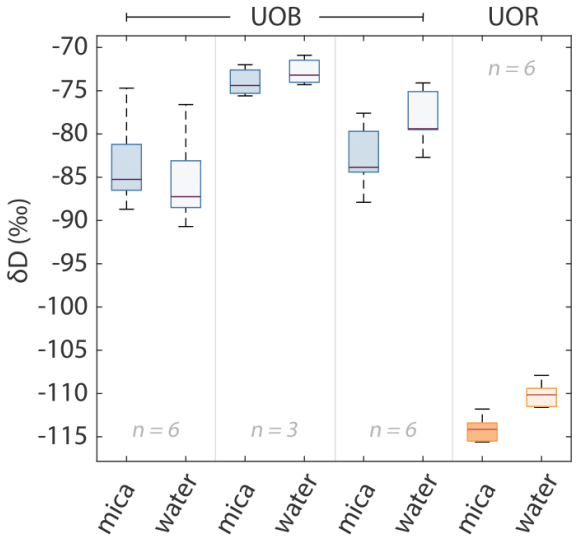

Figure 2. The δD results for UOB (blue) and UOR (orange) calibrated with mica and water reference materials.

USGS57 biotite		USGS58 muscovite	
H_2O (wt%)	δD (‰)	H_2O (wt%)	δD (‰)
3.52	-87.4	4.02	-20.3
3.64	-92.8	4.04	-21.8
3.61	-91.7	3.99	-21.3
3.64	-93.7	4.09	-20.9
3.53	-88.6	4.10	-26.7
3.64	-92.2	4.12	-30.2
3.63	-87.8	4.08	-28.3
3.60	-91.4	4.14	-28.8
3.54	-90.6	4.04	-27.6
3.69	-89.1	4.04	-27.1
3.58	-93.3	3.96	-29.3
3.55	-91.8	4.09	-29.6
3.62	-89.5	4.02	-29.2
3.60	-91.3	4.00	-27.3
3.60	-91.8	4.07	-27.5
3.63	-90.6	3.97	-26.3
3.55	-93.3	3.86	-29.4
3.47	-91.0	3.89	-27.8
3.50	-90.1	3.85	-28.4
3.49	-89.7	3.93	-26.3
3.57	-89.9	3.80	-27.2
3.44	-90.4	4.21	-27.0
3.69	-93.1	4.21	-32.2
3.61	-90.8	4.18	-25.7
3.70	-90.8	4.15	-27.9
3.59	-89.4	4.06	-30.5
3.62	-88.4	4.00	-27.8
3.62	-88.9	4.07	-27.9
3.60	-92.7	4.07	-28.0

Table 6. Values of mica reference materials used for calibration of UOR and UOB.

Water contents in UOB are highly reproducible, with means of 0.37 ± 0.03 wt% H_2O (1 s.d) with and δD of −79.1 ± 6.5‰ (1 s.d., n = 42). However, the scatter in δD increases when different size fractions are considered. Size fractions greater than 43 μm yielded H_2O and δD means of 0.36 ± 0.02 wt% (1 s.d.) and −81.0 ± 4.6‰ (1 s.d.), respectively (Figure 1b). Analyses of UOB without a noted size fraction return values within error of

the >43 μm aliquots. With roughly one tenth the H_2O content of the mica standards (Qi et al., 2017), UOB is expected to have comparable errors for H_2O than the mica standards but comparatively higher δD error as was observed with our previous investigation of silicate glasses (Martin et al., 2017). Both standards have a 1 s.d. of 0.10 wt% H_2O and 2.8‰ δD or less (Table 6; Figure 1b), which is within the analytical error reported for H_2O for this method at UOSIL, but not for δD (Martin et al., 2017). That study focused on analyzing rhyolitic glasses and may not reflect the true variance for basaltic compositions analyzed by TC/EA.

Glass	Laboratory	n =	Median H_2O (wt%)	Mean H_2O (wt%)	1 s.d. (wt%)	Median δD (‰)	Mean δD (‰)	1 s.d. (‰)
UOR	UOSIL	16	1.83	1.83	0.06	-114.7	-114.2	2.4
IDDP-1 (clear)*	UOSIL	15	1.80	1.74	0.15	-112.3	-100.3	8.7
IDDP-1 (brown)*	UOSIL	16	1.80	1.80	0.12	-112.9	-108.4	9.7
UOR	SAS	4	1.81	1.79	0.04	-114.4	-114.1	1.8
UOR	RSIL	11	1.89	1.88	0.02	-118.1	-117.9	1.2
Recommended UOR			***1.83***			***-115.4***		
UOB (no size data)	UOSIL	15	0.36	0.36	0.02	-79.8	-81.0	4.6
UOB (>43 um)	UOSIL	27	0.36	0.37	0.03	-75.7	-79.1	6.5
UOB	SAS	11	0.36	0.37	0.02	-85.4	-84.7	4.2
UOB	RISL	7	0.40	0.40	0.04	-88.7	-88.9	2.0
Recommended UOB			***0.37***			***-83.4***		

Table 7. Means and standard deviations of UOR and UOB in each laboratory.

We evaluated the effect of grain size and mass on H_2O and δD in UOB and found that there was no clear trend in samples with size fractions entirely above 43 μm in diameter (Figure 3) or with mass (Figure 4). Fine sieve fractions of glasses (containing any fraction <43 μm, including the finest particles hereon referred to as powders) have a median H_2O nearly twice that of the mean in all other samples (Figure 3a). The size fraction of 105-250 μm has the lowest median H_2O of 0.34 wt%. The highest medians were 0.38 wt% H_2O for the 43-63 μm and 50-250 μm size fractions. Similarly, δD is notably lower in powders than in any other size fraction with a median of −92.4‰ (Figure 3b). The slightly higher H_2O size fractions, 43-63 μm and 50-250 μm, have lower medians of −82.0‰ and −84.2‰, respectively, compared to the lower H_2O 105-250 μm size fraction (−77.7‰). The δD variability that gives rise to lower reproducibility is not a simple function of particle size or aliquot mass (Figure 4). Instead, the subtle correlation

between H_2O and δD in size fractions in Figure 3 suggests that a separate process: secondary hydration/adsorbtion of concentration of secondary alteration products, controls their covariation.

3.1.3 Homogeneity of H_2O_t and δD within glass fragments by SIMS

Fifteen analyses were made on 5 different glass chips of UOR. The average D/H ion ratio was normalized to the absolute D/H ratio based on bulk analyses showing δD of −114‰, which translates to D/H of 1.381 x 10^{-4}, assuming D/H of VSMOW is 1.5576 x 10^{-4} (Figure 5a; Hagemann et al., 1970). Four of the five chips of glass showed similar values for this normalized D/H ratio, which are referred to as α, of ~1.164 and are shown with 2 SE. The 5th chip yielded a uniformly lower α value. However, because we obtained the $^{16}O^-$ intensity, we can compare the H/O ion ratio (which should be related to the H_2O content as the O contents are unlikely to vary significantly) to the isotope ratio (Figure 5b). Evidently, four of the measurements sampled H-rich, relatively D/H-poor areas of the glass, concentrated in one of the 5 chips. The three spots on the 5th chip constitute three of the four high H/O ratios and low alpha analyses.

Why would H-rich areas result in low D/H ratios? Does this represent zoning or an artifact of the analytical technique? It is possible that as the H count rate increases, uncertainty in the dead-time correction increases, leading to an under-correction and high D/H. However, the last analysis of the 5th chip of glass was conducted using a reduced primary beam current to decrease the count rate for hydrogen. Because this analysis produced a D/H ratio identical (within error) to the other 2 analyses on this chip, it might be suggested that this particular piece of glass actually contains areas high in H_2O and correspondingly, approximately 30‰ lower in δD than most areas of the glass. Hauri et al. (2002) showed that the D/H ion ratio of glasses sputtered (using very similar conditions as here) by Cs^+ ions gradually decreased with increasing H_2O content. The effect was not as large as indicated here, but the effect of increasing H_2O on decreasing D/H ion ratios was independently observed on the ASU Cameca 6f by Befus et al. (2020), lending support to the idea that the change in the SIMS D/H ion ratio is the result of a small change in the H_2O content of one glass fragment.

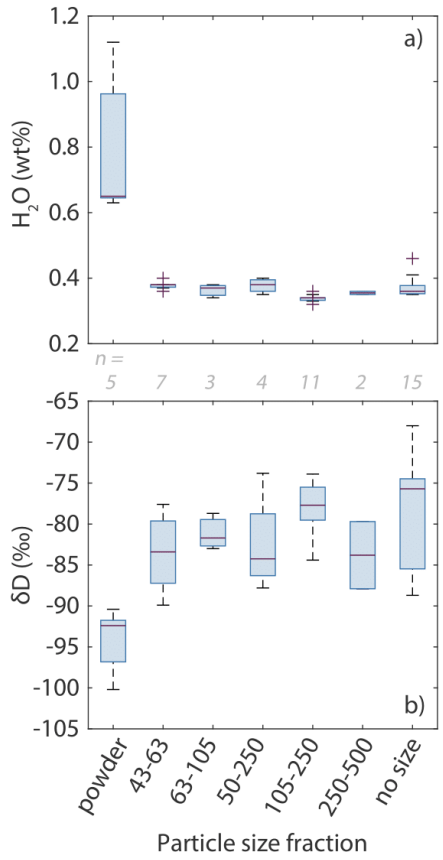

Figure 3. Box and whisker plot as a function of size fraction for UOB H_2O (a) and δD results (b) analyzed at UO. Boxes represent the 25th to 75th percentiles and the central bar represents the median. Whiskers extend to minimum and maximum values not considered outliers, which are shown as crosses. Powders yield high H_2O and low δD, but size fractions greater than 43 μm largely provide consistent results.

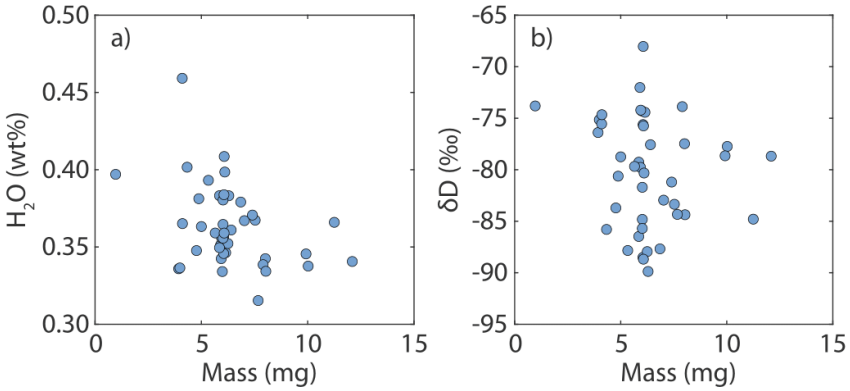

Figure 4. H_2O (a) and δD (b) as a function of the mass of the analyze aliquot of UOB. No systematic trends are observed.

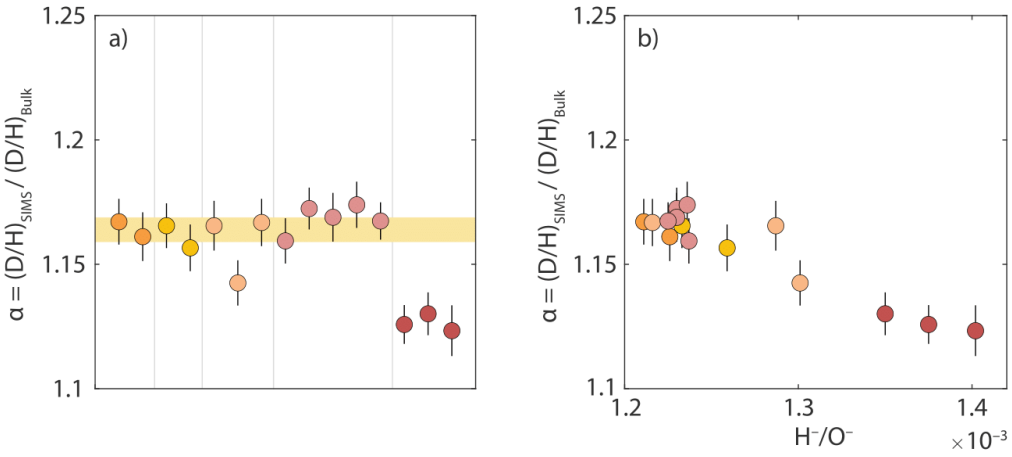

Figure 5. Raw SIMS D/H measurements divided by mean D/H ratios (α) from UOSIL TC/EA results (a) and H^-/O^- ratios vs. SIMS α values for UOR (b). Each color represents a separate chip of the standard. The yellow bar in (a) is 2 SE for the first 4 UOR chips. Measurements with higher H/O trend towards lower δD values. Error bars show 2 SE of measurement.

Overall, however, the UOR sample is quite homogeneous in its hydrogen isotopic content. Taking the 12 measurements with H/O < 1.3 x 10^{-3}, the average value of alpha is 1.1639 ±0.0048 (2 SE). This suggests a 4‰ (2s.d.) uncertainty in selected measurements of the SIMS ion ratio. If all 15 spot analyses on the 5 chips are used, the 2s.d. variation is 8‰. However, calculating standard errors may not be appropriate here, considering the local variation in measured D/H and low numbers of measurements. The homogeneity of the H_2O content is reflected by the variation in the SIMS H/O ion ratio. There are two possible ways of determining this ratio. We can average the H count rate over the ~30 minute-long analysis and divide by the oxygen ion count rate determined at the end of the analysis or only use the average H count rate over the last ten cycles prior to collecting the O signal. That latter value shows an uncertainty of 2.5%, two standard errors.

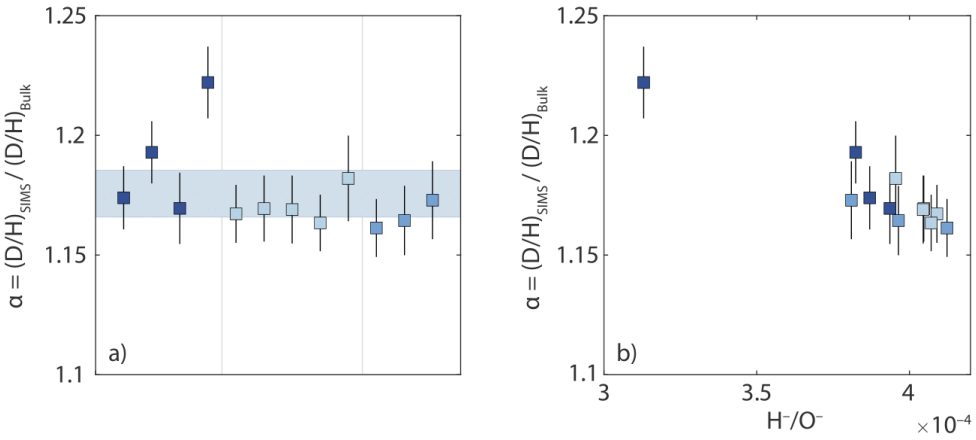

Figure 6. Raw SIMS D/H measurements divided by mean D/H ratios (α) from UOSIL TC/EA results (a) and H^-/O^- ratios vs. SIMS α values for UOB (b). Error bars show 2 SE of measurement. One outlier with lower H_2O has a higher δD. The blue bar in (b) is 2 SE for all UOB data.

Twelve analyses were made on 3 UOB chips of glass. Figure 6a below is similar to Figure 6a except the SIMS D/H ion ratios were normalized to the absolute D/H ratio of the basaltic glass (δD = −80.3 ± 12.2 ‰, or D/H = 1.4338 x 10^{-4}). One of the analyses on the 1st chip is clearly different than the others. In this case, the hydrogen ion signal was significantly lower (by <20%) than the average of the other eleven analyses (Figure 6a). The average SIMS value of α, excluding the outlier, is 1.1714 ± 0.0055 (or ±4.7 ‰, 2 SE). Of course, standard errors are not particularly informative when *n* is so small (11). Except for the one outlier, the H_2O content of the basaltic glass (expressed as the $H^-/^{16}O^-$ ion ratio) is homogeneous (Figure 6b). The average of 11 analyses is 3.98 ± 0.11 x 10^{-4}, 1 s.d. (~3% scatter).

3.2 Interlaboratory comparison

Having evaluated reproducibility for H_2O and δD in UOR and UOB glasses at UOSIL, we compare these results to two sets of data collected by TC/EA in two other laboratories. At the Earth Sciences Institute at the Slovak Academy of Sciences (SAS), like at UOSIL, measurements were made on a Thermo MAT 253 IRMS. Measurements at RSIL were conducted on a Thermo Fisher Delta V Plus IRMS. Results are given in Table 8.

Reference Material	Laboratory	H_2O (wt%)	δD (‰)
UOR	RSIL	1.88	-118.1
UOR	RSIL	1.86	-116.8
UOR	RSIL	1.84	-116.7
UOR	RSIL	1.89	-116.8
UOR	RSIL	1.89	-118.4
UOR	RSIL	1.89	-120.1
UOR	RSIL	1.89	-118.5
UOR	RSIL	1.89	-115.9
UOR	RSIL	1.89	-118.4
UOR	RSIL	1.89	-119.2
UOR	RSIL	1.89	-117.7
UOR	SAS	1.74	-113.4
UOR	SAS	1.82	-115.5
UOR	SAS	1.79	-111.8
UOR	SAS	1.82	-115.6
UOB	RSIL	0.44	-89.5
UOB	RSIL	0.41	-88.7
UOB	RSIL	0.45	-92.5
UOB	RSIL	0.45	-88.2
UOB	RSIL	0.36	-87.4
UOB	RSIL	0.36	-90.0
UOB	RSIL	0.36	-86.2
UOB	SAS	0.35	-86.1
UOB	SAS	0.36	-84.5
UOB	SAS	0.36	-85.4
UOB	SAS	0.36	-88.4
UOB	SAS	0.35	-83.8
UOB	SAS	0.39	-87.9
UOB	SAS	0.37	-84.9
UOB	SAS	0.37	-80.9
UOB	SAS	0.36	-74.3
UOB	SAS	0.40	-85.9
UOB	SAS	0.38	-89.9

Table 8. Results of UOR and UOB analyses from RSIL and SAS.

Each measurement made on UOR or UOB is shown with a bar depicting the mean plus or minus 1 s.d. in Figure 7. For UOB, the mean values are 0.37 ± 0.02 wt% H_2O (1 s.d.) from SAS and 0.44 ± 0.02 wt% H_2O (1 s.d.) from RSIL (Figure 7a). The mean H_2O concentration in UOR from SAS and RSIL are 1.79 ± 0.04 wt% (1 s.d.) and 1.86 ± 0.02 wt% (1 s.d.), respectively (Figure 7b). Histograms showing each analysis from the three laboratories are non-Gaussian for H_2O in both glasses. In both cases, the RSIL

measurements yield relatively high H_2O compared to UOSIL and SAS measurements. Total H_2O measurements from UOSIL and SAS are within error for both UOR and UOB, while measurements conducted at RSIL are only within error of UOSIL for UOR.

Similarly, the δD measurements from UOSIL and SAS are within error for both UOR and UOB, but RSIL data are only with error of UOSIL for UOR (Figure 7b). The mean δD values for UOB, they are −84.7 ± 4.2‰ (1 s.d.) and −89.7 ± 1.9‰ (1 s.d.) δD, respectively (Figure 7a). For UOR are −114.1 ± 1.8‰ (1 s.d.) and −117.2 ± 0.7‰ (1 s.d.) from SAS and RSIL, respectively. Means with 1 s.d. for data from each lab and the IDDP-1 data from Saubin et al. (2021) are shown in Figure 7b. Again, histograms show the distribution of δD from each lab. At first glance, UOB appear bimodal, but analytical sessions with more analyses exert greater influence on the histogram. A second histogram shows mean δD values from analytical session that ran at least UOB in triplicate. This histogram reveals that UOB has a very wide Gaussian distribution for δD, as do the raw δD data for UOR.

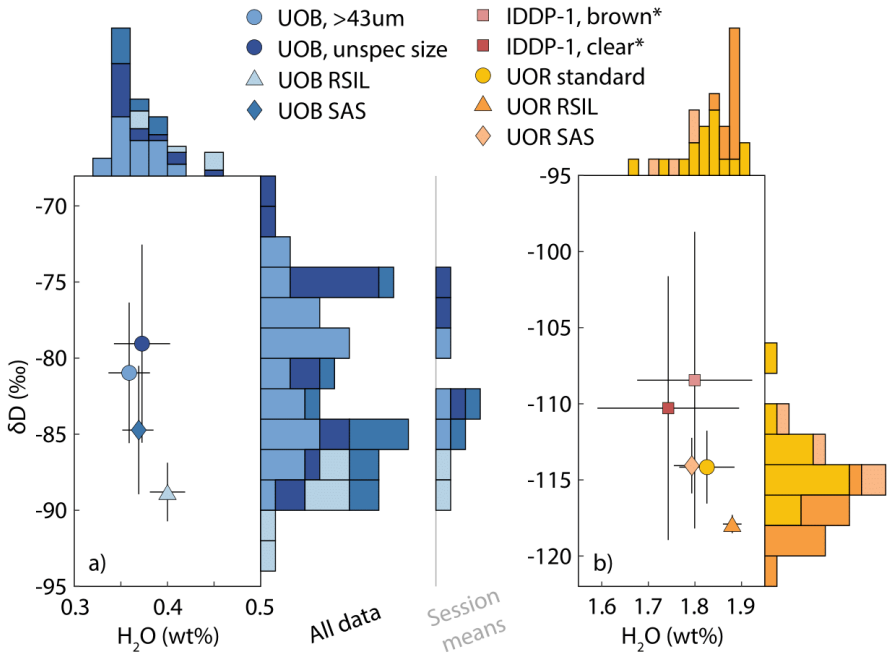

Figure 7. H_2O and δ^2H data for UOB (a) and UOR (b) analyzed by TC/EA at UO, RSIL, and SAS are shown with *IDDP-1 measurements from Saubin et al. (2021). See Fig. 1 caption for detail on samples. Reston data were normalized with H_2O reference materials rather than micas. Histograms show all H_2O and δ^2H data from each of the 3 laboratories. Mean δ^2H values from each analytical session where UOB was run in triplicate are shown as an additional histogram to remove bias towards analytical sessions with many more analyses.

4. Discussion

Investigation of these two natural glasses – UOR and UOB – over 10 years at the University of Oregon and additionally in 2 other labs has resulted in overlapping values that make these two materials appropriate as standards. Table 7 presents preferred values of δD and H_2O that are recommended for use. These preferred values are means of the H_2O and δD means from each laboratory.

There is a weak negative correlation between H_2O and δD over the whole suite of UOB samples, anchored by the high H_2O powders. We consider two hypotheses that could influence this trend. First, high H_2O measurements in powdered samples are likely affected by adsorbed moisture on particle surfaces, despite overnight drying. Mixing calculations between glass (0.34 wt% H_2O and −77.7‰ δD) and condensed moisture in Eugene, Oregon (approximated with a δD = −107‰) trend in the direction of the powders. Although we dry samples in hot vacuum oven overnight prior to analysis, previous research on smectites demonstrates that minor atmospheric exposure results in rapid water re-adsorbtion during transfer between the vacuum oven and the sample carousel purged with He (citation). It is also possible that the finest fraction concentrates hydration and secondary alteration products, including smectite and other clays, of this glass, which was emplaced in submarine conditions and resided under water for many thousands of years before collection by the Alvin submersible apparatus. The δD composition of condensate/alteration product is likely variable through time, so Figure 8a simply illustrates that adsorbed moisture is a sufficient possible explanation for low δD values in the high H_2O powders. However, it fails to explain the variance in compositions at H_2O below 0.4 wt% (Figure 8a).

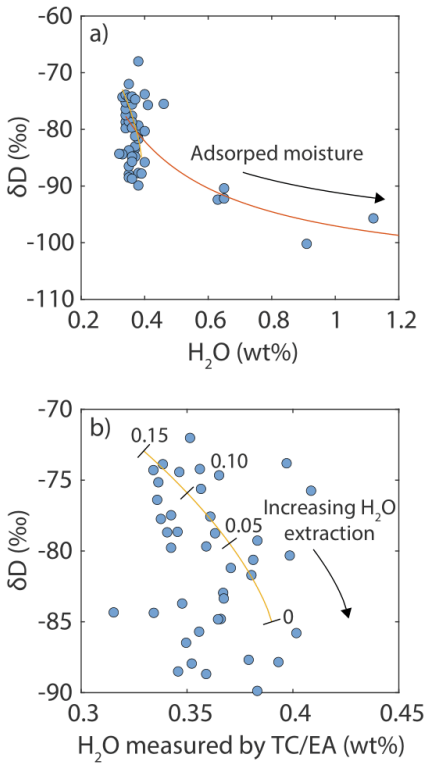

Figure 8. Two models to explain the variation in H_2O and δD results for UOB. High H_2O and low δD results can be explained by adsorbtion of atmospheric moisture (a), but do not explain the variations in δD over a narrow range of H_2O content (~0.34-0.38 wt%). The second model treats the liberated and measured gases from the samples as accumulated magmatic vapor in an open system (b). This model shows that small residual fractions (tick marks) of H_2O in a melt can have large isotopic effects, especially for low H_2O samples, such as UOB.

Alternatively, incomplete extraction of H_2O from the glass in the TC/EA could cause subtle differences in δD composition. Although our FTIR investigation detected no remaining water in extracted glasses suggesting complete extraction, we nonetheless entertain this possibility as the melted glass samples remained at high temperature during the entire analytical session. The H_2O and δD measured by TC/EA are treated as the accumulated magmatic H_2O in an open system using a modified basalt degassing model of de Hoog et al. (2009). Liberated H_2O is rapidly converted to H_2 by a pyrolysis reaction catalyzed by glassy carbon in the reaction chamber and at the front of the GC column before being carried away to CONFLOW open split in front of the the mass spectrometer by He gas. The extraction process likely a of batch nature, so it may be approximated as an open system. If the modeled glass has an initial H_2O of 0.39 wt% and δD of −85‰

because incompletely extracted H_2O (incomplete degassing) from basaltic melts will yield lower H_2O and higher δD values, where a majority of the analyses fall (Figure 8b). The accumulated magmatic vapor curve is calculated using the Rayleigh equation:

$$\bar{R}_v = R_{lo}\left(\frac{f^{\alpha}-1}{f-1}\right). \qquad (Eq.1)$$

In Eq. 1, $\bar{R}_v$ is the D/H ratio of the accumulated vapor, R_{lo} is the initial D/H ratio of the melt prior to degassing (converted from −85‰ using the VSMOW reference frame), f is the fraction of H_2O remaining in the melt, and α is the equilibrium fractionation factor between the vapor and the melt, which is given as a constant, 1.040 (~40‰; Dobson et al., 1989; De Hoog et al., 2009). Calculations are shown for 0.33 and 0.39 wt% of extracted H_2O, which represents fractions of H_2O remaining in the basaltic melt of 15% or less. These H_2O contents have a δD range from −73‰ to −85‰, roughly equivalent to ±1 s.d. in the δD data (Tables 4-5, Figure 1b). Notably, the extraction of the last 5% (or 0.02 wt%) of the H_2O from the melt to a vapor that is measure by the mass spectrometer results in a change of 5‰ δD. While the accumulated magmatic vapor curve cannot explain all the data, it illustrates that incomplete H_2O extraction in low H_2O sample with high liquidus temperature may result in a greater spread in δD, even over narrow H_2O ranges and especially the final few percent of H_2O degassing. However, Fourier transform infrared spectroscopy (FTIR) of a pure UOB melt collected under normal TC/EA operating conditions yielded undetectable H_2O_t at the 3500 cm^{-1} peak (<0.01 wt% in a 840 μm doubly polished wafer; Text E1, Figures E1-E2). Similarly, there is no correlation in between systematic extension of the $^2H_2^+$ and $^3H_2^+$ analytical peak tails and resulting δD (Text E2). For these reasons, incomplete H_2O extraction from melts may be excluded as a source of analytical uncertainty.

A harder to quantify, yet more compelling explanation for the variability in δD of the UOB basaltic glass is its high Fe content. A comparison of high Fe and low Fe biotite (Qi et al., 2014) yielded different hydrogen yields by HTC-CF-IRMS (Qi et al., 2014). These authors posited that high Fe (high metal) concentrations resulted in the formation of metal hydrides, lowering the yield of H_2. The efficiency of H_2 production is likely correlated with the availability of reactive glassy carbon. The TC/EA column is not

repacked with new carbon granules after every analytical session, so H_2 production may not be consistent between runs for high Fe samples.

Formation of iron hydrides and hydroxides (FeH, FeOH, etc.) may retain hydrogen from the melt during the extraction, contributing to the higher background in subsequent analyses. Seligman and Bindeman (2019) experimented with dropping FeO, Fe_3O_4, and Fe-silicates together with water standards in Ag caps to monitor CO gas extracted (i.e. they estimated influence on Fe oxides on degassing of O gas during reduction of Fe). They observed that Fe silicates (even Fe^{3+} bearing) produce little or no O_2 gas, while Fe oxides yielded some O gas. No iron was observed in a metal form during SEM investigation of extracted glass of variable composition as is expected for C-CO buffer conditions in the furnace.

5. Conclusions

Proposed reference materials for rhyolitic (UOR) and basaltic glasses (UOB) are largely homogeneous on small spatial scales and have reproducible bulk H_2O composition within and between laboratories. Hydrogen isotope compositions are also reproducible, although UOB has larger variations in measure δD likely owing to its high Fe content which may cause the formation of iron oxyhydroxides during reduction. We recommend the following values for these reference glasses:

UOR rhyolitic glass:

H_2O = 1.83 wt%, and δD = −115.4‰.

UOB basaltic glass:

H_2O = 0.37 wt%, and δD = −83.4‰.

CHAPTER VII

DISSERTATION SUMMARY

In this dissertation, my research focused on understanding the behavior of water and its constituent isotopes in silicic volcanic glass over a previously understudied range of hydrothermal temperatures between 175°C and 375°C. Experimental approaches underpin two physical parameters of how this work can be applied to diverse geologic processes in natural systems. Specifically, I constrain H_2O diffusivity and solubility in glass and the partitioning of H and O isotopes between glass and a water vapor or fluid phase between 175°C and 375°C and use the insights to study the role of H_2O in cooling ignimbrites and volcanic eruptive plumes.

Chapter II forms the cornerstone of this work by demonstrating glass hydration can and should proceed at high temperatures below the glass transition when H_2O vapor is readily available. Most importantly, I demonstrate that H_2O solubility is >3 wt% over the entire temperature range, significantly higher than predicted for the experimental *P-T* conditions by magmatic H_2O solubility models. This is critical because D_{H2O} is H_2O concentration dependent and, in contrast to the solubility, closely approximates extrapolations from magmatic temperatures to the experimental temperature range. This high solubility facilitates diffusion into silicic glass on relatively short timescales. Oxygen isotopes affirm that the main diffusing species – molecular water, H_2O_m – at high and low temperatures is also the main diffusing species at hydrothermal conditions. The novel $\delta^{18}O_{wig}$ measurements (water in glass) combined with traditional bulk glass $\delta^{18}O$ analyses show that O bound in H_2O species isotopically equilibrates with O in the silicate structure of the glass rapidly and that the partitioning is temperature-dependent.

Chapter III presents on equilibrium and kinetic hydrogen isotope fractionation in the experimental glasses during their hydration. Water speciation data from the 375°C experiments add to a growing body of literature that show H_2O_m can repartition into OH^- below glass transition temperature, T_g. A 1D finite difference isotope diffusion-reaction model was used to evaluate the how this reaction affects the measured bulk glass δD compositions. I showed that the δD of the boundary condition of the model controls the bulk δD rather than any effects from H_2O speciation within the glass structure.

Equilibrium D/H glass-H_2O vapor fractionations below at least 250°C do not deviate my more than ~5‰ from low temperature D/H fractionations and are within the range of magmatic D/H fractionations.

Chapter IV applies the isotopic insights of Chapters II and III to the transient hydrothermal systems and their prominent features – the pinnacles, in cooling ignimbrites at Crater Lake and in the Valley of Ten Thousand Smokes. Oxygen isotopes suggest a glass hydration temperature of ~100°C near the boiling point of water at atmospheric pressures. The H_2O– δD composition of glasses in these low temperature fumarolic features indicate that high H_2O contents can be achieved on the timescales of cooling and that this water faithfully records local meteoric water compositions as water percolates into the ignimbrite during cooling in the days to years after emplacement.

In Chapter V, I build upon these short hydration timescales in hot volcanic deposits by evaluating if glass hydration can occur during an eruption. The H_2O– δD composition of tephras from the 2009 eruption of Redoubt volcano clearly show evidence for hydration rather than degassing on very short timescales of seconds to minutes. Using the experimentally constrained H_2O solubility and D_{H2O} from Chapter II, I demonstrate that high temperature interaction of H_2O vapor and glass is more important than the quench rate for syn-eruptive glass hydration. This result suggests that glass hydration occurs in the margins of the plume that interact with atmosphere immediately after exiting the vent. Ash in the hotter core of the plume that remain separate from entrained atmospheric moisture until they are too cold to rehydrate on the timescales of eruption and is deposited more distally than hydrated ash.

Finally, in Chapter VI, I present the results of work to develop two new H_2O and δD glass reference materials for bulk analysis that are helpful to the rest of the community who are interested in topics of D/H ratio and H_2O in silicic and basaltic glass.

APPENDICES

APPENDIX A
CHAPTER II SUPPLEMENTARY INFORMATION AND FIGURES

Appendix A is broken into three sections following the organization of the Appendices published with this manuscript in *Geochimica et Cosmochimica Acta*. The first section, Appendix A1, characterizes the geochemical compositions of the natural glasses used in hydration experiments in Chapters II and III. Electron microprobe data for three initial glass compositions are either taken from previous studies (see Tables and main text) or were collected by EPMA in the CAMCOR facilities at the University of Oregon. Post-experimental analyses show no change to the glass compositions normalized to 100% between the hydrated rims and the initial compositions retained in the unhydrated cores of LSR glass. Surface coatings of secondary phases are present on some longer duration experimental glasses at high temperatures. These are negligible in volume but may affect subsequent glass hydration dynamics (discussed in Chapter III).

The second section of Appendix A provides all of the experimental conditions as well as the δD and $\delta^{18}O$ compositions of the experimental H_2O and the resulting water vapor in the experiments. At all temperatures (except at 375C where H_2O occurs as a single phase), the δD and $\delta^{18}O$ of H_2O vapor can be determined from the volume of the experimental apparatus and data in steam tables are used to determine the fraction of H_2O as vapor. The vapor-liquid fractionations of Horita and Wesolowski (1994) is then applied to calculate the δD and $\delta^{18}O$ of the water vapor. These data also apply to Chapter III in which the same experimental run products are discussed.

The final section has two additional miscellaneous tables that are not presented in the main text of the published manuscript.

Appendix A1. Glass compositions and experimental conditions

Chapter II, Table A1.1. Major element compositions of initial experimental glass as measured by EMPA. *Perlite data is previously reported in the Supplementary Data of Bindeman and Lowenstern (2016). The HSR is 08-YS-07 in Loewen et al. (2017) and the perlites are YS-13 in Bindeman and Lowenstern (2016). Totals reported here do not include Cl, F, or H_2O. Yellowstone glasses use an an Fe^{3+}/Fe_{total} of 0.15 for an fO_2 of NNO - 0.7 (hotspot). LSR calculations use an fO_2 of NNO + 0.8 and an Fe^{3+}/Fe_{total} of 0.25 (arcs).

Material	Location	n =		SiO_2 (wt.%)	TiO_2 (wt.%)	Al_2O_3 (wt.%)	FeO_t (wt.%)	MgO (wt.%)	CaO (wt.%)	Na_2O (wt.%)	K_2O (wt.%)	Total (wt.%)	NBO/T
Perlite cores*	Nez Perce flow, Yellowstone, WY, USA	20	Mean	76.02		12.00	0.94	0.01	0.36	3.07	5.55	97.96	0.011
			1σ	0.53		0.10	0.21	0.02	0.11	0.19	0.12	0.62	0.009
Perlite skins*	Nez Perce flow, Yellowstone, WY, USA	20	Mean	73.79		11.67	0.88	0.00	0.33	2.96	5.28	95.16	0.007
			1σ	0.54		0.12	0.21	0.00	0.03	0.11	0.08	0.45	0.005
HSR	Summit Lake flow, Yellowstone, WY, USA	25	Mean	75.11	0.12	12.01	1.19	0.02	0.41	4.13	5.39	98.38	0.035
			1σ	0.51	0.02	0.18	0.10	0.01	0.02	0.22	0.03	0.81	0.004
LSR initial	Newberry volcano, OR, USA	27	Mean	71.45	0.22	14.34	2.03	0.17	0.89	6.95	4.20	100.25	0.070
			1σ	0.72	0.01	0.18	0.15	0.02	0.07	0.38	0.07	0.82	0.008
LSR cores	Newberry volcano, OR, USA	49	Mean	72.28	0.23	14.21	1.99	0.16	0.85	6.68	4.24	100.63	0.064
			1σ	0.54	0.01	0.27	0.11	0.01	0.02	0.54	0.07	0.85	0.012
LSR rims	Newberry volcano, OR, USA (T = 175°C; t = 935 hours)	7	Mean	71.70	0.24	13.88	1.90	0.16	0.83	6.52	4.30	99.54	
			1σ	0.41	0.01	0.42	0.17	0.01	0.01	0.44	0.07	0.76	
LSR rims	Newberry volcano, OR, USA (T = 175°C; t = 3000 hours)	8	Mean	70.25	0.22	13.72	1.93	0.17	0.85	5.62	4.09	96.86	
			1σ	0.72	0.01	0.17	0.14	0.01	0.01	0.31	0.05	0.82	
LSR rims	Newberry volcano, OR, USA (T = 175°C; t = 6000 hours)	7	Mean	70.83	0.21	13.91	1.89	0.16	0.83	6.27	4.09	98.20	
			1σ	0.52	0.02	0.10	0.15	0.01	0.01	0.34	0.07	0.65	
LSR rims	Newberry volcano, OR, USA (T = 225°C; t = 240 hours)	8	Mean	70.78	0.22	13.67	1.91	0.16	0.84	6.25	4.00	97.82	
			1σ	0.67	0.02	0.32	0.07	0.01	0.05	0.42	0.11	0.86	
LSR rims	Newberry volcano, OR, USA (T = 225°C; t = 423 hours)	8	Mean	69.30	0.22	14.11	2.04	0.16	0.82	6.33	3.99	96.98	
			1σ	0.47	0.01	0.09	0.11	0.01	0.01	0.48	0.10	0.70	
LSR rims	Newberry volcano, OR, USA (T = 225°C; t = 1010 hours)	9	Mean	70.68	0.22	13.93	1.97	0.17	0.83	6.53	4.12	98.44	
			1σ	0.38	0.02	0.19	0.07	0.01	0.01	0.38	0.09	0.00	

Chapter II, Table A1.2. Major element compositions of low silica rhyolite (LSR) glass starting material as measured by EMPA. NBO/T ratios are calculated with normalized major element compositions. Totals reported here do not include H_2O. Calculation of NBO/T for LSR use an fO_2 of NNO + 0.8 and an Fe^{3+}/Fe_{total} of 0.25 appropriate for arc settings.

	SiO_2 (wt.%)	TiO_2 (wt.%)	Al_2O_3 (wt.%)	FeO (wt.%)	MgO (wt.%)	CaO (wt.%)	Na_2O (wt.%)	K_2O (wt.%)	Total (wt.%)	H_2O (wt.% by diff.)	NBO/T
Low silica rhyolite glass (LSR), Big Obsidian flow, Newberry volcano, OR, USA	72.36	0.21	14.16	1.79	0.17	0.87	7.75	4.17	101.49	-1.04	0.085
	71.89	0.24	14.50	2.22	0.18	0.88	7.25	4.26	101.43	-0.88	0.076
	71.43	0.20	14.63	2.19	0.17	0.87	7.64	4.17	101.30	-0.75	0.081
	71.85	0.24	14.30	1.95	0.25	1.24	7.31	4.04	101.17	-0.69	0.086
	72.55	0.22	14.31	1.92	0.18	0.87	6.83	4.18	101.06	-0.58	0.065
	71.81	0.24	14.52	2.30	0.17	0.88	6.88	4.20	100.98	-0.41	0.068
	72.54	0.22	14.08	2.14	0.17	0.87	6.73	4.22	100.97	-0.43	0.069
	71.45	0.22	14.51	2.29	0.17	0.87	7.00	4.26	100.77	-0.20	0.071
	71.56	0.22	14.37	2.08	0.17	0.87	7.26	4.21	100.74	-0.22	0.076
	71.66	0.22	14.58	2.16	0.17	0.88	6.89	4.10	100.66	-0.12	0.064
	72.70	0.21	14.10	1.70	0.16	0.85	6.64	4.29	100.66	-0.23	0.062
	70.91	0.23	14.46	1.92	0.17	0.87	7.74	4.26	100.57	-0.09	0.085
	71.01	0.22	14.56	2.13	0.17	0.87	7.16	4.25	100.37	0.16	0.073
	71.64	0.23	14.26	2.02	0.16	0.86	7.05	4.12	100.35	0.16	0.071
	71.97	0.21	14.27	2.06	0.17	0.86	6.50	4.29	100.32	0.19	0.061
	71.95	0.21	14.34	1.91	0.17	0.87	6.67	4.16	100.29	0.19	0.061
	71.94	0.21	14.14	1.92	0.17	0.87	6.71	4.14	100.10	0.38	0.064
	70.83	0.24	14.36	2.17	0.17	0.87	7.06	4.14	99.84	0.70	0.072
	71.15	0.21	14.29	2.05	0.17	0.88	6.91	4.13	99.79	0.72	0.069
	71.68	0.20	14.06	2.06	0.17	0.87	6.44	4.25	99.72	0.79	0.063
	71.50	0.25	14.47	1.98	0.17	0.87	6.16	4.23	99.63	0.87	0.050
	70.69	0.23	14.29	2.00	0.18	0.87	6.94	4.29	99.47	1.03	0.071
	71.04	0.23	14.14	2.06	0.17	0.88	6.84	4.11	99.46	1.06	0.069
	70.29	0.24	14.71	1.81	0.17	0.87	7.10	4.23	99.40	1.05	0.066
	70.19	0.25	14.25	2.03	0.17	0.88	6.88	4.27	98.91	1.60	0.071
	70.39	0.23	14.31	2.05	0.17	0.88	6.56	4.21	98.80	1.71	0.062
	70.25	0.24	14.20	1.85	0.18	0.86	6.82	4.11	98.51	1.95	0.066
Mean	*71.45*	*0.22*	*14.34*	*1.52*	*0.17*	*0.89*	*6.95*	*4.20*	*100.25*	*-0.25*	*0.070*
1σ	0.72	0.01	0.18	0.11	0.02	0.07	0.38	0.07	0.82		0.008

Chapter II, Table A1.3. Major element compositions of low silica rhyolite (LSR) glass rims and cores after hydration as measured by EMPA. NBO/T ratios are calculated with normalized major element compositions. Totals reported here do not include H_2O. Calculation of NBO/T for LSR use an fO_2 of NNO + 0.8 and an Fe^{3+}/Fe_{total} of 0.25 appropriate for arc settings.

Rim or core	T (°C)	Duration (hours)	SiO_2 (wt.%)	TiO_2 (wt.%)	Al_2O_3 (wt.%)	FeO (wt.%)	MgO (wt.%)	CaO (wt.%)	Na_2O (wt.%)	K_2O (wt.%)	Total (wt.%)	H_2O (wt.% by diff.)	NBO/T
Rim	225	240	70.56	0.21	13.75	1.97	0.16	0.83	6.56	4.06	98.09	1.91	
Rim	225	240	71.04	0.19	13.88	1.92	0.16	0.95	6.70	3.73	98.55	1.45	
Rim	225	240	70.52	0.21	13.34	1.88	0.16	0.84	5.80	3.99	96.75	3.25	
Rim	225	240	70.85	0.23	13.73	1.78	0.17	0.82	6.40	3.99	97.96	2.04	
Rim	225	240	71.24	0.22	13.88	2.02	0.17	0.82	6.76	4.03	99.13	0.87	
Rim	225	240	69.59	0.24	13.51	1.92	0.17	0.83	5.69	4.02	95.95	4.05	
Rim	225	240	71.90	0.23	14.10	1.93	0.15	0.82	5.89	4.10	99.13	0.87	
Rim	225	240	70.54	0.23	13.14	1.89	0.15	0.80	6.18	4.05	96.96	3.04	
Mean (n=8)			*70.78*	*0.22*	*13.67*	*1.91*	*0.16*	*0.84*	*6.25*	*4.00*	*97.82*	*2.18*	
1σ			0.67	0.02	0.32	0.07	0.01	0.05	0.42	0.11	1.16		
Core	225	240	73.34	0.27	14.20	1.97	0.16	0.84	5.75	4.14	100.67	-0.67	0.042
Core	225	240	72.17	0.24	14.23	1.93	0.18	0.94	7.13	4.27	101.11	-1.11	0.076
Core	225	240	72.07	0.24	14.78	2.12	0.15	0.82	6.83	4.20	101.21	-1.21	0.059
Core	225	240	72.53	0.25	14.26	1.86	0.16	0.84	5.70	4.29	99.88	0.12	0.041
Core	225	240	72.00	0.22	14.67	1.90	0.16	0.84	7.03	4.10	100.91	-0.91	0.062
Core	225	240	73.06	0.21	14.00	2.23	0.16	0.84	6.54	4.39	101.45	-1.45	0.068
Core	225	240	72.17	0.23	14.26	2.08	0.15	0.83	7.08	4.23	101.04	-1.04	0.072
Core	225	240	72.30	0.26	14.15	2.00	0.15	0.84	6.58	4.11	100.39	-0.39	0.060
Core	225	240	72.40	0.25	14.03	1.96	0.16	0.85	5.87	4.16	99.68	0.32	0.047
Core	225	240	72.01	0.25	13.85	2.12	0.16	0.84	6.74	4.20	100.17	-0.17	0.071
Mean (n=10)			*72.40*	*0.24*	*14.24*	*2.02*	*0.16*	*0.85*	*6.53*	*4.21*	*100.65*	*-0.65*	*0.060*
1σ			0.46	0.02	0.29	0.12	0.01	0.03	0.56	0.09	0.60		0.013

Table A1.3 continued.

Rim or core	T (°C)	Duration (hours)	SiO_2 (wt.%)	TiO_2 (wt.%)	Al_2O_3 (wt.%)	FeO (wt.%)	MgO (wt.%)	CaO (wt.%)	Na_2O (wt.%)	K_2O (wt.%)	Total (wt.%)	H_2O (wt.% by diff.)	NBO/T
Rim	225	423	68.51	0.21	14.05	2.18	0.17	0.82	6.25	3.90	96.08	3.92	
Rim	225	423	69.28	0.22	14.00	1.92	0.15	0.80	6.90	3.95	97.21	2.79	
Rim	225	423	68.95	0.23	14.23	1.97	0.17	0.82	6.80	3.86	97.02	2.98	
Rim	225	423	70.05	0.20	14.08	2.09	0.17	0.82	6.01	3.90	97.33	2.67	
Rim	225	423	69.10	0.24	14.27	2.02	0.17	0.83	6.67	4.13	97.43	2.57	
Rim	225	423	69.72	0.20	14.13	2.08	0.16	0.82	6.56	4.03	97.70	2.30	
Rim	225	423	69.44	0.24	14.07	2.19	0.16	0.82	5.53	4.04	96.49	3.51	
Rim	225	423	69.38	0.22	14.05	1.89	0.16	0.83	5.96	4.10	96.59	3.41	
Mean (n=8)			*69.30*	*0.22*	*14.11*	*2.04*	*0.16*	*0.82*	*6.33*	*3.99*	*96.98*	*3.02*	
1σ			0.47	0.01	0.09	0.11	0.01	0.01	0.48	0.10	0.55		
Core	225	423	71.26	0.24	14.27	2.15	0.16	0.84	7.66	4.24	100.80	-0.80	0.086
Core	225	423	71.44	0.23	14.52	2.21	0.16	0.85	7.62	4.21	101.25	-1.25	0.083
Core	225	423	71.91	0.25	14.78	1.86	0.16	0.86	5.12	4.27	99.21	0.79	0.022
Core	225	423	71.35	0.22	14.10	1.90	0.17	0.86	6.16	4.18	98.93	1.07	0.053
Core	225	423	72.05	0.23	14.20	1.90	0.16	0.86	6.74	4.19	100.33	-0.33	0.064
Core	225	423	71.85	0.22	14.27	1.94	0.14	0.83	6.56	4.20	100.02	-0.02	0.059
Core	225	423	71.33	0.22	14.46	1.97	0.17	0.90	6.16	4.22	99.41	0.59	0.050
Core	225	423	72.17	0.23	14.53	1.99	0.16	0.85	7.03	4.14	101.10	-1.10	0.066
Mean (n=8)			*71.67*	*0.23*	*14.39*	*1.99*	*0.16*	*0.86*	*6.63*	*4.21*	*100.13*	*-0.13*	*0.060*
1σ			0.36	0.01	0.22	0.13	0.01	0.02	0.84	0.04	0.89		0.020

Table A1.3 continued.

Rim or core	T (°C)	Duration (hours)	SiO_2 (wt.%)	TiO_2 (wt.%)	Al_2O_3 (wt.%)	FeO (wt.%)	MgO (wt.%)	CaO (wt.%)	Na_2O (wt.%)	K_2O (wt.%)	Total (wt.%)	H_2O (wt.% by diff.)	NBO/T
Rim	225	1010	70.29	0.19	13.95	1.87	0.17	0.84	5.88	4.00	97.20	2.80	
Rim	225	1010	70.63	0.24	14.13	2.07	0.16	0.80	6.82	4.12	98.99	1.01	
Rim	225	1010	70.28	0.21	13.91	1.93	0.16	0.83	6.48	4.12	97.92	2.08	
Rim	225	1010	70.24	0.24	13.72	1.90	0.16	0.83	6.49	4.06	97.64	2.36	
Rim	225	1010	70.85	0.21	13.65	1.99	0.18	0.83	6.74	4.11	98.56	1.44	
Rim	225	1010	70.63	0.23	14.20	1.98	0.18	0.84	6.61	4.29	98.94	1.06	
Rim	225	1010	71.39	0.23	13.96	1.95	0.17	0.83	6.25	4.12	98.89	1.11	
Rim	225	1010	71.00	0.23	14.08	2.05	0.17	0.83	6.28	4.23	98.87	1.13	
Rim	225	1010	70.82	0.21	13.76	1.94	0.17	0.83	7.19	4.04	98.96	1.04	
Mean (n=9)			*70.68*	*0.22*	*13.93*	*1.97*	*0.17*	*0.83*	*6.53*	*4.12*	*98.44*	*1.56*	
1σ			0.38	0.02	0.19	0.07	0.01	0.01	0.38	0.09	0.68		
Core	225	1010	72.34	0.21	14.29	2.10	0.17	0.84	7.17	4.17	101.29	-1.29	0.073
Core	225	1010	72.51	0.24	13.88	1.96	0.16	0.84	6.48	4.19	100.27	-0.27	0.063
Core	225	1010	72.36	0.24	14.04	1.94	0.17	0.85	6.87	4.23	100.69	-0.69	0.070
Core	225	1010	72.13	0.25	13.93	2.03	0.16	0.84	6.44	4.13	99.90	0.10	0.061
Core	225	1010	71.78	0.23	14.10	2.16	0.17	0.86	6.84	4.32	100.46	-0.46	0.073
Core	225	1010	72.32	0.21	13.77	1.99	0.17	0.85	7.15	4.26	100.72	-0.72	0.081
Core	225	1010	72.58	0.21	13.56	1.91	0.17	0.86	6.68	4.32	100.30	-0.30	0.074
Core	225	1010	72.11	0.22	13.39	1.75	0.17	0.86	6.19	4.27	98.95	1.05	0.063
Core	225	1010	72.40	0.23	14.16	1.95	0.17	0.86	6.28	4.33	100.38	-0.38	0.057
Mean (n=9)			*72.28*	*0.23*	*13.90*	*1.98*	*0.17*	*0.85*	*6.68*	*4.25*	*100.33*	*-0.33*	*0.068*
1σ			0.24	0.02	0.29	0.12	0.00	0.01	0.36	0.07	0.64		0.008

Table A1.3 continued.

Rim or core	T (°C)	Duration (hours)	SiO_2 (wt.%)	TiO_2 (wt.%)	Al_2O_3 (wt.%)	FeO (wt.%)	MgO (wt.%)	CaO (wt.%)	Na_2O (wt.%)	K_2O (wt.%)	Total (wt.%)	H_2O (wt.% by diff.)	NBO/T
Rim	175	935	72.28	0.25	14.13	1.88	0.15	0.82	6.82	4.28	100.60	-0.60	
Rim	175	935	71.64	0.24	13.52	1.81	0.14	0.81	5.83	4.39	98.38	1.62	
Rim	175	935	72.00	0.25	13.68	2.23	0.17	0.84	6.82	4.37	100.37	-0.37	
Rim	175	935	71.94	0.24	14.73	2.04	0.18	0.85	6.43	4.29	100.69	-0.69	
Rim	175	935	71.06	0.22	13.74	1.79	0.18	0.84	6.64	4.25	98.73	1.27	
Rim	175	935	71.40	0.24	13.77	1.75	0.17	0.84	7.04	4.19	99.39	0.61	
Rim	175	935	71.58	0.25	13.63	1.81	0.15	0.82	6.04	4.32	98.60	1.40	
Mean (n=7)			*71.70*	*0.24*	*13.88*	*1.90*	*0.16*	*0.83*	*6.52*	*4.30*	*99.54*	*0.46*	
1σ			0.41	0.01	0.42	0.17	0.01	0.01	0.44	0.07	1.00		
Core	175	935	72.62	0.24	14.43	2.01	0.16	0.83	7.42	4.26	101.97	-1.97	0.076
Core	175	935	72.13	0.23	14.63	2.00	0.16	0.82	7.41	4.23	101.62	-1.62	0.073
Core	175	935	73.28	0.24	14.59	1.90	0.15	0.80	7.09	4.34	102.40	-2.40	0.066
Core	175	935	72.72	0.23	14.24	1.99	0.15	0.81	7.02	4.40	101.56	-1.56	0.071
Core	175	935	73.14	0.23	14.35	1.86	0.14	0.80	6.65	4.32	101.50	-1.50	0.059
Core	175	935	72.24	0.24	14.39	1.89	0.16	0.81	7.01	4.33	101.07	-1.07	0.067
Core	175	935	73.16	0.24	14.01	1.84	0.15	0.82	7.27	4.31	101.80	-1.80	0.077
Mean (n=7)			*72.76*	*0.24*	*14.38*	*1.93*	*0.15*	*0.81*	*7.12*	*4.31*	*101.70*	*-1.70*	*0.070*
1σ			0.46	0.01	0.21	0.07	0.01	0.01	0.27	0.06	0.42		0.006

Table A1.3 continued.

Rim or core	T (°C)	Duration (hours)	SiO_2 (wt.%)	TiO_2 (wt.%)	Al_2O_3 (wt.%)	FeO (wt.%)	MgO (wt.%)	CaO (wt.%)	Na_2O (wt.%)	K_2O (wt.%)	Total (wt.%)	H_2O (wt.% by diff.)	NBO/T
Rim	175	3000	71.35	0.22	13.79	2.07	0.16	0.87	6.20	4.07	98.73	1.27	
Rim	175	3000	71.19	0.23	13.46	2.18	0.17	0.85	5.38	4.16	97.62	2.38	
Rim	175	3000	70.00	0.23	13.79	1.88	0.17	0.85	5.47	4.02	96.40	3.60	
Rim	175	3000	69.24	0.24	13.70	1.92	0.17	0.85	5.41	4.12	95.65	4.35	
Rim	175	3000	70.22	0.22	13.79	1.71	0.14	0.82	5.28	4.14	96.31	3.69	
Rim	175	3000	70.27	0.23	14.00	1.95	0.17	0.85	5.60	4.12	97.20	2.80	
Rim	175	3000	70.20	0.22	13.68	1.93	0.17	0.84	5.80	4.05	96.89	3.11	
Rim	175	3000	69.57	0.21	13.54	1.82	0.18	0.86	5.84	4.06	96.09	3.91	
Mean (n=8)			*70.25*	*0.22*	*13.72*	*1.93*	*0.17*	*0.85*	*5.62*	*4.09*	*96.86*	*3.14*	
1σ			0.72	0.01	0.17	0.14	0.01	0.01	0.31	0.05	0.98		
Core	175	3000	72.38	0.25	14.34	2.15	0.16	0.86	7.78	4.19	102.11	-2.11	0.087
Core	175	3000	72.96	0.21	14.05	1.99	0.17	0.88	6.39	4.20	100.85	-0.85	0.060
Core	175	3000	72.85	0.23	14.18	2.15	0.16	0.86	6.60	4.25	101.29	-1.29	0.064
Core	175	3000	73.11	0.22	14.11	2.04	0.17	0.86	5.78	4.22	100.50	-0.50	0.046
Core	175	3000	72.95	0.21	14.20	2.05	0.17	0.87	7.04	4.23	101.71	-1.71	0.072
Core	175	3000	72.74	0.23	14.30	2.13	0.17	0.88	6.44	4.27	101.16	-1.16	0.060
Core	175	3000	72.55	0.21	14.35	1.97	0.15	0.86	7.13	4.25	101.48	-1.48	0.071
Core	175	3000	72.18	0.23	14.16	1.82	0.17	0.88	6.43	4.26	100.13	-0.13	0.059
Mean (n=8)			*72.71*	*0.22*	*14.21*	*2.04*	*0.17*	*0.87*	*6.70*	*4.23*	*101.15*	*-1.15*	*0.065*
1σ			0.32	0.01	0.11	0.11	0.01	0.01	0.61	0.03	0.64		0.012

Table A1.3 continued.

Rim or core	T (°C)	Duration (hours)	SiO_2 (wt.%)	TiO_2 (wt.%)	Al_2O_3 (wt.%)	FeO (wt.%)	MgO (wt.%)	CaO (wt.%)	Na_2O (wt.%)	K_2O (wt.%)	Total (wt.%)	H_2O (wt.% by diff.)	NBO/T
Rim	175	6000	70.67	0.19	13.92	1.78	0.16	0.81	6.33	4.17	98.04	1.96	
Rim	175	6000	71.13	0.21	13.78	1.80	0.16	0.83	6.41	4.09	98.41	1.59	
Rim	175	6000	71.42	0.20	13.82	1.83	0.15	0.83	5.76	4.13	98.14	1.86	
Rim	175	6000	70.14	0.22	14.06	2.09	0.17	0.84	6.56	3.95	98.02	1.98	
Rim	175	6000	71.36	0.21	14.01	1.87	0.17	0.83	6.67	4.10	99.23	0.77	
Rim	175	6000	70.82	0.24	13.85	1.78	0.16	0.84	5.87	4.07	97.64	2.36	
Rim	175	6000	70.23	0.20	13.94	2.12	0.17	0.83	6.27	4.14	97.90	2.10	
Mean (n=7)			*70.83*	*0.21*	*13.91*	*1.89*	*0.16*	*0.83*	*6.27*	*4.09*	*98.20*	*1.80*	
1σ			0.52	0.02	0.10	0.15	0.01	0.01	0.34	0.07	0.51		
Core	175	6000	72.58	0.22	13.99	1.95	0.16	0.84	6.78	4.22	100.74	-0.74	0.068
Core	175	6000	71.91	0.23	14.15	1.88	0.15	0.84	6.34	4.23	99.75	0.25	0.056
Core	175	6000	71.55	0.25	14.25	1.99	0.17	0.85	6.50	4.11	99.66	0.34	0.058
Core	175	6000	71.39	0.22	14.30	1.94	0.16	0.84	6.23	4.29	99.37	0.63	0.053
Core	175	6000	71.57	0.22	13.92	2.18	0.16	0.84	6.35	4.30	99.55	0.45	0.064
Core	175	6000	71.88	0.22	14.23	2.07	0.16	0.82	6.94	4.21	100.54	-0.54	0.069
Core	175	6000	71.82	0.23	14.22	2.03	0.16	0.83	6.29	4.15	99.74	0.26	0.054
Mean (n=7)			*71.82*	*0.23*	*14.15*	*2.01*	*0.16*	*0.84*	*6.49*	*4.22*	*99.91*	*0.09*	*0.060*
1σ			0.39	0.01	0.14	0.10	0.00	0.01	0.27	0.07	0.52		0.007

Chapter II, Table A1.4. Major element compositions of high silica rhyolite (HSR) glass starting material as measured by EPMA. HSR is the same material as 08-YS-07 in Loewen et al. (2017). NBO/T ratios are calculated with normalized major element compositions. Totals reported here do not include H_2O. Calculation of NBO/T for HSR use an fO_2 of NNO - 0.7 and an Fe^{3+}/Fe_{total} of 0.15 appropriate for hotspot settings.

	SiO_2 (wt.%)	TiO_2 (wt.%)	Al_2O_3 (wt.%)	FeO (wt.%)	MgO (wt.%)	CaO (wt.%)	Na_2O (wt.%)	K_2O (wt.%)	Total (wt.%)	H_2O (wt.% by diff.)	NBO/T
High silica rhyolite glass (HSR), Summit Lake flow, Yellowstone National Park, WY, USA	76.07	0.07	12.37	1.15	0.01	0.38	4.71	5.37	100.13	-0.13	0.040
	76.15	0.14	12.25	1.17	0.02	0.39	4.39	5.42	99.92	0.08	0.036
	75.85	0.12	12.14	1.28	0.02	0.41	4.09	5.45	99.36	0.64	0.034
	75.34	0.12	11.80	1.36	0.02	0.42	4.17	5.33	98.55	1.45	0.040
	75.43	0.13	12.03	1.14	0.02	0.41	4.04	5.41	98.62	1.38	0.032
	75.25	0.11	11.96	1.12	0.02	0.38	4.04	5.38	98.26	1.74	0.032
	75.36	0.14	11.86	1.07	0.01	0.39	4.32	5.45	98.61	1.39	0.039
	75.29	0.15	12.05	1.22	0.02	0.40	4.09	5.40	98.62	1.38	0.034
	75.63	0.12	12.14	1.22	0.02	0.41	4.02	5.41	98.99	1.01	0.031
	75.54	0.10	12.09	1.16	0.03	0.41	4.20	5.38	98.91	1.09	0.035
	74.90	0.12	11.69	1.31	0.03	0.43	3.90	5.36	97.74	2.26	0.036
	74.32	0.14	11.70	1.22	0.02	0.42	3.74	5.35	96.90	3.10	0.031
	75.08	0.10	12.02	1.18	0.03	0.40	4.24	5.35	98.40	1.60	0.036
	74.61	0.10	12.04	1.22	0.03	0.40	4.38	5.41	98.18	1.82	0.041
	74.53	0.12	11.79	1.26	0.03	0.40	3.89	5.38	97.40	2.60	0.034
	75.08	0.15	12.27	1.24	0.02	0.42	4.39	5.41	98.98	1.02	0.038
	75.12	0.14	12.18	1.35	0.02	0.43	4.12	5.44	98.78	1.22	0.035
	74.94	0.13	11.99	1.01	0.02	0.38	4.03	5.34	97.84	2.16	0.029
	75.14	0.11	12.12	1.21	0.02	0.41	4.32	5.41	98.73	1.27	0.038
	74.95	0.12	11.97	0.95	0.02	0.39	4.06	5.41	97.87	2.13	0.031
	74.65	0.15	12.10	1.28	0.02	0.43	4.15	5.35	98.14	1.86	0.036
	74.63	0.13	11.86	1.11	0.02	0.42	3.83	5.43	97.43	2.57	0.030
	75.12	0.12	12.10	1.20	0.02	0.42	4.30	5.40	98.70	1.30	0.038
	74.56	0.15	11.71	1.24	0.03	0.41	3.93	5.36	97.38	2.62	0.035
	74.19	0.10	11.99	1.17	0.02	0.42	3.82	5.37	97.07	2.93	0.028
Mean	*75.11*	*0.12*	*12.01*	*1.19*	*0.02*	*0.41*	*4.13*	*5.39*	*98.38*	*1.62*	*0.035*
1σ	0.51	0.02	0.18	0.10	0.01	0.02	0.22	0.03	0.81		0.004

Chapter II, Table A1.5. H and O isotopic compositions of the initial experimental H_2O. Duplicate sets of measurements on a Picarro L2120i cavity ringdown spectrometer at the University of Washington are presented.

Sample Name	Mean δD	δD 1s.d.	Mean $\delta^{18}O$	$\delta^{18}O$ 1s.d.
Exp. Water	74.97	1.11	5.83	0.09
Exp. Water	76.17	0.71	5.93	0.04
	Mean δD (‰)	**δD 1s.d.**	**Mean $\delta^{18}O$ (‰)**	**$\delta^{18}O$ 1s.d.**
MEAN	**75.57**	**1.32**	**5.88**	**0.10**

Chapter II, Table A1.6. Temperature and pressure conditions of experiments and resulting vapor and liquid δD and $\delta^{18}O$ compositions. The pressures, densities, and mass fractions were taken or calculated from steam tables. Fractionation factors (1000lnα) come from Horita and Wesolowski (1994). The experimental vessel is a closed system, so vapor and liquid δD and $\delta^{18}O$ compositions were calculated from the initial H_2O δD and $\delta^{18}O$ compositions, liquid-vapor fractionation, and the mass fractions of each phase. Bolded compositions represent the vapor hydration source and composition. *H_2O is a single phase at this temperature.

T (°C)	P (MPa)	Vapor density (g/cm^3)	Liquid density (g/cm^3)	Mass % vapor	Mass % liquid	D/H $1000ln\alpha_{l\text{-}v}$ (‰)	Vapor δD (‰)	Liquid δD (‰)	$^{18}O/^{16}O$ $1000ln\alpha_{l\text{-}v}$ (‰)	Vapor $\delta^{18}O$ (‰)	Liquid $\delta^{18}O$ (‰)
175	0.892	0.0046	0.8921	17.5%	82.5%	7.41	**69.5**	76.9	2.89	**3.50**	6.39
225	2.548	0.0127	0.8340	18.8%	81.2%	0.39	**75.3**	75.6	1.91	**4.33**	6.24
275	5.942	0.0305	0.7593	22.9%	77.1%	-3.07	**77.9**	74.9	1.14	**5.00**	6.15
375*	21.1	0.1565					**75.6**			**5.88**	

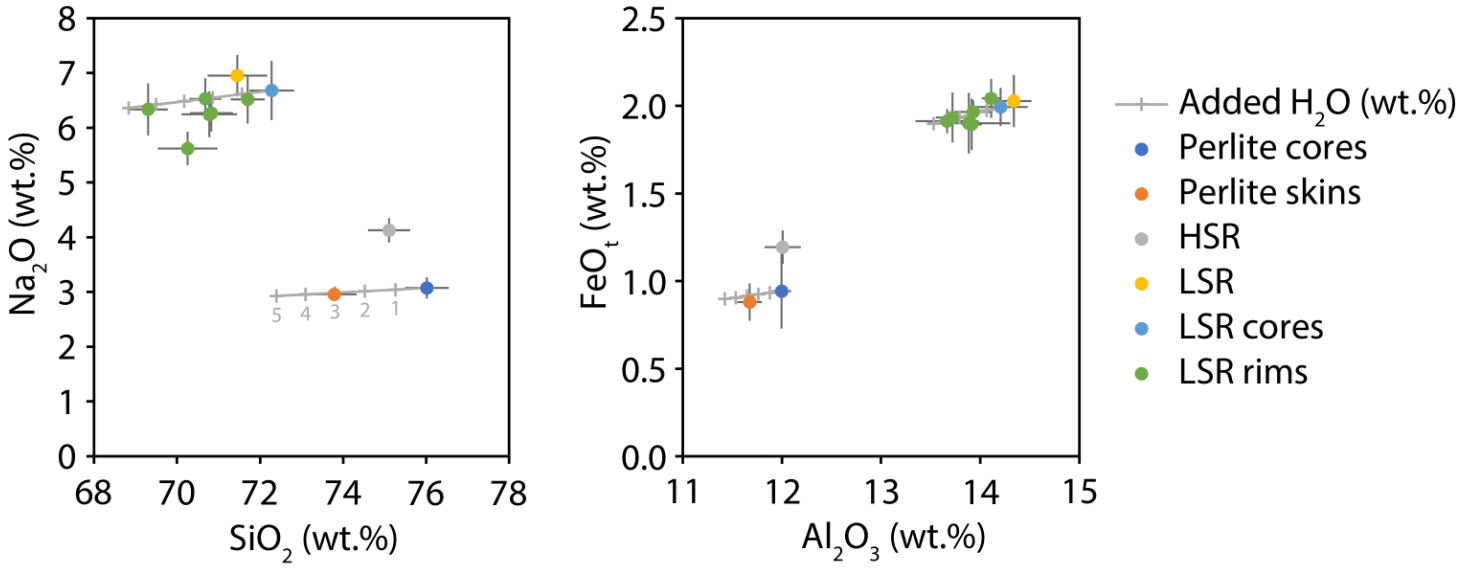

Figure A1.1. Major element plots for starting glasses (LSR, HSR, perlite cores, and perlite rims) and experimentally hydrated LSR glass. Fluid mobile Na_2O is plotted against more refractory SiO_2 to evaluate alkali loss (a) and redox-sensitive FeO_t is plotted against refractory Al_2O_3 to evaluate oxidation (b). Grey curves show how wt.% oxide should change with the addition of H_2O, up to 5 wt.% with tick marks indicating 1 wt.% increments. Perlite rims are approximately 3 wt.% higher in H_2O than their unhydrated cores and their major element compositions are consistent with H_2O addition to the glass without loss of mobile elements. Experimental LSR glasses, with only one exception, are within 1 S.E. (error bars) of this H_2O addition curve suggesting that, like naturally hydrated perlitic rhyolite glass, they have not lost mobile elements.

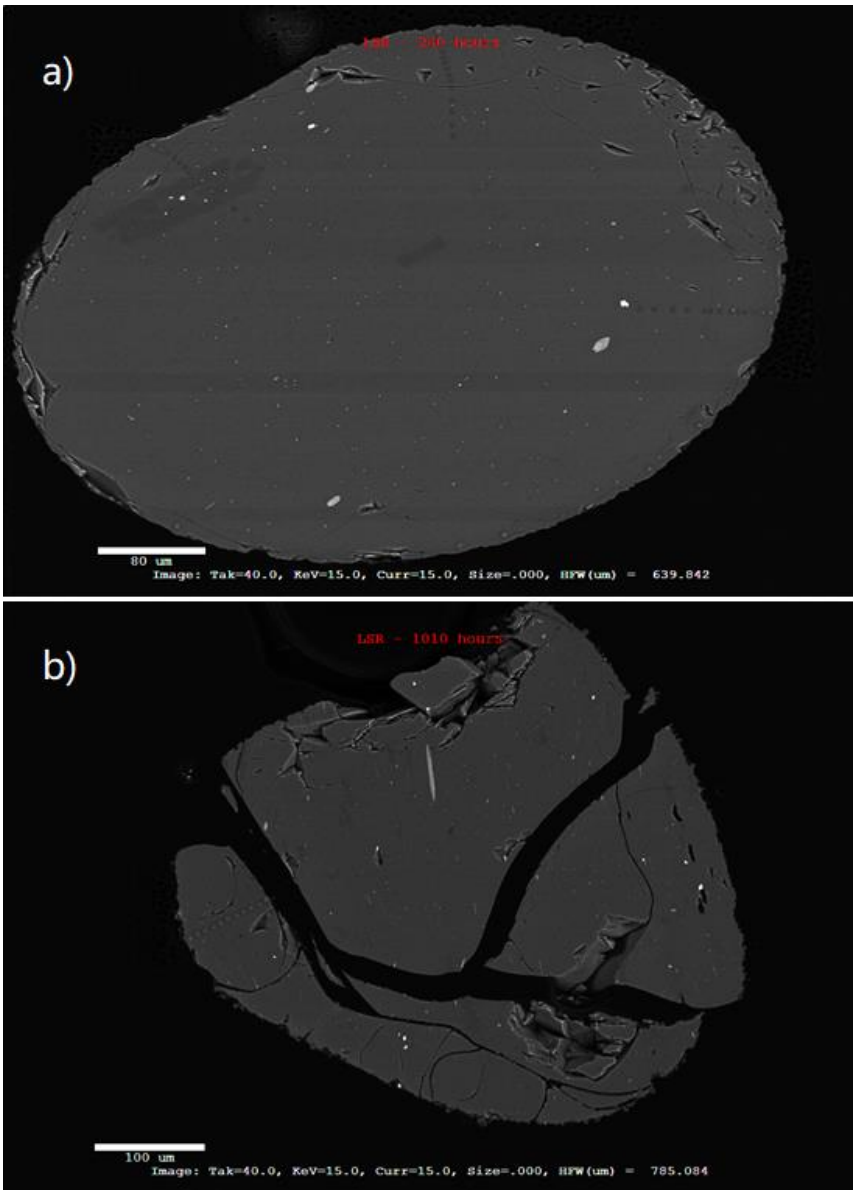

Figure A1.2. (a) Backscatter electron image of characteristic LSR glass that was hydrated for 240 hours. (b) Backscatter electron image of the most altered LSR glass hydrated for 1010 hours. The morphology of fractures and the rounding of interior portions of the glass bears striking similarity to the images of perlites in Bindeman and Lowenstern (2016) that form naturally by hydrothermal hydration.

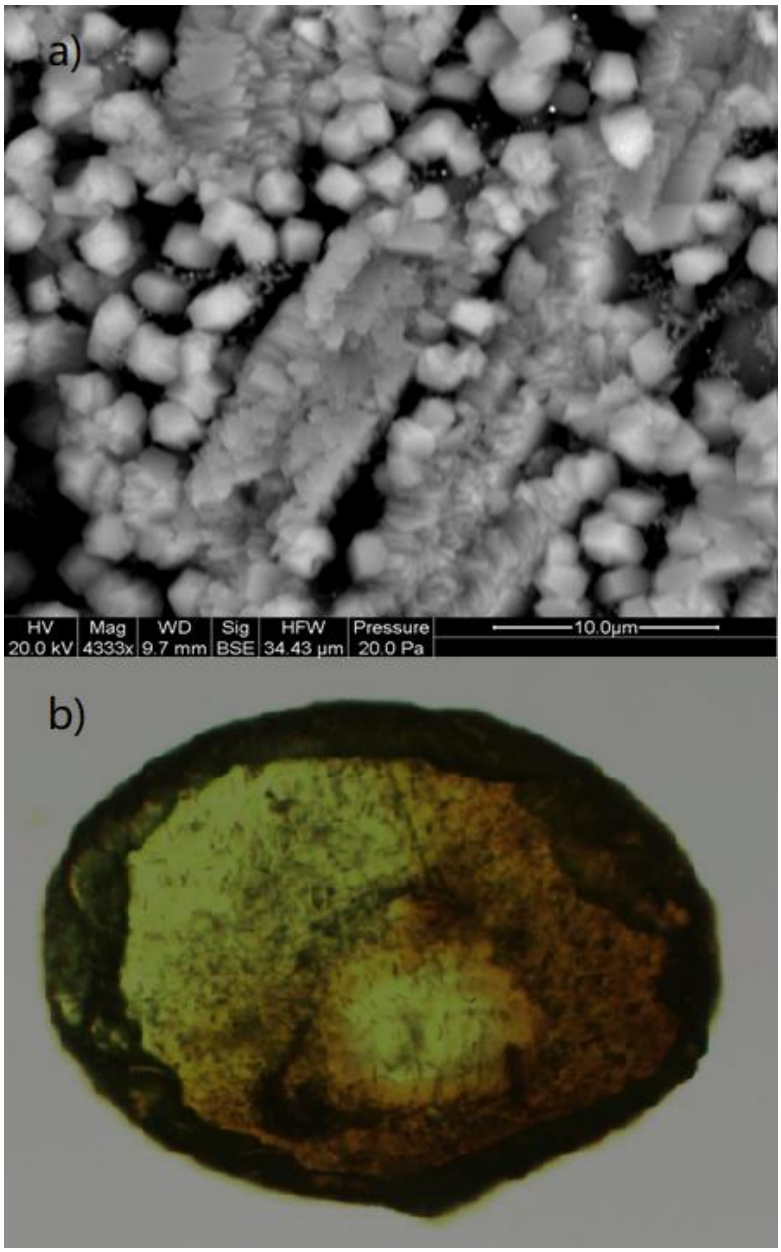

Figure A1.3. (a) Secondary electron image of the surface of LSR glass after 48 hours of hydration. Incipient secondary minerals - likely clays, an SiO_2 phase, or zeolites - have started to form, but are negligible in terms of the overall volume of the particle, so they do not affect the measurements of bulk H_2O or $\delta^{18}O$. (b) Transmitted light image of a doubly polished LSR glass after 48 hours of hydration. The interior remains unaltered glass.

Appendix A2. Physical characterization of experimental glasses

Text A2.1. Sample preparation

To simplify and standardize hydration modeling, glass particles were abraded at the University of Oregon with the goal of creating spherical glass particles. Approximately a gram at a time of material is loaded into a modified mortar that has a stainless-steel lid with an inlet nozzle and outlet covered with fine stainless-steel mesh filter. The lid is sealed shut with several screws. Compressed air is then connected to the inlet and allowed to flow through the air abrader. The glass self-abrades with the air flowing through and fines are flushed out the outlet. Consistent air flow rates or durations were not timed. All material was washed, dried, and sieved following air abrasion.

Thousands of sieved particles are then run on the Microtrac PartAn3D particle size analyzer at the University of Oregon according to the methods developed by Trafton et al. (2019). Particles are loaded onto a vibrating, low-angle tray. Individual particles are gradually sent over the edge of the tray. As they fall, a high-speed camera takes multiple images of the particles as they rotate while falling in front of a backlight. The PartAn3D tracks each individual particle to reconstruct a 3D particle shape which gives volume as well as length, width, and thickness dimensions of each particle. Spherical NIST polydisperse particle standards from 150-650 μm and 50-350 μm are used to ensure that the instrument is giving better than 10% error on each size fraction bin.

Text A2.2. Effective radius calculations

The resulting particles are rounded oblate ellipsoids rather than spheres. Therefore, an effective radius (r_{eff}) must be approximated for the material in order to conduct 1D spherical diffusion and mass balance modeling. The average dimensions of the particles from the PartAn3D were taken and halved to represent radii in each dimension. Assuming differences are negligible in the propagation of the hydration front in each direction of the oblate ellipsoid, the percentage of the volume that remains unhydrated (relative to the total volume) in oblate ellipsoids and spheres can be calculated and compared for every possible hydration length. The calculations of anhydrous percentage for the oblate ellipsoids use the three mean particle dimensions produced by the particle size analysis. Calculations of the total volume (V_{tot}) and

unhydrated volume (V_{dry}) of the glass for the r_{eff} spherical (*sph*) geometry are shown in Eq. A2.1 and A2.2.

$$V_{tot}^{sph} = \frac{4}{3}\pi(r_{eff})^3 \qquad (Eq.\,A2.1)$$

$$V_{dry}^{sph} = \frac{4}{3}\pi(r_{eff} - l_{hydrated})^3 \qquad (Eq.\,A2.2)$$

The true proportion of anhydrous glass in the oblate ellipsoids use slightly different equations that consider each of the measured dimensions (*l*, *w*, and *h*) in Eq. A2.3 and A2.4.

$$V_{tot}^{ell} = \frac{4}{3}\pi(lwh) \qquad (Eq.\,A2.3)$$

$$V_{dry}^{ell} = \frac{4}{3}\pi(l - l_{hydrated})(w - l_{hydrated})(h - l_{hydrated}) \qquad (Eq.\,A2.4)$$

Anhydrous percentages of the measured oblate ellipsoid (*ell*) dimensions are plotted against hydration length ($l_{hydrated}$) and compared to the anhydrous percentage of spheres (Figure A2.1-A2.3).

With progressive hydration, the r_{eff} of the average oblate ellipsoid particle deceases by no more than 5 μm for hydration lengths between 0-30 μm (Table A2.1). Maximum effective radii of 160 μm, 155 μm, and 95 μm are used in the diffusion models as most of the modeled data require short diffusive lengths. Figure 9 shows that for the longest duration experiment (1010 hours) at 225°C, a diffusive length of <30 μm is achieved.

The 375°C experiments in which the glass is fully hydrated are an exception because the effective radius (160 μm) exceeds the minimum dimension of the average particle (114 μm). Once the diffusive length exceeds the minimum dimension, the glass is fully hydrated but the model will not account for this. The result is that the model will take longer to achieve the plateau in the data, which will either cause an overestimate of H_2O solubility or H_2O diffusivity in glass. However, this simple effective radius calculation has strong fidelity for three-quarters of the hydration process. The anhydrous volume percentage remains within 5% error of the unhydrated volume percentage of a sphere for over one-third of the effective radius. This volume – from the edge of the glass to one-third of the r_{eff} into the glass – accounts for 73% of the volume of the particle. Deviation from the spherical anhydrous volume percentages increases to 20% in the

oblate ellipsoid once hydration has penetrated one-half of the r_{eff} into the particle. By this hydration length 89% of the volume of the particle has been hydrated. Despite not having reached the interior of the particle at these diffusive length scales, diffusion through to one-half of r_{eff} approached complete hydration.

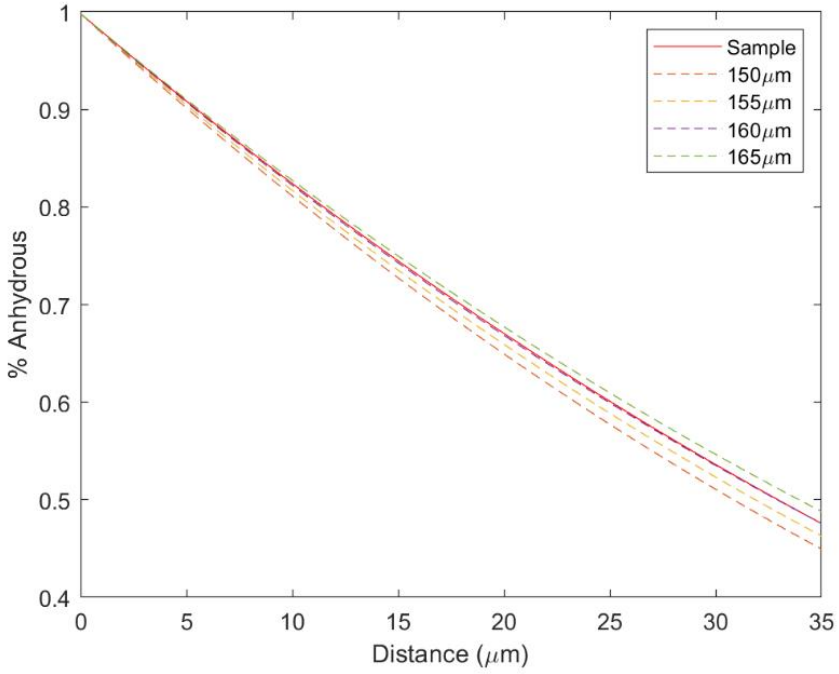

Figure A2.1. Effective radius calculations for the LSR particles used in the 225°C (through 423 hours) and 375°C hydration experiments. The y-axis shows the relative proportion of the particle that remains anhydrous. Dashed lines represent spherical geometries and the solid red line represents the average oblate ellipsoid particle used in the experiments with l = 242 μm, w = 179 μm, and h = 114 μm. The r_{eff} decreases from 162-160 μm between 0 and 30 μm of hydration length. Diffusion modeling uses 160 μm for r_{eff}.

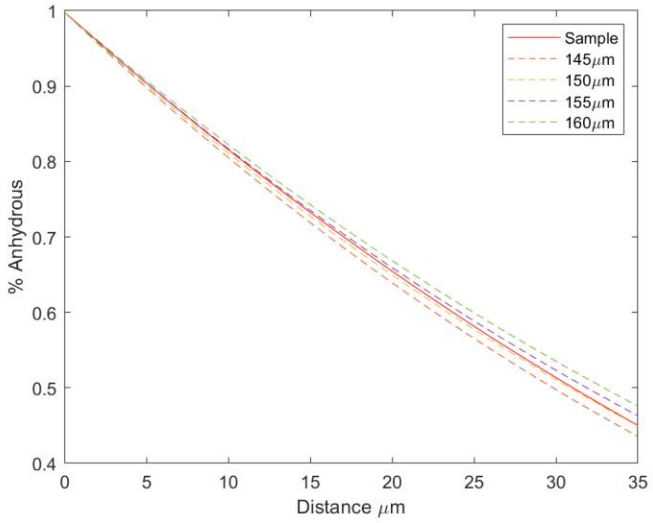

Figure A2.2. Effective radius calculations for the "large" LSR particles used in the 175°C, 225°C (1010 hours) and 275°C hydration experiments. The y-axis shows the relative proportion of the particle that remains anhydrous. Dashed lines represent spherical geometries and the solid red line represents the average oblate ellipsoid particle used in the experiments with l = 280 μm, w = 182 μm, and h = 96 μm. The r_{eff} decreases from 155-150 μm between 0 and 30 μm of hydration length. Diffusion modeling uses 155 μm for r_{eff}.

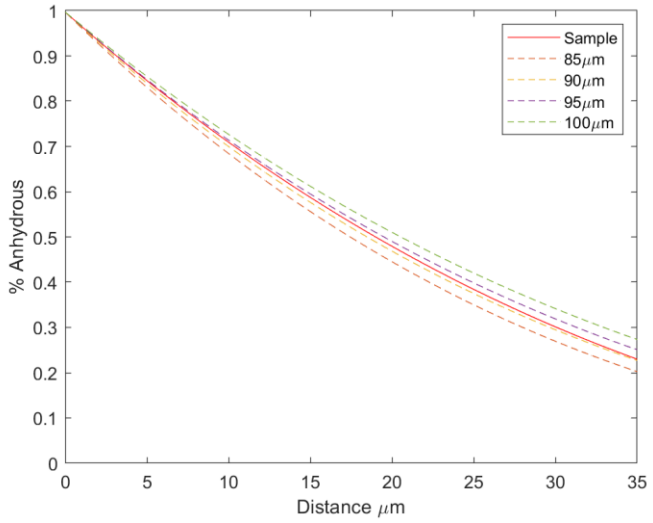

Figure A2.3. Effective radius calculations for the "medium" LSR particles used in the 175°C, 225°C (1010 hours) and 275°C hydration experiments. The y-axis shows the relative proportion of the particle that remains anhydrous. Dashed lines represent spherical geometries and the solid red line represents the average oblate ellipsoid particle used in the experiments with l = 169 μm, w = 92 μm, and h = 66 μm. The r_{eff} decreases from 95-90 μm between 0 and 30 μm of hydration length. Diffusion modeling uses 95 μm for r_{eff}.

Appendix A.3. Miscellaneous Tables

Chapter II, Table A3.1. Raw NanoSIMS counts for D and H as a function of distance for the 225°C, 334 hour-long hydration experiment with an H_2O:D_2O ratio of 1:1. Distance from the rim is corrected for 13° angle of the profile to the rim. Analyses were conducted by Yunbin Guan at the California Institute of Technology.

Distance (μm)	H (raw counts)	D (raw counts)	Distance (μm)	H (raw counts)	D (raw counts)
0.65	3.68E+05	1.62E+05	24.30	9.84E+04	2.80E+01
1.72	3.88E+05	1.60E+05	25.28	1.22E+05	2.50E+01
2.69	3.79E+05	1.51E+05	26.25	1.04E+05	1.30E+01
3.72	3.78E+05	1.46E+05	27.23	1.06E+05	2.90E+01
5.00	3.37E+05	1.29E+05	28.20	1.09E+05	2.60E+01
6.42	2.79E+05	1.04E+05	29.18	9.32E+04	1.90E+01
7.41	2.57E+05	8.65E+04	30.15	1.14E+05	2.70E+01
9.31	2.49E+05	7.41E+04	31.13	1.19E+05	3.10E+01
10.64	2.22E+05	5.68E+04	32.10	1.18E+05	1.90E+01
12.17	1.83E+05	3.66E+04	33.08	1.01E+05	2.00E+01
13.24	1.49E+05	1.57E+04	34.05	9.57E+04	1.20E+01
14.22	1.35E+05	6.36E+03	35.03	1.07E+05	1.60E+01
15.26	1.52E+05	1.16E+03	36.00	1.28E+05	1.70E+01
16.76	1.03E+05	4.70E+01	36.98	9.27E+04	2.10E+01
18.07	1.09E+05	4.00E+01	37.95	1.13E+05	2.30E+01
19.05	1.08E+05	3.10E+01	38.93	1.01E+05	1.60E+01
19.92	1.14E+05	4.10E+01	39.90	9.62E+04	2.40E+01
20.93	1.19E+05	3.20E+01	40.88	1.13E+05	1.80E+01
22.35	1.26E+05	3.10E+01	41.85	1.07E+05	1.60E+01
23.33	1.16E+05	2.00E+01	42.83	1.03E+05	1.80E+01

Chapter II, Table A3.2. Literature compilation of low and moderate T calculations of H_2O diffusivity in rhyolitic glasses. Mazer et al. (1991) and Friedman and Long (1976) conducted experiments above 100°C. Ni and Zhang (2008) values represent maximum and minimum D_{H2O} extrapolations from their high P and high T experiments. The rest of the data come from natural samples.

Authors	Year	T (°C)	T (K)	1000/T (K)	D(H2O) (cm^2/s)
Anovitz et al.	2004	19.4	292.55	3.418	1.00E-18
Anovitz et al.	2004	19.4	292.55	3.418	1.00E-20
Anovitz et al.	2004	75	348.15	2.872	6.64E-16
Anovitz et al.	2004	75	348.15	2.872	9.20E-16
Anovitz et al.	2004	30	303.15	3.299	9.20E-16
Anovitz et al.	2004	75	348.15	2.872	7.50E-16
Anovitz et al.	2004	75	348.15	2.872	2.10E-15
Friedman + Smith	1960	30	303.15	3.299	3.49E-18
Friedman + Smith	1960	28	301.15	3.321	2.57E-18
Friedman + Smith	1960	20	293.15	3.411	1.40E-18
Friedman + Smith	1960	25	298.15	3.354	2.00E-18
Friedman + Smith	1960	5	278.15	3.595	2.90E-19
Friedman + Smith	1960	1	274.15	3.648	1.30E-19
Friedman + Obradovich	1981	12.6	285.75	3.500	3.00E-19
Friedman + Obradovich	1981	12.6	285.75	3.500	1.00E-18
Friedman + Obradovich	1981	5	278.15	3.595	6.00E-19
Friedman + Obradovich	1981	5	278.15	3.595	1.00E-18
Friedman + Obradovich	1981	21.6	294.75	3.393	1.60E-18
Newman et al.	1986	25	298.15	3.354	1.27E-17
Yokoyama et al.	2008	15	288.15	3.470	3.40E-18
Yokoyama et al.	2008	21	294.15	3.400	4.10E-18
Friedman + Long	1976	12	285.15	3.507	2.10E-18
Friedman + Long	1976	16	289.15	3.458	6.30E-18
Friedman + Long	1976	27	300.15	3.332	7.20E-18
Friedman + Long	1976	11.9	285.05	3.508	1.00E-19
Friedman + Long	1976	24.3	297.45	3.362	3.10E-18
Friedman + Long	1976	32.6	305.75	3.271	2.10E-17
Friedman + Long	1976	95	368.15	2.716	1.45E-15
Friedman + Long	1976	150	423.15	2.363	5.75E-14
Friedman + Long	1976	195	468.15	2.136	6.13E-13
Friedman + Long	1976	245	518.15	1.930	5.25E-12
Michels et al.	1983	18.6	291.75	3.428	8.00E-19
Michels et al.	1983	18.6	291.75	3.428	5.10E-18
Anovitz et al.	2004	19.4	292.55	3.418	3.35E-18
Stevenson et al.	2004	20	293.15	3.411	1.95E-18
Anovitz et al.	2009	25	298.15	3.354	1.28E-17
Rogers + Duke	2011	16	289.15	3.458	1.60E-18
Mazer et. al.	1991	175	448.15	2.231	1.70E-12
Mazer et. al.	1991	175	448.15	2.231	2.60E-13
Mazer et. al.	1991	160	433.15	2.309	5.25E-13
Mazer et. al.	1991	160	433.15	2.309	1.04E-13
Mazer et. al.	1991	150	423.15	2.363	2.20E-13

Table A3.2 continued.

Mazer et. al.	1991	150	423.15	2.363	4.45E-14
Giachetti et al.	2020	5	278.15	3.595	3.16E-20
Ni + Zhang (extrapolation)	2008	25	298.15	3.354	1.40E-21
Ni + Zhang (extrapolation)	2008	25	298.15	3.354	1.36E-15

APPENDIX B

CHAPTER III SUPPLEMENTARY INFORMATION AND FIGURES

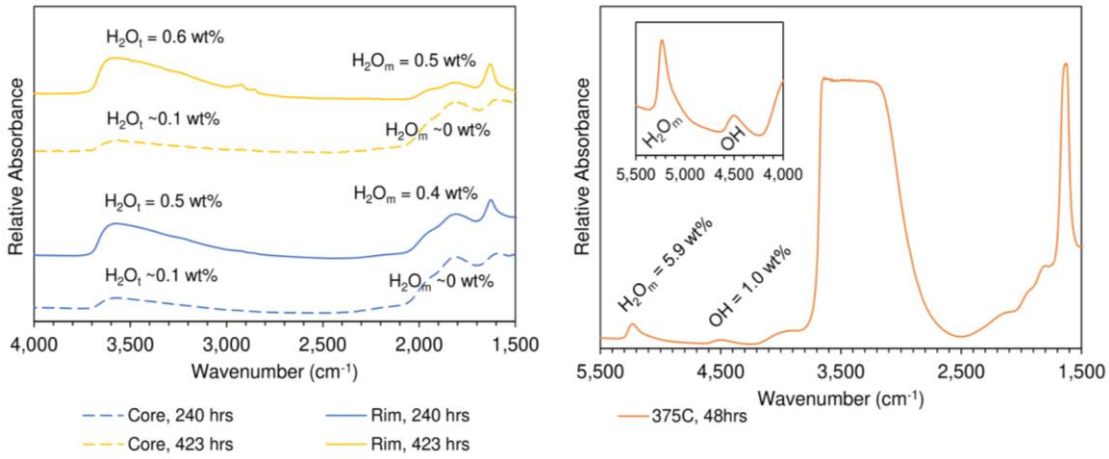

Chapter III, Figure B1. FTIR spectra for 3 of the experimental glass. Mid-IR measurements from the rims and cores of 225°C experimental glasses (left) held for 240 hours (blue) and 423 hours (yellow) are shown on the left. Cores have ~0.1 wt% H_2O_t, which is nearly all OH with negligible amounts of H_2O_m. Rims yield between 0.5-0.6 wt% H_2O_t, and do not record evidence of additional OH growth. Water in the glass from the 375°C experiment (right) saturates the mid-IR 3600 cm-1 H_2O_t peak and the 1600 cm-1 H_2O_m peak after 48 hours. Near-IR measurements suggest 5.9 wt% H_2O_m and 1.0 wt% OH (inset), consistent with equilibrium speciation for that T and H_2O_t.

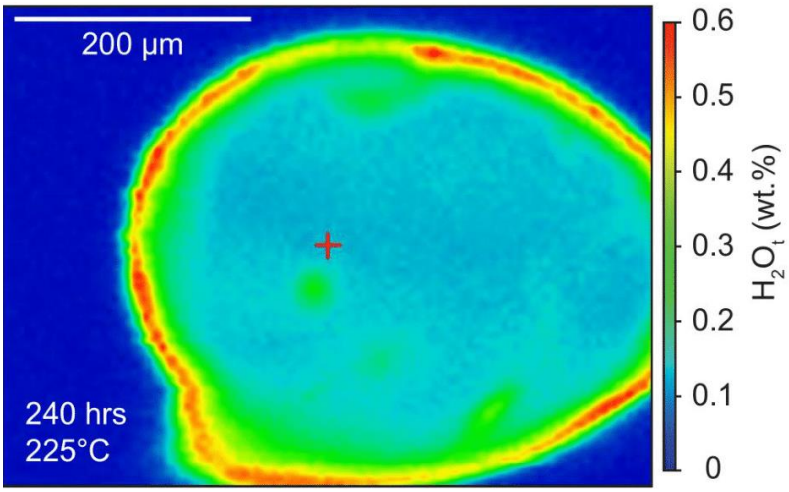

Chapter III, Figure B2. FTIR map of H_2O_t in a glass particle from the 240 hour-long experiment at 225°C. The length scales of hydration are consistent with the profile measured by NanoSIMS in Hudak and Bindeman (2020). Water concentrations get lower towards the edges as they thin from the full thickness of the doubly polished wafer.

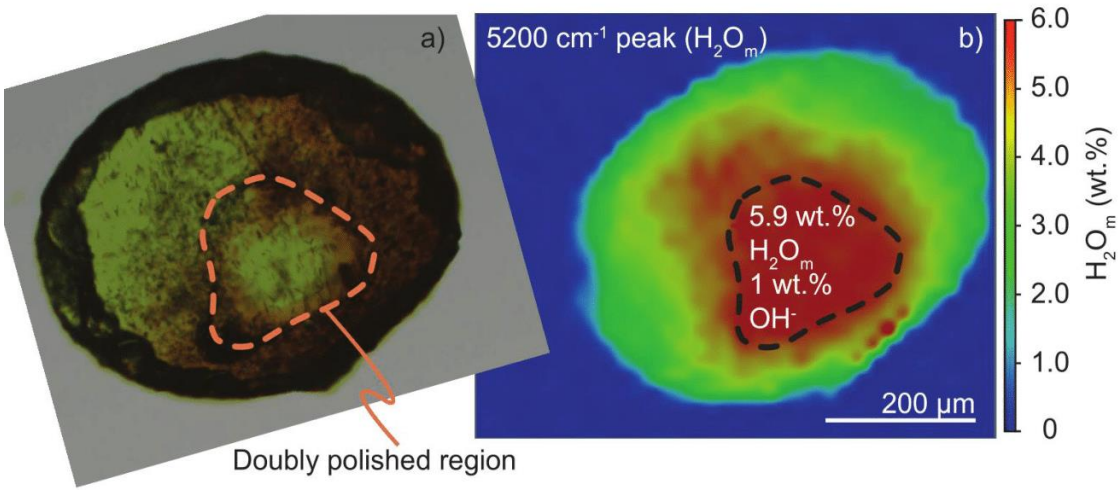

Chapter III, Figure B3. An optical image (a) and an FTIR map of H_2O_m in a glass particle from the 48 hour-long experiment at 375°C (b). The dashed line shows where the wafer is doubly polished to a consistent thickness. Outside of this area, the glass tapers and becomes thinner and therefore yields lower H_2O_m concentrations.

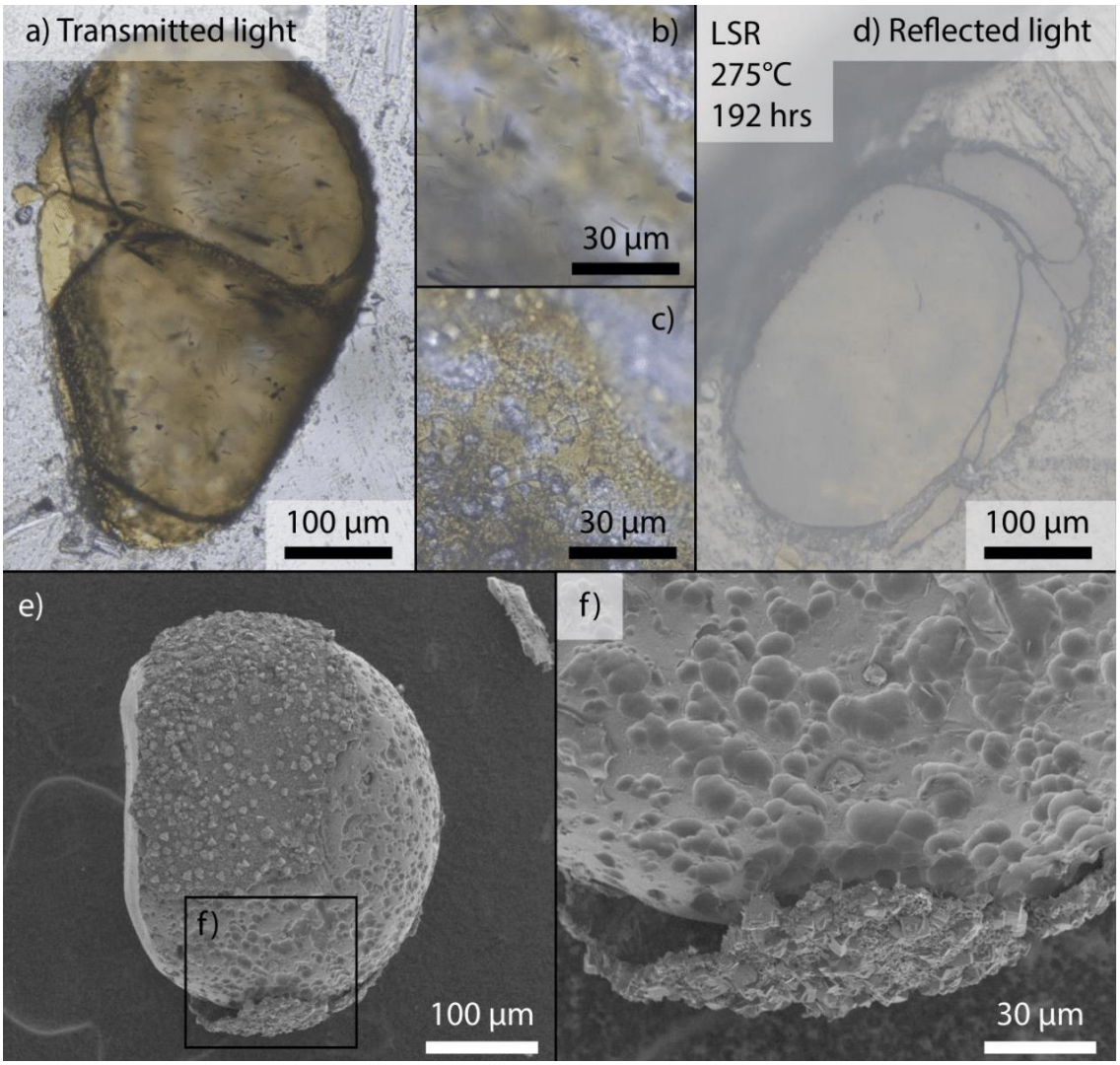

Chapter III, Figure B4. Transmitted (a-c), reflected (d), and secondary electron images (e-f) of LSR glass run at 275°C for 192 hours. Polished sections show conchoidal fractures subparallel to the particle surface (a,d), which likely result from the volume increase of the glass from H2O diffusion, perhaps akin to perlite formation. Secondary phases are not present within the glass (b), but are present on the glass surface (c,e-f). This is evident in transmitted light in images (b) and (c), which were taken in the same spot but at different focal depths at 40x magnification. In (b), acicular plagioclase microlites are visible in the glass interior and lack the cubic phases observed on the surface (c,e-f). These cubic phases, no larger than 10 µm wide, are homogeneously distributed within a matrix of other finer secondary phases that form a coherent rind on the glass surface. Pitting of the glass surface indicates that some glass dissolution may also be occurring (e-f).

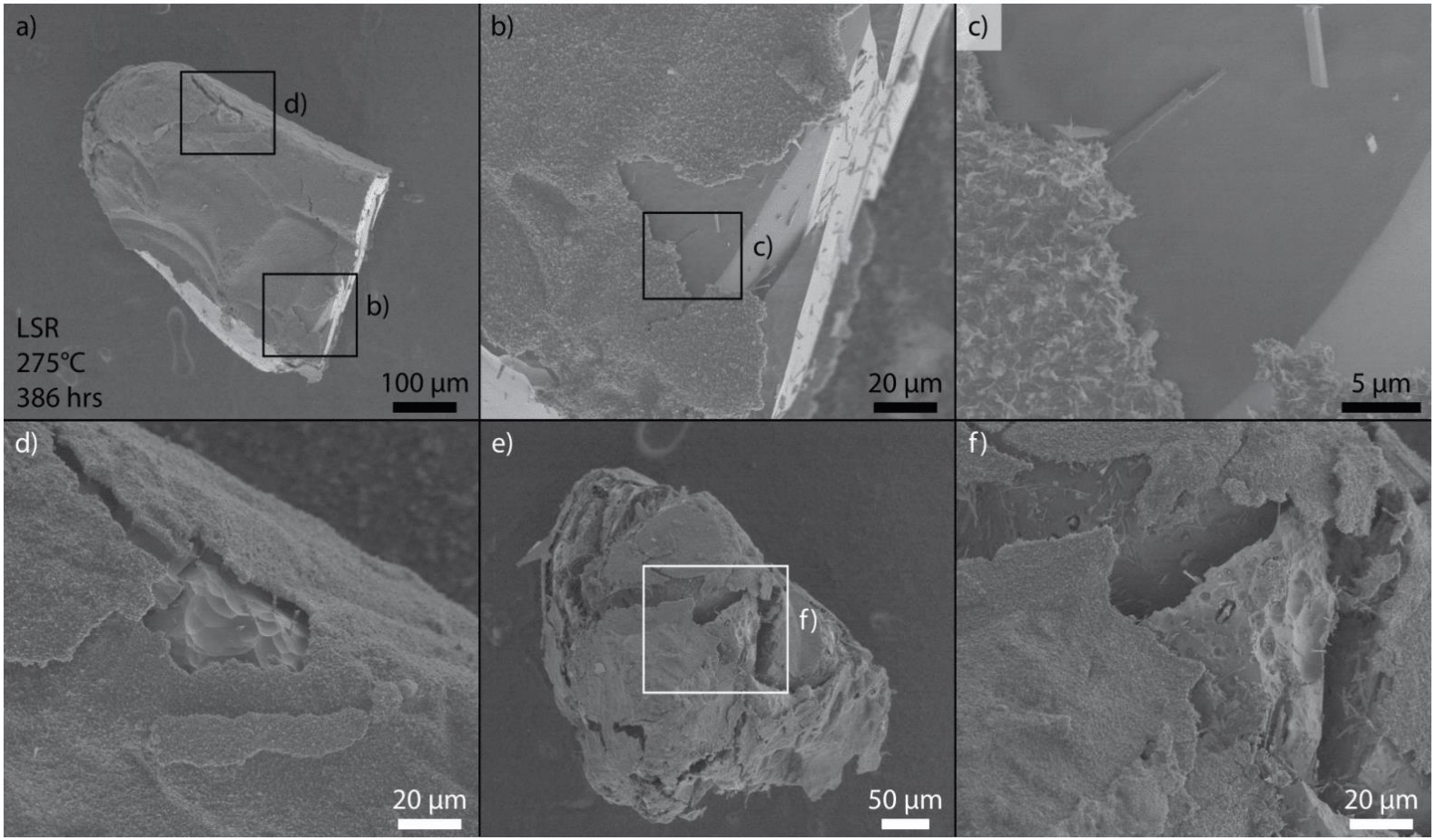

Chapter III, Figure B5. Secondary electron images of two particles of LSR glass (a-d; e-f) run at 275°C for 386 hours. In (a), the surface coating of secondary phases is uniform in thickness (<4 µm). The blanket of alteration products includes needle-like, sheet-like, and tabular forms. Where underlying glass is revealed, it is not uniform in appearance as some areas have smooth, flat surfaces (b-c) while others are pitted (d). Variation between particles is strong, however. Some particles show highly fractured (e) and extensively altered glass (f). Some additional textures in (f) include longer needles extending out from the glass surface and wells around plagioclase microlites where the glass has dissolved (f).

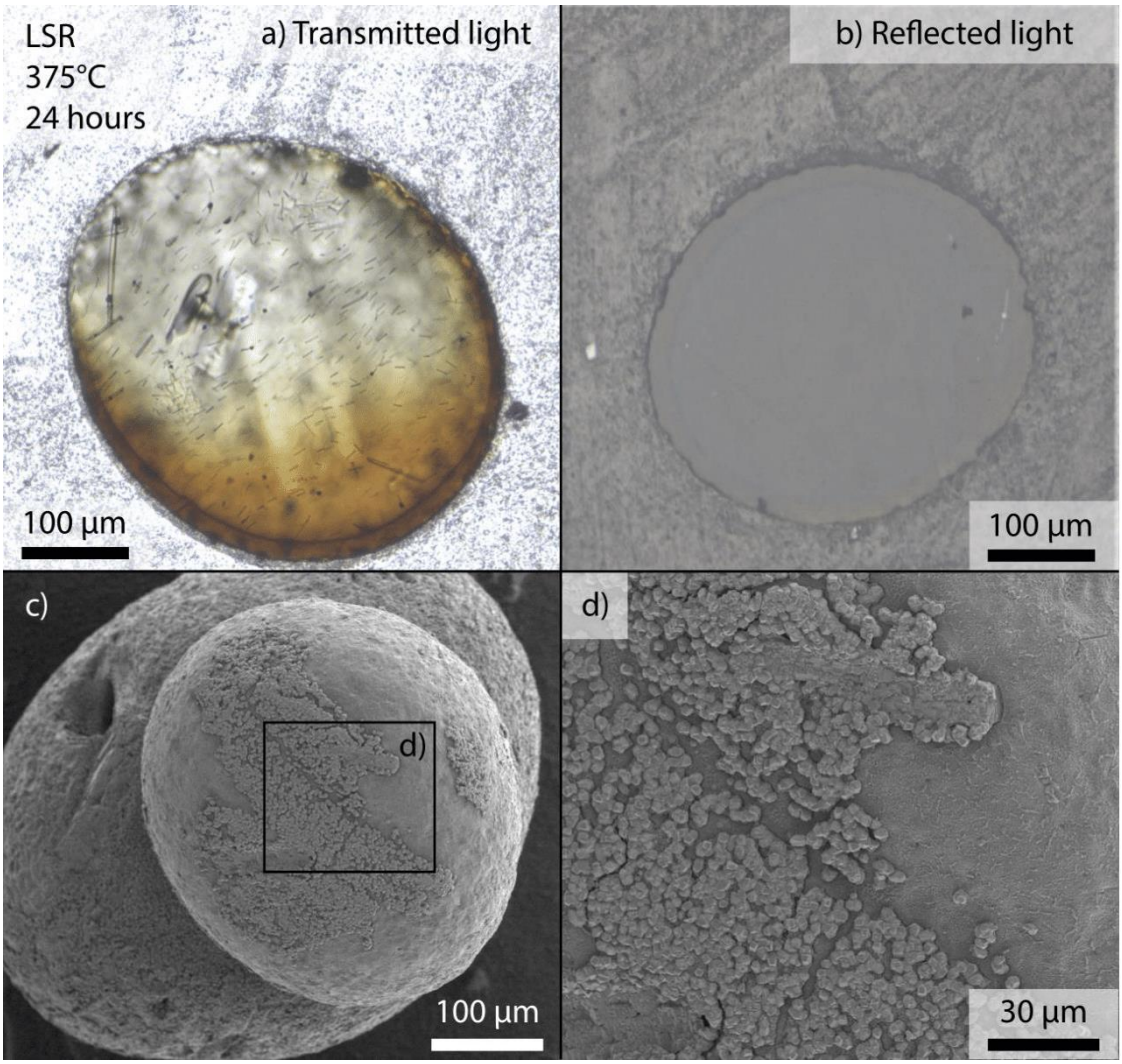

Chapter III, Figure B6. Transmitted (a), reflected (b), and secondary electron images (c-d) of LSR glass run at 375°C for 24 hours. Polished sections show an oxidized rim with a maximum thickness of ~21 µm in multiple glass particles (a-b). Nanocrystalline phases, particularly Fe-oxides, may be present, but no microcrystalline secondary phases detected by our methods. Secondary phases are present on the surface of the glass particles (c) and at the interface of glass and plagioclase microlites where exposed at the surface (d). These phases are no more than 5 µm and do not uniformly coat the glass surface.

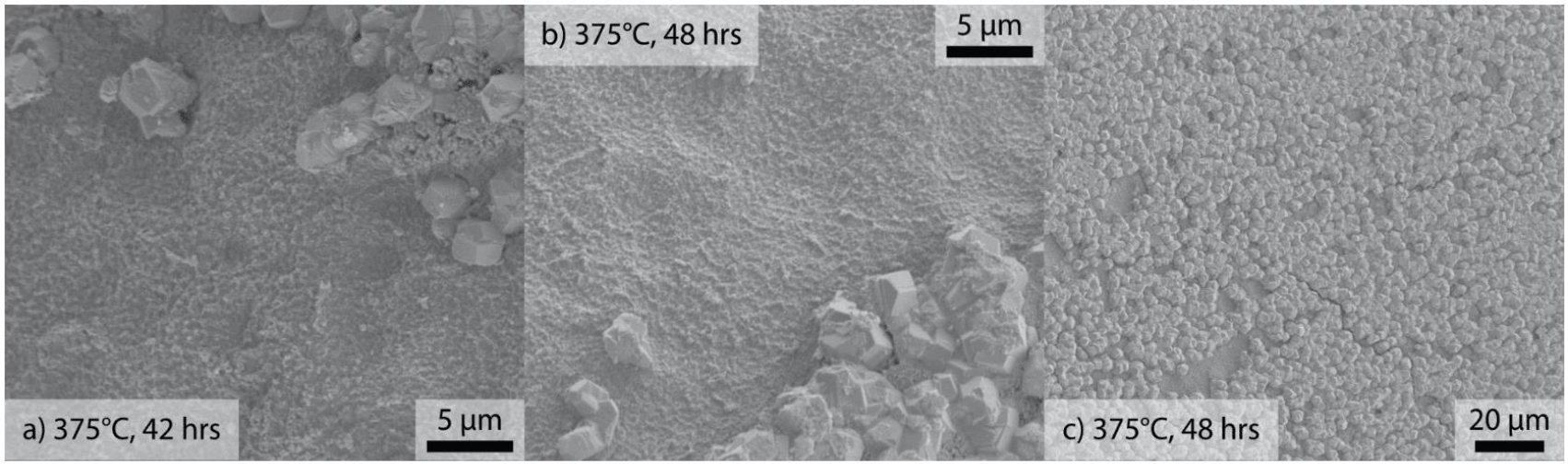

Chapter III, Figure B7. Secondary electron SEM images of LSR glass run at 375°C for 42 hours (a) and 48 hours (b-c). The main, dodecahedral secondary phase on the glass surface remains <5 µm after 42 hours and 48 hours, just as it was after 24 hours (Figure A.3). The dodecahedrons appear to have a layered structure, suggesting it may be a phyllosilicate phase (a, upper right).

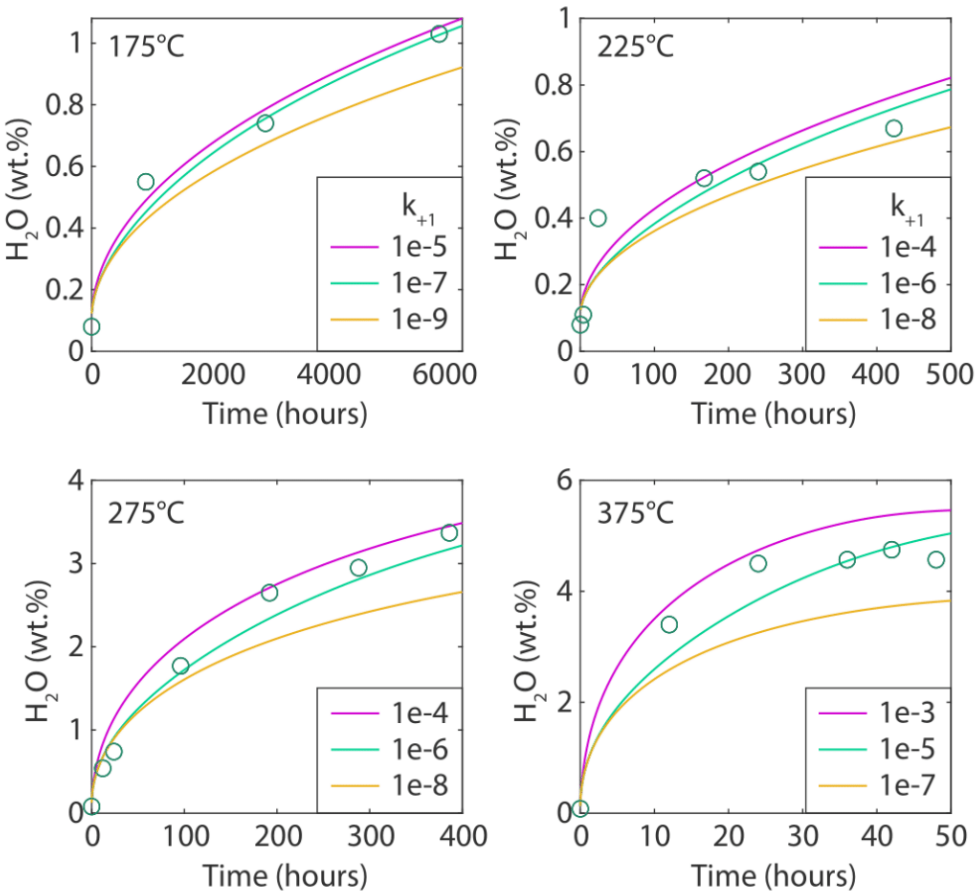

Chapter III, Figure B8. The time evolution of H_2O_t that corresponds to the δD models in Figure 7.

Chapter III, Table B1. Data from the experimental run products Proctor et al. (2017) used in Figure 4. H_2O_m and OH concentrations of glasses formed in 300°C shearing experiments with wet rhyolitic fault gouge. See Proctor et al. (2017) for experimental details and FTIR methods.

Sample	*Point*	*A. 5230 cm^{-1}*	*A. 4520 cm^{-1}*	*Thickness (mm)*	*Density g/cm^3*	*Mass H_2O wt%*	*OH^-/H_2O_m*
wt01_chip 1	1	0.194	0.066	0.213	2.23	5.29	0.340
wt01_chip 1	2	0.190	0.070	0.209	2.23	5.44	0.368
wt01_chip 1	3	0.181	0.056	0.204	2.23	5.01	0.309
wt01_chip 1	4	0.194	0.063	0.211	2.23	5.26	0.325
wt01_chip 1	5	0.200	0.064	0.211	2.23	5.40	0.320
wt01_chip 2	1	0.113	0.039	0.210	2.26	3.11	0.345
wt01_chip 2	2	0.120	0.041	0.250	2.27	2.76	0.342
wt03_grain 1	1	0.018	0.006	0.060	2.30	1.70	0.333

APPENDIX C

CHAPTER IV SUPPLEMENTARY INFORMATION AND FIGURES

Text C1. Isotope geochemistry methods

For δD and H_2O concentrations, 1.5-3.0 mg of hydrated glass were loaded into Ag capsules for analysis on a high temperature conversion elemental analyzer (TC/EA) equipped with a Finnegan MAT-253 mass spectrometer. Precision and reproducibility are ±1.3‰ (2 S.E.) for δD and ±10% of the H_2O_t <1wt.% and ±5% of the H_2O_t for samples >1wt.% (Martin et al., 2017), which in this study is <0.2 wt.%. (See Martin et al., 2017 for detailed description of analytical methods.) Hydrogen isotopes and total H_2O are determined from the yield of H_2 with standards USGS57 (biotite) and USGS58 (muscovite; Qi et al., 2017). Further analytical details can be found in Martin et al. (2017). The $\delta^{18}O$ of water in glass ($\delta^{18}O_{wig}$) was also measured by TC/EA using the CO method produced from pyrolysis of extracted water in a different analytical session, using 0.15 µl USGS water standards (USGS47, USGS53, VSMOW, and W-62001) welded in Ag cups to calibrate the $\delta^{18}O_{wig}$ on a VSMOW scale (Qi et al., 2010). Similar quantities of sample material were also loaded in Ag capsules for separate $\delta^{18}O$ of water in glass ($\delta^{18}O_{wig}$) analyses as developed by Seligman et al. (in review). Biotite standard NBS30 was used to calibrate H_2O concentration. Roughly 1-2 mg of hydrated glass were also used for bulk $\delta^{18}O$ analyses on a CO_2 laser fluorination line. Glass can be reactive and breakdown when exposed to the BrF_5 reagent, so samples were loaded into an airlock and placed under vacuum overnight before being introduced individually into the laser chamber. This prevents contamination between samples and ensures complete yields from each sample. Liquid nitrogen traps and a mercury diffusion pump were used to remove excess fluorine or fluorinated species prior to introduction of the sample gas to the spectrometer. A hot carbon rod converted O_2 gas to CO_2 for analysis on the MAT-253 spectrometer. Gore Mountain garnet (UOG; $\delta^{18}O$ = 6.52‰) were analyzed three times over the course of the airlock run (9 samples + 3 standards). The full procedure is described in Bindeman (2008) and Loewen and Bindeman (2015).

Water samples were manually injected in 2 μL aliquots into the TC/EA. For δD, two H_2 monitoring gas peaks preceded a series of four injections, the first of which was discarded to avoid memory effects in the instrument from the previous sample or standard. Additional injections were used to improve the statistics for a few samples with larger variations in measured δD values. For $\delta^{18}O$, seven CO monitoring gas peaks preceded a single injection. Because of the longer period of time between analyses from the extra reference peaks, no analyses were discarded and 2-4 analyses were conducted per sample. Reported values are means with one standard error. House standards of Fiji water (δD = -41.79‰ and $\delta^{18}O$ = -5.31‰) and Fairbanks water (δD = -154.75‰, $\delta^{18}O$ = -19.37‰) calibrated at the University of Alaska Fairbanks were used.

Text C2. Modeling of glass hydration by addition of meteoric water

Mixing curves for simple addition of meteoric water to glass are calculated for Katmai glasses (Eq. 1, Figure 3).

Eq. 1: $$\delta_{mix} = (\delta_r * f_r * \frac{C_{Xr}}{C_{Xmix}}) + [(\delta_w + 1000 ln\alpha_{glass-water}) * (f_r - 1) * \frac{C_{Xw}}{C_{Xmix}}]$$

The isotopic composition of the mixture is given as δ_{mix}, f_r is the fraction of the mixture that is rock, and C is the concentration of H and O in rock (subscript 'Xr') or water (subscripts 'Xw').

The concentrations of O in H_2O is 89% by mass (and H is 11%) and ~52% in silicate rocks. Hydrogen is only 0.01-0.1% by mass of a mostly degassed volcanic glass. The concentration of H or O in the mixture is $(C_r * f_r) + C_w * (1 - f_r)$. The initial composition of the glass is assumed to be 0.6 wt.% H_2O, −85‰ δD, and 7.0‰ $\delta^{18}O$ (orange stars in Figure 3). A $\delta^{18}O$ of 7.0‰ for the equilibrium melt (interstitial glass) is consistent with the $\delta^{18}O$ of quartz, plagioclase, and magnetite phenocrysts from the crystal-poor Novarupta rhyolite that we measured. The Novarupta rhyolite is very similar in composition to the glass component of the Novarupta dacite (Avery, 1992; Fierstein and Hildreth, 1992). An H_2O of 0.6 wt.% for the initial glass composition is intermediate between the degassed Novarupta dome and the least hydrous dacite pumices of our data set. A δD of −85‰ matching our observation is taken by following a theoretical degassing trend from the Novarupta dome δD values to 0.6 wt.%.

The meteoric water composition used for mixing is based on the isotope compositions from the lakes in the Katmai region (Section 4.1.1, Table C1). Only Hammersly Lake (−15.32‰ $\delta^{18}O$) and Murray Lake (−16.26‰ $\delta^{18}O$) are within 100m elevation of the sample locations at Knife Creek and Mageik Lakes. Following the global average of $\delta^{18}O$ depletion with increasing elevation of −0.29/100m (Poage and Chamberlain, 2001; and references therein), we get a $\delta^{18}O$ of −16.08‰ by adding 100m of elevation to the average $\delta^{18}O$ of these two lakes. The Alaskan MWL given by Lachniet et al. (2016) yields a δD of meteoric water mixing end member of -120.2‰. The $1000\ln\alpha_{\text{glass-water}}$ for δD between water and silicic glass at ambient temperatures has been determined to be −33‰ (Friedman et al., 1993a; Seligman et al., 2016). The mixing calculations add this fractionation to the meteoric water composition. No fractionation is used for the $\delta^{18}O$ data because the equilibrium fractionation between a eutectic composition rhyolite (two-thirds albite, one-third quartz) and water at ambient T is large and positive and the data do not have large excursions from the initial magmatic value (O'Neil and Taylor, 1967; Sharp et al., 2016). Although a smaller magnitude δD fractionation may be expected at hydrothermal temperatures, there are several reasons to apply the ambient T fractionation. The samples from the VTTS are shallow in the deposit and likely cooled quickly, so they may have spent very little time at hydrothermal T. The low water content of the glasses suggests that hydration was inhibited at Mageik Lakes. Magmatic bulk $\delta^{18}O$ of all Katmai samples suggests that isotope exchange, if any, was limited at Knife Creek. Finally, the fractionation between water and glass at higher T is unconstrained, so we first test the fit of the ambient T $1000\ln\alpha_{\text{glass-water}}$ for δD of −33‰. Water addition curves extend from the initial glass composition to a glass that 4.2 wt.% H_2O, equal to the H_2O content of the most hydrous glass analyzed. Hash marks of H_2O content in Figure 3c closely approximate the H_2O of the VTTS glasses.

For Crater Lake pinnacles, a starting composition for the rhyodacite is approximated by the composition of the Cleetwood rhyolite, which has ~0.2 wt.% H_2O, a δD of −110‰, and a $\delta^{18}O$ of 6.4‰ (Mandeville et al., 2009; Seligman et al., 2016). Again, this simple addition of water to glass employs the ambient T $1000\ln\alpha_{\text{glass-water}}$ for δD of −33‰ and no fractionation for $\delta^{18}O$. Andesites are typically slightly lighter in $\delta^{18}O$ than rhyolites derived from the same source, so we use $\delta^{18}O$ of 5.8, which is geologically

reasonable. We also choose a wetter initial H_2O of 0.6 wt.% for a theoretical andesitic pumice to help illustrate a range of reasonable values between the rhyolite-water and andesite-water mixing curves. Finally, a smaller ambient T $1000\ln\alpha_{\text{glass-water}}$ for δD of −24‰ is used based on the results of Seligman et al. (2016) who show that δD fractionation between basalt and water is −19‰.

Text C3. Major and trace element geochemistry methods

Trace element concentrations on sample spots were obtained by laser ablation inductively-coupled plasma mass spectrometry (LA-ICP-MS) at Oregon State University. Vacuum impregnated epoxy mounts of Crater Lake pumices are loaded in the sample chamber for the Photon Machines Analyte G2 193 nm ArF Excimer Laser coupled with a Thermo Scientific X Series 2 Quadrupole Mass Spectrometer. Sample spots of 30 microns were used on interstices of bubble walls. Data reduction and general procedures follow that of Loewen and Kent (2012). Standards GSE-G1 and GSD-G1 were used for calibration and silica was used as an internal standard.

Bulk material analysis for major, minor, and trace elements was conducted at Pomona College by X-ray fluorescence (XRF) following the method of Lackey et al. (2012). Samples were powdered using a tungsten carbide ball mill. Splits of ~3.5 g of powder were fluxed in a 1:2 ratio with ~7.0 g of dilithium tetraborate. Mixtures were melted in graphite crucibles at 1000°C for 10 minutes, crushed and powdered again, and fused a second time. The resulting glasses were then polished on diamond laps for analysis. Data were collected on a Panalytical Axios wavelength-dispersive XRF spectrometer with PE, LiF200, LiF220, PX1, and GE industrial crystals. Calibration curves for elemental concentrations were made from certified reference materials.

Text C4. Element mobility as a function of water to rock ratio

Previous work on ashes from East Africa show a positive correlation between $\delta^{18}O$ and water content, suggesting that oxygen isotopes can monitor water to rock (W/R) ratios (Cerling et al., 1985). These authors also investigate leaching of alkalis by proton (H^+) exchange with progressive hydrations. They argue that $Na^+ – H^+$ exchange is more common and that $K^+ – H^+$ only occurs at higher W/R ratios, which they illustrate with

$\delta^{18}O$ contour on a H_2O-Na_2O-K_2O ternary diagram. Mt. Mazama fumarolic glasses become lighter in $\delta^{18}O$ rather than heavier as Cerling et al. (1985) observed because of the difference in meteoric water compositions between the locations. Since the H_2O of fumarolic glasses is relatively constant, the range in $\delta^{18}O$ values may be interpreted in the framework of Cerling et al. (1985) as W/R ratios to assess if and to what extent glass hydration and hydrothermal conditions perturb the glass chemistry.

Glass analyses by EPMA for major elements and LA-ICP-MS for trace elements are normalized to the bulk composition of Cleetwood rhyolite (Ankney et al., 2013; SEM images in Figure C1). The Cleetwood rhyolite flow erupted contemporaneously with the climactic phase of the 7700 BP eruption and has approximately the same in composition to the early rhyodacitic explosive phase. Alkali concentrations are further normalized to immobile Ti and Zr to avoid conflating variations in magma chemistry with changes from hydrothermal processes. Both whole rock and glass Ti and Zr compositions vary by ~10% or less in the rhyodacite from the climactic phase of the Mt. Mazama eruption even as the fraction of the eruptive products became increasingly mafic (Bacon and Druitt, 1988).

The changes in the normalized alkali concentrations are not systematic, although in general it appears as though there is Na depletion and K enrichment with increasing W/R ratio (decreasing $\delta^{18}O$). Ratios of Na/Ti decrease from 1.03-1.10 at a bulk $\delta^{18}O$ of 5.55‰ to as low as 0.71 at $\delta^{18}O$ of 0.95‰ (Figure B1). K/Ti ratios are more variable, but on average increase, nearly doubling between the lowest and highest $\delta^{18}O$ glasses analyzed. The trace alkalis are more challenging to interpret. Li is uniformly depleted relative to Zr, whereas Rb and Cs are highly variable, but uniformly enriched in the 0.95‰ $\delta^{18}O$ glass. All three trace alkalis are most depleted, and most consistently in the next lowest $\delta^{18}O$ glass with ratios between 0.5-0.7. Bulk glass XRF data from the same pumices show enrichments in K relative to Cleetwood and subtle depletions in Na. No change is observed in Ba or Sr, while Rb is only enriched in the highest W/R ratio sample.

Supplementary Figures

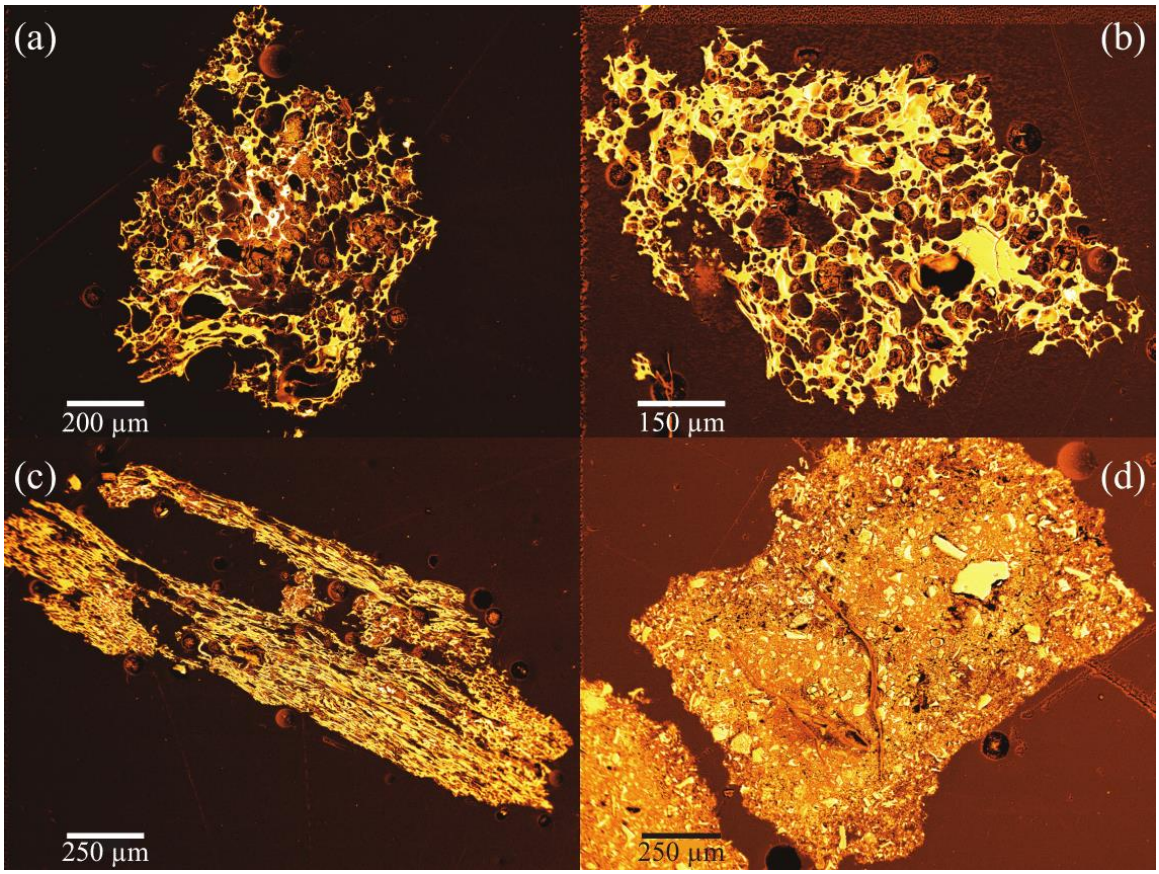

Chapter IV, Figure C1. Backscatter SEM images of fresh, glassy Mt. Mazama pumices collected from fumarolic pinnacles (a,b,c) and an altered air fall pumice (d). Samples SC-63-1 (a) and SC-71-4 (c) are from lower rhyodacitic member and the SCCL-54aw (b) is from the upper andesitic member of the zoned climatic ignimbrite. Sample PD-53-pg (d) is from a locally altered mound in the pumice desert, similar to the localized fumarolic deposits on the floor of the VTTS.

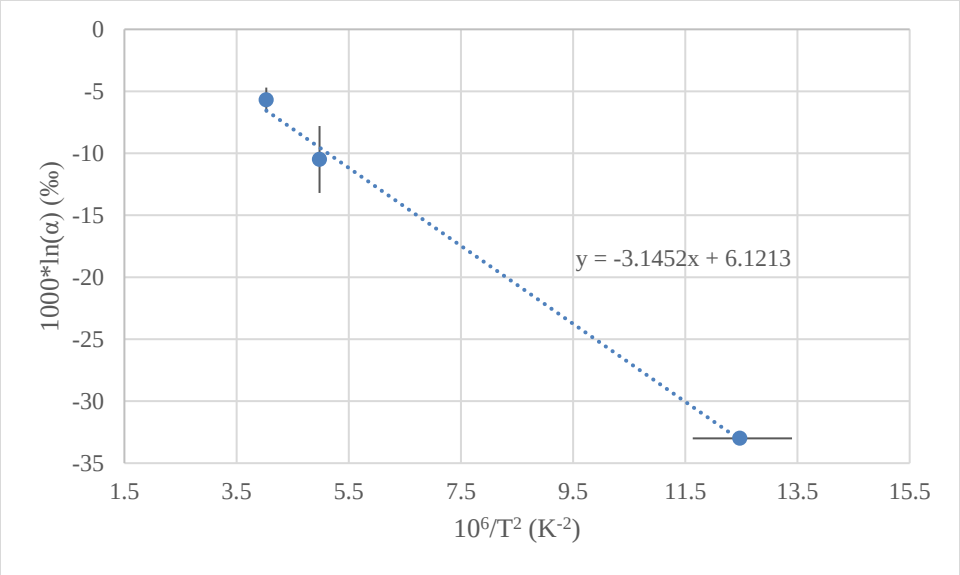

Chapter IV, Figure C2. The relationship between temperature, expressed as $10^6/T^2$ (K^{-2}), and $1000\ln\alpha_{glass\text{-}water}$ (‰) can be fit by a linear function given above and as Eq. 3 in the main text.

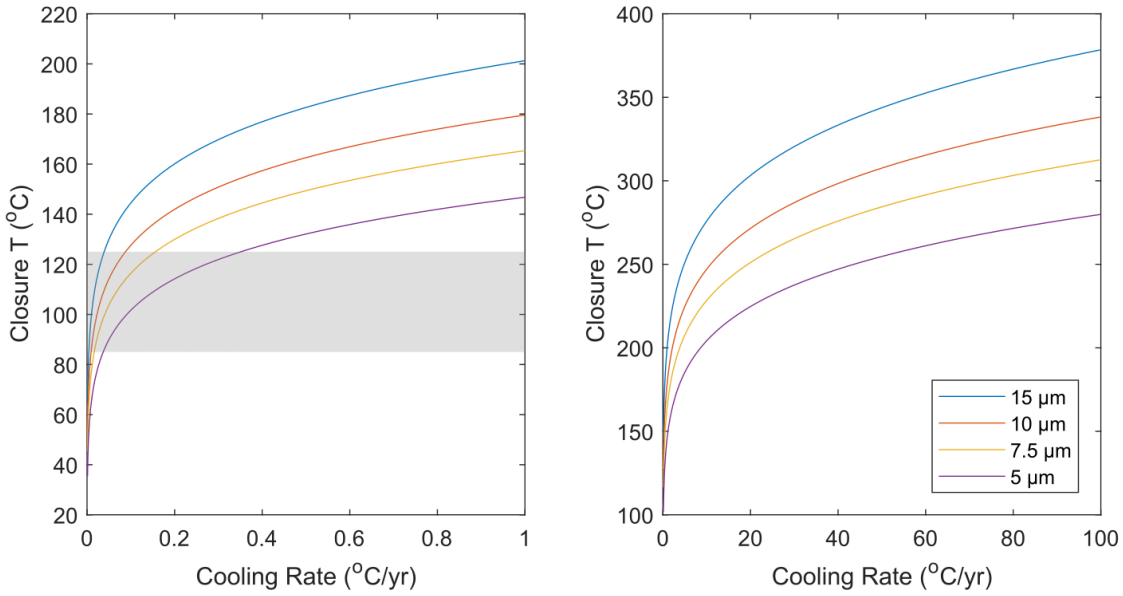

Chapter IV, Figure C3. Closure temperature as a function of cooling rate using the equation of Dodson (1973). As cooling rates increase, T_c asymptotically approaches a high T. A cooling rate of 0.04°C/yr corresponds to a T_c of 100°C for a glass wall half-thickness of 7.5 µm, but may be as high as 0.35°C/yr for thinner bubble wall shards. This slow cooling rate is likely as modeled in ignimbrite cooling models once water can flux through the ignimbrite again around the boiling point (Keating, 2005). The activation energy for water (and therefore hydrogen) in glass is 59500 J/mol (Nolan and Bindeman, 2013) and the D_0 for water and hydrogen is 0.4 x 10^{-12} m^2/s (Zhang and Behrens, 2000). We also assume an intermediate shape between a sheet and a cylinder and a bubble wall half-thickness of the pumices of 7.5 microns.

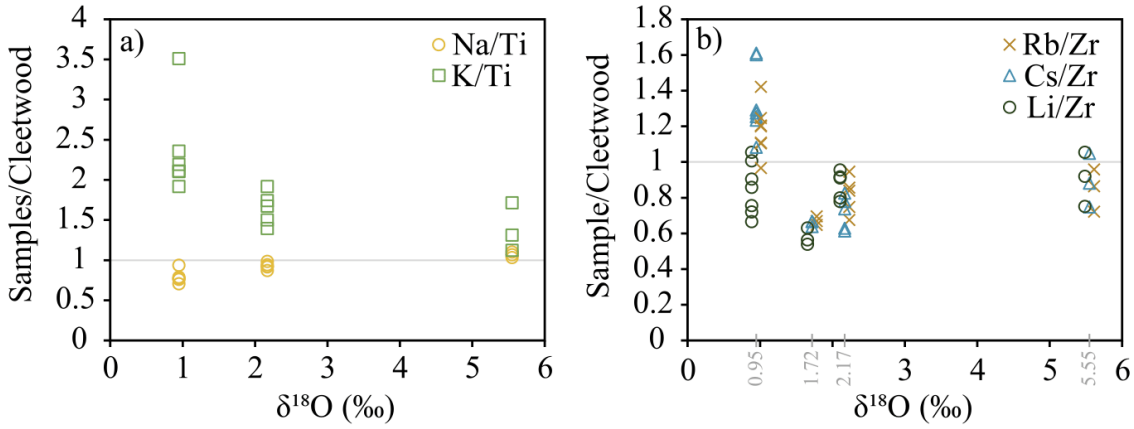

Chapter IV, Figure C4. EPMA (a) and LA-ICP-MS (b) data for Mt. Mazama fumarolic pinnacle glasses normalized to the contemporaneous, co-genetic Cleetwood rhyolite plotted against bulk $\delta^{18}O$. Mobile alkalis are normalized to immobile Ti and Zr concentrations to assess their mobility. The bulk $\delta^{18}O$ of the glass is used as a proxy for water-rock (W/R) ratio. Na becomes moderately depleted with increasing W/R ratio while K becomes enriched. Li, Rb, and Cs do not follow any systematic trends, although Rb and Cs are enriched in the lowest $\delta^{18}O$ (highest W/R) sample. Elemental ratios at a given $\delta^{18}O$ are slightly offset from each other in (b) for clarity but correspond to the grey values on the x-axis.

Chapter IV Supplementary Tables

Chapter IV, Table C1. Sample locations and rock types from the Valley of Ten Thousand Smokes, Katmai National Park, Alaska, USA.

Sample ID	Location	Latitude (dd)	Longitude (dd)	Sample type
ML-30a-1	Mageik Lakes	58.2382	-155.2755	dacite
ML-30a-2	Mageik Lakes	58.2382	-155.2755	dacite
ML-30a-3	Mageik Lakes	58.2382	-155.2755	dacite
ML-31a	Mageik Lakes	58.2378	-155.2773	dacite
ML-33a-1	Mageik Lakes	58.2384	-155.2780	dacite
ML-33a-2	Mageik Lakes	58.2384	-155.2780	dacite
ML-33a-3	Mageik Lakes	58.2384	-155.2780	dacite
ML-30b	Mageik Lakes	58.2382	-155.2755	andesite
ML-31b	Mageik Lakes	58.2378	-155.2773	andesite
ML-33b	Mageik Lakes	58.2384	-155.2780	andesite
KC-15-1	Knife Creek	58.3040	-155.1576	dacite
KC-15-2	Knife Creek	58.3040	-155.1576	dacite
KC-16-1	Knife Creek	58.3040	-155.1576	dacite
KC-16-2	Knife Creek	58.3040	-155.1576	dacite
KC-17-1	Knife Creek	58.3042	-155.1598	dacite
KC-17-2	Knife Creek	58.3042	-155.1598	dacite
KC-18	Knife Creek	58.3061	-155.1665	dacite
KC-19-2	Knife Creek	58.3061	-155.1665	dacite
NV-9-1	Novarupta	58.2271	-155.1265	rhyolite
NV-9-2	Novarupta	58.2271	-155.1265	rhyolite

Chapter IV, Table C2. Sample locations and rock types from the Crater Lake area, Crater Lake National Park (CLNP) and Winema National Forest (WNF), Oregon, USA.

Sample ID	Location	Latitude (dd)	Longitude (dd)	Sample type
PD-53c-1w	CLNP, Pumice Desert	43.0465	-122.1250	altered pumice
PD-53c-1o	CLNP, Pumice Desert	43.0465	-122.1250	altered pumice
PD-53c-2w	CLNP, Pumice Desert	43.0465	-122.1250	altered pumice
PD-53a-1gp	CLNP, Pumice Desert	43.0465	-122.1250	altered pumice
SCCL-57a	CLNP, Sand Creek	42.8799	-122.0375	gas escape pipe
SCCL-54ab	CLNP, Sand Creek	42.8481	-121.9939	andesite
SCCL-54aw	CLNP, Sand Creek	42.8481	-121.9939	andesite
SCCL-54b	CLNP, Sand Creek	42.8481	-121.9939	andesite
SCCL-54cw	CLNP, Sand Creek	42.8481	-121.9939	andesite
SCCL-55	CLNP, Sand Creek	42.8485	-121.9956	andesite
SCCL-56	CLNP, Sand Creek	42.8631	-122.0178	andesite
ACCL-58c	CLNP, Annie Creek			rhyodacite
SC-61-1	WNF, Sand Creek	42.8348	-121.9479	rhyodacite
SC-61-2	WNF, Sand Creek	42.8348	-121.9479	rhyodacite
SC-62-1	WNF, Sand Creek	42.8348	-121.9479	rhyodacite
SC-62-3	WNF, Sand Creek	42.8348	-121.9479	rhyodacite
SC-63-1	WNF, Sand Creek	42.8348	-121.9479	rhyodacite
SC-63-2	WNF, Sand Creek	42.8348	-121.9479	rhyodacite
SC-64-2	WNF, Sand Creek	42.8348	-121.9480	rhyodacite
SC-65-1	WNF, Sand Creek	42.8348	-121.9480	rhyodacite
SC-65-3	WNF, Sand Creek	42.8348	-121.9480	rhyodacite
SC-66-2	WNF, Sand Creek	42.8347	-121.9481	rhyodacite
SC-66-4	WNF, Sand Creek	42.8347	-121.9481	rhyodacite
SC-66-5	WNF, Sand Creek	42.8347	-121.9481	rhyodacite
SC-67-2	WNF, Sand Creek	42.8347	-121.9481	rhyodacite
SC-67-3	WNF, Sand Creek	42.8347	-121.9481	rhyodacite
SC-68-1	WNF, Sand Creek	42.8346	-121.9486	rhyodacite
SC-68-2	WNF, Sand Creek	42.8346	-121.9486	rhyodacite
SC-70-3	WNF, Sand Creek	42.8347	-121.9488	rhyodacite
SC-71-4	WNF, Sand Creek	42.8348	-121.9490	rhyodacite
SC-72-2	WNF, Sand Creek	42.8353	-121.9498	rhyodacite

Chapter IV, Table C3. δD and $\delta^{18}O$ (‰, VSMOW) were measured in separate analytical sessions. Presented values are means of multiple manual injections.

Sample ID	Location	Latitude (dd)	Longitude (dd)	$\delta^{18}O$ (‰)	1 S.E. (‰)	δD (‰)	1 S.E. (‰)
battl01	Battle Lake	59.06124	-154.92123	-15.10	0.48	-110.44	1.66
hamml01	Hammer Lake	58.82948	-155.12036	-15.32	0.08	-114.11	0.33
idval01	Idavain Lake	58.78429	-155.97940	-13.33	0.32	-98.48	1.75
jojol01	Jojo Lake	58.61253	-155.21423	-12.31	0.35	-94.15	1.79
kukal01	Kukaklek Lake	59.17661	-155.27509	-14.94	0.40	-108.97	2.44
kulil01	Kulik Lake	58.97603	-155.02202	-15.98	0.01	-114.54	0.76
lgros01	Lake Grosvenor	58.69017	-155.29798	-14.87	0.42	-112.47	1.93
mirrl01	Mirror Lake	60.36757	-152.93454	-15.63	0.09	-107.49	1.74
murrl01	Murray Lake	58.78453	-155.07230	-16.26	0.63	-114.47	0.80
nonvl01	Nonvianuk Lake	58.97678	-155.19127	-16.81	0.09	-115.00	1.25
piral01	Pirate Lake	59.00415	-154.71960	-15.93	0.17	-107.35	0.57
specl01	Spectacle Lake	59.20781	-154.86394	-14.09	0.30	-100.99	0.65
naknli002	Naknek Lake	58.53148	-155.65945	-16.10	0.24	-111.07	1.45
naknli011	Naknek Lake	58.52379	-155.48985	-16.70	0.04	-113.55	0.73
naknln010	Naknek Lake	58.64213	-155.72232	-15.70	0.21	-111.60	0.86
naknln003	Naknek Lake	58.66759	-155.84348	-15.96	0.18	-113.75	2.16

Chapter IV, Table C4. Total water and hydrogen and oxygen compositions of VTTS glasses. *TCEA, H_2 gas analysis (‰, VSMOW). **CO_2 laser fluorination (‰, VSMOW). ‡TCEA, CO gas analysis (‰, VSMOW). †Calculated from $\delta^{18}O_{bulk}$ and $\delta^{18}O_{wig}$ (‰, VSMOW).

Sample ID	Sample type	H_2O (wt.%)*	δD (‰)*	$\delta^{18}O_{bulk}$ (‰)**	$\delta^{18}O_{bulk}$ 1sd (‰)	$\delta^{18}O_{wig}$ (‰)‡	$\delta^{18}O_{silicate}$ (‰)†
ML-30a-1	dacite	0.95	-114.1	6.49	0.009	-12.8	6.8
ML-30a-2	dacite	1.17	-111.1	6.42	0.030	-11.3	6.8
ML-30a-3	dacite	1.14	-117.8	6.58	0.036	-13.3	7.0
ML-31a	dacite	0.76	-109.0	6.91	0.041	-11.8	7.2
ML-33a-1	dacite	0.86	-94.2	6.83	0.040	-10.6	7.1
ML-33a-2	dacite	1.06	-99.4	7.12	0.023	-11.4	7.5
ML-33a-3	dacite	0.90	-97.9	6.79	0.053	-10.3	7.1
ML-30b	andesite	0.65	-119.9	6.12	0.031	-10.5	6.3
ML-31b	andesite	0.70	-91.6	6.05	0.056	-8.4	6.2
ML-33b	andesite	0.50	-92.8	5.97	0.035	-9.0	6.1
KC-15-1	dacite	3.47	-144.3	5.49	0.039	-10.1	6.4
KC-15-2	dacite	4.18	-152.1	5.87	0.037	-11.5	7.2
KC-16-1	dacite	3.03	-141.7	5.76	0.042	-14.8	6.9
KC-16-2	dacite	3.17	-142.4	5.38	0.033	-15.2	6.5
KC-17-1	dacite	2.76	-132.3	6.27	0.035	-13.9	7.2
KC-17-2	dacite	2.60	-134.3	5.54	0.020	-12.5	6.4
KC-18	dacite	2.31	-138.3	6.14	0.042	-14.1	7.0
KC-19-2	dacite	3.23	-111.8			-13.1	
NV-9-1	rhyolite	0.26	-114.7				
NV-9-2	rhyolite	0.22	-103.7				

Chapter IV, Table C5. Total water and hydrogen and oxygen isotope compositions of Mt. Mazama glasses *TC/EA, H_2 gas analysis (‰, VSMOW); **CO_2 laser fluorination (‰, VSMOW); ‡TC/EA, CO gas analysis (‰, VSMOW); †Calculated from $\delta^{18}O_{bulk}$ and $\delta^{18}O_{wig}$ (‰, VSMOW). Brackets for $\delta'^{18}O_{bulk}$ (‰) in the $\delta'^{17}O_{bulk}$ (‰) column report the linearized $\delta^{18}O_{bulk}$ measured simultaneously with $\delta^{17}O_{bulk}$.

Sample ID	Sample type	H_2O (wt.%)*	D (‰)*	$^{18}O_{bulk}$ (‰)**	$\delta^{18}O_{bulk}$ 1sd (‰)	$^{18}O_{wig}$ (‰)‡	$\delta^{18}O_{silicate}$ (‰)†	$\delta'^{17}O_{bulk}$ (‰)** [$\delta'^{18}O_{bulk}$ (‰)]	$\delta^{17}O_{bulk}$ 1sd (‰) [$\delta^{18}O_{bulk}$ 1sd (‰)]	$\Delta'^{17}O_{bulk}$ (‰)
PD-53c-1w	altered pumice	5.23	-120.2	6.91	0.042	2.4	7.8			
PD-53c-1o	altered pumice	3.62	-133.2	6.08						
PD-53c-2w	altered pumice	4.18	-119.7	6.99	0.027	-12.5	8.4			
PD-53a-1gp	altered pumice	3.54	-112.0	7.08	0.018	-13.7	8.4			
SCCL-57a	gas escape pipe	5.11	-94.9	7.79	0.026	-2.6	8.8			
SCCL-54ab	andesite	1.81	-152.9	3.71	0.031	3.5	3.7			
SCCL-54aw	andesite	1.99	-151.4	3.90	0.050	-2.8	4.1			
SCCL-54b	andesite	1.34	-140.7	4.46	0.037	-10.9	4.8			
SCCL-54cw	andesite	1.91	-149.6	3.59	0.024	-10.0	4.0			
SCCL-55	andesite	0.94	-127.9	5.34	0.020	-5.9	5.5			
SCCL-56	andesite	1.10	-139.6	5.28	0.043	-8.4	5.5			
ACCL-58c	rhyodacite	1.65	-126.5	5.21	0.012	-8.3	5.6			
SC-61-1	rhyodacite	1.71	-147.0	0.95	0.022	-13.7	1.4	0.46 [0.90]	0.004 [0.014]	-0.018
SC-61-2	rhyodacite	1.75	-145.8							
SC-62-1	rhyodacite	1.70	-147.7	3.19	0.028	-12.0	3.6			
SC-62-3	rhyodacite	1.72	-147.8	2.54	0.048	-12.1	3.0			
SC-63-1	rhyodacite	1.82	-140.8	2.17	0.034	-10.0	2.6			
SC-63-2	rhyodacite	1.55	-141.8	3.02	0.033	-10.8	3.4			
SC-64-2	rhyodacite	1.69	-142.7	3.92	0.017	-11.0	4.4			
SC-65-1	rhyodacite	1.67	-142.7	2.31	0.020	-11.5	2.7			
SC-65-3	rhyodacite	1.77	-139.2	3.57	0.029	-11.9	4.1			
SC-66-2	rhyodacite	1.71	-143.2	1.89	0.023	-12.5	2.3			
SC-66-4	rhyodacite	1.73	-145.4	1.53	0.039	-12.3	1.9	1.11 [2.17]	0.013 [0.009]	-0.035
SC-66-5	rhyodacite	1.67	-146.2	1.72	0.024	-12.4	2.1			
SC-67-2	rhyodacite	1.74	-145.3	3.09	0.013	-12.5	3.6			

Table C5 continued.

SC-67-3	rhyodacite	1.84	-143.5	3.85	0.023	-8.5	4.2
SC-68-1	rhyodacite	1.84	-141.4	4.87	0.016	3.2	4.9
SC-68-2	rhyodacite	1.64	-147.5	4.58	0.027	-5.8	4.9
SC-70-3	rhyodacite	1.83	-141.4	4.38	0.021	-13.2	4.9
SC-71-4	rhyodacite	1.96	-132.8	5.55	0.039	-10.3	6.1
SC-72-2	rhyodacite	1.83	-136.8	4.09	0.029	-3.8	4.3

Chapter IV, Table C6. Preliminary D/H fractionation data from ongoing glass hydration experiments at the University of Oregon. Minimum $\Delta D_{glass\text{-}water}$ (‰) give the raw data difference between the initial δD_{glass} and the δD of the hydrating water. *Bracketed values are the $\Delta D_{glass\text{-}water}$ (‰) of the glass after the raw δD_{glass} has been corrected for magmatic H_2O remaining in the glass (initially -110 δD and 0.07 wt.% H_2O). Both the raw and corrected $\Delta D_{glass\text{-}water}$ asymptotically approach a limit. The estimated limits are the inferred $1000ln\alpha_{glass\text{-}water}$ (‰) values. The fit between $10^6/T^2$ (K^{-2}) and $1000ln\alpha_{glass\text{-}water}$ (‰) is given in Figure C2. We note these values were used in for this 2018 publication, but more up to date data are discussed in Chapter II.

T (°C)	Max duration (hrs)	Minimum $\Delta D_{glass\text{-}water}$ (‰)	Inferred $1000ln\alpha_{glass\text{-}water}$ (‰)	Source
10 ± 10			-33	Friedman et al. (1993); Seligman et al. (1993)
175	6000	-22.7 [-12.6*]	-10.5 ± 2.7	Ongoing UO experiments
225	539	-10.7 [-5.7*]	-5.7 ± 1.0	Ongoing UO experiments

Chapter IV, Table C7. Laser ablation inductively coupled plasma mass spectrometry (LA-ICP-MS) trace element data collected at Oregon State University; all data are in ppm. Bold, italicized data are averages of the spots for each pumice sample and are used in Figure C2.

	Li	*B*	*Sc*	*Zn*	*Rb*	*Sr*	*Y*	*Zr*	*Nb*	*Cs*	*Ba*
SCCL-54ab	35.1	17.8	12.1	21.8	82.1	402	22.1	245	5.3	3.3	721
	36.7	16.3	14.2	64.2	80.5	425	19.4	236	5.1	4.0	719
	35.9	***17.1***	***13.2***	***43.0***	***81.3***	***413***	***20.8***	***240***	***5.2***	***3.6***	***720***
SCCL-54aw	23.3	19.6	18.0	7.4	64.0	187	24.0	266	4.3	3.9	561
	26.4	37.4	15.4	9.8	84.3	284	36.2	365	7.0	4.9	785
	28.3	34.7	15.2	12.7	72.6	239	33.5	327	6.0	3.4	695
	26.0	***30.6***	***16.2***	***10.0***	***73.6***	***237***	***31.2***	***319***	***5.8***	***4.1***	***680***
SC-61-1	33.9	28.5	17.2	9.8	107	271	40.1	422	6.5	7.0	864
	34.9	32.3	16.8	21.2	102	288	36.3	402	6.1	8.6	840
	35.8	20.0	13.1	14.6	80.8	310	25.0	294	6.6	5.1	792
	38.3	27.3	19.4	62.2	92.8	291	37.1	420	7.4	6.1	806
	35.7	***27.0***	***16.6***	***26.9***	***95.5***	***290***	***34.6***	***385***	***6.7***	***6.7***	***826***
SC-61-3	38.6	31.7	14.4	20.2	70.0	324	35.9	410	6.4	3.4	913
	37.9	19.1	16.3	28.2	67.6	293	30.1	345	6.7	3.4	854
	39.8	23.0	14.0	43.8	69.1	292	29.1	360	7.0	3.7	849
	35.7	21.3	15.2	26.7	66.8	284	27.0	309	7.1	3.4	838
	43.4	24.2	16.0	53.9	69.4	333	40.7	450	7.4	3.7	903
	39.1	***23.9***	***15.2***	***34.6***	***68.6***	***305***	***32.6***	***375***	***6.9***	***3.5***	***872***
SC-66-5	29.1	24.2	14.7	13.0	58.5	273	34.7	382	6.1	3.4	758
	27.1	26.0	16.3	4.5	63.2	324	38.0	397	6.8	3.4	821
	26.4	25.1	15.3	4.9	59.8	320	34.4	405	6.6	3.6	823
	27.5	***25.1***	***15.5***	***7.5***	***60.5***	***306***	***35.7***	***395***	***6.5***	***3.5***	***801***
SC-71-4	29.9	21.4	14.0	10.6	53.2	227	22.0	269	6.3	3.2	733
	30.3	22.5	12.0	13.0	52.2	190	18.9	238	5.6	3.3	696
	30.1	***22.0***	***13.0***	***11.8***	***52.7***	***209***	***20.4***	***254***	***5.9***	***3.3***	***714***

Table C7 continued.

	La	*Ce*	*Nd*	*Sm*	*Eu*	*Gd*	*Dy*	*Er*	*Yb*	*Hf*	*Pb*	*Th*	*U*
SCCL-54ab	21.3	38.3	23.0	4.2	1.1	4.2	3.6	2.6	2.3	5.3	11.2	5.4	1.4
	23.1	40.5	25.9	3.9	1.4	3.9	3.6	2.5	2.5	6.3	14.2	6.8	1.6
	22.2	***39.4***	***24.5***	***4.1***	***1.3***	***4.0***	***3.6***	***2.6***	***2.4***	***5.8***	***12.7***	***6.1***	***1.5***
SCCL-54aw	21.7	32.7	24.4	4.3	0.1	4.7	3.7	2.2	2.7	5.8	6.4	5.6	1.8
	27.3	44.9	31.1	6.3	1.0	5.3	6.4	3.7	3.7	9.4	9.5	8.1	2.3
	23.6	37.2	26.3	5.0	0.8	5.4	5.2	3.9	3.3	7.6	10.7	6.8	1.8
	24.2	***38.3***	***27.2***	***5.2***	***0.6***	***5.1***	***5.1***	***3.3***	***3.2***	***7.6***	***8.9***	***6.8***	***2.0***
SC-61-1	27.2	43.3	30.0	5.5	1.1	6.3	6.3	4.6	4.2	10.6	9.1	8.5	2.4
	30.6	46.5	32.7	5.4	1.2	7.2	6.5	4.5	4.1	11.4	11.0	9.6	2.9
	21.4	42.1	24.0	4.3	1.1	4.5	4.3	2.6	2.4	7.4	7.9	7.0	2.1
	27.5	45.4	32.5	5.2	1.1	6.1	6.1	4.4	3.6	9.6	11.2	8.4	2.4
	26.7	***44.3***	***29.8***	***5.1***	***1.1***	***6.0***	***5.8***	***4.0***	***3.6***	***9.7***	***9.8***	***8.4***	***2.4***
SC-61-3	28.6	46.7	27.9	5.7	1.0	4.7	6.2	5.3	3.2	9.3	12.1	8.9	2.6
	26.0	50.0	28.8	6.0	1.2	4.5	5.0	4.3	2.4	7.9	11.6	7.4	2.2
	25.8	44.3	29.3	5.1	1.0	5.8	5.7	4.0	2.7	9.0	11.8	9.0	2.3
	22.5	44.3	23.2	5.8	1.1	5.0	4.7	3.4	2.9	8.2	11.0	7.6	2.4
	30.0	47.2	31.7	6.5	1.3	6.9	6.2	4.6	4.7	10.7	13.7	9.0	2.5
	26.6	***46.5***	***28.2***	***5.8***	***1.1***	***5.4***	***5.6***	***4.3***	***3.2***	***9.0***	***12.0***	***8.4***	***2.4***
SC-66-5	26.2	41.1	28.0	6.1	1.2	6.4	5.7	4.8	3.7	8.7	9.9	8.0	2.1
	26.5	43.1	29.5	6.1	1.0	5.6	5.7	4.5	3.1	8.9	8.7	8.5	2.2
	27.8	40.9	27.0	5.1	1.1	5.8	5.3	3.9	3.0	9.1	8.4	7.1	2.0
	26.9	***41.7***	***28.2***	***5.8***	***1.1***	***6.0***	***5.6***	***4.4***	***3.3***	***8.9***	***9.0***	***7.9***	***2.1***
SC-71-4	19.9	41.7	21.1	4.8	0.8	3.7	4.5	2.5	2.2	6.7	7.4	6.1	2.2
	17.2	36.8	19.3	3.7	0.7	3.6	3.4	2.9	2.1	6.1	8.2	5.5	2.4
	18.6	***39.2***	***20.2***	***4.2***	***0.8***	***3.7***	***3.9***	***2.7***	***2.2***	***6.4***	***7.8***	***5.8***	***2.3***

Chapter IV, Table C8. X-ray fluorescence (XRF) bulk chemistry data collected at Pomona College.

Sample ID		*SiO_2 (wt.%)*	*TiO_2 (wt.%)*	*Al_2O_3 (wt.%)*	*Fe_2O_3 (wt.%)*	*MnO (wt.%)*	*MgO (wt.%)*	*CaO (wt.%)*	*Na_2O (wt.%)*	*K_2O (wt.%)*	*P_2O_5 (wt.%)*	*Total*
PD-53a-gp	bulk	56.17	0.94	22.32	6.57	0.08	2.50	6.88	3.18	0.86	0.28	99.78
SCCL-54a	bulk	57.92	0.85	18.93	6.07	0.09	3.47	7.27	3.76	1.23	0.18	99.77
SC-66-5	glass	70.10	0.49	15.25	2.83	0.06	0.82	2.50	4.64	3.00	0.11	99.80
SC-71-4	glass	70.26	0.52	15.32	2.88	0.06	0.80	2.36	4.76	2.73	0.11	99.80
SC-61-1	glass	70.47	0.48	15.09	2.65	0.05	0.72	2.23	3.97	4.03	0.10	99.80

APPENDIX D

CHAPTER V SUPPLEMENTARY INFORMATION AND FIGURES

Text D1. Calculation of glass H_2O

Glass H_2O concentrations may be corrected in two ways. First is to use the modal percentage of glass/groundmass reported for the explosively erupted samples reported in Coombs et al. (2013). We can assume that effectively all H_2O occurs in the glass phase as most phenocrysts are nominally anhydrous, except for hornblende. The highest H_2O hornblende erupted at Redoubt is ~1.5 wt% H_2O (Figure D3; data repository). With ≤8% modal abundance in any eruptive products, the maximum total H_2O contribution of hornblende would be 0.12 wt% and typically much lower. Furthermore, because the higher H_2O hornblende measurements are also high δD, increasing hornblende modes would oppose the negative correlation between H_2O and δD (Figure 1).

The second method is used to generate a range of reasonable H_2O contents and consider microlite contents. We assume that K is perfectly incompatible in the phenocryst phases in Redoubt magmas, so all K occurs in the glass. The ratio of whole rock K_2O to glass K_2O yields the glass fraction of the sample. As none of the sample in Coombs et al. (2013) have both K_2O data for whole rock and glass samples for a sample in this work, we use the full range of relevant samples. These authors report a K_2O of 1.23-1.61 wt% in whole rock samples from the explosive phase of the eruption. Glass K_2O composition reported for proximal tephra samples AT-1609, AT-1610, and AT-1611 (we report data for AT-1611) range between 2.45 and 3.72 wt%. This yields a minimum and maximum glass fraction of 33% and 66%, respectively, which results in a glass H_2O range with a factor of 2.

We treat all samples with the same correction using the former approach (glass modal percentages of 56%). Weakly magnetic and non-magnetic ash separates and bulk ashes form overlapping, inversely correlated H_2O–δD trends over the full range of bulk ash H_2O and δD (Figure D1). No obvious variations in glass content between samples were observed in our own visual inspection with a binocular microscope. Backscatter electron images of ash from a range of depositional distances appear qualitatively similar within the analyzed sized fraction of 63-125 μm (Figure D2). The primary difference

between non-magnetic and weakly magnetic separates is the proportion of plagioclase relative to other phenocryst phases. Finally, the density of dacitic to rhyolitic melt is less than the density of mineral phases present in the Redoubt eruptive products. So if anything, glass fraction, and therefore bulk ash H_2O, should increase with distance if glasses are homogeneously hydrated.

The exception to this approach may be the ultra-distal tephra samples, which would require a smaller correction if their glass fraction were significantly higher. Most samples yielded significant proportions of larger size fractions (>125 μm), but samples deposited beyond 270 km did not yield any. Therefore, the 63-125 μm sieve fraction that was analyzed for all tephra samples may be skewed towards smaller particle sizes and higher glass fractions. Figure 1a shows that this may only be true for 3 of 5 ultra-distal tephra samples (open symbols).

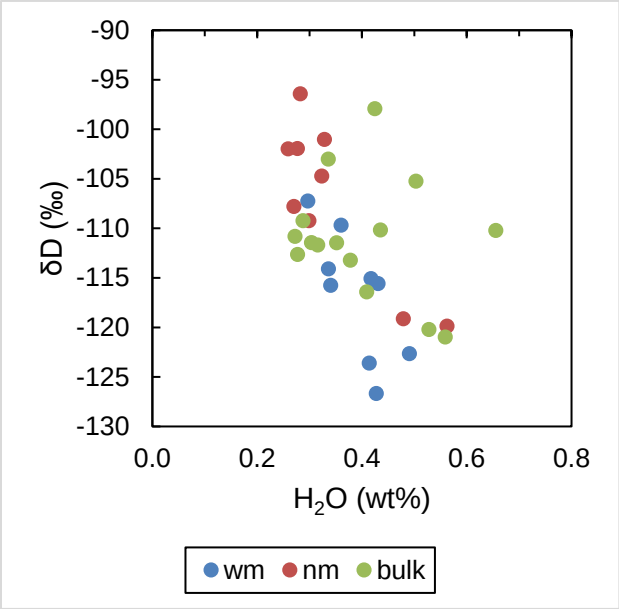

Figure D1. Weakly magnetic (wm, blue), non-magnetic (nm, orange), and bulk tephra (grey) H_2O and δD data. All three suites span an equivalent range of H_2O values and are all negatively correlated with δD. The three bulk samples at high δD for their H_2O are the ultra-distal samples discussed in Text D1.

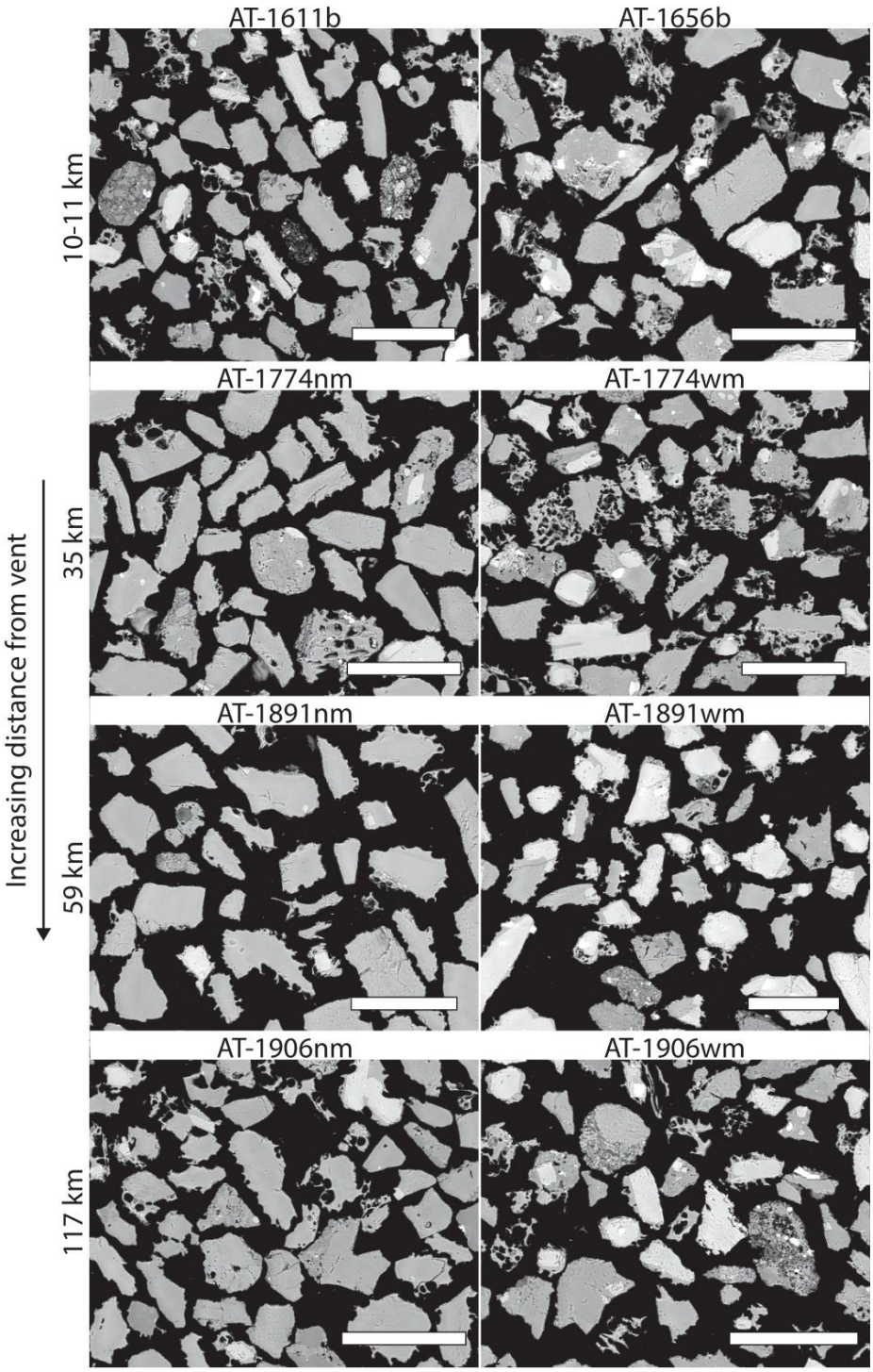

Figure D2. Backscatter electron images of Redoubt tephra including bulk (b), non-magnetic (nm) and weakly magnetic fractions as a function of increasing distance from the vent. Scale bars are 200 μm.

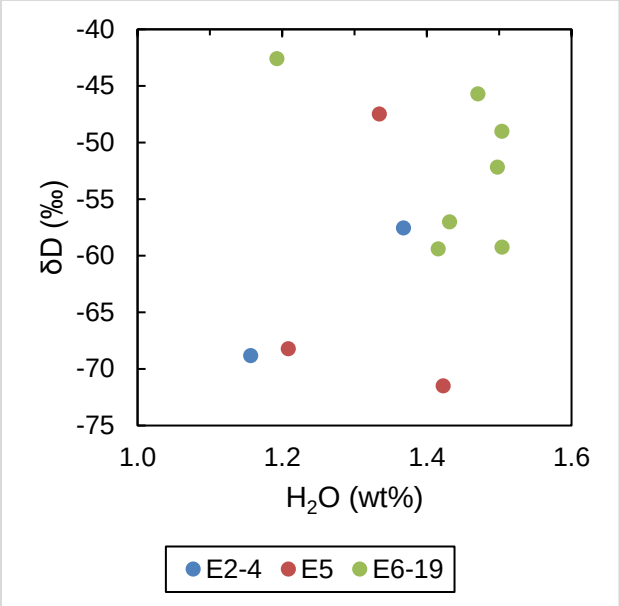

Figure D3. Hornblende H_2O and δD compositions from Event 2-4 (blue), Event 5 (orange) and Event 6-19 (grey) tephra samples. The highest undegassed hornblende composition (>1.4 wt% H_2O) has a δD of −46‰, which given an equilibrium magmatic δD of ~−35‰ using the hornblende-melt δD fractionations of Suzuoki and Epstein (1976) and the magmatic storage temperatures of Coombs et al. (2013).

APPENDIX E

CHAPTER VI SUPPLEMENTARY INFORMATION AND FIGURES

Text E1. FTIR experiment

A dozen aliquots of ~6 mg of UOB were wrapped in Ag capsules and dropped into the TC/EA under normal operating conditions, but without standards or any other materials. The melt collected in the graphite crucible contained immiscible basaltic melt and liquid Ag. At the conclusion of the experiment, the quenched melt was collected from the crucible and prepared as a doubly polished 840 μm thick wafer for FTIR analysis. Three 150 μm x 150 μm spots were analyzed using white light. These spots were chosen to avoid vesicles at all levels in the wafer. Despite adequate signal at each spot, H_2O_t was undetectable (<0.01 wt%) at the 3500 cm^{-1} peak in the IR spectra (Figures S1, S2). These results indicate that no H_2O is retained in the basaltic melt. However, we note that sustained temperatures above the basalt liquidus for the duration and during initial cooling of the furnace may have facilitated prolonged extraction of small amounts of residual H_2O. Water extracted beyond the measurement timescales of <2 minutes may instead have contributed to elevated background counts.

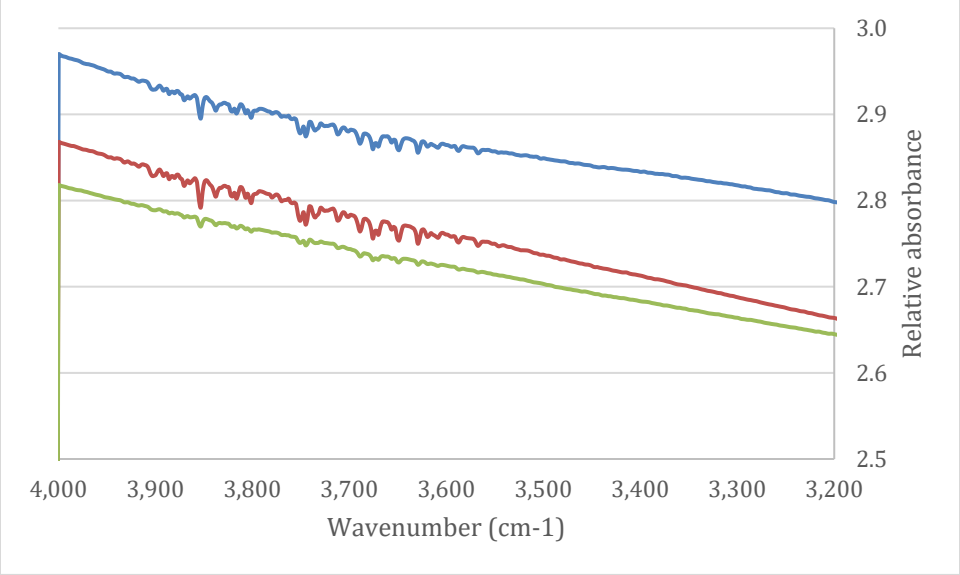

Figure E1. Zoom in of the 3500 cm^{-1} peak for H_2O_t in the IR spectra for each of the 3 spots. Small, broad humps in relative absorbance over several hundred cm^{-1} were measured but for the thickness of 840 μm still yielded <0.01 wt% H_2O_t.

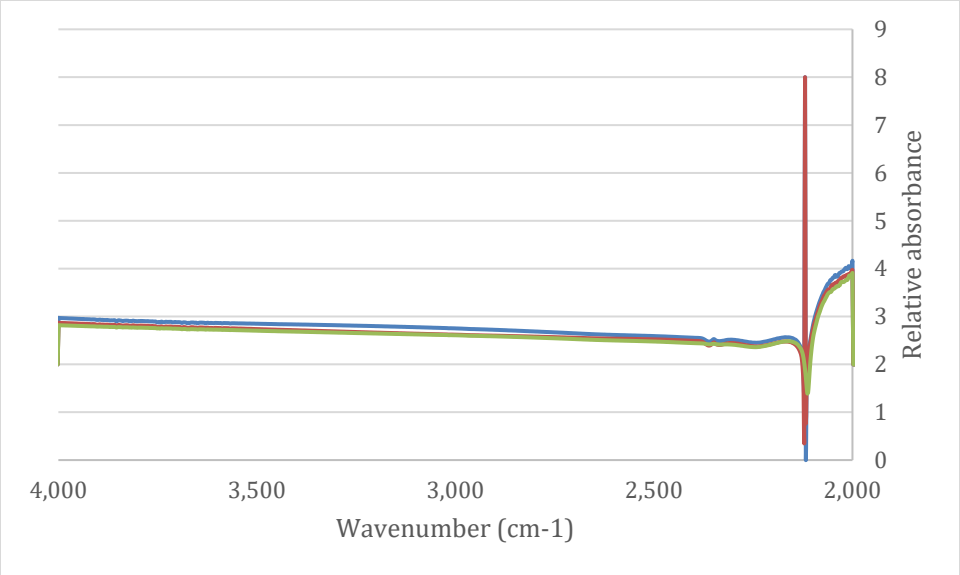

Figure E2. Full spectra for the 3 measurements. The large peak at ~2200 cm^{-1} is CO_2. No peaks for H_2O species are detectable.

Text E2. Peak tail experiment

Water and δD data are determined from automatic peak detection. If there is a significant isotope fractionation, the heavier isotope may be undercounted in the automatically determined peak. We test this by extending the measurement duration (usually ~60 seconds) or peak width by 30 seconds and 60 seconds for an analytical session of UOB analyses (n = 14). Some samples increased in δD while others decreased with increased peak width. Some samples increased in δD after the 30 s extension but decreased after the 60 s increase in the peak width. A few samples had a pronounced increased in δD with extended peak width and this increased the mean δD from −72.6‰ to −70.9‰ (30 s) and then to −70.4‰ (60s). However, the median only changed from −72.2‰ to −72.0‰, suggesting that there is some noise in the measured δD, but basaltic glasses does not generate long ^{2}H-enriched peaks.

REFERENCES CITED

Chapter II

Anovitz L. M., Cole D. R. and Fayek M. (2008) Mechanisms of rhyolitic glass hydration below the glass transition. Am. Mineral. 93, 1166–1178.

Anovitz L. M., Cole D. R. and Riciputi L. R. (2009) Low-temperature isotopic exchange in obsidian: Implications for diffusive mechanisms. Geochim. Cosmochim. Acta 73, 3795–3806.

Anovitz L. M., Elam J. M., Riciputi L. R. and Cole D. R. (2004) Isothermal time-series determination of the rate of diffusion of water in Pachuca obsidian. Archaeometry 2, 301–326.

Von Aulock F. W., Nichols A. R. L., Kennedy B. M. and Oze C. (2013) Timescales of texture development in a cooling lava dome. Geochim. Cosmochim. Acta 114, 72–80.

Befus K. S., Watkins J., Gardner J. E., Richard D., Befus K. M., Miller N. R. and Dingwell D. B. (2015) Spherulites as in-situ recorders of thermal history in lava flows. Geology 43, 647–650.

Behrens H. and Nowak M. (1997) The mechanisms of water diffusion in polymerized silicate melts. Contrib. to Mineral. Petrol. 126, 377–385.

Behrens H., Zhang Y., Leschik M., Wiedenbeck M., Heide G. and Frischat G. H. (2007) Molecular H2O as carrier for oxygen diffusion in hydrous silicate melts. Earth Planet. Sci. Lett. 254, 69–76.

Bindeman I. N. and Lowenstern J. B. (2016) Low-δD hydration rinds in Yellowstone perlites record rapid syneruptive hydration during glaical and interglacial conditions. Contrib. to Mineral. Petrol. 171.

Breitkreuz C. (2013) Spherulites and lithophysae-200 years of investigation on high-temperature crystallization domains in silica-rich volcanic rocks. Bull. Volcanol. 75, 1–16.

Canavan R. R., Carrapa B., Clementz M. T., Quade J., DeCelles P. G. and Schoenbohm L. M. (2014) Early cenozoic uplift of the Puna plateau, central andes, based on stable isotope paleoaltimetry of hydrated volcanic glass. Geology 42, 447–450.

Cassel E. J. and Breecker D. O. (2017) Long-term stability of hydrogen isotope ratios in hydrated volcanic glass. Geochim. Cosmochim. Acta 200, 67–86.

Cassel E. J., Breecker D. O., Henry C. D., Larson T. E. and Stockli D. F. (2014) Profile of a paleo-orogen: High topography across the present-day Basin and Range from 40 to 23 Ma. Geology 42, 1007–1010.

Cassel E. J., Graham S. A. and Chamberlain C. P. (2009) Cenozoic tectonic and topographic evolution of the northern Sierra Nevada, California, through stable isotope paleoaltimetry in volcanic glass. Geology 37, 547–550.

Cassel E. J., Graham S. A., Chamberlain C. P. and Henry C. D. (2012) Early Cenozoic topography, morphology, and tectonics of the northern Sierra Nevada and western Basin and Range. Geosphere 8, 229–249.

Cerling T. E., Brown F. H. and Bowman J. R. (1985) Low-temperature alteration of volcanic glass: hydration, Na, K, 18O and Ar mobility. Chem. Geol. 52, 281–293.

Colwyn D. A. and Hren M. T. (2019) An abrupt decrease in Southern Hemisphere terrestrial temperature during the Eocene–Oligocene transition. Earth Planet. Sci. Lett. 512, 227–235.

Cullen J. T., Hurwitz S., Barnes J. D., Lassiter J. C., Penniston-Dorland S., Kasemann S. A. and Thordsen J. J. (2019) Temperature-dependent variations in mineralogy, major element chemistry and the stable isotopes of boron, lithium and chlorine resulting from hydration of rhyolite: Constraints from hydrothermal experiments at 150 to 350 °C and 25 MPa. Geochim. Cosmochim. Acta 261, 269–287.

Delaney J. R. and Karsten J. L. (1982) Ion microprobe studies of water in silicate melts: temperature-dependent water diffusion in obsidian. Earth Planet. Sctence Lett. 59, 420–428.

Dettinger M. P. and Quade J. (2015) Testing the analytical protocols and calibration of volcanic glass for the reconstruction of hydrogen isotopes in paleoprecipitation. Mem. Geol. Soc. Am. 212, 261–276.

Dingwell D. B. (1995) Relaxation in silicate melts: some applications. In Reviews in Mineralogy and Geochemistry: Structure, Dynamics and Properties of Silicate Melts pp. 21–66.

Dingwell D. B. and Webb S. L. (1990) Relaxation in silicate melts. Eur. J. Mineral., 427–449.

Eichelberger J. C. and Westrich H. R. (1981) Magmatic volatiles in explosive rhyolitic eruptions. Geophys. Res. Lett. 8, 757–760.

Friedman I., Gleason J., Sheppard R. A. and Gude A. J. (1993a) Deuterium Fractionation as Water Diffuses into Silicic Volcanic Ash. In Climate Change in Continental Isotopic Records (eds. P. K. Swart, K. C. Lohmann, J. Mckenzie, and S. Savin). pp. 321–323.

Friedman I., Gleason J. and Warden A. (1993b) Ancient climate from deuterium content of water in volcanic glass. In Climate Change in Continental Isotopic Records (eds. P. K. Swart, K. C. Lohmann, J. Mckenzie, and S. Savin). pp. 309–319.

Friedman I. and Long W. (1976) Hydration Rate of Obsidian. Science. 191, 347–352.

Friedman I. and Obradovich J. (1981) Obsidian Hydration Dating of Volcanic Events. Quat. Res. 16, 37–47.

Friedman I. and Smith R. L. (1960) A New Dating Method Using Obsidian: Part I, The Development of the Method. Am. Antiq. 25, 476–493.

Friedman I., Smith R. L. and Long W. D. (1966) Hydration of Natural Glass and Formation of Perlite. Geol. Soc. Am. Bull. 77, 323–328.

Gardner J. E., Befus K. S., Watkins J., Hesse M. and Miller N. (2012) Compositional gradients surrounding spherulites in obsidian and their relationship to spherulite growth and lava cooling. Bull. Volcanol. 74, 1865–1879.

Giachetti T., Gonnermann H. M., Gardner J. E., Shea T. and Gouldstone A. (2015) Discriminating secondary from magmatic water in rhyolitic matrix-glass of volcanic pyroclasts using thermogravimetric analysis. Geochim. Cosmochim. Acta 148, 457–476.

Giachetti T., Hudak M. R., Shea T., Bindeman I. N. and Hoxsie E. C. (2020) D/H ratios and H2O contents record degassing and rehydration history of rhyolitic magma and pyroclasts. Earth Planet. Sci. Lett. 530.

Hess K. U. and Dingwell D. B. (1996) Viscosities of hydrous leucogranitic melts: a non-Arrhenian model. Am. Mineral. 81, 1297–1300.

Horita J. and Wesolowski D. J. (1994) Liquid-vapor fractionation of oxygen and hydrogen isotopes of water from the freezing to the critical temperature. Geochim. Cosmochim. Acta 58, 3425–3437.

Hudak M. R. and Bindeman I. N. (2018) Conditions of pinnacle formation and glass hydration in cooling ignimbrite sheets from H and O isotope systematics at Crater Lake and the Valley of Ten Thousand Smokes. Earth Planet. Sci. Lett. 500, 56–66.

Jackson L. J., Horton B. K., Beate B. O., Bright J. and Breecker D. O. (2019) Testing stable isotope paleoaltimetry with Quaternary volcanic glasses from the Ecuadorian Andes. Geology 47, 411–414.

Keating G. N. (2005) The role of water in cooling ignimbrites. J. Volcanol. Geotherm. Res. 142, 145–171.

Lapham K. E., Holloway J. R. and Delaney J. R. (1984) Diffusion of H2O and D2O in obsidian at elevated temperatures and pressures. J. Non. Cryst. Solids 67, 179–191.

Liritzis I. and Laskaris N. (2011) Fifty years of obsidian hydration dating in archaeology. J. Non. Cryst. Solids 357, 2011–2023.

Liu Y., Zhang Y. and Behrens H. (2005) Solubility of H2O in rhyolitic melts at low pressures and a new empirical model for mixed H2O-CO2 solubility in rhyolitic melts. J. Volcanol. Geotherm. Res. 143, 219–235.

Loewen M. W., Bindeman I. N. and Melnik O. E. (2017) Eruption mechanisms and short duration of large rhyolitic lava flows of Yellowstone. Earth Planet. Sci. Lett. 458, 80–91.

Manga M. (1998) Orientation distribution of microlites in obsidian. J. Volcanol. Geotherm. Res. 86, 107–115.

Martin E., Bindeman I., Balan E., Palandri J., Seligman A. and Villemant B. (2017) Hydrogen isotope determination by TC/EA technique in application to volcanic glass as a window into secondary hydration. J. Volcanol. Geotherm. Res.

Mazer J. J., Stevenson C. M., Ebert W. L. and Bates J. K. (1991) The experimental hydration of obsidian as a function of relative humidty and temperature. Am. Antiq. 56, 504–513.

Michels J. W., Tsong I. S. T. and Nelson C. M. (1983) Obsidian Dating and East African Archeology. Science. 219, 361–366.

Mitchell S. J., McIntosh I. M., Houghton B. F., Carey R. J. and Shea T. (2018) Dynamics of a powerful deep submarine eruption recorded in H2O contents and speciation in rhyolitic glass: The 2012 Havre eruption. Earth Planet. Sci. Lett. 494, 135–147.

Newman S. and Lowenstern J. B. (2002) Volatile Calc: a silicate melt – H2O – CO2 solution model written in Visual Basic for excel. Comput. Geosci. 28, 597–604.

Ni H. and Zhang Y. (2008) H2O diffusion models in rhyolitic melt with new high pressure data. Chem. Geol. 250, 68–78.

Nolan G. S. and Bindeman I. N. (2013) Experimental investigation of rates and mechanisms of isotope exchange (O, H) between volcanic ash and isotopically-labeled water. Geochim. Cosmochim. Acta 111, 5–27.

O'Neil J. R. and Taylor H. P. (1967) The oxygen isotope and cation exchange chemistry of feldspars. Am. Mineral. 52, 1414–1437.

Randolph-Flagg N., Breen S., Hernandez A., Manga M. and Self S. (2017) Evenly spaced columns in the Bishop Tuff (California, USA) as relicts of hydrothermal cooling. Geology 45, 1015–1018.

Riciputi L. R., Elam J. M., Anovitz L. M. and Cole D. R. (2002) Obsidian Diffusion Dating by Secondary Ion Mass Spectrometry: A Test using Results from Mound 65, Chalco, Mexico. J. Archaeol. Sci. 29, 1055–1075.

Rogers A. K. and Duke D. (2011) An archaeologically validated protocol for computing obsidian hydration rates from laboratory data. J. Archaeol. Sci. 38, 1340–1345.

Roskosz M., Deloule E., Ingrin J., Depecker C., Laporte D., Merkel S., Remusat L. and Leroux H. (2018) Kinetic D/H fractionation during hydration and dehydration of silicate glasses, melts and nominally anhydrous minerals. Geochim. Cosmochim. Acta 233, 14–32.

Ryan A. G., Russell J. K., Nichols A. R. L., Hess K.-U. and Porritt L. A. (2015) Experiments and models on H2O retrograde solubility in volcanic systems. Am. Mineral. 100, 774–786.

Seligman A. N., Bindeman I., Van Eaton A. and Hoblitt R. (2018) Isotopic insights into the degassing and secondary hydration of volcanic glass from the 1980 eruptions of Mount St. Helens. Bull. Volcanol. 80.

Seligman A. N. and Bindeman I. N. (2019) The δ18O of primary and secondary waters in hydrous volcanic glass. J. Volcanol. Geotherm. Res. 371, 72–85.

Seligman A. N., Bindeman I. N., Watkins J. M. and Ross A. M. (2016) Water in volcanic glass: From volcanic degassing to secondary hydration. Geochim. Cosmochim. Acta 191, 216–238.

Sharp Z. D., Gibbons J. A., Maltsev O., Atudorei V., Pack A., Sengupta S., Shock E. L. and Knauth L. P. (2016) A calibration of the triple oxygen isotope fractionation in the SiO2-H2O system and applications to natural samples. Geochim. Cosmochim. Acta 186, 105–119.

Shelby J. E. (1977) Molecular diffusion and solubility of hydrogen isotopes in vitreous silica. J. Appl. Phys. 48, 3387–3394.

Sparks R. S. J. (1978) The dynamics of bubble formation and growth in magmas: A review and analysis. J. Volcanol. Geotherm. Res. 3, 1–37.

Stevenson C. M., Ladefoged T. N. and Novak S. W. (2013) Prehistoric settlement chronology on Rapa Nui, Chile: Obsidian hydration dating using infrared photoacoustic spectroscopy. J. Archaeol. Sci. 40, 3021–3030.

Stroncik N. A. and Schmincke H. U. (2001) Evolution of palagonite: Crystallization, chemical changes, and element budget. Geochemistry, Geophys. Geosystems 2.

Sturchio N. C., Keith T. E. C. and Muehlenbachs K. (1990) Oxygen and carbon isotope ratios of hydrothermal minerals from Yellowstone drill cores. J. Volcanol. Geotherm. Res. 40, 23–37.

Thien B. M. J., Kosakowski G. and Kulik D. A. (2015) Differential alteration of basaltic lava flows and hyaloclastites in Icelandic hydrothermal systems. Geotherm. Energy 3, 11.

Trafton K., Giachetti T. and Kruse H. (2019) Pumice: The size dependency of density. In American Geophysical Union Fall Meeting San Francisco, CA.

Watkins J. M., Manga M. and Depaolo D. J. (2012) Bubble geobarometry: A record of pressure changes, degassing, and regassing at Mono Craters, California. Geology, 699–702.

Watkins J., Manga M., Huber C. and Martin M. (2009) Diffusion-controlled spherulite growth in obsidian inferred from H2O concentration profiles. Contrib. to Mineral. Petrol. 157, 163–172.

Wilding M. C., Webb S. L. and Dingwell D. B. (1995) Evaluation of a relaxation geospeedometer for volcanic glasses. Chem. Geol. 125, 137–148.

Wilding M., Dingwell D., Batiza R. and Wilson L. (2000) Cooling rates of hyaloclastites: Applications of relaxation geospeedometry to undersea volcanic deposits. Bull. Volcanol. 61, 527–536.

Xu Z. and Zhang Y. (2002) Quench rates in air, water, and liquid nitrogen, and inference of temperature in volcanic eruption columns. Earth Planet. Sci. Lett. 200, 315–330.

Yokoyama T., Okumura S. and Nakashima S. (2008) Hydration of rhyolitic glass during weathering as characterized by IR microspectroscopy. Geochim. Cosmochim. Acta 72, 117–125.

Zhang Y. and Behrens H. (2000) H2O diffusion in rhyolitic melts and glasses. Chem. Geol. 169, 243–262.

Zhang Y., Jenkins J. and Xu Z. (1997) Kinetics of the reaction H2O + O →2OH in rhyolitic glasses upon cooling: Geospeedometry and comparison with glass transition. Geochim. Cosmochim. Acta 61, 2167‑2173.

Zhang Y., Stolper E. M. and Wasserburg G. J. (1991) Diffusion of water in rhyolitic glasses. Geochim. Cosmochim. Acta 55, 441–456.

Zhang Y., Xu Z., Zhu M. and Wang H. (2007) Silicate melt properties and volcanic eruptions. Rev. Geophys. 45, 1–27.

Chapter III

Anovitz L. M., Cole D. R. and Fayek M. (2008) Mechanisms of rhyolitic glass hydration below the glass transition. Am. Mineral. 93, 1166–1178.

Anovitz L. M., Cole D. R. and Riciputi L. R. (2009) Low-temperature isotopic exchange in obsidian: Implications for diffusive mechanisms. Geochim. Cosmochim. Acta 73, 3795–3806.

Anovitz L. M., Elam J. M., Riciputi L. R. and Cole D. R. (2004) Isothermal time-series determination of the rate of diffusion of water in Pachuca obsidian. Archaeometry 2, 301–326.

Behrens H., Zhang Y., Leschik M., Wiedenbeck M., Heide G. and Frischat G. H. (2007) Molecular H2O as carrier for oxygen diffusion in hydrous silicate melts. Earth Planet. Sci. Lett. 254, 69–76.

Bindeman I. N. and Lowenstern J. B. (2016) Low-δD hydration rinds in Yellowstone perlites record rapid syneruptive hydration during glaical and interglacial conditions. Contrib. to Mineral. Petrol. 171.

Capuano R. M. (1992) The temperature dependence of hydrogen isotope fractionation between clay minerals and water: evidence from a geopressurized system. Geochim. Cosmochim. Acta 56, 2547–2554.

Cassel E. J. and Breecker D. O. (2017) Long-term stability of hydrogen isotope ratios in hydrated volcanic glass. Geochim. Cosmochim. Acta 200, 67–86.

Cassel E. J., Breecker D. O., Henry C. D., Larson T. E. and Stockli D. F. (2014) Profile of a paleo-orogen: High topography across the present-day Basin and Range from 40 to 23 Ma. Geology 42, 1007–1010.

Cassel E. J., Graham S. A. and Chamberlain C. P. (2009) Cenozoic tectonic and topographic evolution of the northern Sierra Nevada, California, through stable isotope paleoaltimetry in volcanic glass. Geology 37, 547–550.

Cassel E. J., Graham S. A., Chamberlain C. P. and Henry C. D. (2012) Early Cenozoic topography, morphology, and tectonics of the northern Sierra Nevada and western Basin and Range. Geosphere 8, 229–249.

Castro J. M., Bindeman I. N., Tuffen H. and Ian Schipper C. (2014) Explosive origin of silicic lava: Textural and δD-H2O evidence for pyroclastic degassing during rhyolite effusion. Earth Planet. Sci. Lett. 405, 52–61. Available at: http://dx.doi.org/10.1016/j.epsl.2014.08.012.

Christensen J. N., Watkins J. M., Devriendt L. S., DePaolo D. J., Conrad M. E., Voltolini M., Yang W. and Dong W. (2021) Isotopic Fractionation Accompanying CO2 Hydroxylation and Carbonate. Geochim. Cosmochim. Acta. Available at: https://doi.org/10.1016/j.gca.2021.01.003.

Colwyn D. A. and Hren M. T. (2019) An abrupt decrease in Southern Hemisphere terrestrial temperature during the Eocene–Oligocene transition. Earth Planet. Sci. Lett. 512, 227–235.

Coumans J. P., Llewellin E. W., Humphreys M. C. S., Nowak M., Brooker R. A., Mathias S. A. and McIntosh I. M. (2020) An experimentally-validated numerical model of diffusion and speciation of water in rhyolitic silicate melt. Geochim. Cosmochim. Acta 276, 219–238. Available at: https://doi.org/10.1016/j.gca.2020.02.026.

Cullen J. T., Hurwitz S., Barnes J. D., Lassiter J. C., Penniston-Dorland S., Kasemann S. A. and Thordsen J. J. (2019) Temperature-dependent variations in mineralogy, major element chemistry and the stable isotopes of boron, lithium and chlorine resulting from hydration of rhyolite: Constraints from hydrothermal experiments at 150 to 350 °C and 25 MPa. Geochim. Cosmochim. Acta 261, 269–287.

Dettinger M. P. and Quade J. (2015) Testing the analytical protocols and calibration of volcanic glass for the reconstruction of hydrogen isotopes in paleoprecipitation. Mem. Geol. Soc. Am. 212, 261–276.

Dingwell D. B. (1995) Relaxation in silicate melts: some applications. In Reviews in Mineralogy and Geochemistry: Structure, Dynamics and Properties of Silicate Melts pp. 21–66.

Dingwell D. B. (1998) The glass transition in hydrous granitic melts. Phys. Earth Planet. Inter. 107, 1–8.

Dingwell D. B., Romano C. and Hess K. U. (1996) The effect of water on the viscosity of a haplogranitic melt under P-T-X conditions relevant to silicic volcanism. Contrib. to Mineral. Petrol. 124, 19–28.

Dobson P. F., Epstein S. and Stolper E. M. (1989) Hydrogen isotope fractionation between coexisting vapor and silicate glasses and melts at low pressure. Geochim. Cosmochim. Acta 53, 2723–2730.

Ferguson D. J., Gonnermann H. M., Ruprecht P., Plank T., Hauri E. H., Houghton B. F. and Swanson D. A. (2016) Magma decompression rates during explosive eruptions of Kīlauea volcano, Hawaii, recorded by melt embayments. Bull. Volcanol. 78. Available at: http://dx.doi.org/10.1007/s00445-016-1064-x.

Friedman I., Gleason J., Sheppard R. A. and Gude A. J. (1993a) Deuterium Fractionation as Water Diffuses into Silicic Volcanic Ash. In Climate Change in Continental Isotopic Records (eds. P. K. Swart, K. C. Lohmann, J. Mckenzie, and S. Savin). pp. 321–323.

Friedman I., Gleason J. and Warden A. (1993b) Ancient climate from deuterium content of water in volcanic glass. In Climate Change in Continental Isotopic Records (eds. P. K. Swart, K. C. Lohmann, J. Mckenzie, and S. Savin). pp. 309–319.

Friedman I. and Long W. (1976) Hydration Rate of Obsidian. Science. 191, 347–352.

Gardner J. E., Llewellin E. W., Watkins J. M. and Befus K. S. (2017) Formation of obsidian pyroclasts by sintering of ash particles in the volcanic conduit. Earth Planet. Sci. Lett. 459, 252–263.

Del Gaudio P., Behrens H. and Deubener J. (2007) Viscosity and glass transition temperature of hydrous float glass. J. Non. Cryst. Solids 353, 223–236.

Giachetti T. and Gonnermann H. M. (2013) Water in volcanic pyroclast: Rehydration or incomplete degassing? Earth Planet. Sci. Lett. 369–370, 317–332.

Giachetti T., Gonnermann H. M., Gardner J. E., Shea T. and Gouldstone A. (2015) Discriminating secondary from magmatic water in rhyolitic matrix-glass of volcanic pyroclasts using thermogravimetric analysis. Geochim. Cosmochim. Acta 148, 457–476.

Giachetti T., Hudak M. R., Shea T., Bindeman I. N. and Hoxsie E. C. (2020) D/H ratios and H2O contents record degassing and rehydration history of rhyolitic magma and pyroclasts. Earth Planet. Sci. Lett. 530.

Giordano D., Nichols A. R. L. and Dingwell D. B. (2005) Glass transition temperatures of natural hydrous melts: A relationship with shear viscosity and implications for the welding process. J. Volcanol. Geotherm. Res. 142, 105–118.

Giordano D., Russell J. K. and Dingwell D. B. (2008) Viscosity of magmatic liquids: A model. Earth Planet. Sci. Lett. 271, 123–134.

Graham C. M., Sheppard S. M. F. and Heaton T. H. E. (1980) Experimental hydrogen isotope studies-I. systematic of hydrogen isotope fractionation in the systems epidote-H2O, and AlO(OH)-H2O. Geochim. Cosmochim. Acta 44, 353–364.

Griggs R. K. (1922) The Valley of Ten Thousand Smokes., The National Geographic Society, Washington.

Hudak M. R. and Bindeman I. N. (2018) Conditions of pinnacle formation and glass hydration in cooling ignimbrite sheets from H and O isotope systematics at Crater Lake and the Valley of Ten Thousand Smokes. Earth Planet. Sci. Lett. 500, 56–66.

Hudak M. R. and Bindeman I. N. (2020) Solubility, diffusivity, and O isotope systematics of H2O in rhyolitic glass in hydrothermal temperature experiments. Geochim. Cosmochim. Acta 283, 222–242. Available at: https://doi.org/10.1016/j.gca.2020.06.009.

Humphreys M. C. S., Menand T., Blundy J. D. and Klimm K. (2008) Magma ascent rates in explosive eruptions: Constraints from H2O diffusion in melt inclusions. Earth Planet. Sci. Lett. 270, 25–40.

Ihinger P. D., Zhang Y. and Stolper E. M. (1999) The speciation of dissolved water in rhyolitic melt. Geochim. Cosmochim. Acta 63, 3567–3578. Available at: http://linkinghub.elsevier.com/retrieve/pii/S001670379900277X.

Jackson L. J., Horton B. K., Beate B. O., Bright J. and Breecker D. O. (2019) Testing stable isotope paleoaltimetry with Quaternary volcanic glasses from the Ecuadorian Andes. Geology 47, 411–414.

Keating G. N. (2005) The role of water in cooling ignimbrites. J. Volcanol. Geotherm. Res. 142, 145–171.

Kodosky L. G. and Keith T. E. C. (1993) Factors controlling the geochemical evolution of fumarolic encrustations, Valley of Ten Thousand Smokes, Alaska. J. Volcanol. Geotherm. Res. 55, 185–200.

Kodosky L. G. and Keith T. E. C. (1995) Further insights into the geochemical evolution of fumarolic alteration, Valley of Ten Thousand Smokes, Alaska. J. Volcanol. Geotherm. Res. 65, 181–190.

Kuroda Y. (1979) The lowest δD value found in a hydrous silicate, pectolite. Nature 279, 227–228.

Lambert S. J. and Epstein S. (1980) Stable isotope investigations of an active geothermal system in Valles Caldera, Jemez Mountains, New Mexico. J. Volcanol. Geotherm. Res. 8, 111–129.

Liu Y., Zhang Y. and Behrens H. (2005) Solubility of H2O in rhyolitic melts at low pressures and a new empirical model for mixed H2O-CO2 solubility in rhyolitic melts. J. Volcanol. Geotherm. Res. 143, 219–235.

Lloyd A. S., Ruprecht P., Hauri E. H., Rose W., Gonnermann H. M. and Plank T. (2014) NanoSIMS results from olivine-hosted melt embayments: Magma ascent rate during explosive basaltic eruptions. J. Volcanol. Geotherm. Res. 283, 1–18. Available at: http://dx.doi.org/10.1016/j.jvolgeores.2014.06.002.

Lowenstern J. B. and Pitcher B. W. (2013) Analysis of H2O in silicate glass using attenuated total refectance (ATR) micro-FTIR spectroscopy. Am. Mineral. 98, 1660–1668.

Martin E., Bindeman I., Balan E., Palandri J., Seligman A. and Villemant B. (2017) Hydrogen isotope determination by TC/EA technique in application to volcanic glass as a window into secondary hydration. J. Volcanol. Geotherm. Res.

Mazer J. J., Stevenson C. M., Ebert W. L. and Bates J. K. (1991) The experimental hydration of obsidian as a function of relative humidty and temperature. Am. Antiq. 56, 504–513.

Méheut M., Lazzeri M., Balan E. and Mauri F. (2010) First-principles calculation of H/D isotopic fractionation between hydrous minerals and water. Geochim. Cosmochim. Acta 74, 3874–3882.

Mitchell S. J., McIntosh I. M., Carey R., Houghton B. F., Hudak M. and Bindeman I. (2018a) Resolving rehydration in pumice: Methods for deriving original H2O content and quenching pressures using H2O speciation and H isotope analysis. In American Geophysical Union Fall Meeting pp. V51F-0163.

Mitchell S. J., McIntosh I. M., Houghton B. F., Carey R. J. and Shea T. (2018b) Dynamics of a powerful deep submarine eruption recorded in H2O contents and speciation in rhyolitic glass: The 2012 Havre eruption. Earth Planet. Sci. Lett. 494, 135–147.

Moussallam Y., Rose-Koga E. F., Koga K. T., Médard E., Bani P., Devidal J. L. and Tari D. (2019) Fast ascent rate during the 2017–2018 Plinian eruption of Ambae (Aoba) volcano: a petrological investigation. Contrib. to Mineral. Petrol. 174, 1–24. Available at: https://doi.org/10.1007/s00410-019-1625-z.

Myers M. L., Wallace P. J., Wilson C. J. N., Morter B. K. and Swallow E. J. (2016) Prolonged ascent and episodic venting of discrete magma batches at the onset of the Huckleberry Ridge supereruption, Yellowstone. Earth Planet. Sci. Lett. 451, 285–297. Available at: http://dx.doi.org/10.1016/j.epsl.2016.07.023.

Myers M. L., Wallace P. J., Wilson C. J. N., Watkins J. M. and Liu Y. (2018) Ascent rates of rhyolitic magma at the onset of three caldera-forming eruptions. Am. Mineral. 103, 952–965.

Newman S., Epstein S. and Stolper E. (1988) Water, carbon dioxide, and hydrogen isotopes in glasses from the ca. 1340 A.D. eruption of the Mono Craters, California: Constraints on degassing phenomena and initial volatile content. J. Volcanol. Geotherm. Res. 35, 75–96.

Newman S. and Lowenstern J. B. (2002) Volatile Calc: a silicate melt – H2O – CO2 solution model written in Visual Basic for excel. Comput. Geosci. 28, 597–604.

Ni H. and Zhang Y. (2008) H2O diffusion models in rhyolitic melt with new high pressure data. Chem. Geol. 250, 68–78.

Nolan G. S. and Bindeman I. N. (2013) Experimental investigation of rates and mechanisms of isotope exchange (O, H) between volcanic ash and isotopically-labeled water. Geochim. Cosmochim. Acta 111, 5–27.

Papike J. J. (1992) The valley of ten thousand Smokes, Katmai, Klaska: A unique geochemistry laboratory. Geochim. Cosmochim. Acta 56, 1429–1449.

Proctor B. P., Lockner D. A., Lowenstern J. B. and Beeler N. M. (2017) Conversion of wet glass to melt at lower seismogenic zone conditions: implications for pseudotachylyte creep. Geophys. Res. Lett., 1–8. Available at: http://doi.wiley.com/10.1002/2017GL075344.

Qi H., Coplen T. B., Gehre M., Vennemann T. W., Brand W. A., Geilmann H., Olack G., Bindeman I. N., Palandri J., Huang L. and Longstaffe F. J. (2017) New biotite and muscovite isotopic reference materials, USGS57 and USGS58, for δ2H measurements - A replacement for NBS 30. Chem. Geol. 467, 89–99.

Randolph-Flagg N., Breen S., Hernandez A., Manga M. and Self S. (2017) Evenly spaced columns in the Bishop Tuff (California, USA) as relicts of hydrothermal cooling. Geology 45, 1015–1018.

Rempel A. W. and Bindeman I. N. (2019) A model for the development of stable isotopic water signatures of tephra deposited on ice following subglacial caldera collapse. J. Volcanol. Geotherm. Res. 377, 131–145. Available at: https://doi.org/10.1016/j.jvolgeores.2019.03.015.

Roskosz M., Deloule E., Ingrin J., Depecker C., Laporte D., Merkel S., Remusat L. and Leroux H. (2018) Kinetic D/H fractionation during hydration and dehydration of silicate glasses, melts and nominally anhydrous minerals. Geochim. Cosmochim. Acta 233, 14–32.

Satake H. and Matsuo S. (1984) Hydrogen isotopic fractionation factor between brucite and water in the temperature range 100° to 510° C. Contrib. to Mineral. Petrol. 86, 19–24.

Seligman A. N., Bindeman I., Van Eaton A. and Hoblitt R. (2018) Isotopic insights into the degassing and secondary hydration of volcanic glass from the 1980 eruptions of Mount St. Helens. Bull. Volcanol. 80.

Seligman A. N. and Bindeman I. N. (2019) The δ18O of primary and secondary waters in hydrous volcanic glass. J. Volcanol. Geotherm. Res. 371, 72–85.

Seligman A. N., Bindeman I. N., Watkins J. M. and Ross A. M. (2016) Water in volcanic glass: From volcanic degassing to secondary hydration. Geochim. Cosmochim. Acta 191, 216–238.

Shelby J. E. (1977) Molecular diffusion and solubility of hydrogen isotopes in vitreous silica. J. Appl. Phys. 48, 3387–3394.

Sheppard S. M. F. and Gilg H. A. (1996) Stable isotope geochemistry of clay minerals. Clay Miner. 31, 1–24.

Silver L. A., Ihinger P. D. and Stolper E. (1990) The influence of bulk composition on the speciation of water in silicate glasses. Contrib. to Mineral. Petrol. 104, 142–162.

Stolper E. (1982) Water in silicate glasses: An infrared spectroscopic study. Contrib. to Mineral. Petrol. 81, 1–17.

Suzuoki T. and Epstein S. (1976) Hydrogen isotope fractionation between OH-bearing minerals and water. Geochim. Cosmochim. Acta 40, 1229–1240.

Taylor B. E., Eichelberger J. C. and Westrich H. R. (1983) Hydrogen isotopic evidence of rhyolitic magma degassing during shallow intrusion and eruption. Nature 306, 541–545.

Vennemann T. W. and O'Neil J. R. (1996) Hydrogen isotope exchange reactions between hydrous minerals and molecular hydrogen: I. A new approach for the determination of hydrogen isotope fractionation at moderate temperatures. Geochim. Cosmochim. Acta 60, 2437–2451.

Walter S. and Castro J. (2020) VolcDeGas: A program for modelling hydrogen isotope fractionation during degassing of rhyolitic melts. Volcanica 3, 155–168.

Watkins J. M., Gardner J. E. and Befus K. S. (2016) Nonequilibrium degassing, regassing, and vapor fluxing in magmatic feeder systems. Geology, 1–4.

Watkins J. M., Manga M. and Depaolo D. J. (2012) Bubble geobarometry: A record of pressure changes, degassing, and regassing at Mono Craters, California. Geology, 699–702.

Wenner D. B. (1979) Hydrogen, oxygen and carbon isotopic evidence for the origin of rodingites in serpentinized ultramafic rocks. Geochim. Cosmochim. Acta 43, 603–614.

Wilding M. C., Webb S. L. and Dingwell D. B. (1995) Evaluation of a relaxation geospeedometer for volcanic glasses. Chem. Geol. 125, 137–148.

Wilding M., Webb S., Dingwell D., Ablay G. and Marti J. (1996) Cooling rate variation in natural volcanic glasses from Tenerife, Canary Islands. Contrib. to Mineral. Petrol. 125, 151–160.

Withers A. C., Zhang Y. and Behrens H. (1999) Reconciliation of experimental results on H2O speciation in rhyolitic glass using in-situ and quenching techniques. Earth Planet. Sci. Lett. 173, 343–349.

Xu B. L. and Zheng Y. F. (1999) Experimental studies of oxygen and hydrogen isotope fractionations between precipitated brucite and water at low temperatures. Geochim. Cosmochim. Acta 63, 2009–2018.

Yeh H. W. (1980) D/H Ratios and late-stage dehydration of shales during burial. Geochim. Cosmochim. Acta 44, 341–352.

Zhang Y. (2008) Geochemical Kinetics., Princeton University Press.

Zhang Y. (1999) H2O in rhyolitic glasses and melts: Measurement, speciation, solubility, and diffusion. Rev. G 37, 493–516.

Zhang Y. and Behrens H. (2000) H2O diffusion in rhyolitic melts and glasses. Chem. Geol. 169, 243–262.

Zhang Y., Jenkins J. and Xu Z. (1997) Kinetics of the reaction H2O + O →2OH in rhyolitic glasses upon cooling: Geospeedometry and comparison with glass transition. Geochim. Cosmochim. Acta 61, 2167‑2173.

Zhang Y., Stolper E. M. and Wasserburg G. J. (1991) Diffusion of water in rhyolitic glasses. Geochim. Cosmochim. Acta 55, 441–456.

Chapter IV

Anovitz, L.M., Cole, D.R., Fayek, M., 2008. Mechanisms of rhyolitic glass hydration below the glass transition. Am. Mineral. 93, 1166–1178. https://doi.org/10.2138/am.2008.2516

Avery, V.F., 1992. A petrogenetic study of the dacite from the 1912 eruption of Novarupta, Katmai National Park, Alaska: Implications for magma storage locations. University of Alaska, Fairbanks.

Bacon, C.R., Druitt, T.H., 1988. Compositional evolution of the zoned calcalkaline magma chamber of Mount Mazama, Crater Lake, Oregon. Contrib. to Mineral. Petrol. 98, 224–256.

Bacon, C.R., Lanphere, M.A., 2006. Eruptive history and geochronology of Mount Mazama and the Crater Lake region, Oregon. Bull. Geol. Soc. Am. 118, 1331–1359. https://doi.org/10.1130/B25906.1

Banks, N.G., Hoblitt, R.P., 1981. Summary of temperature studies of the 1980 deposits, in: Lipman, P.W., R, M.D. (Eds.), The 1980 Eruptions of Mount St. Helens, Washington. p. U.S. Geological Survey Professional Paper 1250:295.

Bindeman, I.N., Lowenstern, J.B., 2016. Low-δD hydration rinds in Yellowstone perlites record rapid syneruptive hydration during glaical and interglacial conditions. Contrib. to Mineral. Petrol. 171.

Bindeman, I.N., Zakharov, D.O., Palandri, J., Greber, N.D., Dauphas, N., Retallack, G.J., Hofmann, A., Lackey, J.S., Bekker, A., 2018. Rapid emergence of subaerial landmasses and onset of a modern hydrologic cycle 2.5 billion years ago. Nature 545–548. https://doi.org/10.1038/s41586-018-0131-1

Brooks, J.R., Gibson, J.J., Birks, S.J., Weber, M.H., Rodecap, K.D., Stoddard, J.L., 2014. Stable isotope estimates of evaporation: Inflow and water residence time for lakes across the united states as a tool for national lake water quality assessments. Limnol. Oceanogr. 59, 2150–2165. https://doi.org/10.4319/lo.2014.59.6.2150

Cassel, E.J., Breecker, D.O., 2017. Long-term stability of hydrogen isotope ratios in hydrated volcanic glass. Geochim. Cosmochim. Acta 200, 67–86. https://doi.org/10.1016/j.gca.2016.12.001

Cassel, E.J., Graham, S.A., Chamberlain, C.P., 2009. Cenozoic tectonic and topographic evolution of the northern Sierra Nevada, California, through stable isotope paleoaltimetry in volcanic glass. Geology 37, 547–550. https://doi.org/10.1130/G25572A.1

Dansgaard, W., 1964. Stable isotopes in precipitation. Tellus 16.

Dodson, M.H., 1973. Closure temperature in cooling geochronological and petrological systems. Contrib. to Mineral. Petrol. 40, 259–274. https://doi.org/10.1007/BF00373790

Druitt, T.H., Bacon, C.R., 1986. Lithic breccia and ignimbrite erupted during the collapse of Crater Lake Caldera, Oregon. J. Volcanol. Geotherm. Res. 29, 1–32. https://doi.org/10.1016/0377-0273(86)90038-7

Fierstein, J., Hildreth, W., 1992. The plinian eruptions of 1912 at Novarupta, Katmai National Park, Alaska. Bull. Volcanol. 54, 646–684.

Friedman, I., Gleason, J., Sheppard, R.A., Gude, A.J., 1993a. Deuterium Fractionation as Water Diffuses into Silicic Volcanic Ash, in: Swart, P.K., Lohmann, K.C., Mckenzie, J., Savin, S. (Eds.), Climate Change in Continental Isotopic Records. pp. 321–323.

Friedman, I., Gleason, J., Warden, A., 1993b. Ancient climate from deuterium content of water in volcanic glass, in: Swart, P.K., Lohmann, K.C., Mckenzie, J., Savin, S. (Eds.), Climate Change in Continental Isotopic Records. pp. 309–319.

Friedman, I., Long, W., 1976. Hydration Rate of Obsidian. Science (80-.). 191, 347–352.

Gat, J.R., 1996. Oxygen and Hydrogen Isotopes in the Hydrologic Cycle. Annu. Rev. Earth Planet. Sci. 24, 225–62. https://doi.org/10.1146/annurev.earth.24.1.225

Gazis, C., Taylor, H.P., Hon, K., Tsvetkov, A., 1996. Oxygen isotopic and geochemical evidence for a short-lived, high-temperature hydrothermal event in the Chegem caldera, Caucasus Mountains, Russia. J. Volcanol. Geotherm. Res. 73, 213–244.

Griggs, R.K., 1922. The Valley of Ten Thousand Smokes. The National Geographic Society, Washington.

Hildreth, W., 1983. The compositionally zoned eruption of 1912 in the Valley of Ten Thousand Smokes, Katmai National Park, Alaska. J. Volcanol. Geotherm. Res. 18, 1–56.

Hildreth, W., Fierstein, J., 2012. The Novarupta-Katmai Eruption of 1912 — Largest Eruption of the Twentieth Century: Centennial Perspectives: U.S. Geological Survey Professional Paper 1791.

Holt, E.W., Taylor, H.P., 2001. 18O/16O studies of fossil fissure fumaroles from the Valley of Ten Thousand Smokes, Alaska. Bull. Volcanol. 63, 151–163. https://doi.org/10.1007/s004450100131

Holt, E.W., Taylor, H.P., 1998. 18O/16O mapping and hydrogeology of a short-lived (~10 years) fumarolic (>500°C) meteoric-hydrothermal event in the upper part of the 0.76 Ma Bishop Tuff outflow sheet, California. J. Volcanol. Geotherm. Res. 83, 115–139.

James, E.R., Manga, M., Rose, T.P., Hudson, G.B., 2000. The use of temperature and the isotopes of O, H, C, and noble gases to determine the pattern and spatial extent of groundwater flow. J. Hydrol. 237, 100–112. https://doi.org/10.1016/S0022-1694(00)00303-6

Jasechko, S., Gibson, J., Edwards, T., 2014. Stable isotope mass balance of the Laurentian Great Lakes. J. Great Lakes Res. 40, 336–346.

Keating, G.N., 2005. The role of water in cooling ignimbrites. J. Volcanol. Geotherm. Res. 142, 145–171. https://doi.org/10.1016/j.jvolgeores.2004.10.019

Kodosky, L.G., Keith, T.E.C., 1995. Further insights into the geochemical evolution of fumarolic alteration, Valley of Ten Thousand Smokes, Alaska. J. Volcanol. Geotherm. Res. 65, 181–190. https://doi.org/10.1016/0377-0273(94)00117-Y

Lachniet, M.S., Lawson, D.E., Patterson, W.P., 2016. Isoscapes of δ18O and δ2H reveal climatic forcings on Alaska and Yukon precipitation. Water Resour. Res. https://doi.org/10.1002/2016WR019436

Lambert, S.J., Epstein, S., 1980. Stable isotope investigations of an active geothermal system in Valles Caldera, Jemez Mountains, New Mexico. J. Volcanol. Geotherm. Res. 8, 111–129. https://doi.org/10.1016/0377-0273(80)90010-4

Loewen, M.W., Bindeman, I.N., 2015. Oxygen isotope and trace element evidence for three-stage petrogenesis of the youngest episode (260-279 ka) of Yellowstone rhyolitic volcanism. Contrib. to Mineral. Petrol. 170.

Luz, B., Barkan, E., 2010. Variations of 17O/16O and 18O/16O in meteoric waters. Geochim. Cosmochim. Acta 74, 6276–6286. https://doi.org/10.1016/j.gca.2010.08.016

Mandeville, C.W., Webster, J.D., Tappen, C., Taylor, B.E., Timbal, A., Sasaki, A., Hauri, E., Bacon, C.R., 2009. Stable isotope and petrologic evidence for open-system degassing during the climactic and pre-climactic eruptions of Mt . Mazama, Crater Lake, Oregon. Geochim. Cosmochim. Acta 73, 2978–3012. https://doi.org/10.1016/j.gca.2009.01.019

Manga, M., 2001. Using Springs to Study Groundwater Flow and Active Geologic Processes. Annu. Rev. Earth Planet. Sci. 29, 201–228. https://doi.org/10.1146/annurev.earth.29.1.201

Martin, E., Bindeman, I., Balan, E., Palandri, J., Seligman, A., Villemant, B., 2017. Hydrogen isotope determination by TC/EA technique in application to volcanic glass as a window into secondary hydration. J. Volcanol. Geotherm. Res. https://doi.org/10.1016/j.jvolgeores.2017.10.013

Masson, V., Vimeux, F., Jouzel, J., Morgan, V., Delmotte, M., Ciais, P., Hammer, C., Johnsen, S., Lipenkov, V.Y., Mosley-Thompson, E., Petit, J.R., Steig, E.J., Stievenard, M., Vaikmae, R., 2000. Holocene climate variability in Antartica based on 11 ice-core isotopic records. Quat. Res. 54, 348–358. https://doi.org/10.1006/qres.2000.2172

Matsuhisa, Y., Goldsmith, J.R., Clayton, R.N., 1978. Mechanisms of hydrothermal crystallization of quartz at 250°C and 15 kbar. Geochim. Cosmochim. Acta 42, 173–182. https://doi.org/10.1016/0016-7037(78)90130-8

Mayewski, P.A., Rohling, E.E., Stager, J.C., Karlén, W., Maasch, K.A., Meeker, L.D., Meyerson, E.A., Gasse, F., van Kreveld, S., Holmgren, K., Lee-Thorp, J., Rosqvist, G., Rack, F., Staubwasser, M., Schneider, R.R., Steig, E.J., 2004. Holocene climate variability. Quat. Res. 62, 243–255. https://doi.org/10.1016/j.yqres.2004.07.001

Mix, H.T., Chamberlain, C.P., 2014. Stable isotope records of hydrologic change and paleotemperature from smectite in Cenozoic western North America. Geochim. Cosmochim. Acta 141, 532–546. https://doi.org/10.1016/j.gca.2014.07.008

Nolan, G.S., Bindeman, I.N., 2013. Experimental investigation of rates and mechanisms of isotope exchange (O, H) between volcanic ash and isotopically-labeled water. Geochim. Cosmochim. Acta 111, 5–27. https://doi.org/10.1016/j.gca.2013.01.020

O'Neil, J.R., Taylor, H.P., 1967. The oxygen isotope and cation exchange chemistry of feldspars. Am. Mineral. 52, 1414–1437.

Pack, A., Herwartz, D., 2014. The triple oxygen isotope composition of the Earth mantle and understanding Δ17O variations in terrestrial rocks and minerals. Earth Planet. Sci. Lett. 390, 138–145. https://doi.org/10.1016/j.epsl.2014.01.017

Papike, J.J., 1992. The valley of ten thousand Smokes, Katmai, Klaska: A unique geochemistry laboratory. Geochim. Cosmochim. Acta 56, 1429–1449. https://doi.org/10.1016/0016-7037(92)90214-4

Qi, H., Coplen, T.B., Gehre, M., Vennemann, T.W., Brand, W.A., Geilmann, H., Olack, G., Bindeman, I.N., Palandri, J., Huang, L., Longstaffe, F.J., 2017. New biotite and muscovite isotopic reference materials, USGS57 and USGS58, for δ2H measurements - A replacement for NBS 30. Chem. Geol. 467, 89–99.

Qi, H., Gröning, M., Coplen, T.B., Buck, B., Mroczkowski, S.J., Brand, W.A., Geilmann, H., Gehre, M., 2010. Novel silver-tubing method for quantitative introduction of water into high-temperature conversion systems for stable hydrogen and oxygen isotopic measurements. Rapid Commun. Mass Spectrom. 24, 1821–1827.

Randolph-Flagg, N., Breen, S., Hernandez, A., Manga, M., Self, S., 2017. Evenly spaced columns in the Bishop Tuff (California, USA) as relicts of hydrothermal cooling. Geology 45, 1015–1018. https://doi.org/10.1130/G39256.1

Riehle, J.R., Miller, T.F., Bailey, R.A., 1995. Cooling, degassing, and compaction of rhyolitic ash flow tuffs: a computational model. Bull. Volcanol. 57, 319–336.

Seligman, A.N., Bindeman, I.N., Watkins, J.M., Ross, A.M., 2016. Water in volcanic glass: From volcanic degassing to secondary hydration. Geochim. Cosmochim. Acta 191, 216–238. https://doi.org/10.1016/j.gca.2016.07.010

Sharp, Z.D., Gibbons, J.A., Maltsev, O., Atudorei, V., Pack, A., Sengupta, S., Shock, E.L., Knauth, L.P., 2016. A calibration of the triple oxygen isotope fractionation in the SiO2-H2O system and applications to natural samples. Geochim. Cosmochim. Acta 186, 105–119. https://doi.org/10.1016/j.gca.2016.04.047

Sheppard, S.M.F., Gilg, H.A., 1996. Stable isotope geochemistry of clay minerals. Clay Miner. 31, 1–24.

Sheridan, M.F., 1970. Fuarmolic mounds and ridges of the Bishop Tuff, California. Bull. Geol. Soc. Am. 81, 851–868. https://doi.org/10.1130/0016-7606(1970)81[851:FMAROT]2.0.CO;2

Taylor, B.E., Eichelberger, J.C., Westrich, H.R., 1983. Hydrogen isotopic evidence of rhyolitic magma degassing during shallow intrusion and eruption. Nature 306, 541–545. https://doi.org/10.1038/306541a0

Thompson, J.M., White, L.D., Nathenson, M., 1987. Chemical Analyses of Waters from Crater Lake, Oregon, and Nearby Springs.

Zhang, Y., Behrens, H., 2000. H2O diffusion in rhyolitic melts and glasses. Chem. Geol. 169, 243–262.

Chapter V

Anovitz, L. M., Riciputi, L. R., Cole, D. R., Fayek, M., & Elam, J. M. (2006). Obsidian hydration: A new paleothermometer. Geology, 34(7), 517–520. https://doi.org/10.1130/G22326.1

Anovitz, L. M., Cole, D. R., & Fayek, M. (2008). Mechanisms of rhyolitic glass hydration below the glass transition. American Mineralogist, 93, 1166–1178.

Bailey, H. L., Klein, E. S., & Welker, J. M. (2019). Synoptic and Mesoscale Mechanisms Drive Winter Precipitation δ18O/δ2H in South-Central Alaska. Journal of Geophysical Research: Atmospheres, 124(7), 4252–4266. https://doi.org/10.1029/2018JD030050

Brown, R. J., Branney, M. J., Maher, C., & Dávila-Harris, P. (2010). Origin of accretionary lapilli within ground-hugging density currents: Evidence from pyroclastic couplets on Tenerife. Bulletin of the Geological Society of America, 122(1–2), 305–320. https://doi.org/10.1130/B26449.1

Brown, R. J., Bonadonna, C., & Durant, A. J. (2012). A review of volcanic ash aggregation. Physics and Chemistry of the Earth, 45–46, 65–78. https://doi.org/10.1016/j.pce.2011.11.001

Bull, K. F., & Buurman, H. (2013). An overview of the 2009 eruption of Redoubt Volcano, Alaska. Journal of Volcanology and Geothermal Research, 259, 2–15. https://doi.org/10.1016/j.jvolgeores.2012.06.024

Büttner, R., Dellino, P., & Zimanowski, B. (1999). Identifying magma-water interaction from the surface features of ash particles. Nature, 401(6754), 688–690. https://doi.org/10.1038/44364

Castro, J. M., Bindeman, I. N., Tuffen, H., & Ian Schipper, C. (2014). Explosive origin of silicic lava: Textural and δD-H2O evidence for pyroclastic degassing during rhyolite effusion. Earth and Planetary Science Letters, 405, 52–61. https://doi.org/10.1016/j.epsl.2014.08.012

Coombs, M. L., Sisson, T. W., Bleick, H. A., Henton, S. M., Nye, C. J., Payne, A. L., et al. (2013). Andesites of the 2009 eruption of Redoubt Volcano, Alaska. Journal of Volcanology and Geothermal Research, 259, 349–372. https://doi.org/10.1016/j.jvolgeores.2012.01.002

Cullen, J. T., Hurwitz, S., Barnes, J. D., Lassiter, J. C., Penniston-Dorland, S., Kasemann, S. A., & Thordsen, J. J. (2019). Temperature-dependent variations in mineralogy, major element chemistry and the stable isotopes of boron, lithium and chlorine resulting from hydration of rhyolite: Constraints from hydrothermal experiments at 150 to 350 °C and 25 MPa. Geochimica et Cosmochimica Acta, 261, 269–287. https://doi.org/10.1016/j.gca.2019.07.012

Dobson, P. F., Epstein, S., & Stolper, E. M. (1989). Hydrogen isotope fractionation between coexisting vapor and silicate glasses and melts at low pressure. Geochimica et Cosmochimica Acta, 53(10), 2723–2730. https://doi.org/10.1016/0016-7037(89)90143-9

Van Eaton, A. R., Mastin, L. G., Herzog, M., Schwaiger, H. F., Schneider, D. J., Wallace, K. L., & Clarke, A. B. (2015). Hail formation triggers rapid ash aggregation in volcanic plumes. Nature Communications, 6, 1–7. https://doi.org/10.1038/ncomms8860

Friedman, I., Gleason, J., Sheppard, R. A., & Gude, A. J. (1993). Deuterium Fractionation as Water Diffuses into Silicic Volcanic Ash. In P. K. Swart, K. C. Lohmann, J. Mckenzie, & S. Savin (Eds.), Climate Change in Continental Isotopic Records (pp. 321–323).

Giachetti, T., & Gonnermann, H. M. (2013). Water in volcanic pyroclast: Rehydration or incomplete degassing? Earth and Planetary Science Letters, 369–370, 317–332. https://doi.org/10.1016/j.epsl.2013.03.041

Giachetti, T., Gonnermann, H. M., Gardner, J. E., Shea, T., & Gouldstone, A. (2015). Discriminating secondary from magmatic water in rhyolitic matrix-glass of volcanic pyroclasts using thermogravimetric analysis. Geochimica et Cosmochimica Acta, 148, 457–476. https://doi.org/10.1016/j.gca.2014.10.017

Giachetti, T., Hudak, M. R., Shea, T., Bindeman, I. N., & Hoxsie, E. C. (2020). D/H ratios and H2O contents record degassing and rehydration history of rhyolitic magma and pyroclasts. Earth and Planetary Science Letters, 530. https://doi.org/10.1016/j.epsl.2019.115909

Gilbert, J. S., & Lane, S. J. (1994). The origin of accretionary lapilli. Bulletin of Volcanology, 56(5), 398–411. https://doi.org/10.1007/BF00326465

Giordano, D., Nichols, A. R. L., & Dingwell, D. B. (2005). Glass transition temperatures of natural hydrous melts: A relationship with shear viscosity and implications for the welding process. Journal of Volcanology and Geothermal Research, 142(1-2 SPEC. ISS.), 105–118. https://doi.org/10.1016/j.jvolgeores.2004.10.015

Giordano, D., Russell, J. K., & Dingwell, D. B. (2008). Viscosity of magmatic liquids: A model. Earth and Planetary Science Letters, 271(1–4), 123–134. https://doi.org/10.1016/j.epsl.2008.03.038

Herzog, M., Graf, H. F., Textor, C., & Oberhuber, J. M. (1998). The effect of phase changes of water on the development of volcanic plumes. Journal of Volcanology and Geothermal Research, 87(1–4), 55–74. https://doi.org/10.1016/S0377-0273(98)00100-0

Hudak, M. R., & Bindeman, I. N. (2018). Conditions of pinnacle formation and glass hydration in cooling ignimbrite sheets from H and O isotope systematics at Crater Lake and the Valley of Ten Thousand Smokes. Earth and Planetary Science Letters, 500, 56–66. https://doi.org/10.1016/j.epsl.2018.07.032

Hudak, M. R., & Bindeman, I. N. (2020). Solubility, diffusivity, and O isotope systematics of H2O in rhyolitic glass in hydrothermal temperature experiments. Geochimica et Cosmochimica Acta, 283, 222–242. https://doi.org/10.1016/j.gca.2020.06.009

Hudak, M. R., Bindeman, I. N., & Guan, Y. (2018). Solubility and diffusivity of H2O in rhyolitic glass at hydrothermal temperatures. In American Geophysical Union Fall Meeting.

Kendall, C., & Coplen, T. B. (2001). Distribution of oxygen-18 and deuterium in river waters across the United States. Hydrological Processes, 15, 1363–1393. https://doi.org/10.1002/hyp.217

Liu, Y., Zhang, Y., & Behrens, H. (2005). Solubility of H2O in rhyolitic melts at low pressures and a new empirical model for mixed H2O-CO2 solubility in rhyolitic melts. Journal of Volcanology and Geothermal Research, 143(1–3), 219–235. https://doi.org/10.1016/j.jvolgeores.2004.09.019

Mandeville, C. W., Webster, J. D., Tappen, C., Taylor, B. E., Timbal, A., Sasaki, A., et al. (2009). Stable isotope and petrologic evidence for open-system degassing during the climactic and pre-climactic eruptions of Mt . Mazama, Crater Lake, Oregon. Geochimica et Cosmochimica Acta, 73(10), 2978–3012. https://doi.org/10.1016/j.gca.2009.01.019

Martin, E., Bindeman, I., Balan, E., Palandri, J., Seligman, A., & Villemant, B. (2017). Hydrogen isotope determination by TC/EA technique in application to volcanic glass as a window into secondary hydration. Journal of Volcanology and Geothermal Research. https://doi.org/10.1016/j.jvolgeores.2017.10.013

Mastin, L. G., Guffanti, M., Servranckx, R., Webley, P., Barsotti, S., Dean, K., et al. (2009). A multidisciplinary effort to assign realistic source parameters to models of volcanic ash-cloud transport and dispersion during eruptions. Journal of Volcanology and Geothermal Research, 186(1–2), 10–21. https://doi.org/10.1016/j.jvolgeores.2009.01.008

Mastin, L. G., Spieler, O., & Downey, W. S. (2009). An experimental study of hydromagmatic fragmentation through energetic, non-explosive magma-water mixing. Journal of Volcanology and Geothermal Research, 180(2–4), 161–170. https://doi.org/10.1016/j.jvolgeores.2008.09.012

Mastin, L. G., Schwaiger, H., Schneider, D. J., Wallace, K. L., Schaefer, J., & Denlinger, R. P. (2013). Injection, transport, and deposition of tephra during event 5 at Redoubt Volcano, 23 March, 2009. Journal of Volcanology and Geothermal Research, 259, 201–213. https://doi.org/10.1016/j.jvolgeores.2012.04.025

McIntosh, I. M., Llewellin, E. W., Humphreys, M. C. S., Nichols, A. R. L., Burgisser, A., Schipper, C. I., & Larsen, J. F. (2014). Distribution of dissolved water in magmatic glass records growth and resorption of bubbles. Earth and Planetary Science Letters, 401, 1–11. https://doi.org/10.1016/j.epsl.2014.05.037

Mitchell, S. J., McIntosh, I. M., Houghton, B. F., Carey, R. J., & Shea, T. (2018). Dynamics of a powerful deep submarine eruption recorded in H2O contents and speciation in rhyolitic glass: The 2012 Havre eruption. Earth and Planetary Science Letters, 494(September), 135–147. https://doi.org/10.1016/j.epsl.2018.04.053

Moitra, P., Sonder, I., & Valentine, G. A. (2018). Effects of Size and Temperature-Dependent Thermal Conductivity on the Cooling of Pyroclasts in Air. Geochemistry, Geophysics, Geosystems, 19(10), 3623–3636. https://doi.org/10.1029/2018GC007510

Newman, S., Epstein, S., & Stolper, E. (1988). Water, carbon dioxide, and hydrogen isotopes in glasses from the ca. 1340 A.D. eruption of the Mono Craters, California: Constraints on degassing phenomena and initial volatile content. Journal of Volcanology and Geothermal Research, 35(1–2), 75–96. https://doi.org/10.1016/0377-0273(88)90007-8

Poage, M. A., & Chamberlain, C. P. (2001). Empirical relationships between elevation and the stable isotope composition of precipitation and surface waters: Considerations for studies of paleoelevation change. American Journal of Science, 301(1), 1–15. https://doi.org/10.2475/ajs.301.1.1

Proctor, B. P., Lockner, D. A., Lowenstern, J. B., & Beeler, N. M. (2017). Conversion of wet glass to melt at lower seismogenic zone conditions: implications for pseudotachylyte creep. Geophysical Research Letters, 1–8. https://doi.org/10.1002/2017GL075344

Qi, H., Coplen, T. B., Gehre, M., Vennemann, T. W., Brand, W. A., Geilmann, H., et al. (2017). New biotite and muscovite isotopic reference materials, USGS57 and USGS58, for δ2H measurements - A replacement for NBS 30. Chemical Geology, 467, 89–99.

Rust, A. C., Cashman, K. V., & Wallace, P. J. (2004). Magma degassing buffered by vapor flow through brecciated conduit margins. Geology, 32(4), 349–352. https://doi.org/10.1130/G20388.2

Schwaiger, H. F., Denlinger, R. P., & Mastin, L. G. (2012). Ash3d: A finite-volume, conservative numerical model for ash transport and tephra deposition. Journal of Geophysical Research: Solid Earth, 117(4), 1–20. https://doi.org/10.1029/2011JB008968

Seligman, A. N., Bindeman, I. N., Watkins, J. M., & Ross, A. M. (2016). Water in volcanic glass: From volcanic degassing to secondary hydration. Geochimica et Cosmochimica Acta, 191, 216–238. https://doi.org/10.1016/j.gca.2016.07.010

Seligman, A. N., Bindeman, I., Van Eaton, A., & Hoblitt, R. (2018). Isotopic insights into the degassing and secondary hydration of volcanic glass from the 1980 eruptions of Mount St. Helens. Bulletin of Volcanology, 80(4). https://doi.org/10.1007/s00445-018-1212-6

Sparks, R. S. J. (1986). The dimensions and dynamics of volcanic eruption columns. Bulletin of Volcanology, 48(1), 3–15. https://doi.org/10.1007/BF01073509

Suzuki, Y. J., & Koyaguchi, T. (2013). 3D numerical simulation of volcanic eruption clouds during the 2011 Shinmoe-dake eruptions. Earth, Planets and Space, 65(6), 581–589. https://doi.org/10.5047/eps.2013.03.009

Suzuki, Y. J., & Koyaguchi, T. (2015). Effects of wind on entrainment efficiency in volcanic plumes. Journal of Geophysical Research: Solid Earth, 120(9), 6122–6140. https://doi.org/10.1002/2015JB012208

Suzuoki, T., & Epstein, S. (1976). Hydrogen isotope fractionation between OH-bearing minerals and water. Geochimica et Cosmochimica Acta, 40(10), 1229–1240. https://doi.org/10.1016/0016-7037(76)90158-7

Taylor, B. E., Eichelberger, J. C., & Westrich, H. R. (1983). Hydrogen isotopic evidence of rhyolitic magma degassing during shallow intrusion and eruption. Nature, 306(8), 541–545. https://doi.org/10.1038/306541a0

Wallace, K. L., Schaefer, J. R., & Coombs, M. L. (2013). Character, mass, distribution, and origin of tephra-fall deposits from the 2009 eruption of Redoubt Volcano, Alaska — Highlighting the significance of particle aggregation. Journal of Volcanology and Geothermal Research, 259, 145–169. https://doi.org/10.1016/j.jvolgeores.2012.09.015

Walter, S., & Castro, J. (2020). VolcDeGas: A program for modelling hydrogen isotope fractionation during degassing of rhyolitic melts. Volcanica, 3(1), 155–168. https://doi.org/10.30909/vol.03.01.155168

Waythomas, C. F., Pierson, T. C., Major, J. J., & Scott, W. E. (2013). Voluminous ice-rich and water-rich lahars generated during the 2009 eruption of Redoubt Volcano, Alaska. Journal of Volcanology and Geothermal Research, 259, 389–413. https://doi.org/10.1016/j.jvolgeores.2012.05.012

Woods, A. W. (1993). Moist convection and the injection of volcanic ash into the atmosphere. Journal of Geophysical Research, 98(B10). https://doi.org/10.1029/93jb00718

Woods, Andrew W, & Bursik, M. I. (1991). Particle fallout, thermal disequilibrium and volcanic plumes. Bulletin of Volcanology, 53(7), 559–570.

Zhang, Y., & Behrens, H. (2000). H2O diffusion in rhyolitic melts and glasses. Chemical Geology, 169, 243–262.

Zhang, Y., & Ni, H. (2010). Diffusion of H, C, and O components in silicate melts. Reviews in Mineralogy and Geochemistry, 72(3), 171–225. https://doi.org/10.2138/rmg.2010.72.5

Zhang, Y., Stolper, E. M., & Wasserburg, G. J. (1991). Diffusion of water in rhyolitic glasses. Geochimica et Cosmochimica Acta, 55(2), 441–456. https://doi.org/10.1016/0016-7037(91)90003-N

Zimanowski, B., Büttner, R., Dellino, P., White, J. D. L., & Wohletz, K. H. (2015). Magma–Water Interaction and Phreatomagmatic Fragmentation. The Encyclopedia of Volcanoes, 473–484. https://doi.org/10.1016/b978-0-12-385938-9.00026-2

Chapter VI

Anderson S. W. and Fink J. H. (1989) Hydrogen isotope evidence for extrusion mechanisms of the Mount St. Helens lava dome. *Nature* **341**, 521-523 doi: 10.1038/341521a0.

Bauer K. K. and Vennemann T. W. (2014) Analytical methods for the measurement of hydrogen isotope composition and water content in clay minerals by TC/EA. *Chem. Geol.* **363**, 229–240. Available at: http://dx.doi.org/10.1016/j.chemgeo.2013.10.039.

Befus K. S., Walowski K. J., Hervig R. L. and Cullen J. T. (2020) Hydrogen Isotope Composition of a Large Silicic Magma Reservoir Preserved in Quartz-Hosted Glass Inclusions of the Bishop Tuff Plinian Eruption. *Geochemistry, Geophys. Geosystems* **21**, 1–22.

Begley I. S. and Scrimgeour C. M. (1996) On-line Reduction of H2O for δ^2H and δ18O Measurement by Continuous-flow Isotope Ratio Mass Spectrometry. *Rapid Commun. Mass Spectrom.* **10**, 969–973.

Bigeleisen J., Perlman M. L. and Prosser H. C. (1952) Conversion of Hydrogenic Materials to Hydrogen for Isotopic Analysis. *Anal. Chem.* **24**, 1356–1357.

Brand W. A., Tegtmeyer A. R. and Hilkert A. (1994) Compound-specific isotope analysis: extending toward 15N14N and 18O16O. *Org. Geochem.* **21**, 585–594.

Burgoyne T. W. and Hayes J. M. (1998) Quantitative production of H2 by pyrolysis of gas chromatographic effluents. *Anal. Chem.* **70**, 5136–5141.

Cassel E. J., Breecker D. O., Henry C. D., Larson T. E. and Stockli D. F. (2014) Profile of a paleo-orogen: High topography across the present-day Basin and Range from 40 to 23 Ma. *Geology* **42**, 1007–1010.

Cassel E. J., Graham S. A., Chamberlain C. P. and Henry C. D. (2012) Early Cenozoic topography, morphology, and tectonics of the northern Sierra Nevada and western Basin and Range. *Geosphere* **8**, 229–249.

Castro J. M., Bindeman I. N., Tuffen H. and Ian Schipper C. (2014) Explosive origin of silicic lava: Textural and δ^2H-H2O evidence for pyroclastic degassing during rhyolite effusion. *Earth Planet. Sci. Lett.* **405**, 52–61. Available at: http://dx.doi.org/10.1016/j.epsl.2014.08.012.

Coleman M. L., Shepherd T. J., Durham J. J., Rouse J. E. and Moore G. R. (1982) Reduction of Water with Zinc for Hydrogen Isotope Analysis. *Anal. Chem.* **54**, 993–995.

Craig H. (1961) Isotope Variations in Meteoric Waters. *Science.* **133**, 1702–1703.

Dansgaard W. (1964) Stable isotopes in precipitation. *Tellus* **16**.

Deering C. D., Horton T. W., Gravley D. M. and Cole J. W. (2012) Hornblende, cummingtonite, and biotite hydrogen isotopes: Direct evidence of slab-derived fluid flux in silicic magmas of the Taupo Volcanic Zone, New Zealand. *J. Volcanol. Geotherm. Res.* **233**–**234**, 27–36. Available at: http://dx.doi.org/10.1016/j.jvolgeores.2012.04.010.

Dettinger M. P. and Quade J. (2015) Testing the analytical protocols and calibration of volcanic glass for the reconstruction of hydrogen isotopes in paleoprecipitation. *Mem. Geol. Soc. Am.* **212**, 261–276.

Dobson P. F., Epstein S. and Stolper E. M. (1989) Hydrogen isotope fractionation between coexisting vapor and silicate glasses and melts at low pressure. *Geochim. Cosmochim. Acta* **53**, 2723–2730.

Elders W. A., Fridleifsson G. Ó., Zierenberg R. A., Pope E. C., Mortensen A. K., Gudmundsson Á., Lowenstern J. B., Marks N. E., Owens L., Bird D. K., Reed M., Olsen N. J. and Schiffman P. (2011) Origin of a rhyolite that intruded a geothermal well while drilling at the Krafla volcano, Iceland. *Geology* **39**, 231–234.

Friedman I. (1953) Deuterium content of natural waters and other substances. *Geochim. Cosmochim. Acta* **4**, 89–103.

Friedman I., Gleason J., Sheppard R. A. and Gude A. J. (1993a) Deuterium Fractionation as Water Diffuses into Silicic Volcanic Ash. In *Climate Change in Continental Isotopic Records* (eds. P. K. Swart, K. C. Lohmann, J. Mckenzie, and S. Savin). pp. 321–323.

Friedman I., Gleason J. and Warden A. (1993b) Ancient climate from deuterium content of water in volcanic glass. In *Climate Change in Continental Isotopic Records* (eds. P. K. Swart, K. C. Lohmann, J. Mckenzie, and S. Savin). pp. 309–319.

Friedman I. and Smith R. L. (1960) A New Dating Method Using Obsidian: Part I, The Development of the Method. *Am. Antiq.* **25**, 476–493.

Friedman I. and Smith R. L. (1958) The deuterium content of water in some volcanic glasses. *Geochim. Cosmochim. Acta* **15**.

Gehre M., Hoefling R., Kowski P. and Strauch G. (1996) Sample preparation device for quantitative hydrogen isotope analysis using chromium metal. *Anal. Chem.* **68**, 4414–4417.

Giachetti T., Hudak M. R., Shea T., Bindeman I. N. and Hoxsie E. C. (2020) D/H ratios and H_2O contents record degassing and rehydration history of rhyolitic magma and pyroclasts. *Earth Planet. Sci. Lett.* **530**.

Godfrey J. D. (1962) The deuterium content of hydrous minerals from the East-Central Sierra Nevada and Yosemite National Park. *Geochim. Cosmochim. Acta* **26**, 1215–1245.

Gong B., Zheng Y.-F. and Chen R.-X. (2010) An online method combining a thermal conversion elemental analyzer with isotope ratio mass spectrometry for the determination of hydrogen isotope composition and water concentration in geological samples. *Rapid Commun. Mass Spectrom.* **24**, 1457–1466.

Gong B., Zheng Y. F. and Chen R. X. (2007) TC/EA-MS online determination of hydrogen isotope composition and water concentration in eclogitic garnet. *Phys. Chem. Miner.* **34**, 687–698.

Goss A. R., Perfit M. R., Ridley W. I., Rubin K. H., Kamenov G. D., Soule S. A., Fundis A. and Fornari D. J. (2010) Geochemistry of lavas from the 2005-2006 eruption at the East Pacific Rise, 9°46'N-9°56N: Implications for ridge crest plumbing and decadal changes in magma chamber compositions. *Geochemistry, Geophys. Geosystems* **11**, 1–35.

Greenwood J. P. (2018) Hydrogen and D/H analysis of apatite by Elemental Analyzer-Chromium/High-Temperature Conversion-Isotope Ratio Mass Spectrometry (EA-Cr/HTC-IRMS). *Chem. Geol.* **500**, 175–181. Available at: https://doi.org/10.1016/j.chemgeo.2018.09.029.

Hagemann R., Nief G. and Roth E. (1970) Absolute isotopic scale for deuterium analysis of natural waters. Absolute D/H ratio for SMOW. *Tell* **22**, 712–715.

Halas S. and Jasińska B. (1996) Platinized Magnesium as Reducing Agent for Hydrogen Isotope Analysis. *Isotopes Environ. Health Stud.* **32**, 105–109.

Hauri E., Wang J., Dixon J. E., King P. L., Mandeville C. and Newman S. (2002) SIMS analysis of volatiles in silicate glasses 1. Calibration, matrix effects and comparisons with FTIR. *Chem. Geol.* **183**, 99–114.

Hilkert A. W., Douthitt C. B., Schlüter H. J. and Brand W. A. (1999) Isotope ratio monitoring gas chromatography/mass spectrometry of D/H by high temperature conversion isotope ratio mass spectrometry. *Rapid Commun. Mass Spectrom.* **13**, 1226–1230.

De Hoog J. C. M., Taylor B. E. and Van Bergen M. J. (2009) Hydrogen-isotope systematics in degassing basaltic magma and application to Indonesian arc basalts. *Chem. Geol.* **266**, 256–266. Available at: http://dx.doi.org/10.1016/j.chemgeo.2009.06.010.

Hudak M. R. and Bindeman I. N. (2018) Conditions of pinnacle formation and glass hydration in cooling ignimbrite sheets from H and O isotope systematics at Crater Lake and the Valley of Ten Thousand Smokes. *Earth Planet. Sci. Lett.* **500**, 56–66.

Jackson L. J., Horton B. K., Beate B. O., Bright J. and Breecker D. O. (2019) Testing stable isotope paleoaltimetry with Quaternary volcanic glasses from the Ecuadorian Andes. *Geology* **47**, 411–414.

Kendall C. and Copien T. B. (1985) Multi-Sample Conversion of Water to Hydrogen by Zinc for Stable Isotope Determination. *Anal. Chem.* **57**, 1437–1440.

Mandeville C. W., Webster J. D., Tappen C., Taylor B. E., Timbal A., Sasaki A., Hauri E. and Bacon C. R. (2009) Stable isotope and petrologic evidence for open-system degassing during the climactic and pre-climactic eruptions of Mt . Mazama, Crater Lake, Oregon. *Geochim. Cosmochim. Acta* **73**, 2978–3012. Available at: http://dx.doi.org/10.1016/j.gca.2009.01.019.

Martin E., Bindeman I., Balan E., Palandri J., Seligman A. and Villemant B. (2017) Hydrogen isotope determination by TC/EA technique in application to volcanic glass as a window into secondary hydration. *J. Volcanol. Geotherm. Res.*

Midwood A. J. and McGaw B. A. (1999) Recent developments in the analysis of light isotopes by continuous flow isotope ratio mass spectrometry. *Anal. Commun.* **36**, 291–294.

Mulch A., Sarna-Wojcicki A. M., Perkins M. E. and Chamberlain C. P. (2008) A Miocene to Pleistocene climate and elevation record of the Sierra Nevada (California). *Proc. Natl. Acad. Sci.* **105**, 6819–6824.

Newman S., Epstein S. and Stolper E. (1988) Water, carbon dioxide, and hydrogen isotopes in glasses from the ca. 1340 A.D. eruption of the Mono Craters, California: Constraints on degassing phenomena and initial volatile content. *J. Volcanol. Geotherm. Res.* **35**, 75–96.

Pope E. C., Bird D. K. and Arnórsson S. (2014) Stable isotopes of hydrothermal minerals as tracers for geothermal fluids in Iceland. *Geothermics* **49**, 99–110. Available at: http://dx.doi.org/10.1016/j.geothermics.2013.05.005.

Pope E. C., Bird D. K., Arnórsson S., Fridriksson T., Elders W. A. and Gudmundur, Fridleifsson Ó. (2009) Isotopic constraints on ice age fluids in active geothermal systems: Reykjanes, Iceland. *Geochim. Cosmochim. Acta* **73**, 4468–4488.

Qi H., Coplen T. B., Gehre M., Vennemann T. W., Brand W. A., Geilmann H., Olack G., Bindeman I. N., Palandri J., Huang L. and Longstaffe F. J. (2017) New biotite and muscovite isotopic reference materials, USGS57 and USGS58, for δ^2H measurements - A replacement for NBS 30. *Chem. Geol.* **467**, 89–99.

Qi H., Coplen T. B., Olack G. A. and Vennemann T. W. (2014) Caution on the use of NBS 30 biotite for hydrogen-isotope measurements with on-line high-temperature conversion systems. *Rapid Commun. Mass Spectrom.* **28**, 1987–1994.

Qi H., Gröning M., Coplen T. B., Buck B., Mroczkowski S. J., Brand W. A., Geilmann H. and Gehre M. (2010) Novel silver-tubing method for quantitative introduction of water into high-temperature conversion systems for stable hydrogen and oxygen isotopic measurements. *Rapid Commun. Mass Spectrom.* **24**, 1821–1827.

Rust A. C., Cashman K. V. and Wallace P. J. (2004) Magma degassing buffered by vapor flow through brecciated conduit margins. *Geology* **32**, 349–352.

Saubin E., Kennedy B., Tuffen H., Nichols A. R. L., Villeneuve M., Bindeman I., Mortensen A., Schipper C. I., Wadsworth F. B., Watson T. and Zierenberg R. (2021) Textural and geochemical window into the IDDP-1 rhyolitic melt, Krafla, Iceland, and its reaction to drilling. *Geol. Soc. Am. Bull.* **1**, 1–16.

Seligman A. N., Bindeman I., Van Eaton A. and Hoblitt R. (2018) Isotopic insights into the degassing and secondary hydration of volcanic glass from the 1980 eruptions of Mount St. Helens. *Bull. Volcanol.* **80**.

Seligman A. N., Bindeman I. N., Watkins J. M. and Ross A. M. (2016) Water in volcanic glass: From volcanic degassing to secondary hydration. *Geochim. Cosmochim. Acta* **191**, 216–238.

Sharp Z. D., Atudorei V. and Durakiewicz T. (2001) A rapid method for determination of hydrogen and oxygen isotope ratios from water and hydrous minerals. *Chem. Geol.* **178**, 197–210.

Suzuoki T. and Epstein S. (1976) Hydrogen isotope fractionation between OH-bearing minerals and water. *Geochim. Cosmochim. Acta* **40**, 1229–1240.

Tanweer A. and Han L.-F. (1996) Reduction of Microliter Amounts of Water with Manganese for D/H Isotope Ratio Measurement by Mass Spectrometry. *Isotopes Environ. Health Stud.* **32**, 97–103.

Taylor B. E. (1991) Degassing of Obsidian Dome rhyolite, Inyo volcanic chain, California. *Stable Isot. Geochemistry A Tribut. to Samuel Epstein*, 339–353.

Taylor B. E., Eichelberger J. C. and Westrich H. R. (1983) Hydrogen isotopic evidence of rhyolitic magma degassing during shallow intrusion and eruption. *Nature* **306**, 541–545.

Underwood S. J., Feeley T. C. and Clynne M. A. (2012) Hydrogen isotope investigation of amphibole and biotite phenocrysts in silicic magmas erupted at Lassen Volcanic Center, California. *J. Volcanol. Geotherm. Res.* **227**–**228**, 32–49. Available at: http://dx.doi.org/10.1016/j.jvolgeores.2012.02.019.

Underwood S. J., Feeley T. C. and Clynne M. A. (2013) Hydrogen isotope investigation of amphibole and glass in dacite magmas erupted in 1980-1986 and 2005 at Mount St. Helens, Washington. *J. Petrol.* **54**, 1047–1070.

Vennemann T. W. and O'Neil J. R. (1993) A simple and inexpensive method of hydrogen isotope and water analyses of minerals and rocks based on zinc reagent. *Chem. Geol.* **103**, 227–234.

Walter S. and Castro J. (2020) VolcDeGas: A program for modelling hydrogen isotope fractionation during degassing of rhyolitic melts. *Volcanica* **3**, 155–168.

Waters C. L., Sims K. W. W., Perfit M. R., Blichert-Toft J. and Blusztajn J. (2011) Perspective on the genesis of E-MORB from chemical and isotopic heterogeneity at 9-10°n East Pacific Rise. *J. Petrol.* **52**, 565–602.

Zakharov D. O. and Bindeman I. N. (2019) Triple oxygen and hydrogen isotopic study of hydrothermally altered rocks from the 2.43–2.41 Ga Vetreny belt, Russia: An insight into the early Paleoproterozoic seawater. *Geochim. Cosmochim. Acta* **248**, 185–209. Available at: https://doi.org/10.1016/j.gca.2019.01.014.

Zakharov D. O., Bindeman I. N., Tanaka R., Friðleifsson G., Reed M. H. and Hampton R. L. (2019) Triple oxygen isotope systematics as a tracer of fluids in the crust: A study from modern geothermal systems of Iceland. *Chem. Geol.* **530**.

Zierenberg R. A., Schiffman P., Barfod G. H., Lesher C. E., Marks N. E., Lowenstern J. B., Mortensen A. K., Pope E. C., Bird D. K., Reed M. H., Friðleifsson G. Ó. and Elders W. A. (2013) Composition and origin of rhyolite melt intersected by drilling in the Krafla geothermal field, Iceland. *Contrib. to Mineral. Petrol.* **165**, 327–347.